Universität der Bundeswehr München

Secondary debris resulting from concrete slabs subjected to contact detonations

Dissertation

Moritz Achim Hupfauf

Secondary debris resulting from concrete slabs subjected to contact detonations

Moritz Achim Hupfauf

Vollständiger Abdruck der von der Fakultät für Bauingenieurwesen und Umweltwissenschaften der Universität der Bundeswehr München zur Erlangung des akademischen Grades eines

Doktor-Ingenieur (Dr.-Ing.)

angenommenen Dissertation.

Gutachter:

1. Prof. Dr.-Ing. habil. Norbert Gebbeken (EE)
2. Univ.-Prof. Dr.-Ing. Dr.-Ing. E.h. Manfred Curbach

Die Dissertation wurde am 29.01.2024 bei der Universität der Bundeswehr München eingereicht und durch die Fakultät für Bauingenieurwesen und Umweltwissenschaften am 09.05.2024 angenommen. Die mündliche Prüfung fand am 22.07.2024 statt.

Abstract

The present work addresses the secondary debris from concrete slabs subjected to contact detonations. The analysis is based on a series of experimental tests using a newly developed test setup. This test setup allows a detailed analysis of the protective side of the concrete slab regarding the spatial velocity distribution of the secondary debris and the preceding fragmentation of the concrete.

The variables of the test series are the thickness of the concrete slab, the steel fiber content and the mass of the explosive charge. The influence of the geometry of the explosive charge on the resulting load is determined using numerical simulations and taken into account in the experimental evaluations.

Both, the spatial velocity distribution of the secondary debris and the geometry of the spalling crater are approximated by rotationally symmetric descriptions to derive the kinetic energy of the secondary debris. The derived kinetic energy of the secondary debris is then used for a quantitative evaluation of steel fibers in the concrete.

In addition, numerical simulations are performed using two well-established material models to investigate their ability to simulate the resulting secondary debris. The most critical factors are determined to be the direction of the plastic flow and the fracture energy of the concrete at high strain rates.

In the last chapter, the impact of the secondary debris on people is analyzed using a demonstrator that has been developed based on the experimental findings.

Kurzfassung

Die vorliegende Arbeit befasst sich mit den sekundären Bruchstücken von Betonplatten, die einer Kontaktdetonation ausgesetzt sind. Die Analyse basiert auf einer Reihe von experimentellen Versuchen unter Verwendung eines neu entwickelten Versuchsaufbaus. Dieser Versuchsaufbau ermöglicht eine detaillierte Analyse der Schutzseite der Betonplatte hinsichtlich der räumlichen Geschwindigkeitsverteilung der sekundären Betonbruchstücke und der vorausgehenden Fragmentierung.

Die Variablen der Versuchsreihe sind die Dicke der Betonplatte, der Stahlfasergehalt und die Masse der Sprengladung. Der Einfluss der Sprengladungsgeometrie auf die resultierende Beanspruchung wird mittels numerischer Simulationen ermittelt und in den experimentellen Auswertungen berücksichtigt.

Sowohl die räumliche Geschwindigkeitsverteilung der sekundären Betonbruchstücke als auch die Geometrie des Abplatzkraters werden durch rotationssymmetrische Beschreibungen approximiert, um die kinetische Energie der sekundären Betonbruchstücke abzuleiten. Die kinetische Energie der sekundären Betonbruchstücke wird dann für eine quantitative Bewertung der Stahlfasern im Beton verwendet.

Zusätzlich werden numerische Simulationen mit zwei etablierten Materialmodellen durchgeführt, um deren Eignung für die Simulation von sekundären Betonbruchstücken zu untersuchen. Die kritischsten Faktoren sind dabei die plastische Fließrichtung und die Bruchenergie des Betons bei hohen Verzerrungsraten.

Im letzten Kapitel werden die Auswirkungen der sekundären Betonbruchstücke auf Personen anhand eines Demonstrators untersucht, der auf der Grundlage der experimentellen Ergebnisse entwickelt wurde.

Contents

List of Figures

List of Tables

1. Introduction

1.1. Motivation

Although the total number of terrorist attacks has mostly decreased in the recent years [IEP, 2023], their public awareness has increased significantly. This is largely due to the ongoing crises, their unpredictable nature, and the extensive media coverage of attacks [Karlos and Larcher, 2020]. As a result, there is a growing need for countermeasures to protect people and critical infrastructure from explosive attacks.

In the past, the focus of explosive attacks on buildings has been on the lower floors, where large quantities of explosives can be transported in a vehicle. The primary countermeasure to this threat is hardening of structures and adding perimeter controls to create distance between the explosive attack and the target building.

Due to developments in the field of unmanned aircraft systems (UAS), commonly referred to as drones, UAS are becoming commercially available at a relatively low purchase cost and are capable of carrying significant amounts of explosives over long distances [Karlos and Larcher, 2023]. This completely changes the scenario of an attack, as explosives can now be transported to locations on higher floors of a building that were previously considered safe. It also allows the explosives to be transported much closer to the target, since the airspace around a building in an urban environment is difficult to control. As a result, attacks become more focused on a specific area of a building and can cause significant damage with smaller amounts of explosives than those transported in a vehicle.

Another scenario results from the densification of urban spaces. This leads to much shorter distances between production facilities and offices or living spaces, which in some cases may even be located in the same building. As a consequence, an explosion caused by a malfunctioning machine can also become a threat for people in surrounding spaces that are not directly connected to the location of the original accident.

Both of these scenarios result in an explosive loading in close proximity to, or even in contact with, a concrete structure. In contrast to an explosion far away from a structure, the loading is much more localized and the resulting damage depends on the direct interaction of the blast wave with the material rather than on global parameters such as support conditions.

This localized interaction of the explosion with a concrete structure can result in concrete fragments being propelled away from the structure on the supposedly protected side, where they become a threat for people or technical installations. As the concrete fragments originate from the loaded structure and not from the explosive or its casing, they are referred to as secondary debris. Figure 1.1 shows an example of the secondary debris being propelled away on the protective side of a concrete slab loaded by a contact detonation.

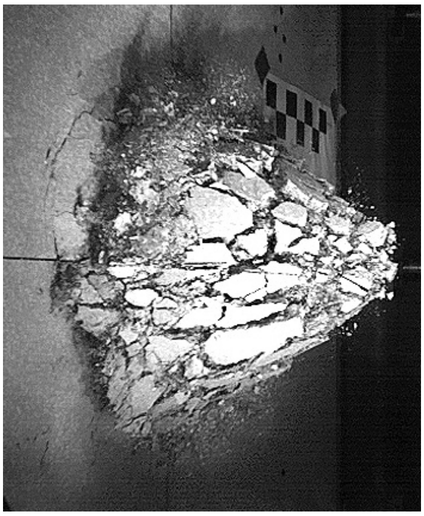

Figure 1.1.: Secondary debris on the protective side of a concrete slab loaded by a contact detonation

1.2. State of the art

In the case of a contact detonation, the shock wave is transmitted directly from the explosive charge into the loaded structure, where it induces an expanding shock wave [Tu et al., 2019]. During the propagation, the total energy of the shock wave spreads over the continuously expanding shock wave (divergence) [McVay, 1988]. The work done by the shock wave on the material converts the induced energy into forms of energy associated with heat, pore crushing and the generation of cracks (attenuation) [Meyers, 1994].

Both, the divergence of the shock wave and its interaction with the material change the shape and magnitude of the shock wave as it propagates through the concrete [McVay, 1988]. As long as the pressure exceeds the dynamic compressive strength of the material, the concrete is crushed and a crushing crater is formed [Gebbeken and Krauthammer, 2013].

When the shock wave reaches the opposite side of the concrete structure, it is reflected at this free surface. Due to the large impedance difference between the concrete and the surrounding air, the compressive shock wave is converted to a tensile wave during the reflection. The reflected tensile wave is initially superimposed on the remaining portion of the incoming compressive shock wave. If the resulting stress is greater than the dynamic tensile strength of the material, tensile cracks occur [McVay, 1988].

These tensile cracks result in fragmentation of the concrete on the protective side of the concrete structure, referred to as spalling. Because spalling results from a region of tensile failure on the protective side of a concrete slab, it can also occur without a complete breach of the concrete slab. In contrast to spalling, scabbing describes the ejection of concrete from the same side of the structure from which it was loaded [McVay, 1988].

The resulting secondary debris (spalled concrete fragments) has a momentum caused by the impulse of the shock wave trapped between the free surface of the concrete structure and the tensile cracks, minus the impulse of the resisting forces of the concrete [McVay, 1988], described by the fracture energy. The secondary debris poses a hazard on the protective side of a concrete structure, since it can harm people or damage technical installations.

Figure 1.2 shows a schematic depiction of two concrete slabs after being loaded by a contact detonation. The left figure shows the situation without a breach and the right figure shows the situation with a breach. The crushing crater is the region of mainly compressive failure and the spalling crater results mainly from tensile failure. The breach is the location of the narrowest opening, and represents the geometric transition between the crushing crater and the spalling crater.

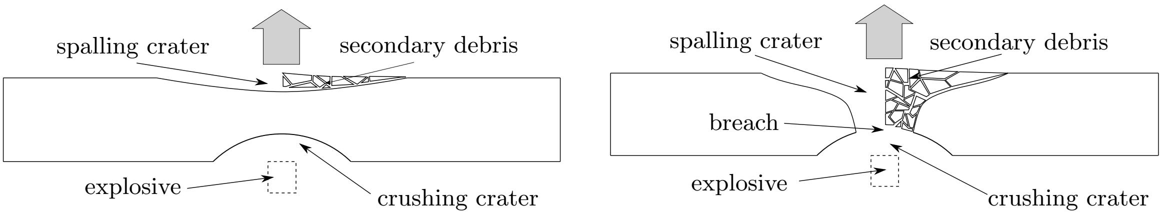

Figure 1.2.: Damaged areas without breach (left) and with breach (right)

Table 1.1 lists experimental test series with contact detonations on concrete slabs in chronological order. Some test series without contact detonations are included in the list because they provide information on the velocity of the secondary debris. Although this list does not claim to be complete, it is considered to be a good representation of tests that are publicly available in the literature.

Since experimental testing is expensive, many of the test series listed use a scaled test setup with reduced dimensions of the concrete slabs to reduce costs and make the test specimens easier to handle. Although the explosive mass can be scaled to some extent, strain rate effects and the porous mesoscopic structure of the concrete cannot be adequately accounted for by this scaling.

An important consequence of this scaling is that only few test series include tests in which the concrete slab is not breached by the detonation [Morishita et al., 2000], [Landmann, 2001], [Beppu et al., 2010], [Yamaguchi et al., 2011], [Dua and Braimah, 2020], which allows the different failure mechanisms (compressive and tensile) to be studied separately.

Most experimental test series focus on the damage of the concrete slab, which is evaluated in terms of the dimensions of the crushing crater, the breach and the spalling crater. Only a few authors provide information on the fragmentation and the velocity of the secondary debris.

HS recordings from the protective side of the concrete slab were performed by [van Amelsfort and Weerheijm, 1988] and [Lönnqvist, 1993] in order to determine the average velocity of the secondary debris. Using a ballistic pendulum, [van Amelsfort and Weerheijm, 1988] also make statements about the impact of the secondary debris based on experimental tests. The maximum velocity of the secondary debris was determined by [McVay, 1988] using HS recording. Since the quality of the HS recordings in these series of tests was not as advanced as it is today, it was not possible to measure the

Table 1.1.: Selected experimental test series from the literature

Reference	Number of Tests	Location of Detonation	Expl. mass (Type)	Thickness of concrete slab	Material
[McVay, 1988]	40	contact, near- and far-field	0.5–13.2 kg (C4)	13.7–28.5 cm	NSC, HSC SFR-NSC
[van Amelsfort and Weerheijm, 1988]	64	contact	0.07–0.17 kg (PETN)	6 cm	NSC
[Lönnqvist, 1993]	28	contact	0.01–1.0 kg (scaled) 5.0 kg (full scale) (NSP 71)	4–7 cm (scaled) 32 cm (full scale)	NSC
[Morishita et al., 2000]	40	contact and near-field	0.11–0.44 kg (Pentolite)	10 cm	NSC
[Landmann, 2001]	18	contact	0.35–0.85 kg (PETN1.5)	20–45 cm	NSC
[Herrmann, 2002]	5	contact	0.6–3.3 kg (scaled) (TNT+COMP B)	25–50 cm	NSC (no reinf.)
[Rickman et al., 2007]	4	contact	0.55–6.2 kg (C4)	20 cm	NSC
[Beppu et al., 2010]	14	contact	0.05 kg (C4)	8 cm	NSC +FRP Laminate
[Yamaguchi et al., 2011]	13	contact	0.1–0.2 kg (Penthrite)	5–10 cm	NSC,PFR-NSC
[Li et al., 2015]	2	contact	1.0 kg (not specified)	10 cm	NSC, UHPC
[Li et al., 2016]	7	contact	0.1–1.0 kg (TNT)	10–15 cm	NSC, UHPC
[Bewick, 2017]	6	shock tube	-	5 cm	NSC (no reinf.)
[Luccioni et al., 2018]	15	contact and near-field	0.05–0.49 kg (TNT equiv.)	5 cm	HSC
[Remennikov et al., 2018]	3	contact	0.15–0.25 kg (COMP B)	10 cm	NSC, HSC
[Dua and Braimah, 2020]	5	contact	0.5 kg (TNT)	7.5–20 cm	NSC
[Shi et al., 2020]	5	near-field	2.0–6.0 kg (TNT)	12 cm	NSC
[Grisaro et al., 2021]	6	near-field	2.0 kg (TNT)	15 cm	HSC, SFR-HSC

NSC: normal strength conrete, HSC: high strength concrete, UHPC: ultra high performance concrete, SFR: steel fiber reinforced, FRP: fiber reinforced polymer, PFR: Polyethylen fiber reinforcement velocity of the secondary debris in more detail.

An alternative approach was employed by [Landmann, 2001], who evaluated the velocity of the secondary debris from projectile motion and the location of the secondary debris fragments on the ground after the detonation test.

A series of tests in which the velocity of the secondary debris was determined in more detail using HS recordings was conducted by [Bewick, 2017]. The tests involved 5 cm thick unreinforced concrete slabs that were loaded by a shock tube. The experimental setup of [Bewick, 2017] inspired the setup for the tests in the present work.

Two more recent series of tests with near-field detonations, that provide information on the velocity of the secondary debris were performed by [Shi et al., 2020] and [Grisaro et al., 2021]. The HS recordings in these tests were heavily disturbed by the effects of the explosion (light and dust), such that only the maximum velocity [Shi et al., 2020] and the average velocity [Grisaro et al., 2021] of the secondary debris could be determined. Nevertheless, [Grisaro et al., 2021] also includes some estimates about the impact of the secondary debris on people on the protective side of the concrete slab.

The experimental tests are usually accompanied by numerical simulations with the aim to achieve a good agreement between the experimental test and the numerical simulations. Calibrated numerical simulations can help to gain a better insight into the occurring processes, allowing the evaluation of parameters that cannot be directly measured in experimental tests. Due to their implementation in the hydrocode LS-Dyna, the most commonly used plasticity based material models for this purpose are the Karagozian & Case model (KCC) [Crawford et al., 2012], the Riedel, Hiermaier, and Thoma model (RHT) [Grunwald et al., 2017], and the Continous Surface Cap Model (CSCM) [Murray, 2007].

An example for the simulation of a contact detonation using the CSCM model can be found in [Dua and Braimah, 2020], who calibrates the numerical simulations on experimental tests with plain and reinforced concrete slabs with thicknesses of 10 cm and 20 cm loaded with 500 g of TNT. The calibrated numerical simulations are then used for a parametric study regarding the influences of the explosive mass, the concrete slab thickness, the concrete strength and the reinforcement ratio.

Probably the most commonly used model for the simulation of contact detonations on concrete slabs using different types of concrete is the KCC model. [Li et al., 2015] use the KCC model to simulate contact detonations on concrete slabs made of ultra high performance concrete (UHPC) and compare them to the same setup with normal strength concrete. [Zhao et al., 2019] perform simulations of concrete slabs that have been reinforced with steel plates attached with shear studs, while [Wang et al., 2021] investigate the influence of a polymer coating on the concrete slab. Simulations of contact detonations on concrete slabs using modified versions of the KCC model can be found in [Hong et al., 2017], [Wang et al., 2021].

In the case of the RHT model, there are quite a few simulations of concrete slabs loaded by near-field detonations [Riedel et al., 2010], [Wang et al., 2013], [Wu et al., 2020], but very few with contact detonations [Luccioni et al., 2018], [Esteban and Gebbeken, 2017]. A comparison of the RHT model for the simulation of a contact detonation with the Hartmann, Pietzsch Gebbeken model (HPG) [Hartmann et al., 2010] can be found in [Esteban and Gebbeken, 2017].

The HPG model is not as widely used in the research community because it is not readily implemented in any of the commercial hydrocodes. Nevertheless, different versions of this model are used, in the works of [Greulich, 2004] and [Hartmann, 2009]. A notable difference is that the simulations using the HPG model do not rely on an erosion criterion to predict the damage to the concrete slab, while this is the case in most simulations of contact detonations using other material models.

The focus of most publications on the simulation of contact detonations is the resulting damage to the concrete slab. The only cases where the author could find statements on the fragmentation and velocity of the secondary debris from contact detonations are [Zhou and Hao, 2009] and [Greulich, 2004]. [Zhou and Hao, 2009] performs 2D simulations of the concrete at the mesoscopic scale, including the individual aggregates, to analyze the fracture mechanism and the velocity of the secondary debris. However, there were no experimental results available to validate the simulations performed. [Greulich, 2004] shows an evaluation of the velocity distribution of the secondary debris from the numerical simulations, but only roughly compares it with the experimental results of [Landmann, 2001], who gives a velocity for the secondary debris in the range from $6\,\mathrm{m\,s^{-1}}$ to $50\,\mathrm{m\,s^{-1}}$.

Consequently, a detailed analysis of the velocity of secondary debris based on experimental tests is required to better understand the underlying processes and to validate the existing material models in more detail.

1.3. Objective and structure of this work

To the author's knowledge, there is no comprehensive description of the velocity of the secondary debris from a concrete slab due to a contact detonation. Therefore, the main objective of this work is to experimentally determine the velocity distribution of the secondary debris in order to gain a better understanding of the underlying mechanisms and to make predictions about the impact on the protective side.

After this introduction, chapter 2 gives an overview of the fundamentals of the formation, propagation and reflection of shock waves, which are necessary to describe the damage of the concrete slab. This is followed by a description of the main principles of the equations of state and strength models used for the simulation of solids in hydrocodes.

Chapter 3 addresses the loading from a contact detonation based on numerical simulations. In a first step, a convergence study is performed to determine the necessary mesh size for a correct simulation of the detonation. This is followed by an evaluation of the influence of the different length to diameter ratios of the cylindrical explosive charges used in the series of tests presented in chapter 4.

After a description of the experimental setup and the measurements performed, the damage to the concrete slab is documented in chapter 4. The focus is on the dimensions of the spalling crater, since it is the most important damaged region for the resulting secondary debris. For this purpose, a rotationally symmetric description of the spalling crater is derived from the 3D scans to allow a better comparison of different tests.

In addition, a tracking algorithm is developed and applied to the acquired HS recordings to determine the velocity and trajectory of the secondary debris. For further evaluation, the velocity distribution in the radial direction is approximated by an enveloping curve and validated based on the fracture pattern of the spalling crater and the DIC measurements performed. Based on the rotationally symmetric descriptions of the spalling crater and the velocity distribution, the kinetic energy of the secondary debris is derived. The kinetic energy is then used to quantitatively evaluate the influence of steel fibers in the concrete on the secondary debris.

Chapter 5 provides a comparison of two well-established material models (KCC and RHT) with respect to their ability to represent the behavior of a concrete slab loaded by a contact detonation. First, these material models are calibrated to give a similar description of the concrete. The most important parameter in this context is the fracture energy, since it describes the resistance of the concrete, which is decisive for the velocity of the secondary debris. The calibrated material models are then used to simulate two characteristic experimental test constellations representing the situations with and without a breach in the concrete slab. The comparison of the two material models is used to evaluate the different influences of the fracture energy, the porosity and the direction of plastic flow, but also the influence of erosion on the simulation of a contact detonation.

Based on the experimental findings, chapter 6 presents a demonstrator that allows predictions of the impact of the secondary debris on people on the protective side of concrete slabs. For this purpose, existing models for the description of a lethal impact of flying debris on a person are compared in detail.

2. Theoretical principles

2.1. Fundamentals on blast

An explosion is defined as the sudden release of energy in a very short time. The source of the energy is not important in this context and can result from chemical or nuclear reactions as well as from the rapid combustion of dust in confined spaces or under high pressure, e.g. in a tank.

Depending on the speed u at which the reaction propagates relative to the speed of sound c of the propellant, the explosion is called a deflagration ($u < c$) or a detonation ($u \geq c$). The main difference between this and other exothermic processes is not the total amount of energy released, but the fact that the release of energy occurs within an extremely short period of time in the order of 10^9 W cm^{-2} [Meyers, 1994].

The information about an applied load propagates through a medium in the form of waves at their respective speed of sound. In quasi-static processes, the velocity of the loading is significantly smaller than the speed of sound of the medium. Therefore, the material response is not determined by a single wave passage, but by the final state that occurs after multiple reflections at different surfaces.

When the duration of the load application is in the order of magnitude of the sound velocity of the respective medium or occurs in the form of shock waves, the final state is no longer sufficient to describe the behavior of the material. As a result, the different waves and their interaction with the material during the propagation must be considered.

Different types of loading can be classified according to the so-called strain rate, which is defined as the change in strain over time $\dot{\varepsilon} = d\varepsilon/dt$. Figure 2.1 shows different types of loading and their associated range of strain rates.

The strain rate in concrete directly behind a contact detonation is in the order of 10^4 s^{-1}

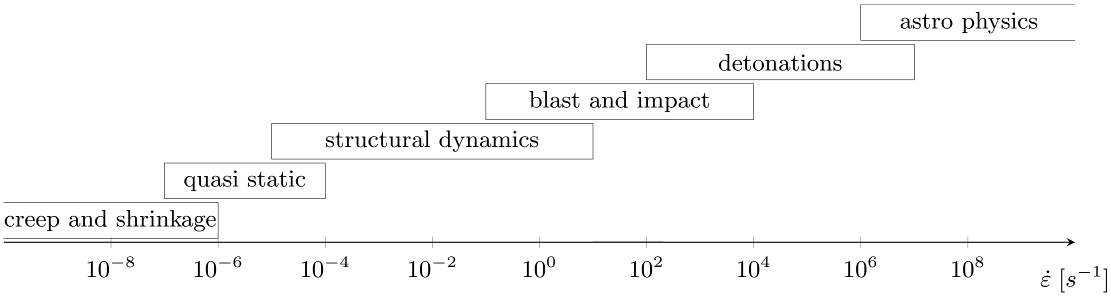

Figure 2.1.: Different load types and associated strain rates [Gebbeken et al., 2013]

[Tu et al., 2022] and significantly exceeds the sound velocity of concrete in the order of $10^3\,\mathrm{m\,s^{-1}}$. Therefore, the interaction of the occurring waves with the concrete must be considered in detail.

The loading of a structure by an explosion depends on the mass of the explosive charge and its distance from the loaded structure. In this context, it is common to classify detonations as either near-field detonations or far-field detonations, since the resulting response of the structure varies significantly between the two cases. An empirical quantity used to distinguish between near-field detonations and far-field detonations is the scaled distance Z:

$$Z = R \cdot W^{-1/3} \tag{2.1}$$

Where R is the shortest distance between the center of the explosive charge and the surface of the loaded structure in m and W is the TNT-equivalent mass of the respective explosive in kg. Detonations with $Z \leq 0.5\,\mathrm{m\,kg^{-1/3}}$ are defined as near-field detonations, and detonations with $Z > 0.5\,\mathrm{m\,kg^{-1/3}}$ are defined as far-field detonations [Gebbeken et al., 2012]. Some authors extend the definition of the near field to an "extreme" near field for $Z \leq 0.5\,\mathrm{m\,kg^{-1/3}}$ and a "late" near field for $0.5 < Z \leq 2\,\mathrm{m\,kg^{-1/3}}$ [Barr et al., 2023].

The cubic relationship reflects the fact that the energy of an undisturbed detonation propagates approximately spherically in space. Thus, the resulting pressure decreases continuously in proportion to the increasing surface area of the propagating shock wave. Consequently, the most effective measure to minimize the effects of a detonation is to increase the distance.

In a far-field detonation, the shock wave initially propagates through the air and the resulting load can be assumed to act uniformly over the relevant surface of a structure. The response of the loaded structure is then dominated by global parameters such as the static system and support conditions.

In near-field detonations, the load on the structure from the detonation becomes more localized with decreasing distance. As a result, the structural response does not occur in the form of global bending and shear failure, but local material failure due to the introduced pressure waves and reflected tensile waves is the governing factor. Global influences, such as the support conditions, play only a minor role.

A contact detonation is a special case of a near-field detonation where the explosive is in direct contact with the surface of the loaded structure. Therefore, the shock wave is transmitted directly from the explosive charge into the loaded structure without first propagating through the air and the structural response is extremely localized.

2.2. Waves in solids

The following section provides an overview of the formation, propagation, interaction, and reflection of shock waves. These fundamentals are necessary to describe the damage mechanisms inside of the concrete as result of a contact detonation. For more detailed information, the reader is referred to the literature such as [Meyers, 1994], [Hiermaier, 2008] and [Forbes, 2012].

When a load is applied to a structure, the information about that load is not immediately available throughout the whole structure. Rather, it is first transmitted by waves with a propagation velocity c, starting from the location of the load application to the different locations within the structure. At the atomistic level, these waves can be thought of as a sequence of collisions between neighboring atoms/particles. The velocity of the individual oscillating atoms/particles, and thus the velocity of the associated mass, is called the particle velocity u_p.

The occurring wave types can be classified according to their propagation velocity c and the direction of the associated oscillation of the individual particles with velocity u_p:

- The type of wave with the highest propagation velocity is the longitudinal wave.

Longitudinal waves are characterized by an oscillation of the individual particles in parallel to the propagation direction of the wave propagation. The oscillation of the particles relative to each other results in local density and pressure changes in the material, which are a necessary condition for the formation of shock waves. If the directions of the wave propagation and the particle oscillation have the same sign, the wave is referred to as a compressive wave. Conversely, if the sign is opposite, the wave is referred to as a tensile wave.

- Another type of wave that propagates at a slower velocity is the transversal wave. In a transversal wave, the individual particles oscillate perpendicular to the direction of wave propagation. Unlike the longitudinal wave, there is no change in the density of the medium. Consequently, shock waves cannot occur because they are the result of different propagation velocities of the different parts of a wave at different pressures interacting with each other.
- Another type of wave is the surface or Rayleigh wave, which propagates along the surface of the respective medium. The particles move along elliptical paths, and the oscillation decays rapidly. The Rayleigh wave velocity provides the theoretical maximum velocity for crack propagation.

2.2.1. Formation of shock waves

At high stresses, solid materials lose most of their deviatoric strength and behave like fluids under hydrostatic pressure. As a result, the deviatoric stress components can initially be neglected and the material response is described in terms of the hydrostatic pressure. The point at which this behavior becomes relevant is called the Hugoniot Elastic Limit (HEL). The HEL represents the dynamic yield strength of the material beyond which the material begins to deform plastically.

The propagation velocity c of hydrodynamic compressive waves in materials can be described as the derivative of the pressure p with respect to the density ρ.

$$c^2 = \frac{dp}{d\rho} \tag{2.2}$$

Intuitively, this relation can be explained by the fact that at higher pressures, and thus higher densities, the individual particles of the medium move closer together, allowing the information about an applied load to propagate more quickly in the form of waves.

Figure 2.2 shows qualitatively the nonlinear compression curve of an elastic-plastic material (left). This curve is also called Hugoniot and shows the pressure p as a function on the specific volume $V = \rho^{-1}$ of the material, with its slope proportional to the propagation velocity according to equation (2.2). Figure 2.2 (right) shows the resulting formation of a shock front.

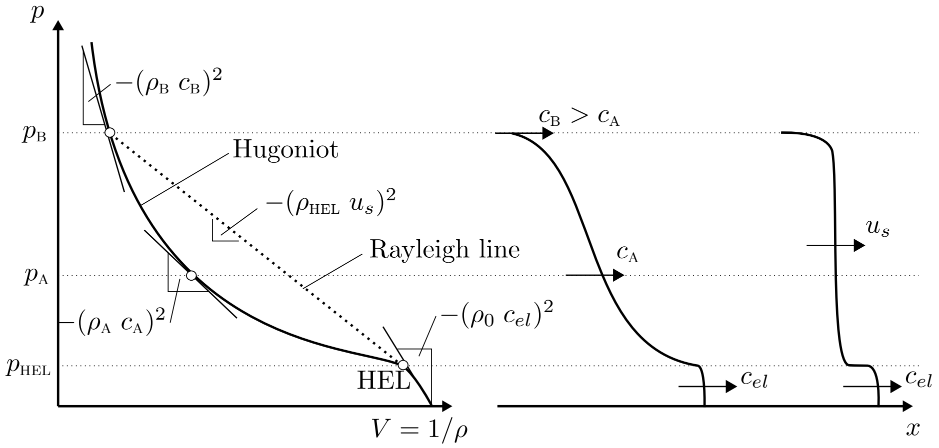

Figure 2.2.: Hugoniot and Rayleigh line (left) and resulting formation of a shock wave (right)

As long as the hydrostatic pressure is in the region below the Hugoniot elastic limit (HEL), only elastic waves with a constant velocity c_{el} occur.

Once the HEL is exceeded, the slope of the Hugoniot decreases and plastic wave components occur. According to equation (2.2), the propagation velocity of the longitudinal waves is proportional to the slope of the Hugoniot . Consequently the plastic wave components initially have a lower propagation velocity than the elastic wave components ($c_{pl} < c_{el}$) resulting in a dispersion of the wave.

As the pressure increases, the slope of the Hugoniot, and therefore the plastic wave velocity, increases steadily. As a result, the slower moving plastic wave components at lower pressures are caught up by subsequent faster wave components with greater amplitude. This leads to an increasingly steep front of the resulting wave called a shock front. As long as the propagation velocity of the shock front is slower than the elastic wave velocity, the shock front is preceded by an elastic precursor.

Accordingly, a concave shape with $d^2p/dV^2 > 0$ as well as a negative slope $dp/dV < 0$ of the Hugoniot are necessary conditions for the formation of a shock front.

At the shock front propagating with a velocity u_s, the change of pressure p, density ρ, specific internal energy e and particle velocity u_p does not occur continuously along the Hugoniot, but abruptly. Figure 2.3 shows the situation at the shock front for the one-dimensional case with the corresponding parameters of the undisturbed case (e_0, ρ_0, p_0, $u_{p,0}$) and the situation after passage of the shock front (e, ρ, p, u_p). For the following derivation, the particle velocity in front of the shock front is assumed to be zero $u_{p,0} = 0$.

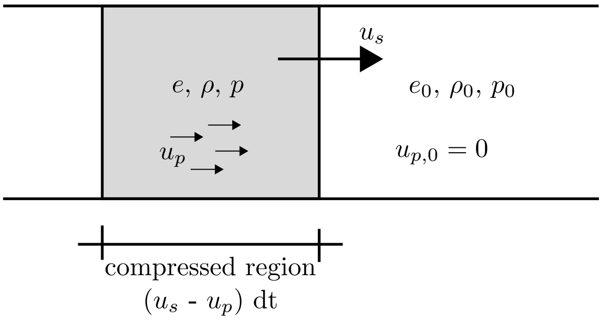

Figure 2.3.: Change of state of the material at the shock front

The processes at the shock front can be described by the conservation equations for mass, momentum and energy, also called Rankine-Hugoniot equations. For the one-dimensional case these equations can be derived as:

$$\text{Mass:} \quad \rho - \rho_0 = \rho \, \frac{u_p}{u_s} \tag{2.3}$$

$$\text{Momentum:} \quad p - p_0 = \rho_0 \, u_s \, u_p \tag{2.4}$$

$$\text{Energy:} \quad e - e_0 = \frac{p + p_0}{2} \, (\frac{1}{\rho_0} - \frac{1}{\rho}) \tag{2.5}$$

The resulting Hugoniot is defined as the locations of all possible states that can be reached after the passage of a shock wave. These locations are not reached by following the path of the Hugoniot, but occur by a discontinuous jump along the so-called Rayleigh line shown in figure 2.2. When plotted in the $p-V$ space, the Rayleigh line is a straight line.

Solving equation (2.3) by u_p and substituting into equation (2.4) together with the definition of the specific volume $V = \rho^{-1}$ gives the slope of the Rayleigh line:

$$-\,(\rho_0\, u_s)^2 = \frac{p - p_0}{V - V_0} \tag{2.6}$$

As long as the slope of the Rayleigh line is smaller than that of the elastic part of the Hugoniot, the shock front has an elastic precursor with faster propagation velocity. This elastic precursor increases the pressure in front of the shock front to that of the HEL. Consequently the reference state 0 in equation (2.6) becomes the HEL.

As soon as the slope of the Rayleigh line is steeper than the elastic part of the Hugoniot, the elastic wave parts are overtaken by the following plastic wave parts and a completely vertical shock front without elastic precursor is established.

From the three conservation equations (2.3) - (2.5) there are five variable parameters: pressure p, particle velocity u_p, shock velocity u_s, density ρ and specific internal energy e. Consequently, an additional equation is needed to solve the resulting system of equations in dependence on one of the parameters.

For this purpose, pairs of particle velocity u_p and shock velocity u_s for a material at different pressures are measured experimentally and usually approximated by a linear relation of the following form:

$$u_s = c_0 + S\, u_p \tag{2.7}$$

Where c_0 is the bulk sound speed of the material at zero pressure and S the slope of the u_s-u_p-relation.

Figure 2.4 shows experimentally measured u_s-u_p pairs for normal strength concrete from different authors including fitted linear polynomials according to equation (2.7) for three different regions.

Based on figure 2.4 three different regions of the u_s-u_p relation can be identified.

Initially, the shock velocity decreases rapidly up to a particle velocity of about $100\,\mathrm{m\,s^{-1}}$.

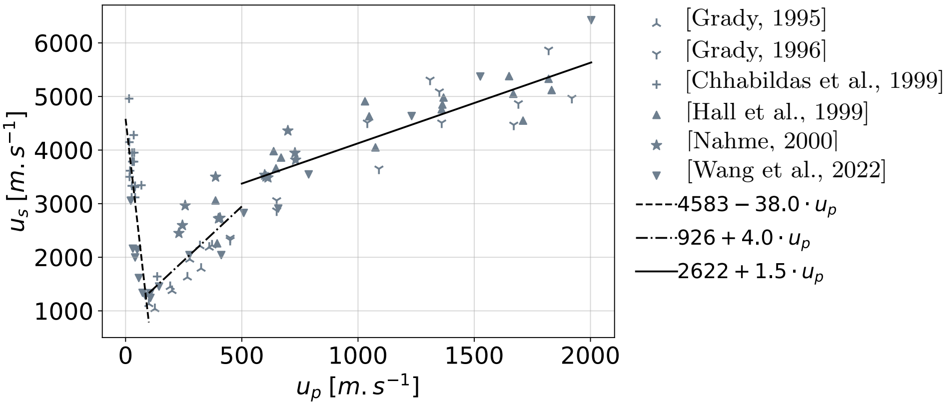

Figure 2.4.: u_s-u_p relation from the literature including fitted linear polynomials

Then the concrete begins to compact by a crushing of its porous structure. This results in an increasing shock velocity up to a particle velocity of about $500\,\mathrm{m\,s^{-1}}$ [Neel, 2018], [Hall et al., 1999]. The behavior in this region is heavily depended on the porosity of the concrete. Due to its lower porosity high strength concrete shows a smaller decrease of the shock velocity in this region [Neel, 2018].

In the third region, the concrete is fully compacted and the properties of the matrix material dominate the behavior. Differences between concretes with different static compressive strength and density become negligible in this region [Neel, 2018].

The linear relation between the shock velocity and the particle velocity according to equation (2.7) can be used to solve the Rankine-Hugoniot equations for the conservation of mass (2.3), momentum (2.4) and energy (2.5). To describe the material behavior under explosive loading, the third region of the fully compacted matrix material is usually used for the u_s-u_p relation. The pressure p_{H} and the energy e_{H} behind the shock front (hugoniot state) can then be formulated as a function of the density ρ:

$$p_{\mathrm{H}} = p_0 + c_0^2\,\rho_0\,\frac{\eta}{(1-S\eta)^2} \tag{2.8}$$

$$e_{\mathrm{H}} = e_0 + \frac{\eta}{\rho_0}\,p - \frac{\eta^2\,c_0^2}{2\,(1-S\,\eta)^2} \tag{2.9}$$

$$\text{with} \qquad \eta = 1 - \frac{\rho_0}{\rho}$$

2.2.2. Attenuation of shock waves

A complete shock wave consists of the shock front, a flat top and a release part. As long as the velocity of the shock front is smaller than the elastic wave speed it is preceded by an elastic precursor. Figure 2.5 shows the idealized shape of a shock wave during its propagation.

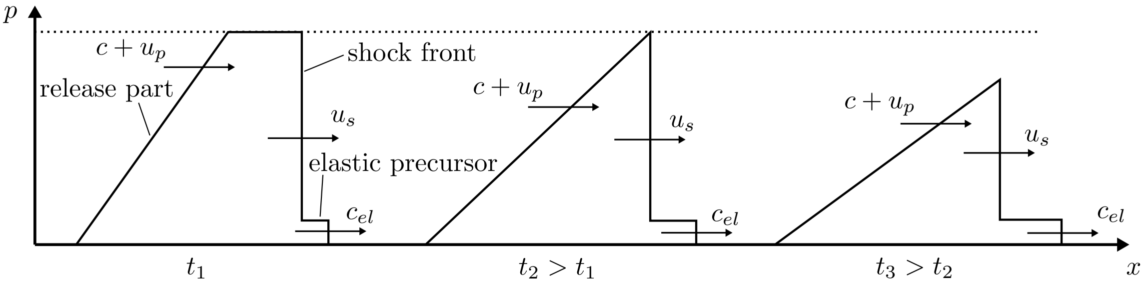

Figure 2.5.: Attenuation of a shock wave as consequence of the release part

The shock front travels at a constant velocity u_s depending on its maximum pressure (slope of the Rayleigh line). The flat top occurs only in impact situations and depends on the duration of the load, dictated by the size of the impactor. In the case of a detonation, this region can be described by a reaction zone that converts the solid explosive into gaseous detonation products (ZND model [Forbes, 2012]).

The reaction zone of a detonation does not have a constant pressure, but starts with the von Neumann spike at the front of the chemical reaction and ends with the Chapman-Jouget pressure when the reaction is complete. For practical applications, this very narrow reaction zone is often neglected and the pressure at the front of the shock wave is assumed to be the Chapman-Jouget pressure.

At the Chapman-Jouget pressure, the propagation velocity of the shock front reaches the sound velocity of the gaseous product from the explosive plus the associated particle velocity $D = c_{\text{CJ}} + u_{p,\text{CJ}}$. Therefore, the Chapman-Jouget pressure is a necessary condition to generate a stable propagation of a shock front from an explosive.

The following release wave has a propagation velocity $c + u_p$, which depends on the respective pressure. As can be seen from the slope of the Hugoniot and the Rayleigh line in figure 2.2, the propagation velocity of the release wave is faster than that of the shock front. However, as long as the shock wave propagates in the explosive at a velocity that correlates with the Chapman-Jouget pressure, the energy of the chemical reaction will drive the shock front and prevent the release portion from catching up and attenuating the peak pressure.

As soon as the shock front propagates outside of the driving explosive or at a peak pressure below the Chapman-Jouget pressure, the release part overtakes the preceding shock front and continuously reduces the peak pressure back to the surrounding ambient pressure (see figure 2.5).

2.2.3. Reflection and interaction of shock waves

The influence of reflections at the interface/boundary between different media plays an important role in the propagation of shock waves. Since there is a change in the equation of state at the interface between different media, the associated parameters of pressure and particle velocity must also change. According to the continuity principle, both the particle velocity and the resulting pressure must be equal on both sides of the interface.

The resulting reflection of the shock wave can be described in terms of the shock impedance, which is defined as the product of the density ρ and the shock propagation velocity u_s of a material. Broadly speaking, the transmission of a shock wave from one medium to another medium with a higher impedance results in a higher pressure and particle velocity on both sides of the interface. The transmission of a shock wave from one medium to a medium with lower impedance results in a lower pressure and particle velocity on both sides of the interface.

The decisive quantity in this context is initially not the pressure, but the particle velocity, which in turn corresponds to an associated pressure. Thus, for example, the superposition of two equal pressure waves does not lead to a doubling of the pressure, but to a doubling of the particle velocity with the associated higher pressure [Meyers, 1994].

Figure 2.6 qualitatively shows the sequence of events during the interaction of the shock wave from an explosive with a concrete slab.

The explosive changes from a solid state to a gaseous state during the detonation. Therefore, the impedance of the gaseous state is the relevant parameter to describe the interaction with the concrete at the interface. Since the impedance of the gaseous state of the explosive is usually lower than the impedance of the concrete, this leads to a

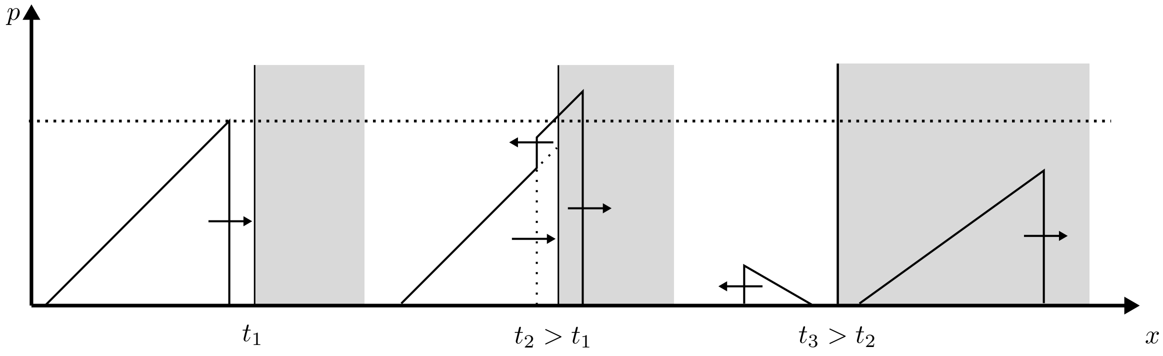

Figure 2.6.: Interaction of the shock wave from an explosive with the concrete slab (gray)

higher pressure at both sides of the interface. This is achieved by a superposition of the reflected portion of the shock wave with the remaining incoming shock wave, while a shock wave with the same higher pressure is transmitted into the concrete.

The transmitted portion of the shock wave then propagates through the concrete while its peak pressure continuously decreases due to the interaction with the surrounding material and the absence of a propellant.

When the shock wave reaches the protective surface of the concrete slab, it is reflected again. Since the impedance of the surrounding air is much smaller than that of the concrete, this reflection can be treated analogous to the reflection of a shock wave at the interface to a medium with zero impedance (free surface).

During this reflection at the free surface, the pressure on both sides must be zero. Therefore, the reflected part of the incoming shock wave must cancel out the remaining incoming parts of the shock wave. This results in a particle velocity at the reflecting surface that is approximately twice that of the incoming shock wave. Since the reflected part of the shock wave propagates in the opposite direction to the motion of the individual particles, it creates a tensile stress in the material.

After the reflection, the reflected tensile wave is initially superimposed on the remaining incoming compressive wave. As soon as the amplitude of the reflected tensile wave is greater than that of the incoming compressive wave, a tensile stress occurs in the concrete. Since tensile waves do not have a concave pressure-density relation they cannot form a shock front and exhibit a dispersive behavior.

Figure 2.7 qualitatively shows the sequence of events during the reflection of the shock wave at the protective surface of a concrete slab.

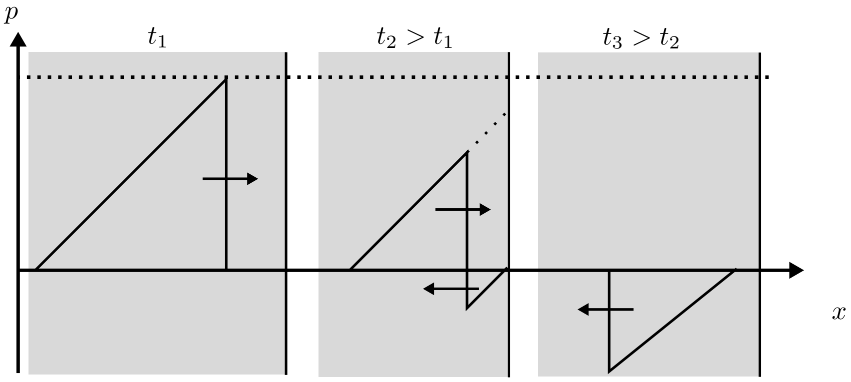

Figure 2.7.: Reflection of the shock wave at the protective surface of the concrete slab (gray)

2.3. Equation of state

In the following section, the necessary theory to describe the hydrostatic behavior of the concrete is given. For this purpose, the presented equations are oriented on the material model by the Riedel, Hiermaier and Thoma (RHT) [Grunwald et al., 2017], which is also used for the derivation of the equation of state (EOS) in chapter 5.

2.3.1. Mie-Grüneisen theory

The Hugoniot state given by equations (2.8) and (2.9) describes only the state directly behind a shock front and not the whole spectrum of possible states of the material. To derive a complete equation of state, an additional assumption is necessary. For this purpose, the Mie-Grüneisen [Grüneisen, 1912] theory can be used, which describes the macroscopic behavior of a solid by the interaction of its different atoms. Based on the associated assumptions, the complete equation of state is derived from a reference state given by the Hugoniot state p_{H} and the associated energy difference together with the Grüneisen parameter Γ.

$$p = p_{\mathrm{H}} + \frac{\Gamma}{V}\left(e - e_{\mathrm{H}}\right) \tag{2.10}$$

Where the Mie-Grüneisen parameter Γ represents the change in pressure p with the internal energy e for a given volume V. According to [Meyers, 1994], a good approximation of the Grüneisen parameter Γ for a material at zero pressure can be obtained from the slope S of the u_s-u_p-relation:

$$\Gamma \cong 2S - 1 \tag{2.11}$$

Figure 2.8 shows an example of a nonlinear equation of state based on the Mie-Grüneisen theory (2.10) including the shocked states along the Hugoniot curve calculated by the Rankine-Hugoniot equations (2.8) and (2.9).

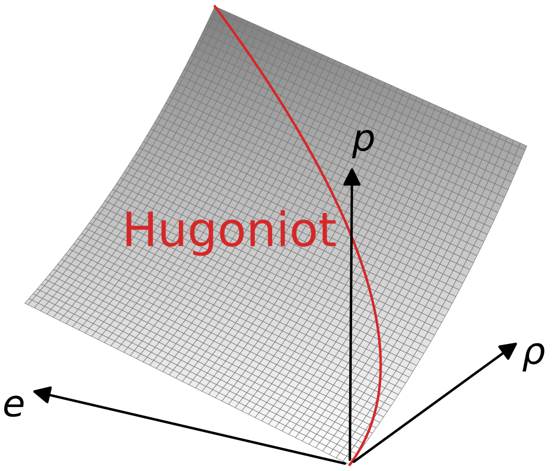

Figure 2.8.: Non linear equation of state based on the Mie-Grüneisen theory including the shocked states along the Hugoniot curve

2.3.2. Porosity of concrete

Concrete is a porous material, and its macroscopic behavior is strongly dependent on the underlying mesoscopic scale. Figure 2.9 shows the characteristic compaction curve (Hugoniot) of concrete that consist of the shocked states of a full equation of state.

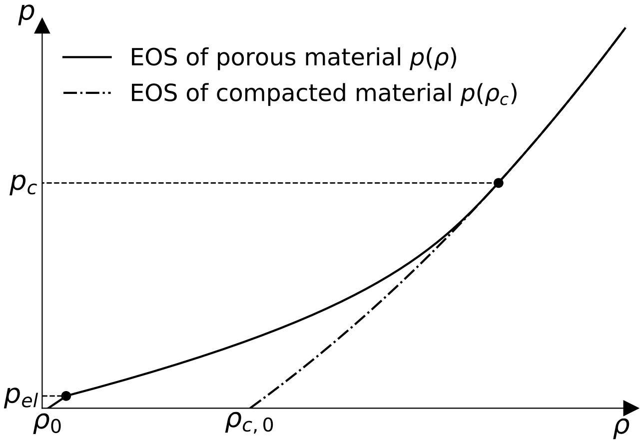

Figure 2.9.: Compaction curve of porous concrete according to $p - \alpha -$EOS

The behavior of a porous material such as concrete can be divided into three distinct regions. First, there is a region of predominantly elastic deformation below the pressure at the Hugoniot elastic limit (p_{el}).

This is followed by a region of initially lower stiffness than the elastic part, called the compaction phase. In this region, the stiffness of the material continuously increases as the pressure increases. During this process, the concrete undergoes irreversible plastic deformation, mainly in the form of stability failure of the regions between the individual pores and a resulting compaction of the material.

The third region is reached after the pores in the concrete are fully compacted at the compaction pressure p_c. The material behavior in this region can be described by the EOS of the compacted material without pores and the parameters from the associated u_s-u_p-relation (compacted/third region in figure 2.4).

A model to describe the phenomenological behavior during the compaction phase is the p-α equation of state introduced by [Herrmann, 1969]. The idea is to describe the hydrostatic behavior of the concrete based on the equation of state of the compacted matrix material with density $\rho_{c,0}$ and relate it to the porous material with density ρ through the porosity value α.

$$p = \frac{1}{\alpha} f(\rho\, \alpha, e) \tag{2.12}$$

Where the porosity α is defined as the ratio between the density of the compacted matrix material without pores at zero pressure $\rho_{c,0}$ and the current density of the porous material ρ.

$$\alpha = \frac{\rho_{c,0}}{\rho} \tag{2.13}$$

In equation (2.12) the function $f(\rho\ \alpha, e)$ can be given by any equation of state for a solid material like for example that given by equation (2.10). The factor α^{-1} is an extension of the p-α equation by [Carroll and Holt, 1972] to average the pressure in the compacted matrix material over the total porous volume [Hiermaier, 2008].

To describe the porosity as a function of the pressure, [Butcher and Karnes, 1969] derived a relation originally used to describe porous iron:

$$\alpha = 1 + (\alpha_{\text{HEL}} - 1)\left(\frac{p_c - p}{p_c - p_{\text{HEL}}}\right)^n \tag{2.14}$$

This equation fulfills the necessary criteria, that $\alpha = \alpha_{\text{HEL}}$ at the Hugoniot elastic limit, $\alpha = 1$ at the compaction pressure p_c and $\frac{d\alpha}{dp} < 0$ in between. The exponent n can be used to calibrate the curvature for different materials based on experimental data.

The Equations (2.12) and (2.14) must then be solved iteratively to describe the hydrostatic behavior of the material.

2.3.3. Polynomial description

The description of the EOS as implemented in the RHT model is based on a polynomial description of the Hugoniot depending on the ratio between the current density ρ and the density of the compacted matrix material $\rho_{c,0}$ at zero pressure.

$$p = A_1\mu + A_2\mu^2 + A_3\mu^3 + (B_0 + B_1\mu)\rho_{c,0}e \qquad \mu \geq 0 \tag{2.15}$$

$$p = T_1\mu + T_2\mu^2 + B_0\rho_{c,0}e \qquad \mu < 0 \tag{2.16}$$

$$\tag{2.17}$$

with:

$$\mu = \frac{\rho}{\rho_{c,0}} - 1 \tag{2.18}$$

By comparing the polynomial EOS in equation (2.15) with the Hugoniot state in equations (2.8) and (2.9) the parameters A_i of the polynomial EOS for the compacted material can be approximated according to [Riedel, 2000] by:

$$A_1 = \rho_0 \, c_{B,c}^2 \tag{2.19}$$

$$A_2 = A_1(1 + S(S-1)) \tag{2.20}$$

$$A_3 = A_1(2(S-1) + 3(S-1)^2) \tag{2.21}$$

Where ρ_0 is the density of the porous concrete, $c_{B,c}$ is the bulk velocity of the compacted concrete at zero pressure and S the associated slope of the u_s-u_p-relation.

Since the Hugoniot state in equations (2.8) and (2.9) is derived from the conditions at the shock front, it is only valid for positive hydrostatic pressure. In the case of negative hydrostatic tensile states, this derivation is not relevant since no shock waves can occur. Consequently, the EOS for tensile states in equation (2.15) ($\mu < 0$) is not based on the same derivation, but has to be calibrated on experimental tests. If no other data is available, the linear parameter is usually set analogue to the compressive value $T_1 = A_1$ and the quadratic parameter is $T_2 = 0$.

Since $c_{B,c}$ and S are derived from the part of the u_s-u_p-relation describing the compacted concrete, the resulting equation of state also describes the associated material behavior. The compaction path of the porous concrete between the Hugoniot elastic limit p_{el} and the compaction pressure p_c is then derived from the EOS of the compacted material according to equation 2.12 based on the porosity α.

2.4. Strength model

The remainder of the description of the material with plasticity models is based on the separated description of hydrostatic and deviatoric parts of the stress tensor. While the hydrostatic behavior of the material is described by the EOS, the deviatoric material behavior is given by a strength model. This strength model describes the homogenized material behavior of concrete on the macroscopic scale.

After a brief introduction to some theoretical background of the principal stress space, the following section describes the most important points for the description of concrete behavior with the plasticity models used for the numerical simulations in this work.

2.4.1. Principal stress space and invariants

In the three-dimensional space the stress state in a point can be described using the Chauchy stress tensor, which is a symmetric tensor of second order in Cartesian coordinates. As mentioned, the basis for the description of the material behavior in the context with hydrocodes is the separation of the Cauchy stress tensor σ_{ij} in a hydrostatic part $p\ \delta_{ij}$ described by the equation of state and a deviatoric part s_{ij} described by the strength model.

$$\sigma_{ij} = s_{ij} - \delta_{ij} p \tag{2.22}$$

In this Einsteins summation convention is used to describe summation over repeated indices and δ_{ij} is the Kronecker delta. The negative sign for the hydrostatic parts is owed to the general agreement, that compressive stresses are defined as negative while hydrostatic compression p is defined as positive.

The Cauchy stress tensor can be transformed into the principal stress space where all shear stresses vanish. The stress state is then described by the stresses in the three principal directions n_i satisfying the condition:

$$\sigma_{ij} n_j = \lambda n_i \tag{2.23}$$

$$(\sigma_{ij} - \lambda \delta_{ij}) n_j = 0 \tag{2.24}$$

Where λn_i are the components of the stress tensor parallel to the normal vectors in the principal directions $n_i = \delta_{ij} n_j$. Equation (2.24) is a homogeneous system of equations which has a non trivial solution for $n_j \neq 0$ if the determinant of the coefficients vanishes. By solving for the determinant, the characteristic polynomial is obtained:

$$det(\sigma_{ij} - \lambda\delta_{ij}) = \lambda^3 - I_1\lambda^2 + I_2\lambda - I_3 = 0 \tag{2.25}$$

with:

$$I_1 = \sigma_{ii} = \sigma_1 + \sigma_2 + \sigma_3 \tag{2.26}$$

$$I_2 = \frac{1}{2}(\sigma_{ii}\sigma_{jj} - \sigma_{ij}\sigma_{ji}) = \sigma_1\sigma_2 + \sigma_2\sigma_3 + \sigma_3\sigma_1 \tag{2.27}$$

$$I_3 = det(\sigma_{ij}) = \sigma_1\sigma_2\sigma_3 \tag{2.28}$$

The characteristic polynomial in equation (2.25) has three roots, namely the eigenvalues λ_i of the stress tensor, which can be identified as the principal stresses σ_i. For the description of the strength surfaces theses principal stresses are sorted in descending order as $\sigma_1 \geq \sigma_2 \geq \sigma_3$. The coefficients I_1, I_2, I_3 can be derived from the principal stresses and are independent of the orientation of the coordinate system. Therefore, they are called invariants of the stress tensor.

The invariants of the deviatoric stress tensor can be calculated accordingly in arbitrary direction s_{ij} and in principal directions s_i. By definition the first invariant of the deviatoric stress tensor is equal to zero.

$$J_1 = s_{ii} = 0 \tag{2.29}$$

$$J_2 = \frac{1}{2}s_{ij}s_{ji} = \frac{1}{2}tr(s^2) = \frac{1}{2}(s_1^2 + s_2^2 + s_3^2) \tag{2.30}$$

$$J_3 = \frac{1}{3}s_{ij}s_{jk}s_{ki} = \frac{1}{3}tr(s^3) = s_1s_2s_3 \tag{2.31}$$

An illustrative representation of stress states in the principal stress space $(\sigma_1, \sigma_2, \sigma_3)$ can be given by the Haigh-Westergaard coordinates (ξ, ρ, θ). The Haigh-Westergaard coordinates specify different stress states by cylindrical coordinates as a function on the invariants of the stress tensor (I_1, J_2, J_3). The main diagonal of the principal stress space with $\sigma_1 = \sigma_2 = \sigma_3$ gives the hydrostatic axis with pressure $p = -\frac{1}{3}I_1$. Associated deviatoric stress states are located on deviatoric planes perpendicular to this hydrostatic axis with a distance ξ from the origin of the principal stress space.

$$\xi = \frac{I_1}{\sqrt{3}} \tag{2.32}$$

The position on the deviatoric plane is given by the distance from the hydrostatic axis ρ and the angle θ. The distance from the hydrostatic axis is also called deviatoric length, and can be described in dependence on the second invariant by:

$$\rho = \sqrt{2J_2} \tag{2.33}$$

The angle θ, also called Lode angle, includes varying behavior in compression and tension and can be described in dependence on the third invariant as:

$$\cos(3\theta) = \frac{J_3}{2}\left(\frac{3}{J_2}\right)^{3/2} \tag{2.34}$$

An angle $\theta = 0$ describes deviatoric tension, an angle $\theta = \pi/3$ deviatoric compression and an angle $\theta = \pi/6$ describes a state of pure shear. For isotropic materials, this pattern is repeated over the entire circumference of the circle.

A three-dimensional depiction of the Haigh-Westergaard coordinates (ξ, ρ, θ) for a stress state Q in the principal stress space is illustrated in figure 2.10. The associated pressure at the point P is located in the deviatoric plane, which is perpendicular to the hydrostatic axis ($\sigma_1 = \sigma_2 = \sigma_3$). The distance of this surface to the origin along the hydrostatic axis is given by the first Haigh-Westergaard coordinate ξ. The second and third Haigh-Westergaard coordinates ρ and θ then describe the length and direction of the vector $\overline{PQ}$ inside of the deviatoric plane. Planes which are perpendicular to the deviatoric planes along the hydrostatic axis are called meridian planes.

2.4.2. Characteristics of deviatoric concrete behavior

In order to describe the macroscopic behavior of concrete, it is important to also consider the highly inhomogeneous mesoscopic structure of the concrete. This mesoscopic structure consists of the porous mortar, coarser aggregates and an interfacial transition

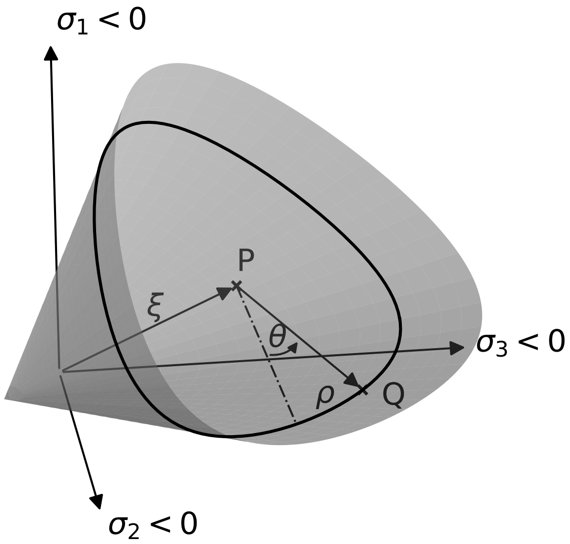

Figure 2.10.: 3-dimensional depiction of the Haigh-Westergaard coordinates (ξ, ρ, θ) for a stress State Q in the principal stress space

zone (ITZ) in between. In general, the ITZ is the weakest link in the mesoscopic structure of the concrete and cracks propagate mainly in the mortar along the surfaces of the individual aggregates [van Mier, 1984].

As the contained aggregates are usually much stiffer than the surrounding mortar, compressive loading leads to an inhomogeneous stress distribution in the concrete. Therefore, concrete under uni-axial compressive loading will fail primarily due to internal lateral tension in the mortar between the individual aggregates [Häussler-Combe, 2022].

Under hydrostatic confining pressure concrete can withstand much higher loads than in the purely uni-axial case. Although the concrete is compacted due to hydrostatic loading (section 2.3), the lateral confinement supports the granular structure of the concrete leading to a higher load bearing capacity. This effect influences the maximum strength of the concrete as well as the residual strength of the compacted concrete after failure. Figure 2.11 show qualitatively the compressive stress-strain relation of concrete for different confining pressures.

Below the elastic limit of the concrete, the stress increases almost linearly with the strain, which is uniformly distributed throughout the material. As the stress approaches the maximum strength of the concrete, the behavior becomes highly non-linear and

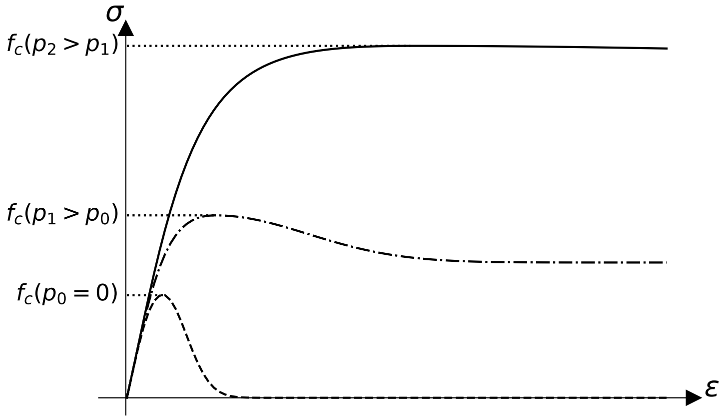

Figure 2.11.: Compressive stress strain relation of concrete for different confining pressures

microcracks start to form, resulting in a decreasing stiffness of the material (hardening). This effect is much more pronounced in the case of compressive loading.

Once the maximum strength has been reached, the formation of the microcracks manifests itself in a continuous reduction in material strength as the strain increases (softening). Under a sustained tensile load, the strain localizes itself in the form of a crack that separates the material.

Figure 2.12 qualitatively shows the tensile stress-strain relation of concrete for uni-axial tensile loading. For tensile loading there is no remaining strength due to hydrostatic confinement.

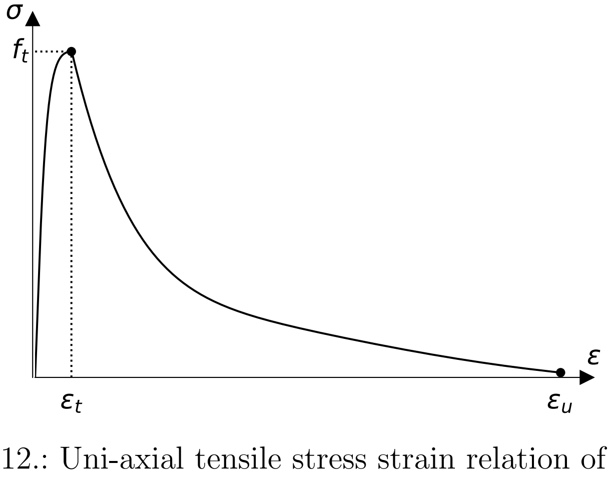

Figure 2.12.: Uni-axial tensile stress strain relation of concrete

2.4.3. Strength surfaces

Plasticity models describe the phenomenological behavior of materials on the macroscopic scale as an isotropic material. Effects at the mesoscopic and microscopic scales are not directly considered, but only the resulting behavior of the homogenized material. This is done on the basis of limiting strength surfaces in the principal stress space.

Typically, these surfaces are the elastic limit (Y_e), the maximum strength (Y_m), and the residual strength after failure (Y_r). The basis for these surfaces is usually given by the compressive meridian of the respective surface. A qualitative example of the compressive meridians for the different surfaces is given in figure 2.13 (left).

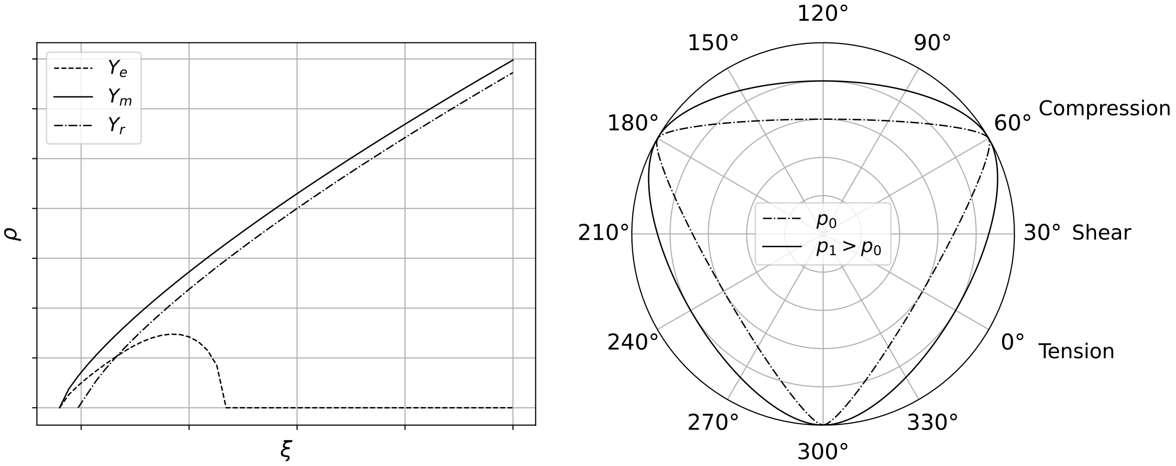

Figure 2.13.: Strength surfaces: compressive meridians (left) and deviatoric plane (right)

The compressive meridians start at the point of hydrostatic tensile failure (Y_m, Y_e) or at zero (Y_r) and increase continuously with increasing pressure, following a concave shape. Failure from purely hydrostatic compressive loading is initially not described by the strength model. Some models add a cap to the elastic limit (Y_e), which limits the elastic material behavior in the direction of hydrostatic pressure.

The tensile and shear meridians are then derived from the compressive meridian using the third invariant of the deviatoric stress tensor J_3. In both material models used in this work, the resulting shape of the strength surface in the deviatoric plane is described by the Willam and Warnke formulation [Willam, K.J. and Warnke, E.P., 1974] in equation (2.35).

$$\rho(\theta, Q) = \frac{2(1-Q^2)\cos\theta + (2Q-1)[4(1-Q^2)\cos^2\theta + 5Q^2 - 4Q]^{1/2}}{4(1-Q^2)\cos^2\theta + (1-2Q)^2} \tag{2.35}$$

Here, Q is a parameter that changes the shape of the surface from a Rankine triangle at $Q = 0.5$ to a Drucker-Prager circle at $Q = 1$. For concrete, the shape of the strength surfaces in the deviatoric plane is approximately triangular at low pressure (brittle material behavior) and approaches a circle with increasing hydrostatic pressure (ductile material behavior). Figure 2.13 (right) shows a qualitative example of a deviatoric plane according to Willam and Warnke for two different pressures.

The Willam and Warnke formulation has a continuous curvature around the entire circumference without sharp edges. This is advantageous in avoiding numerical problems because the direction of the plastic flow typically depends on the normal vector of the yield surface (associativity), which is not unique in the case of a discontinuous shape of the strength surface.

2.4.4. Plastic flow

To describe the associated deformation, the tensor of the deviatoric strain increment $d\varepsilon$ is decomposed in an elastic part $d\varepsilon^e$ and a plastic part ε^p:

$$d\varepsilon = d\varepsilon^e + d\varepsilon^p \tag{2.36}$$

In case of a isotropic material the elastic part can be described by a linear elastic material law (e.g.Hook's law) that links the elastic strains to the associated stresses in dependence on the bulk modulus K and the shear modulus G.

Once the elastic limit is reached, the material starts to deform plastically and the plastic strain increment needs an additional assumption referred to as the plastic flow rule. Mathematically the flow rule of a plastic strain increment $d\lambda$ is defined to be in the direction normal to a plastic potential $f(\sigma)$.

$$d\varepsilon^p = d\lambda \frac{\partial f}{\partial \sigma} \tag{2.37}$$

If the plastic potential f is given by the current yield surface Y, the flow rule is called associative because it is directly associated with the current yield surface. Consequently, any flow rule that is not perpendicular to the current yield surface is called non-associative. Figure 2.14 qualitatively shows a yield surface with vectors indicating the direction of associative and non-associative plastic flow rules.

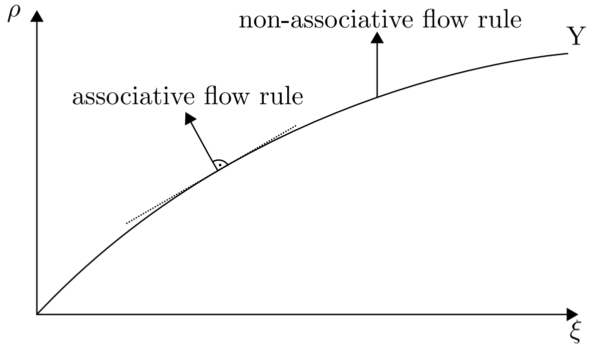

Figure 2.14.: Current yield surface with associative and non-associative flow rule

If the vector of the plastic strain increment has a component in the hydrostatic direction, this leads to a volume change due to a plastic strain increment from deviatoric stresses, also called shear dilatation. Graphically, this volume change can be explained by the fact, that the granular mesoscopic structure of the concrete is pushed apart by shear deformations, resulting in an increase in volume. Figure 2.15 shows a graphical representation of shear dilatation due to the granular mesoscopic structure of the concrete.

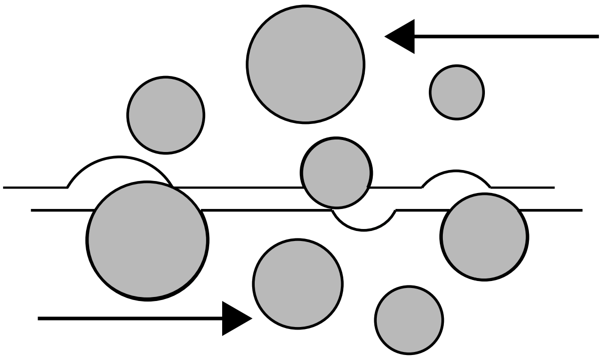

Figure 2.15.: Graphical representation of shear dilatation

2.4.5. Fracture energy and regularization

Most cracks in normal strength concrete propagate through the mortar matrix and along the mortar-aggregate interface [van Mier, 1984]. This leads to a distribution of the associated strain over a region called the fracture process zone. For a description of the material behavior the microcracks are assumed to be uniformly distributed over the fracture process zone (FPZ). Due to the heterogeneity of the concrete and the size of the included aggregate d_a, the FPZ of concrete extends over a much larger region than, for example, in metals. According to [Bažant and Oh, 1983], the size of the fracture process zone l_c for concrete can be estimated to be about $l_c = 3\,d_a$.

In practical applications, strain cannot be measured directly, but is always a relative displacement of different points with respect to a reference length that depends on the measurement method. This does not have a big influence in case of purely elastic deformations with a strain that is uniformly distributed over the tested specimen. But, as soon as the material gets close to the maximum strength, the strain starts to localize in an increasingly smaller region. Therefore, a constant measurement length will result in a smaller strain although the total displacement is the same [Chen and Han, 1988].

In numerical simulations, the reference length for the calculation of the strain is given by the characteristic length of the elements. In case of solid elements this characteristic length l_e is defined as a function of its volume $l_e = V^{1/3}$. This predefined reference length can lead to a non-objective behavior in numerical simulations, since the size of the spatial discretization strongly influences the resulting strains [Bažant and Oh, 1983].

Plasticity models are based on the assumption, that the stress and strain can be averaged over a representative volume. However, this also implies, that the inhomogeneities of the material are much smaller than this representative volume. Therefore, the size of the FPZ l_c is considered to be the minimum acceptable size of the spatial discretizations in numerical simulations when modeling the material with homogeneous models [Bažant and Oh, 1983]. For a smaller spatial discretization, the assumption of a homogeneous distribution of stress and strain is not valid anymore, since the influence of the mesoscopic structure starts to dominate the resulting behavior.

This correlation between the heterogeneity of the concrete and a minimal spatial discretization is a challenge for numerical simulations of contact detonations, since a spatial discretization well below the size of the FPZ is required to accurately describe the propagating shock waves within the material [Khoe and Weerheijm, 2012]. A possible solution for this is to model the mesoscopic structure of the concrete including the individual aggregates [Riedel, 2000], [Hartmann, 2009], [Zhou and Hao, 2009], [Grunwald, 2023]. While this is feasible for small structures and simplified 2D simulations, simulations of larger structures still have to rely on a homogeneous description of the material due to the immense computational requirements [Häussler-Combe, 2022].

A simple method to minimize the non-objectivity of the numerical simulations with respect to the element size is a regularization scheme based on the fracture energy of the concrete (Crack Band Model). For this, the area under the softening part of the tensile stress-strain relation is calibrated to the fracture energy of the concrete G_f with a size of the FPZ l_c equal to the characteristic size of the spatial discretization ($l_c = l_e$).

$$G_f = l_c \int_{\varepsilon_t}^{\varepsilon_u} \sigma d\varepsilon \tag{2.38}$$

A graphical representation of this correlation can be found in figure 2.16

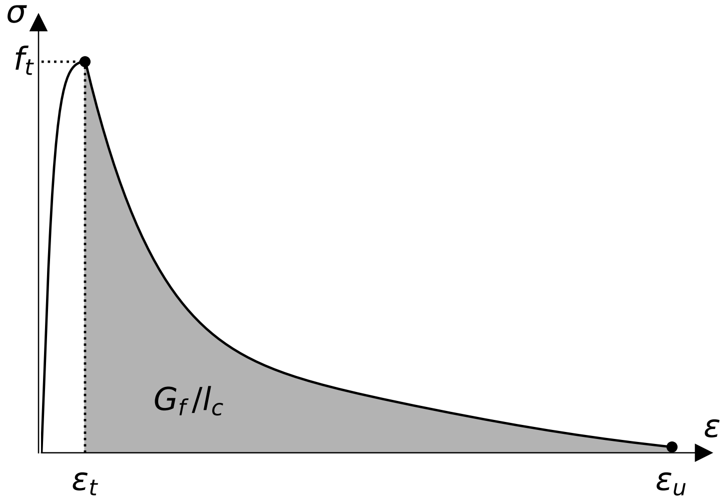

Figure 2.16.: Empirical tensile stress-strain-relation for concrete [Hordijk, 1991] and correlation with fracture energy

The parameters of the material model are then calibrated so that each element with a characteristic size l_e dissipates the total fracture energy G_f. However, this also implies that each element contains the entire fracture process zone. While this is true for element sizes larger than the FPZ ($l_e \geq l_c$), the regularization overestimates the fracture energy of a structure discretized by an element size smaller than the FPZ ($l_e < l_c$), since several elements span the FPZ [Khoe and Weerheijm, 2012].

Another possibility is to reduce the fracture energy of the individual elements so that several elements spanning the FPZ sum up to the total fracture energy. However, this can lead to localization of the strain in a single element (failure of the weakest link) and consequently an underestimation of the total fracture energy.

2.4.6. Influence of the strain rate

Concrete, like many other materials that exhibit damage and fracture, shows an increase in strength, stiffness, fracture energy and ductility at high strain rates. In the case of concrete, this increase occurs much earlier than in other materials such as ceramics and metals. The main reasons for this, according to [Weerheijm and Vegt, 2010], are the comparatively low quasi-static tensile strength of the concrete and its coarse heterogeneity at the mesoscopic scale. As a consequence, the failure process is dominated by the mesoscopic structure with aggregates in the order of 10 mm.

While the increase in the fracture energy, ductility and stiffness are still part of the ongoing discussion, the effect on the strength of the concrete is widely accepted. However, the reasons for this increase in strength and whether it is a true material property or due to structural effects such as inertia and triaxiality is not fully understood [Xu and Wen, 2013].

Ozbolt [Ožbolt and Riedel, 2013] lists three different effects that influence the time dependent behavior of concrete. These are the influence of inertia at the microcrack level, a viscous behavior of the matrix material between the cracks, and inertia effects on a structural level. While the first two effects prevail at low and medium loading rates up to about $1\,\mathrm{s}^{-1}$, the third effect is dominant at higher loading rates. Therefore, different parts of the strength increase have to be included in the constitutive law based on the numerical simulation performed. While in implicit simulations the full effect has to be included, in explicit simulations the inertia effects can already be partially taken into account by the numerical model depending on the discretized scale.

Based on experimental results and additional numerical simulations, [Li et al., 2009] concludes that the increase in compressive strength at high strain rates derived from Split

Hopkinson Pressure Bar (SHPB) tests is significantly overestimated. This is due to lateral inertia effects resulting from the influence of Poisson's ratio on the axial acceleration, leading to a lateral confinement. This lateral confinement increases the measured axial material strength and therefore leads to an incorrect interpretation of the strength increase. Nevertheless, according to [Lu and Li, 2011] and [Xu and Wen, 2013] the strength increase due to lateral confinement is only relevant in case of the compressive strength.

The tensile strength increase is mainly attributed to the inertia of microcracks in between the aggregates. Therefore, in the context of plasticity models that describe the concrete as homogenized on the macroscopic scale, the strength increase in tension can be considered a material property.

For implementation in a constitutive law, the strength increase is usually given by a dynamic increase factor (DIF).

$$DIF = \frac{f_{dyn}}{f_{qs}} \tag{2.39}$$

Where the DIF is a dimensionless factor relating the dynamic strength of the concrete f_{dyn} to the quasi-static strength of the concrete f_{qs}.

Figure 2.17 shows the apparent strength increase of the concrete in compression and tension with increasing strain rate. The gray dots mark measurements from different authors that have been collected by [Xu and Wen, 2013]. The large scatter of the data, especially for compressive loading, is due to the fact that the tests were performed by many different authors using different test setups and a variety of concrete mixtures and strengths. The lines show empirically fitted curves from different authors for concrete with a mean compressive strength of 43 MPa.

The increase in strength is much more pronounced in the case of the tensile strength. While the measured compressive strength shows a maximum increase by a factor of about $DIF = 2$ at a strain rate of $10^2\,\mathrm{s}^{-1}$ the tensile strength is increased by a factor of about $DIF = 8$ at the same strain rate. Measurements for strain rates higher than $10^3\,\mathrm{s}^{-1}$ are not available in the literature and extrapolations are merely assumptions. According to [Riedel, 2000] the increase of the tensile strength is limited to a factor of $DIF_t = 8$ at a strain rate of $10^4\,\mathrm{s}^{-1}$ for practical applications in the SHB bar (tensile

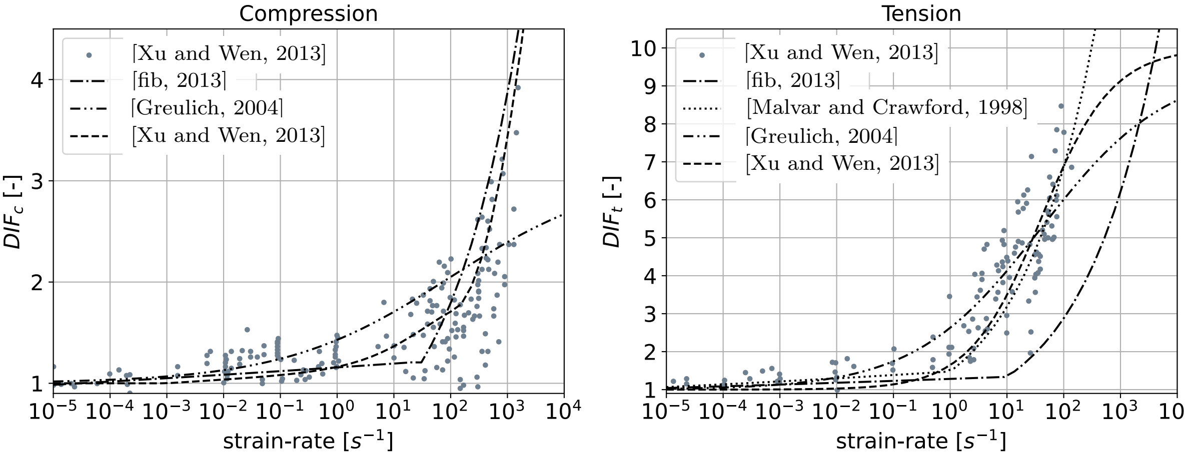

Figure 2.17.: Apparent Dynamic Increase Factor (DIF) for the strength of concrete in compression (left) and tension (right)

configuration). This is due to the assumption that at higher strain rates the incident compressive wave would already destroy the concrete before it can be reflected, resulting in a tensile stress.

3. Numerical simulation of contact detonations

In contrast to far-field detonations, the pressure wave from a contact detonation does not first propagate through the air, but is transmitted directly from the explosive charge into the loaded structure. As a result, the pressure and strain rate in a loaded structure are much higher than in far-field detonations and the resulting structural response is dominated by local material failure rather than global parameters, such as support conditions.

For far-field detonations, there are established methods for determining the required blast parameters, such as the semi-empirical method of [Kingery and Bulmash, 1984]. [Kingery and Bulmash, 1984] classify the propagation of the shock wave as either spherical, for cases where the shock wave can propagate freely in all directions, or hemispherical, for cases where the propagating shock wave is influenced by reflections on a surface in contact with the explosive charge. In addition, the method of [Kingery and Bulmash, 1984] assumes a spherical shaped explosive charge that is ignited at its center. This assumption is valid for far-field detonations, since the shock waves of differently shaped explosive charges approach those of spherical charges during their propagation [Xiao et al., 2020a].

Below a scaled distance of $Z \lesssim 4.0\,\mathrm{m\,kg^{-1/3}}$, this is no longer true, since the geometry and orientation of the charge, as well as the location of the ignition within the charge, have a large influence on the peak pressure and the maximum impulse of the emerging shock wave [Xiao et al., 2020b], [Sherkar et al., 2016].

In order to quantitatively analyze the influence of the charge geometry on the resulting load from the contact detonations in the present test series, numerical simulations are performed by the author. These numerical simulations can help to gain a deeper insight into the physical processes and thus improve the understanding of the associated phenomena.

After an initial description of the numerical model and the employed material models, the influence of the numerical spatial discretization is analyzed in a mesh sensitivity study. Subsequently, numerical simulations with different length to diameter ratios of the cylindrical charges are performed.

The influence of the different length to diameter ratios of the cylindrical charges is compared on the basis of the resulting total impulse and an energy equivalent impulse introduced by [Rigby et al., 2019]. The result of this comparison is a factor that relates the mass of cylindrical charges with different length to diameter ratios to that of equivalent spherical charges based on the total impulse and the energy equivalent impulse.

The numerical simulations are performed by the author with the commercial hydrocode LS-Dyna version R13.1.0 [Lsdyna, 2021]. To reduce the computational cost, the symmetry of the test setup is exploited by modeling only a quarter of the setup with symmetry boundary conditions. Both the explosive and the airspace are described using the structured arbitrary Lagrangian Eulerian solver (S-ALE) as implemented in LS-Dyna.

ALE is a numerical method that couples the formulations of the Eulerian and Lagrangian descriptions of physical problems. In the Eulerian description, the motion of a structure or a fluid is numerically described within a fixed mesh. This enables the simulation of very large deformations without running into numerical problems due to disadvantageous distortions of the underlying elements. At the same time, this can lead to a loss of the exact interfaces of a structure as it moves through the mesh, since the associated material points are not directly bound to distinct nodes of the numerical discretization.

In the Lagrangian description, the motion of a structure is described within a mesh that is directly fixed to the structure. This allows a very precise description of the geometry of the structure, which is especially relevant at the interfaces between different materials. However, for large deformations this can lead to numerical problems if the elements become too distorted.

The ALE method combines these two descriptions by computing each time step time steps using a Lagrangian discretization and performing additional Eulerian steps, called advection, when the mesh becomes too distorted. These advection steps return the mesh to an undistorted configuration, while the material remains in its deformed configuration. The advection scheme employed in the presented simulations is the van Leer half-index shift advection algorithm (METH=-2) [Lsdyna, 2021].

3.1. Material models

3.1.1. Explosive

The explosive is modeled with the empirical Jones-Wilkins-Lee equation of state [Lee et al., 1968], [Lsdyna, 2021]:

$$p(V,e) = A\left(1-\frac{\Gamma}{R_1 V}\right)\exp\left(-R_1 V\right) + B\left(1-\frac{\Gamma}{R_2 V}\right)\exp\left(-R_2 V\right) + \frac{\Gamma}{V}e \tag{3.1}$$

Where V is the volume relative to the initial state and e is the specific detonation energy per volume. These variables are set to $V = 1.0$ and $e = e_0$ at the beginning of the simulation. A constant Grüneisen coefficient is included as Γ. The parameters A and B have the unit of pressure while $R1$ and $R2$ are dimensionless.

The detonation process is controlled by the *MAT_HIGH_EXPLOSIVE_BURN material model with the density ρ, the detonation velocity d and the Chapman-Jouguet pressure p_{cj}.

The ignition of the detonation takes place at the center of the surface of the explosive charge facing away from the concrete slab (see figure 3.1).

The explosive used in this series of tests is SEMTEX10. SEMTEX10 is a commercially available plastic explosive containing PETN as its main component. Table 3.1 shows the relevant parameters based on a thermochemical simulation in the thermochemical code CHEETAH [Fried and P., 1994]. The detailed output of the CHEETAH simulations can be found in appendix section A.7.

For comparison with other test series, the explosive mass is compared to that of an equivalent explosive charge of TNT. The parameters used for TNT according to [Dobratz, 1981] are also given in table 3.1.

Table 3.1.: Material parameters for explosives (appendix A.7)

	A [MPa]	B [MPa]	E_0 [MPa]	$R1$ [-]	$R2$ [-]	Γ [-]	ρ [$\mathrm{kg\,m^{-3}}$]	d [$\mathrm{m\,s^{-1}}$]	p_{cj} [MPa]
Semtex10	6711×10^2	9370	8447	4.91	1.19	0.4	1631	7474	22.62×10^3
TNT	3712×10^2	3231	7000	4.15	0.95	0.3	1630	6930	21.00×10^3

In the following, the curved surface of the cylindrical charge will be referred to as the side, and the flat surfaces as the ends. The radial direction is perpendicular to the curved side and the axial direction is perpendicular to the flat ends.

3.1.2. Air

Although the influence of the surrounding air is negligible in a contact detonation, it must be modeled as the base material of the ALE domain in which the explosive propagates during the detonation. The air is modeled as an ideal gas using the purely hydrostatic material model *MAT_NULL in conjunction with a linear equation of state *MAT_LINEAR_POLYNOMIAL:

$$p = (\gamma - 1)\frac{\rho}{\rho_0}e \tag{3.2}$$

Where ρ is the current density, $\rho_0 = 1.255\,\mathrm{kg\,m^{-3}}$ is the initial density, and e and $e_0 = 0.253\,\mathrm{MPa}$ are the current and initial internal energies. $\gamma = c_p/c_V = 1.4$ is the isentropic coefficient defined as the quotient of the specific heat capacities at constant pressure c_p and constant volume c_V.

3.2. Spatial discretization - mesh sensitivity

To determine the necessary element size for the simulation, a mesh sensitivity study is performed for the ALE domain including the explosive charge and the ambient air. A cylindrical explosive charge of 1500 g SEMTEX10 with a radius of 50 mm and a height of 120 mm is selected for this study.

The explosive charge is modeled as a quarter cylinder inside a 100 x 100 x 130 mm ALE domain with symmetric boundary conditions (figure 3.1). Instead of modeling a concrete structure in contact with the explosive charge, one side of the ALE domain has reflecting boundary conditions (gray shaded in figure 3.1). This removes the influence of a contact algorithm between the explosive charge and the concrete structure from the simulation and allows a separate investigation. The flat surface of the charge in contact with the concrete structure is modeled flush with this reflecting boundary. The remaining boundaries are defined with flow-out conditions to allow a free propagation of the blast wave out of the simulated ALE domain.

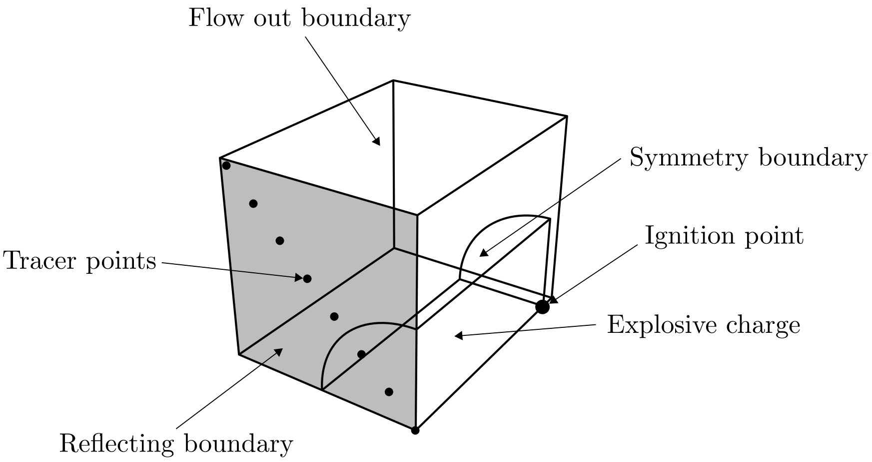

Figure 3.1.: Numerical model explosive ALE

The total impulse along the reflecting boundary is used as the criterion for convergence. Integrated and averaged quantities, such as the impulse, converge faster with mesh refinement than quantities directly linked to the underlying equations [Oberkampf and Roy, 2010]. Therefore, the pressure would in principle be a better quantity for the mesh sensitivity study as it is directly linked to the underlying conservation equations.

The problem with using pressure as a convergence criterion is that the steep shock front immediately behind the driving explosive has a thickness in the order of only 10^{-4} mm [Cowan and Hornig, 1950]. In the numerical simulation, the thickness of this shock front is limited by the size of the spatial discretization and the peak pressure is smeared over at least one element. At the same time, the total impulse, and thus the shape of the shock wave, is related to the energy of the explosive. As a consequence, the peak pressure of the shock front will only show a converging behavior when the discretization reaches a size that can represent the real size of the shock front and the associated peak pressure. Therefore, the total impulse is used as the convergence criterion instead.

To quantify the quality of the results with incremental mesh refinements, they are compared using Richardson's extrapolation method [Richardson and Gaunt, 1927], [Oberkampf and Roy, 2010]. This method uses the results from three different mesh sizes to extrapolate an estimated "exact" solution f_{re} for a theoretical mesh size of zero. The results are then presented as fractions of this theoretical value to give an estimated error resulting from the discretization.

Richardson extrapolation method states, that if the mesh is refined uniformly over the entire domain by a constant factor $r = h_{i+1}/h_i = const.$, for three levels of refinement h_i with $h_i < h_{i+1}$, the order of convergence p for the associated solutions f_i can be approximated by:

$$p = \frac{|\ln \frac{f_3 - f_2}{f_2 - f_1}|}{\ln r} \tag{3.3}$$

Using the approximated order of convergence p, an estimated "exact" solution f_{re} can be extrapolated based on the solution of the two finest meshes f_1, f_2:

$$f_{re} = f_1 + \frac{(f_1 - f_2)}{(r^p - 1)} \tag{3.4}$$

This requires that the solutions f_i are within an asymptotic range of convergence.

An additional error band indicating the quality of the extrapolated results can be calculated using the Grid Convergence Index (GCI) introduced by [Roache, 1994]:

$$GCI = \frac{F_s}{r^p - 1} \left| \frac{f_2 - f_1}{f_1} \right| \tag{3.5}$$

Here, F_s is a safety factor which is set to 1.25 when three solutions are available [Oberkampf and Roy, 2010] and the observed order of convergence p is within 10% of the theoretical order of the underlying numerical method. [Schwer, 2009a] suggest that an order of convergence around $p = 2.0$ can be considered favorable for the simulations performed.

In addition, the GCI provides a way to check the asymptotic behavior of the solutions [Schwer, 2009a], which is an important requirement for Richardson extrapolation. This is done by calculating the GCI for the two refinement steps and comparing it with the approximated order of convergence.

$$ac = \frac{GCI_{32}}{r^p GCI} \tag{3.6}$$

A value of ac close to unity indicates, that the assumption of an asymptotic behavior is valid. Here, GCI_{32} is the GCI with respect to the solutions of the two coarser mesh/grid refinements f_2, f_3:

$$GCI_{32} = \frac{F_s}{r^p - 1}\left|\frac{f_3 - f_2}{f_2}\right| \tag{3.7}$$

Based on existing numerical simulations, [Roache, 1998] found that the GCI provides an error band that contains the exact solution in 95 % of the cases. This error band is defined around the solution of the finest mesh/grid f_1 as:

$$f_1[(1 - GCI), (1 + GCI)] \tag{3.8}$$

Detailed descriptions and applications of this method in context of shock wave simulations can be found in [Roache, 1994], [Slater et al., 2000], [Oberkampf and Roy, 2010], [Schwer, 2008], [Schwer, 2009a], [Castedo et al., 2020].

In the present mesh sensitivity study, the mesh is progressively refined by a factor of two until asymptotic behavior is observed. This results in mesh sizes of 5 mm, 2.5 mm, 1.25 mm and 0.625 mm.

The reflected pressure is output at 10 mm intervals in the radial direction along the reflecting boundary of the ALE domain (figure 3.1). To ensure, that the results are not affected by boundary effects, the tracer points are aligned along the diagonal of the quarter-symmetric model. The resulting specific impulse histories are calculated from the pressure histories by cumulative numerical integration. The total impulses are then calculated by rotational integration of the specific impulse histories.

Figure 3.2 shows the reflected pressure at the center ($r = 0$ mm) over the time (left) and the resulting specific impulse over the radial location at 0.1 ms (right) for the different mesh sizes.

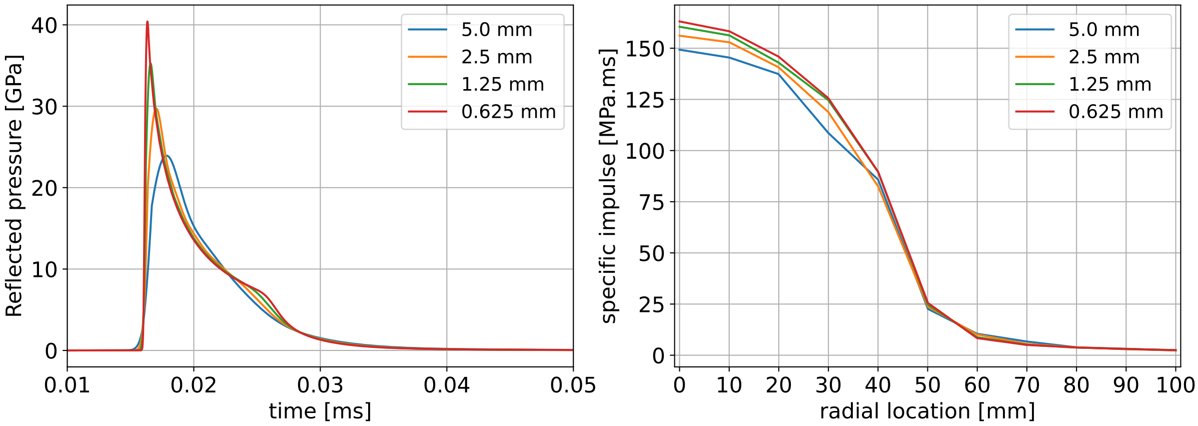

Figure 3.2.: Reflected pressure over time (left) and specific impulse over radial location at 0.1 ms (right) for different mesh sizes

From figure 3.2 (right) it can be seen that the effect of the explosive is very localized in the area directly behind the explosive charge and decreases rapidly in the radial direction. The shape of the specific impulses in radial direction is very similar for all evaluated mesh sizes. While the difference is larger in the center, it becomes smaller with increasing radius.

The influence of the different mesh sizes is evaluated based on the total impulse shown in figure 3.3 (left). For this, and to provide an estimate of the error, figure 3.3 (right) shows the total impulses after 0.1 ms normalized by the Richardson extrapolated estimate f_{re}. The x-axis shows the different mesh sizes normalized by the finest mesh of 0.625 mm.

The asymptotic range is reached starting from a mesh size of 2.5 mm (normalized: 4). This is confirmed by an asymptotic control value of ac =1.01 (equation (3.6)). The observed order of convergence calculated by equation (3.3) is $p = 1.99$. The GCI gives an error band for the approximated solution, around the solution of the finest mesh, of $\pm 0.35\,\%$.

The "exact" total impulse estimated by Richardson extrapolation is 951 kN ms with an error band from 945 kN ms to 952 kN ms. The mesh size of 2.5 mm, which is within 5 %

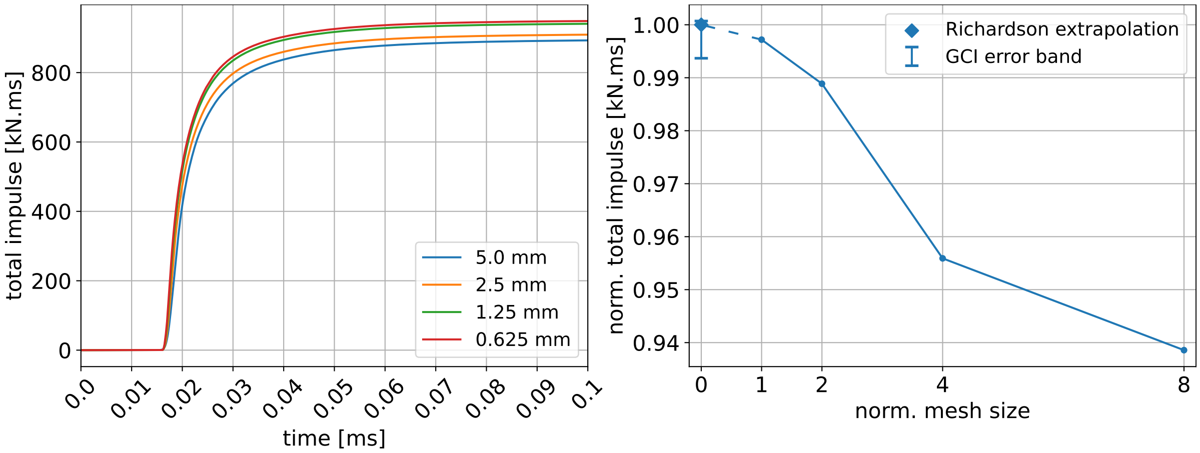

Figure 3.3.: Total impulse over time(left) and normalized total impulse over normalized mesh size (right)

of the estimated "exact" solution, is consistent with the recommendations of [Schwer et al., 2015] of 20 elements over the radius of the charge as well as similar simulations performed by [Michaloudis, 2019].

3.3. Influence of the charge geometry

Besides the explosive mass, the geometry of the explosive charge is a very important criterion for the resulting load on a structure. In the presented test series, the explosive charges were cylinders with length to diameter (L/D)-ratios of 0.71, 1.07 and 1.43. These charges were placed with one of their flat surfaces on the surfaces of the concrete slabs.

There are many studies about cylindrical charge geometries with different L/D-ratios. However, these studies are mostly concerned with far-field and near-field detonations. A good overview of different studies can be found in [Langran-Wheeler et al., 2021], who investigated the near-field pressure distributions of cylindrical charges with their symmetry axis parallel to the surface of the concrete slabs and compared them with those of spherical charges.

The shock wave of a centrally ignited spherical charge propagates equally in all radial directions. The shock wave from a cylindrical charge is divided into a side-wave propagating in the radial direction and an end-wave propagating in the axial direction (figure 3.4). The area in between is formed by the so called bridge-wave, which results from the interaction of the expanding end-wave and side-wave [Knock et al., 2014].

The L/D-ratio of a cylindrical charge is an important criterion to determine where the energy from the detonation is directed to. Since the amount of energy is correlated with the size of the associated surface area, more energy is directed in radial direction in case of larger L/D-ratios, while for smaller L/D-ratios more energy is directed in the axial direction of the cylindrical charge [Wu et al., 2010].

In the case of a contact detonation, no bridge-wave is formed because the end wave interacts with the side-wave only after the reflection. This results in a region, where the reflected pressure wave (end-wave and side-wave) interacts with the remaining incoming pressure wave, resulting in a so-called mach stem. The direction of propagation of this Mach stem is nearly parallel to the reflecting surface, and most of the components perpendicular to the reflecting surface cancel out. Therefore, the side-wave plays only a minor role in the context of a contact detonation and the resulting load on a surface in contact with the explosive is dominated by the end-wave.

Figure 3.4 shows the resulting shock waves from a cylindrical charge with a L/D-ratio of 1.2 ignited at one flat end. The figure is the result of two axisymmetric 2D S-ALE simulations. The red line shows the undisturbed propagation of the shock wave and the blue line shows the shock wave from the same explosive charge after reflection from a rigid surface aligned flush with the flat surface of the cylindrical charge opposite to ignition point.

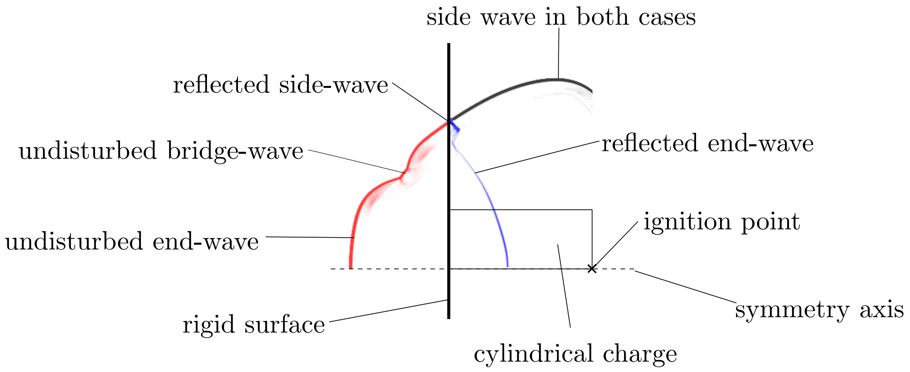

Figure 3.4.: Undisturbed (red) and reflected (blue) propagation of shock waves from cylindrical charge

The influence of different L/D-ratios of the explosive charge is investigated with the help of numerical simulations. For this purpose, simulations analogous to those of the mesh sensitivity study in section 3.2 are being performed with different L/D-ratios for 1000 g of SEMTEX10. The mesh size selected for this simulation is 1.25 mm, which gives a total impulse within about 1.0 % of the estimated "exact" solution according to Richardson extrapolation. The resulting dimensions of the charges with L/D-ratios between 0.2 and 2.0 are listed in table 3.2.

Table 3.2.: Dimensions of charges with different L/D-ratios (1000 g SEMTEX10)

L/D	0.2	0.4	0.6	0.8	1.0	1.2	1.4	1.6	1.8	2.0
L [mm]	31.5	50.0	65.5	79.3	92.1	104.0	115.2	126.0	136.2	146.2
D [mm]	157.4	125.0	109.2	99.2	92.0	86.6	82.4	78.8	75.6	73.0

Figure 3.5 shows the specific impulse over the radial location at 0.1 ms for spherical charges with different explosive masses (left) and cylindrical charges with the different L/D-ratios (right). The mass of the cylindrical charges is 1000 g of SEMTEX10 in all cases.

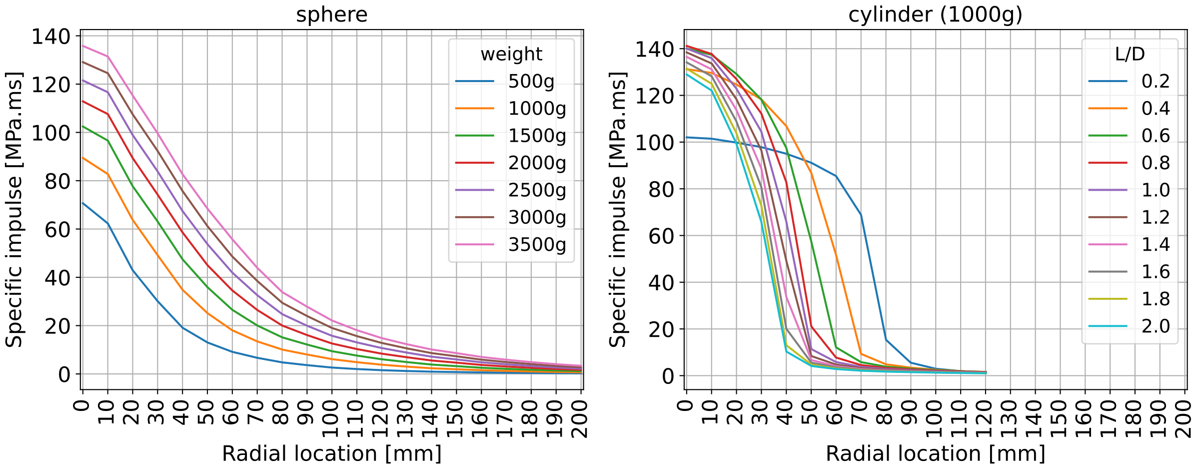

Figure 3.5.: Specific impulse over the radial location at 0.1 ms for spherical charges with different explosive masses (left) and cylindrical charges with different L/D-ratios (right)

The specific impulse of the spherical charges increases continuously over the entire radial range with an increasing mass of the explosive charge (figure 3.5, left). In case of the cylindrical charges (figure 3.5, right), the maximum specific impulse at the center increases rapidly between the L/D-ratios of 0.2 and 0.8 before decreasing slowly with increasing L/D-ratios. At the same time, the previously mentioned strong dependence of the loading on the end wave from the cylindrical charge becomes apparent, since the specific impulse is mostly limited to the area in direct contact with the charge.

The load on a structure by the different explosive charges can be compared by the total impulse $I = \int_A i\, dA$, which is calculated by integrating the specific impulse i over the area A on which it acts. An additional measure for this comparison, which was introduced by [Rigby et al., 2019], is the so-called energy equivalent impulse. The energy equivalent impulse is based on the fact, that under a uniformly distributed impulsive load I the kinetic energy E_k of a discrete mass $\rho t A$ is given by:

$$E_k = \frac{I^2}{2\rho t A} \tag{3.9}$$

Where ρ and t are the density and thickness of the mass in loading direction, and A is the surface area on which the impulsive load acts. Based on this, the behavior of a plane structural element (plate) can be represented by a series of discrete masses. These discrete masses initially move independently of each other, but are connected by spring elements with arbitrary shear stiffness. Depending on the magnitude of this shear stiffness, the loaded structure will be described differently.

In the case of an infinite shear stiffness all discrete masses move simultaneously representing a rigid plate (figure 3.6, left). The velocity profile and thus the total kinetic energy of the system is then independent of the distribution of the impulsive loading, which represents a lower limit of the energy uptake of the plate $E_{k,l}$.

In the case of zero shear stiffness, all discrete masses move independently and the velocity profile is directly proportional to the distribution of the applied specific impulse. The resulting kinetic energy gives an upper limit of the energy uptake of the plate $E_{k,u}$ (figure 3.6, right).

The upper $E_{k,u}$ and lower $E_{k,l}$ limits of the kinetic energy can be derived on the basis of equation (3.9) as:

$$E_{k,u} = \frac{1}{2\rho t} \int_A \frac{(i\, dA)^2}{dA} \tag{3.10}$$

$$E_{k,l} = \frac{1}{2\rho t A} \left(\int_A i\, dA \right)^2 \tag{3.11}$$

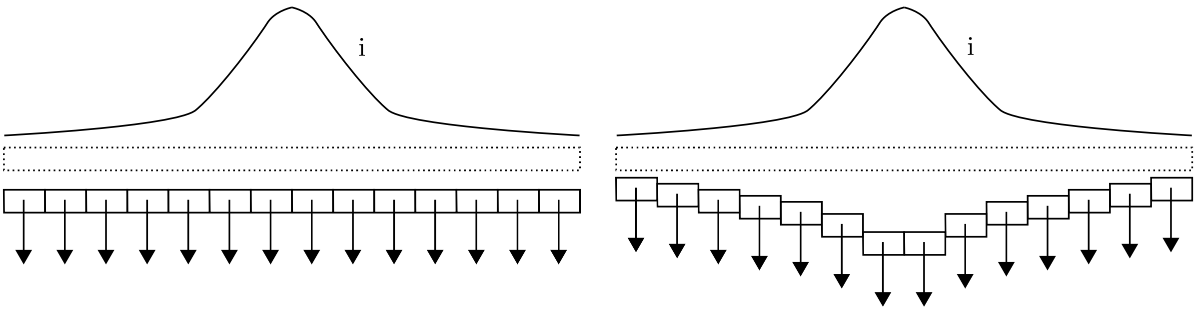

Figure 3.6.: Deformation of a plate loaded by distributed impulse represented by discrete masses linked by spring elements with infinite (left) and zero (right) shear stiffness

The energy equivalent impulse is then defined as a uniform impulse, that results in the same energy uptake as the upper limit of the energy uptake $E_{k,u}$, while the total impulse is proportional to the lower limit $E_{k,l}$. Unlike the total impulse I, which is independent of the distribution of the specific impulse i, the energy equivalent impulse I_{Ek} also contains information about the specific impulse distribution. Since the impulse is proportional to the square root of the kinetic energy, the energy equivalent impulse can be derived as:

$$\frac{I_{Ek}}{I} = \left(\frac{E_{k,u}}{E_{k,l}}\right)^{1/2} = \left(\frac{A\int_A i^2\,dA}{I^2}\right)^{1/2} \tag{3.12}$$

$$I_{Ek} = \left(A\int_A i^2\,dA\right)^{1/2} \tag{3.13}$$

In [Rigby et al., 2021], the application of the energy equivalent impulse is restricted to thin steel plates (span-thickness ratio >20) with out-of-plane displacements that are several times larger than the plate thickness. This thin plate requirement is not given for the concrete slabs investigated. However, the failure of the concrete slab results in very large deformations that are strongly localized in the region behind the explosive charge. Therefore, the energy equivalent impulse is analyzed for its suitability to describe the investigated processes.

To compare the cylindrical charges with the spherical charges, equivalence factors EF_{sp} are defined as the ratio between the masses of a spherical charge W_{sp} and a cylindrical charge W_{cy} that generate an equivalent total impulse (t) or an energy equivalent impulse (e).

$$EF_{sp,e/t} = \frac{W_{sp}}{W_{cy}} \tag{3.14}$$

Figure 3.7 shows both spherical equivalence factors $EF_{sp,e/t}$ for the inspected range. The blue solid line shows the equivalence factor based on the total impulse (t) and the orange dash-dotted line shows the equivalence factor based on the energy equivalent impulse (e). For further use, fitted equations are added with the L/D-ratio as a linear variable.

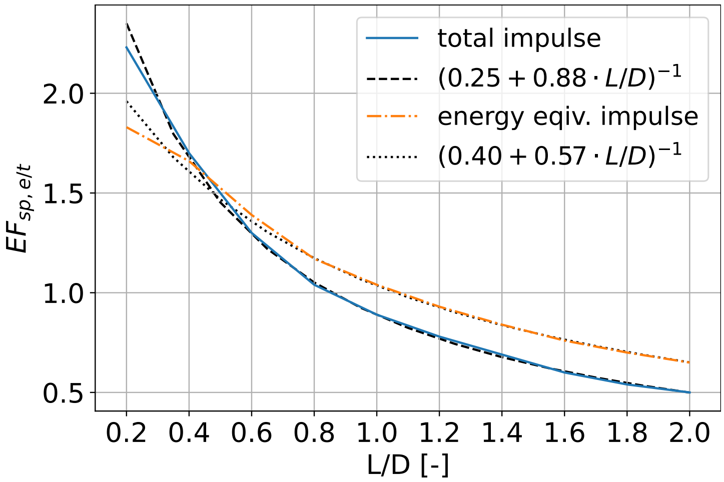

Figure 3.7.: Spherical equivalence factor $EF_{sp,e/t}$ over L/D-ratio for total impulse and energy equivalent impulse

As can be seen in figure 3.7, a spherical and a cylindrical charge with the same explosive mass generate an energy equivalent impulse for $L/D = 1.0$ and an equivalent total impulse for $L/D = 0.85$. For greater L/D-ratios, the cylindrical charge generates a smaller load on a structure in contact because more energy is directed in the radial direction of the cylindrical charge. For smaller L/D-ratios, the cylindrical charge generates a greater load than the spherical charge.

The fitted equations in figure 3.7 give good approximations for the examined L/D-range. For L/D-ratios smaller than 0.6 the approximations start to slightly differ from the numerical results, but for the range of the conducted test series this is of no relevance.

To compare the different equivalence factors, the maximum x-velocities measured in the test series (chapter 4) are plotted in figure 3.8 against the inverse of the scaled concrete slab thickness calculated according to equation (3.15).

$$T_{SX10,*} = \frac{T}{W_{SX10,*}^{1/3}} \tag{3.15}$$

Where T is the thickness of the concrete slab in cm and $W_{SX10,*}$ is the explosive mass of SEMTEX10 in g. The three plots in figure 3.8 show the results without considering the shape of the explosive (left), using the spherical equivalence factor with respect to the total impulse (center) and the spherical equivalence factor with respect to the energy equivalent impulse (right).

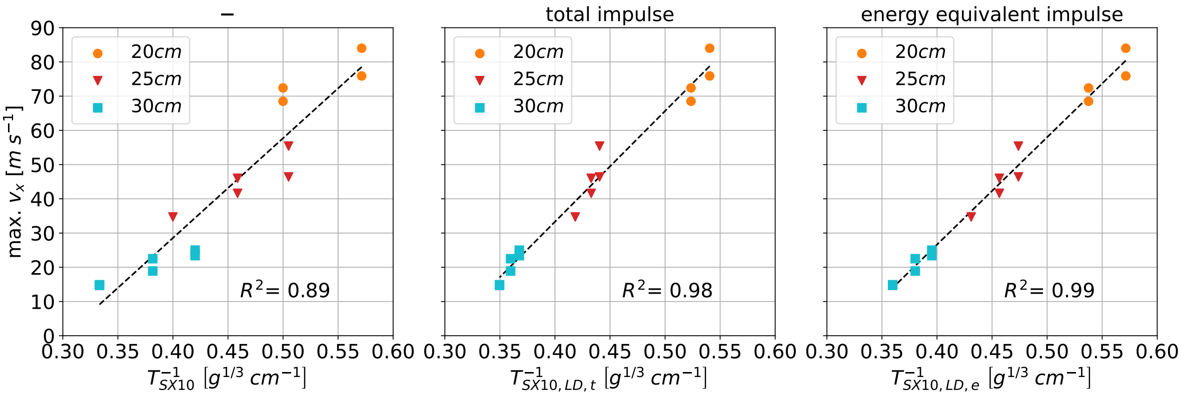

Figure 3.8.: Maximum x-velocities over scaled thickness without consideration of the shape of the explosive (left), using the spherical equivalence factor with respect to the total impulse (center) and the spherical equivalence factor with respect to the energy equivalent impulse (right)

The coefficients of determination R^2 show a significant improvement in the linear correlation between the scaled concrete slab thickness and the maximum x-velocity due to the additional spherical equivalence factors. The main difference is, that without considering the shape of the explosive (left), there is an overlap in the direction of the scaled thickness between the groups of the different concrete slab thicknesses at $T_{SX10}^{-1} \approx 0.4$ and 0.5. This overlap does not correspond to the increase in x-velocity between the different concrete slab thicknesses.

Between the two cases with the additional spherical equivalence factors, the correlation improves only slightly from $R^2 = 0.98$ to $R^2 = 0.99$. However, there is an improvement that is visually apparent especially in the region of the concrete slabs with a thickness of 25 cm. Therefore, the spherical equivalence factor in terms of the energy equivalent impulse is used for the evaluations of the test series in chapter 4.

3.4. Summary

A convergence study was conducted to determine the mesh size required to simulate a contact detonation with S-ALE. This was done using the Richardson extrapolation method, which uses the results of successive mesh refinements to extrapolate an estimated "exact" solution. This allows the influence of the mesh refinements to be evaluated qualitatively. For the simulations performed, a mesh size of 2.5 mm was found to be within 5 % of the estimated "exact" solution.

The influence of the different length to diameter ratios of the cylindrical charges on the impact on the concrete slab was analyzed. This was done by comparing the impact of cylindrical charges with different length to diameter ratios to that of spherical charges. The criteria for this comparison are the total impulse and an energy equivalent impulse introduced by [Rigby et al., 2019].

Based on this comparison, an equivalence factor was derived that can be used to compare the different experimental tests, taking into account the length to diameter ratios of the cylindrical charges. When this equivalence factor is used to calculate a scaled thickness of the concrete slab, a linear correlation can be found with the maximum x-velocity of the secondary debris fragments measured in the test series (chapter 4). Therefore, the spherical equivalence factor in terms of the energy equivalent impulse is used for the evaluations of the experimental tests in chapter 4.

4. Test series

A series of test was conducted by the author to improve the understanding of the mechanics of secondary debris from reinforced concrete slabs subjected to contact detonations. The concrete slabs in this test series have external dimensions of 200 cm x 200 cm and different thicknesses of 20 cm, 25 cm and 30 cm. The external dimensions of the concrete slabs were chosen so that the very localized effects of the contact detonations are not influenced by the support conditions.

To investigate the influence of steel fibers in the concrete, some of the specimens were produced with steel fiber contents of 0.5 Vol %, 1.0 Vol %, and 2.0 Vol %. The use of steel fibers was limited to 30 cm thick reinforced concrete slabs, which reduces the number of input parameters and allows for a focused evaluation of the influence of the steel fibers.

In order to investigate a measure for existing structures, some concrete slabs without steel fibers were retrofitted prior to the detonation test. The retrofit consisted of a 5 cm thick layer of fiber reinforced concrete that was applied to the protective side of an existing 25 cm thick concrete slab, resulting in a total thickness of 30 cm.

The explosives are cylindrical charges with a diameter of 103 mm and masses of 1000 g, 1500 g and 2000 g of SEMTEX10. These cylindrical charges were placed so that one of their flat surfaces was flush with the surface of the reinforced concrete slabs. The charges were ignited in the center of the surface of the explosive charge facing away from the reinforced concrete slab at a depth of approximately 1.0 cm.

Table 4.1 gives an overview of the tests performed in chronological order.

The objective of this series of tests is to investigate the secondary debris resulting from concrete slabs subjected to contact detonations. The key parameters are the damage to the concrete slabs, the velocity distribution of the secondary debris, and the preceding fragmentation process.

Table 4.1.: Overview of the test series

name (shot nr.)	concrete slab thickness	steel fiber content	explosive mass (SEMTEX 10)
SN80	20 cm	0.0 Vol %	1500 g
SN81	30 cm	1.0 Vol %	1500 g
SN82	25 cm	0.0 Vol %	1500 g
SN128	25 cm	0.0 Vol %	1500 g
SN129	20 cm	0.0 Vol %	1000 g
SN130	25 cm	0.0 Vol %	2000 g
SN131	30 cm	0.0 Vol %	1000 g
SN132	30 cm	0.0 Vol %	1000 g
SN142	20 cm	0.0 Vol %	1000 g
SN143	30 cm	0.0 Vol %	1500 g
SN144	25 cm	0.0 Vol %	2000 g
SN145	30 cm	0.0 Vol %	1500 g
SN146	30 cm	0.0 Vol %	2000 g
SN147	30 cm	0.0 Vol %	2000 g
SN148	30 cm	0.5 Vol %	2000 g
SN149	30 cm	0.5 Vol %	2000 g
SN150	30 cm	1.0 Vol %	1500 g
SN151	30 cm	0.5 Vol %	1500 g
SN152	30 cm	0.5 Vol %	1500 g
SN153	30 cm	1.0 Vol %	2000 g
SN154	30 cm	aFRC [1]	2000 g
SN155	30 cm	aFRC [1]	2000 g
SN161 [2]	30 cm	aFRC [1]	1500 g
SN162 [2]	30 cm	aFRC [1]	1500 g
SN163 [2]	30 cm	2.0 Vol %	1500 g
SN164 [2]	30 cm	2.0 Vol %	1500 g
SN171 [2]	30 cm	2.0 Vol %	2000 g
SN172 [2]	30 cm	2.0 Vol %	2000 g
SN173	30 cm	1.0 Vol %	2000 g
SN174	20 cm	0.0 Vol %	1500 g
SN175	25 cm	0.0 Vol %	1000 g

1) Layer of 5 cm fiber reinforced concrete (2.0 Vol %) retrofitted to the protective surface of a 25 cm thick concrete slab

2) Tests with DIC measurement

To observe the secondary debris, the concrete slabs were installed in an upright position during the detonation tests. High-speed (HS) cameras were used to record the protective side of the concrete slabs. The HS recordings were then analyzed to determine both, the velocity of the secondary debris and the preceding fragmentation.

After the detonation tests, 3D-scans were used to measure the damaged areas of the concrete slabs. The secondary debris was collected, sieved, and weighed. These data were then evaluated with respect to the geometry of the spalling crater as well as the mass and size distribution of the secondary debris.

The chapter begins with a description of the materials used, followed by a presentation of the test setup developed and the measurements performed.

Subsequently, the geometry of the damaged areas of the concrete slabs is evaluated with special emphasis on the spalling crater, which is the most important region for the secondary debris. This is followed by a detailed analysis of the fragmentation process and the velocity distribution of the secondary debris.

The geometry of the damaged regions and the velocity of the secondary debris are then used to derive the kinetic energy of the secondary debris. The kinetic energy is a suitable quantity to evaluate the impact of the secondary debris on people and technical installations on the protective side of a concrete structure. A discussion of this impact is carried out in chapter 6.

The influence of the steel fibers is analyzed quantitatively on the basis of the kinetic energy. In some tests, where only little secondary debris was expected in advance, DIC measurements were performed from the protective surface of the concrete slabs. These DIC measurements are used to verify the identified load bearing mechanisms of the different reinforcements (steel fibers and retrofit layer) as well as the derived velocity distributions.

4.1. Explosive charges

The explosive used in this series of tests is SEMTEX10 (section 3.1.1). After weighing, the explosive was molded into a PVC pipe with a circular cross-section and an internal diameter of 103 mm.

The explosive charges were placed with one end flush with the center of the surface of the concrete slab. The resulting length to diameter ratios (explosive without PVC pipe) of the different charges are given in table 4.2.

The charges were ignited with a Dynadet-C2 detonator, which was pressed about 10 mm deep into the center of the end of the explosive charge opposite to the concrete slab. Figure 4.1 shows the experimental setup from the detonation side (left) and a detail of the prepared explosive charge without detonator (right).

Figure 4.1.: Experimental setup from detonation side (left) and detail explosive (right)

Besides the explosive mass, the geometry of the explosive charge is a very important criterion for the resulting load on a structure. To compensate for the different length to diameter ratios (L/D) of the explosive charges, the mass W of the explosive charge is additionally scaled by a factor $EF_{sp,e}$ derived in chapter 3. This factor relates the given cylindrical charge to an equivalent spherical charge. The criterion of equivalence for the following discussion is the energy equivalent impulse proposed by [Rigby et al., 2021].

To make different test series comparable, the explosive mass of the charge is expressed as the mass of an equivalent charge of TNT. The TNT equivalence factor for SEMTEX10 is determined by numerical simulations as $EF_{TNT,e} = 1.24$. Analogous to the influence of the L/D-ratios, the criterion for TNT equivalence is the energy equivalent impulse. This TNT equivalence factor is consistent with the results of [Shirbhate and Goel, 2021], who determined a TNT equivalence factor of 1.25 for SEMTEX10 based on the heat of detonation.

The equivalent explosive mass of the explosive charge $W_{TNT,sp}$ is calculated by multiplying the mass of the cylindrical charge of SEMTEX10 $W_{Semtex10,cy}$ by the equivalence factor for TNT $EF_{TNT,e}$ and the factor for an equivalent spherical charge $EF_{sp,e}$.

$$W_{TNT,sp} = W_{Semtex10,cy}\, EF_{TNT}\, EF_{sp,e} \tag{4.1}$$

Table 4.2 shows the relevant values required to determine the TNT and spherical equivalent mass of the explosives in the conducted test series.

Table 4.2.: TNT and spherical equivalent mass of the explosive charges

$W_{Semtex10,cy}$	$EF_{TNT,e}$	L/D	$EF_{sp,e}$	$W_{TNT,sp}$
1000 g	1.24	0.71	1.25	1550 g
1500 g	1.24	1.07	0.99	1841 g
2000 g	1.24	1.43	0.83	2058 g

4.2. Test specimens

The concrete slabs in this test series have external dimensions of 200 cm x 200 cm and thicknesses of 20 cm, 25 cm and 30 cm. They are reinforced crosswise on both sides using rebars with a diameter of 10 mm, a spacing of 150 mm and a concrete cover of 35 mm. The reinforcing steel is made of high ductility steel B500B.

To analyze the influence of steel fibers in the concrete, the 30 cm thick concrete slabs have varying steel fiber contents of 0.0 Vol %, 0.5 Vol %, 1.0 Vol % and 2.0 Vol %. The steel fibers are Dramix 4D 65/35 BG from Bekaert [Bakaert, 2023]. They are hooked steel fibers with a length of 35 mm and a diameter of 0.55 mm. The steel fibers have been carefully mixed with the concrete to ensure that they are distributed as evenly as possible. A data sheet with more information about the steel fibers can be found in the appendix section A.2.

In order to investigate a measure for existing structures, some concrete slabs without steel fibers were retrofitted prior to the detonation test. The retrofit consisted of a 5 cm thick layer of fiber reinforced concrete (2.0 Vol %). This retrofit layer was applied to the protective surface of an existing 25 cm thick concrete slab after more than 28 days. The resulting total thickness of the retrofitted concrete slab is therefore 30 cm. To ensure good bonding conditions between the individual concrete layers, the surfaces of the concrete slabs were roughened with a rake in advance (figure 4.2).

Figure 4.2.: roughened concrete surface before addition of fiber-reinforced layer

The concrete slabs were produced by a commercial manufacturer. The specified target strength of the concrete was $f_{ck,cube} = 40\,\mathrm{MPa}$ with a maximum aggregate size of 8 mm. Information on the concrete mixture is given in the appendix section A.1. The concrete slabs used in tests SN80-SN82 were part of a pre-test series and were produced by a different manufacturer than the concrete slabs used in the main test series. However, the essential parameters of the concrete are in good agreement.

4.2.1. Determined material parameters

In order to verify the specified concrete properties, both the static compressive strength and the concrete density were measured at the Laboratory for Structural Engineering of the University of the Bundeswehr in Munich. Corresponding test cubes with an edge length of 15 cm were produced from the same concrete as the corresponding concrete slabs and transported to Munich. There they were stored outdoors, covered with tarpaulins, in the same way as the concrete slabs at the TNO in The Hague.

On the days of the detonation tests, all the concrete slabs had an age of at least 25 days, but on average 70 days. The static compressive strength and density of the concrete were measured for each concrete slab on three corresponding test cubes with a side length of 15 cm. The resulting mean static compressive strength is $f_{cm,cube} = 42.7 \pm 4.8\,\mathrm{MPa}$ and the mean density is $\rho = 2.22 \pm 0.04\,\mathrm{g\,cm^{-3}}$ (mean ± standard deviation). An overview of these measurements is given in the appendix section A.1.

In a parallel series of tests, spallation tests were carried out on the Split Hopkinson Bar (SHB) using the same concrete. The results of this series of tests are presented in [Mosig et al., 2021]. The concrete used for the concrete slabs of the detonation tests is referred to as C30/37 in [Mosig et al., 2021]. The relevant parameters for the following discussion are the longitudinal wave velocity c_L, the tensile strength f_t, and the specific fracture energy G_f including the tested strain rate $\dot{\varepsilon}$. These parameters are given in table 4.3 for the different steel fiber contents.

Table 4.3.: Results from Split-Hopkinson-Bar experiments [Mosig et al., 2021]

Steel Fiber Content [Vol %]	c_L [m s^{-1}]	$f_{t,dyn}$ [MPa]	G_f [J m^{-2}]	$\dot{\varepsilon}$ [s^{-1}]
0.0	3751	6.67	234	15.1
0.5	3744	7.6	1586	21.1
1.0	3782	9.12	2512	17.3
2.0	3737	8.13	2685	22.4

4.2.2. Scaled concrete slab thickness

For the following evaluations of the experimental tests, a scaled thickness of the concrete slab is introduced. This quantity has already been used by other authors like [Weerheijm et al., 1988] and [Morishita et al., 2000] to describe the impact of a contact detonation on a concrete slab. The scaled thickness is defined similarly to the scaled distance, which is a common quantity used to differentiate the impact of near-field and far-field detonations (equation (2.1)). The scaled thickness allows a combined description of the concrete slab thickness T and the equivalent explosive mass $W_{sp,TNT}$ by a single parameter T_W.

$$T_W = \frac{T}{W_{TNT,sp}^{1/3}} \tag{4.2}$$

The cube root of the explosive mass reflects the fact, that the detonation initially propagates in all directions. An overview of the scaled thicknesses T_W in the presented test series can be found in Table 4.4:

Table 4.4.: Scaled thickness of the concrete slab with regard to the TNT and spherical equivalent mass

T	$W_{Semtex10}$	$W_{TNT,sp}$	T_W
20 cm	1500 g	1841 g	$1.63\,\mathrm{cm\,g^{-1/3}}$
20 cm	1000 g	1550 g	$1.73\,\mathrm{cm\,g^{-1/3}}$
25 cm	2000 g	2058 g	$1.97\,\mathrm{cm\,g^{-1/3}}$
25 cm	1500 g	1841 g	$2.04\,\mathrm{cm\,g^{-1/3}}$
25 cm	1000 g	1550 g	$2.16\,\mathrm{cm\,g^{-1/3}}$
30 cm	2000 g	2058 g	$2.36\,\mathrm{cm\,g^{-1/3}}$
30 cm	1500 g	1841 g	$2.45\,\mathrm{cm\,g^{-1/3}}$
30 cm	1000 g	1550 g	$2.59\,\mathrm{cm\,g^{-1/3}}$

4.3. Experimental setup

The tests were conducted in a bunker at a facility of the Netherlands Organization for Applied Scientific Research (TNO) near The Hague. The vaulted cross-section of the oblong bunker has approximate dimensions of 6 m in width and 4 m in height. The experimental setup is shown in figure 4.3.

For the following discussion, the side of the concrete slab facing the explosive charge will be referred to as the detonation side and the opposite side will be referred to as the protective side.

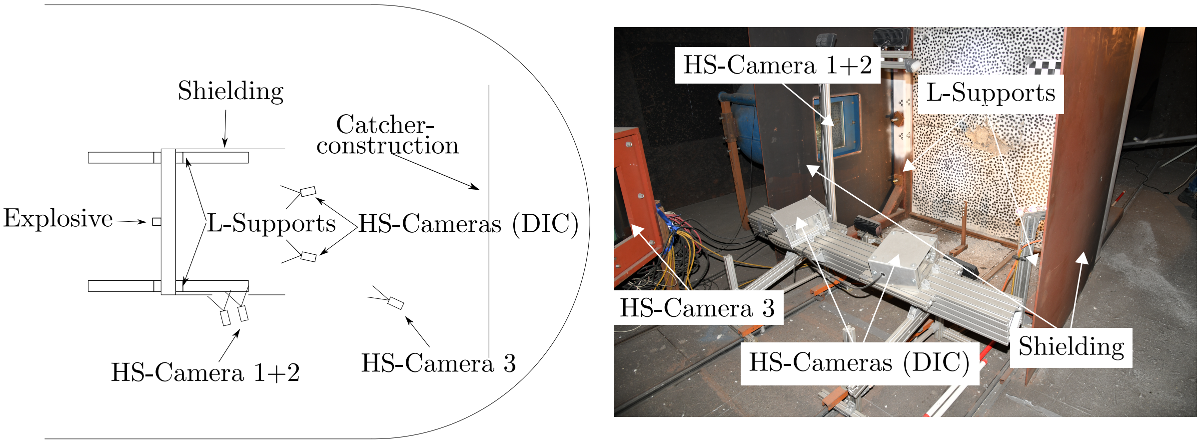

Figure 4.3.: Layout of the experimental setup (left) and a photo of the protective side (right)

The concrete slabs were held in an upright position by L-shaped steel beams (rectangular cross-section). These 20 cm wide steel beams (L-supports) were placed in front of both surfaces of the concrete slabs, and held together with threaded steel rods. The resulting horizontal clearance between the steel beams was 160 cm.

The dimensions of the test setup were chosen so that the influence of the support conditions on the relevant localized response of the concrete slabs is considered negligible.

4.3.1. High-speed recordings

The protective side of the concrete slabs was recorded by high-speed (HS) cameras from different angles. HS cameras 1+2 recorded from the side, covering an area up to a horizontal distance of 110 cm behind the concrete slabs. HS camera 3 recorded the protective surface of the concrete slabs during the fragmentation.

The HS cameras were placed inside of steel boxes with armored glass windows to protect them from the detonation. In order to minimize the negative effects of the detonation on the HS recordings, a steel shield was installed around the observation area on the protective side of the concrete slab.

The recordings were started before the detonation, and received the information about the time of detonation from a trigger placed in between the explosive charge and the concrete slab.

The HS recordings were performed at a frame rate of $5000\,\mathrm{s}^{-1}$. The spatial resolution of the HS recordings provides a precision of $1.8\,\mathrm{mm\,px}^{-1}$ for distance measurements in the calibrated plane (section 4.4.2).

4.3.2. Digital image correlation

For the tests with a steel fiber content of 2.0 Vol % and the retrofit concrete slabs loaded with 1500 g of SEMTEX10, very little secondary debris was expected in advance. Therefore, digital image correlation (DIC) was used to measure the deformation and velocity at the protective surface of the concrete slabs in these tests.

The reduced fragmentation in these tests has two advantages for the DIC measurements. First, the DIC recordings are less disturbed by the fragmentation of the concrete, allowing measurements to be taken over a longer period of time. Second, the DIC cameras, which are located directly behind the concrete slab, are exposed to less secondary debris.

Two additional HS camera were used to capture the recordings for DIC. These HS cameras recorded the protective surface of the concrete slab from a distance of 150 cm. The distance between the two cameras was 100 cm and the mutual angle of the orientation between the cameras was 30°. In addition, the protective surface of the concrete slabs was painted white and marked with a pattern of randomly distributed ellipses. This pattern is shown in figure 4.4.

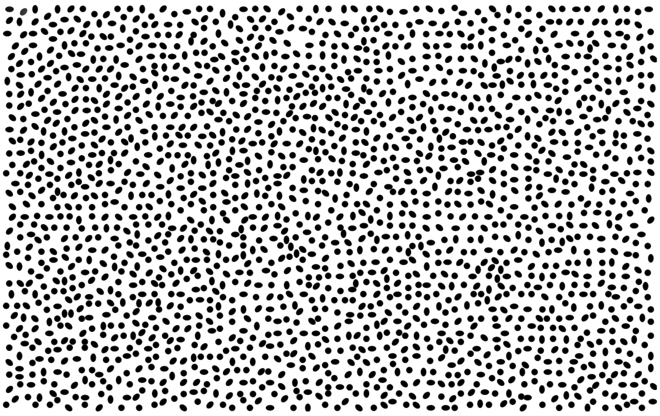

Figure 4.4.: DIC pattern on the protective surface of the concrete slabs

The DIC recordings of SN161 were taken at a frame-rate of 5000 s^{-1}, analogue to the other HS recordings. For all subsequent DIC recordings the frame-rate was increased to 9000 s^{-1} in order to obtain a higher time resolution of the measurements.

4.3.3. Collection of secondary debris fragments

To stop the resulting debris and minimize further fragmentation, a curtain structure was installed at a distance of approximately 4 m behind the concrete slabs. After the detonation, the resulting debris was collected in segmented areas. Figure 4.5 shows the different collecting areas (left) and the curtain construction (right).

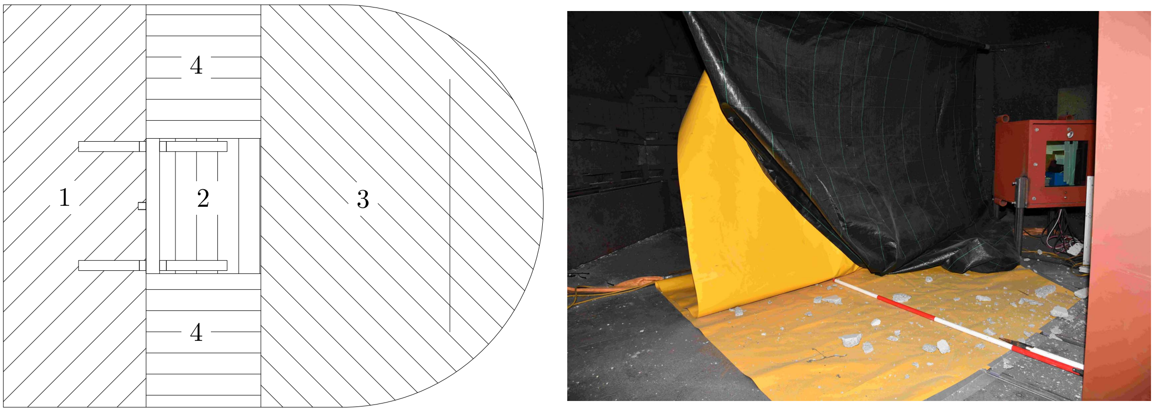

Figure 4.5.: Areas for collection of secondary debris (left), curtain construction to stop the secondary debris (right)

4.3.4. Comment on pretests

Tests SN80-SN82 were part of a pre-test series using a slightly different test setup. The main difference is a 10 cm wide, vertical slit construction installed at a horizontal distance of 100 cm behind the concrete slab.

The idea of this setup was to reduce the debris cloud to a smaller lateral dimension to ensure a more accurate distance between the HS camera and the tracked features. However, the slit construction disturbed the flight of the resulting secondary debris too much and was therefore removed from the main test series.

4.4. Measurements performed

This section describes the evaluation methods for the measurements made using a Cartesian coordinate system depcited in figure 4.6. The origin of the coordinate system is located in the center of the protective surface of the concrete slab, the x-axis is perpendicular to the concrete surface, and the y-axis points upwards.

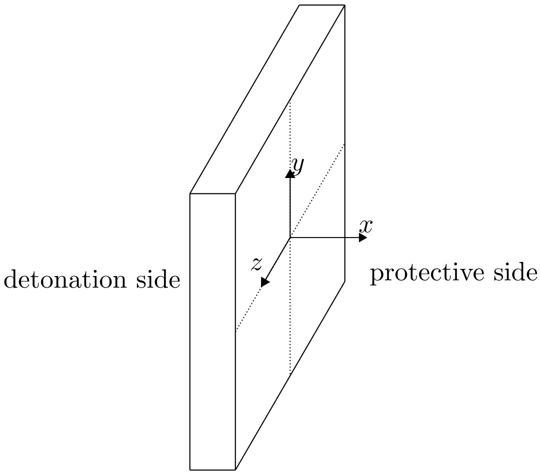

Figure 4.6.: Coordinate system for the evaluation of the measurements

The evaluation of the visible damaged areas of the concrete slabs is done separately for the different areas: crushing crater, breach and spalling crater. Figure 4.7 shows these areas and the associated dimensions for the situation without a breach (left) and with a breach (right).

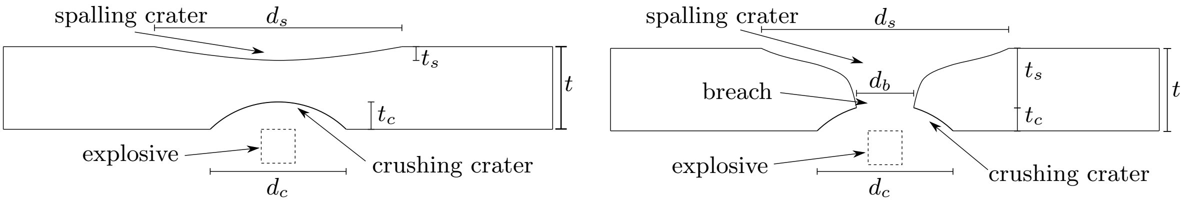

Figure 4.7.: Dimensions of the damaged areas without breach (left) and with breach (right)

In figure 4.7, the letter d is used for diameters and the letter t is used for measurements in the direction of the concrete slab thickness (depth). The subscripts indicate whether the respective dimension corresponds to a crushing crater c, a breach b, or a spalling crater s.

4.4.1. Geometry of the damaged areas

The diameters of the **crushing craters** are measured in images taken immediately after the tests. These images are transformed into the y-z plane (x=-t) of the concrete slab surface in the same way as the HS recordings to allow true measurements in this plane. In order to derive comparable quantities, area equivalent circles are determined from the measured areas of the crushing craters and the corresponding diameters are used for the following evaluations.

The depths of the crushing craters were measured in the center of the crushing crater immediately after the test with a folding rule.

To evaluate the shapes of the **spalling craters**, the tested concrete slabs were measured with 3D scans. Prior to performing the 3D scans, concrete fragments that could be visually identified as spalled, but were still loosely attached, were removed from the concrete slabs. This is particularly relevant in the case of the fiber reinforced concrete slabs.

Approximately half of the 3D scans were carried out using a laser scanner and the other half using photogrammetry. The photogrammetry software used is Agisoft Metashape. The accuracy of the distance measurements provided by the software is 1 mm. For the tests performed, this accuracy is considered sufficient. The higher resolution of the laser scans in the sub-millimeter range can cause problems in tests with steel fibers, since the scanned steel fibers make it difficult to identify the concrete surface within the point cloud. The 3D scans using photogrammetry did not capture the protruding steel fibers, and the resulting point cloud clearly represents the concrete surface.

To evaluate the 3D shape of the spalling crater, the scanned points of the spalling crater in Cartesian coordinates are transformed into cylindrical coordinates with the x-axis as the axis of rotation. The location of the origin of the coordinate system is calculated as the center of all scanned points of the spalling crater projected onto the surface of the undamaged concrete slab ($x = 0$).

Figure 4.8 (left) shows a photo of the spalling crater from SN142 with a breach. Figure 4.8 (right) shows the scanned points from the surface of the spalling crater in the z-y plane for the same test (gray dots). The averaged dimensions for the breach and the spalling crater are added as red circles. The radii of these circles are determined by averaging the radii of the scanned points at the location of the breach ($x = -t_s$) and at the surface of the concrete slab ($x = 0$) for the diameter of the spalling crater.

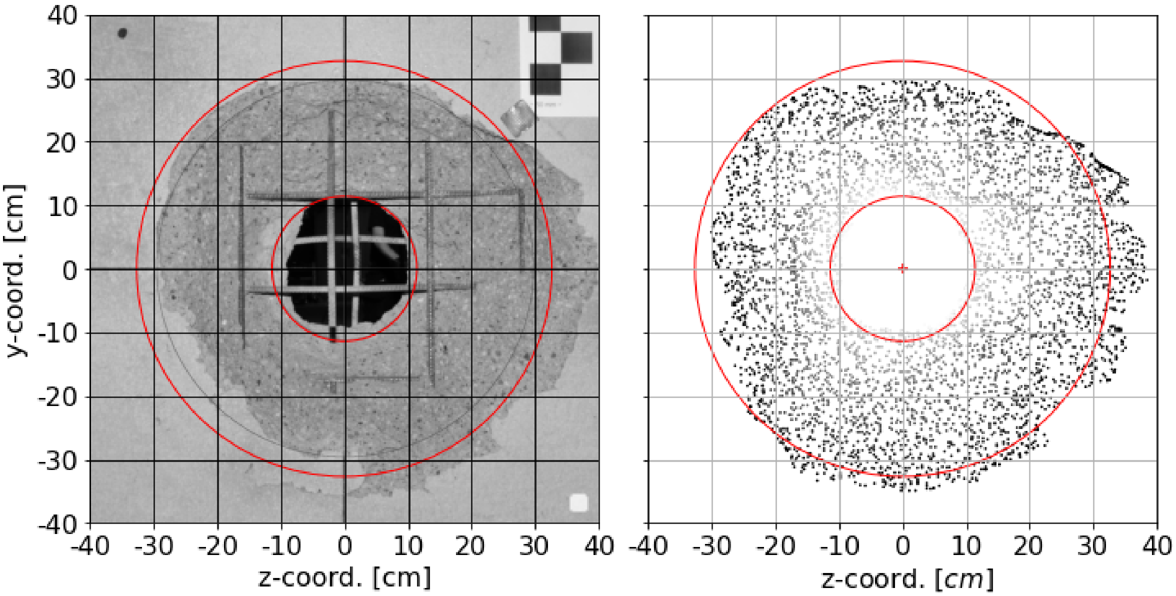

Figure 4.8.: Photo of spalling crater from SN142 (left) and scanned points projected into z-y plane (right, number of points reduced for plot) including averaged dimensions for breach and spalling crater (red circles)

Slight deviations between the photo and the 3D scan are caused by the fact that the photo was taken immediately after the test and the 3D scan was performed after removal of visually loose parts. In addition, very shallow areas of the spalling crater (e.g. z-coord.=40 cm) were sometimes cut off during post-processing of the 3D scan.

Figure 4.9 shows the scanned coordinates from the surface of the spalling crater in the z-x plane for test SN142 with a breach (gray dots). The cylindrical coordinates of these points are rotated around the x-axis to show them in one common radius-depth plane (black dots). The points in the radius-depth plane (black dots) are then approximated by a polynomial, shown as a red line.

This transformation and subsequent approximation unifies the irregular geometry of the spalling crater and thus allows a better comparison of different tests under the assumption of rotational symmetry.

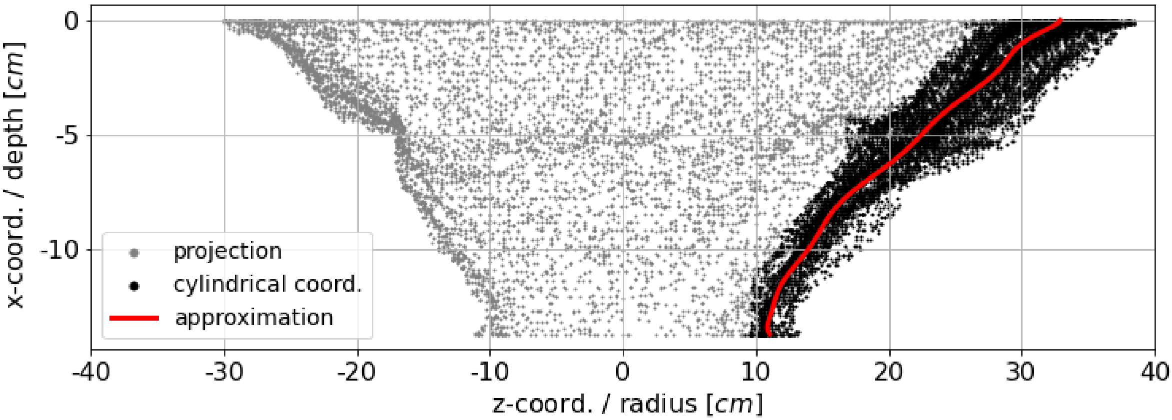

Figure 4.9.: Scanned coordinates of spalling crater projected into z-x plane (gray dots) transformed into cylindrical coordinates and depicted in the radius-depth plane (black dots) including an approximation by a higher order polynomial (red line) - SN142 (number of points reduced for plot)

4.4.2. High-speed recordings / tracking

The analysis of the HS recordings is performed using the open source library OpenCV. More information about the implemented algorithms can be found in the literature [Hartley and Zisserman, 2004], [Kaehler and Bradski, 2017], [Schreer, 2005], [Szeliski, 2011].

HS cameras 1+2 were oriented at a horizontal angle of about 75° relative to the x-axis. In order to perform measurements in the HS recordings, the perspective of the image plane is transformed into a target plane so that distances and angles are correctly represented in this target plane (x-y plane, z=0). Marks on the surface of the concrete slabs with known relative coordinates are used as a reference to determine the corresponding homography and scale. The spatial resolution of the HS recordings results in an accuracy for distance measurements of $1.8\,\mathrm{mm\,px^{-1}}$ in the calibrated plane.

The same procedure is used for HS camera 3 with the difference that the target plane of the transformation is located in the surface of the concrete slab (y-z plane, x=0, target plane of HS camera 3). More details about this transformation process can be found in the appendix section F.

All distances in front of or behind the calibrated target plane are displayed too long or too short according to the intercept theorem. The resulting maximum error of the distance measurements from HS camera 1+2 can be estimated based on the assumption of rotational symmetry of the debris cloud.

For example, the diameter of the debris cloud in test SN142 is 60 cm. The shortest distance between the calibrated target plane in the center of the concrete slab (x-y plane z=0) and the HS camera is 120 cm. Consequently, the maximum error of the distance measurements is ±25 %.

Because the debris cloud is very dense in the test SN142, the debris behind the target plane (x-y plane, z=0) is less likely to be tracked. Therefore the measured distances are more likely to be too short and the derived velocities too slow. In tests with less secondary debris, the debris cloud is not as dense. In these tests distance measurements are equally likely to be too short or too long. This is particularly relevant for tests with steel fiber reinforcement. However, the diameter of the debris cloud in these tests is also significantly smaller, resulting in a smaller maximum error.

Assuming rotational symmetry, the error of the measured distances at the outer edge of the debris cloud in the HS recording is much smaller because this debris is close to the calibrated target plane (x-y plane, z=0).

To determine the velocities of the secondary debris, a tracking algorithm is applied to the transformed recordings of HS camera 1+2. This algorithm detects characteristic features in the HS recordings and follows these features between successive time steps using optical flow [Lucas and Kanade, 1981], [Bouguet, 1999]. A flowchart of the tracking algorithm developed can be found in the appendix section C.

In this context, a feature describes a unique pattern of adjacent pixels based on their intensity/brightness values, rather than a discrete concrete fragment. The optical flow then determines the movement of these features between successive time steps based on the intensity/brightness gradients within the neighborhood of the associated pixels. The underlying assumptions are that the intensity value of a feature does not change between successive time steps, and that movements within the neighborhood of a pixel are similar.

For additional robustness, an expected search location for a feature in the following time step is prescribed based on the velocity and direction of movement of that feature in the preceding time steps.

During tracking, the algorithm continuously checks the quality of the tracked features in successive time steps. This is done by applying the optical flow algorithm backwards and comparing the position of the same feature from both time directions in the same time step. If the calculated distance is greater than one pixel, the feature is discarded from further tracking.

The algorithm also checks for new characteristic features at every fifth time step (1.0 ms) and adds them to the list of tracked features.

In addition to the negative effects of light and dust, the shaking of the HS cameras poses a challenge to the tracking algorithm. As a countermeasure, the velocity of each tracked feature is averaged over all previous time steps.

To avoid tracking parts in the background, features with a x-velocity less than $0.1\,\mathrm{m\,s^{-1}}$ are discarded and the search area is restricted by a mask.

To eliminate tracking of swirled-up dirt not resulting from the concrete slab, features with a movement outside of three times the standard deviation of the movement of all features in the same time step are discarded. This excludes particles moving backward and perpendicular to the main flight direction from tracking.

An example of the tracking performed using the HS recordings from HS camera 1+2 is shown in figure 4.10 for test SN144. The dots mark the tracked features, with their color representing the determined velocity, and the black dotted lines are the corresponding trajectories.

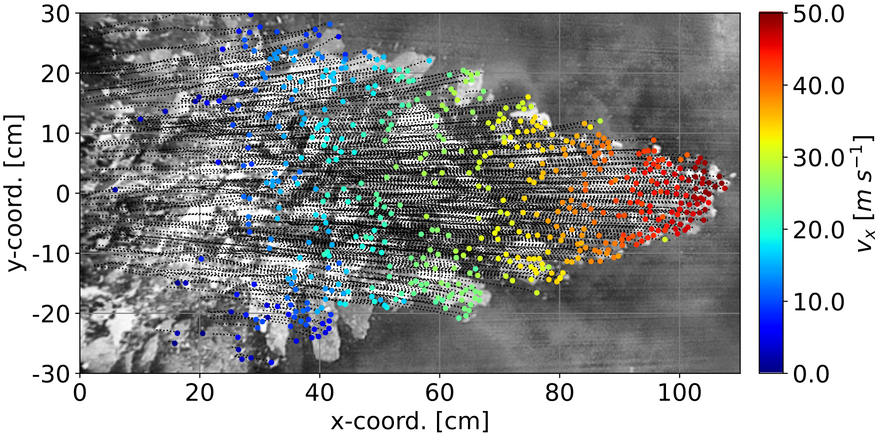

Figure 4.10.: Tracking of SN144

In the first pretest SN80, the HS recording was not successful, so no tracking can be done. Due to a slightly different setup, tracking in the tests SN82-SN129 is done by a manually tracking of a small number of fragments using the Open Source Physics Software Tracker. Starting from test SN130, automated tracking with optical flow is used for all tests.

4.4.3. Digital image correlation - DIC

The evaluation of the DIC recordings is performed using the commercial software GOM correlate 2020. No additional calibration was performed to validate the measurements of the DIC recordings. The accuracy of the distance measurements can be estimated based on the resolution of the HS recordings, which gives an accuracy of $1.8\,\mathrm{mm\,px^{-1}}$. However, DIC measurements can evaluate the recordings in the sub pixel range, leading to a much higher accuracy compared to just the pixel scaling alone. The scale deviation calculated by the software used is 0.01 mm.

4.4.4. Debris collection

The resulting secondary debris was collected separately for each test. A vacuum cleaner was used to ensure that very fine debris was also collected.

During transportation and storage, some of the collected secondary debris became wet and therefore cannot be used to evaluate the total mass of the secondary debris. Therefore, the total mass of the secondary debris is calculated using the volume of the spalling crater measured from the 3D scans together with the density of the dry concrete measured on the test cubes.

In order to obtain the size distribution of the secondary debris on the protective side of the concrete slab, the collected debris was sieved and the associated masses were determined separately by size. The influence of the wetness of the debris is acceptable for the size distribution as the proportions of the different debris sizes are evaluated using relative masses with respect to the total mass of equally wet debris.

4.5. Evaluation of the damaged areas

In this section, the different damaged areas are evaluated in terms of their influence on the secondary debris. Firstly, the crushing crater is discussed as it reflects the direct interaction of the explosive with the concrete slab. Then, the occurrence of a breach in the tests performed is compared with threshold curves given in the literature. Finally, the geometry of the spalling crater is discussed in detail, as this is the most important region for the secondary debris. This includes an analysis of the underlying damage mechanism as well as the mass and size distribution of the secondary debris fragments.

4.5.1. Crushing crater

The crushing crater is the region of the concrete structure where the induced pressure occurs in the form of a shock wave that completely crushes the concrete. The shock wave decays rapidly as it propagates through the concrete, resulting in a limited expansion of the crushing crater. Once the peak pressure of the shock wave has been reduced below the dynamic compressive strength of the concrete, it will only cause further damage after it is reflected at the protective surface of the concrete slab, resulting in tensile stresses.

The dimensions of the crushing crater are of little relevance to the resulting secondary debris on the protective side of a concrete slab. Nevertheless, they are evaluated because they reflect the direct interaction of the explosive with the concrete. Also, in the case of a breach, the depth of the crushing crater interacts directly with the depth of the spalling crater.

Figure 4.11 shows the diameter d_c (left) and the depth t_c of the crushing crater (right) in dependence on the TNT and spherical equivalent explosive mass $W_{TNT,sp}$. The shapes of the markers indicate whether a breach occurred in the test (circle) or not (triangle). The values for the crushing crater depth were only measured up to an accuracy of 5 mm. For better readability the markers are slightly offset in the horizontal direction.

The retrofit layer does not affect the dimensions of the crushing crater because it is located on the protective side of the concrete slab and there was no breach in the corresponding tests. Therefore, these tests are included in the evaluation of the crushing crater as a concrete slabs without steel fibers.

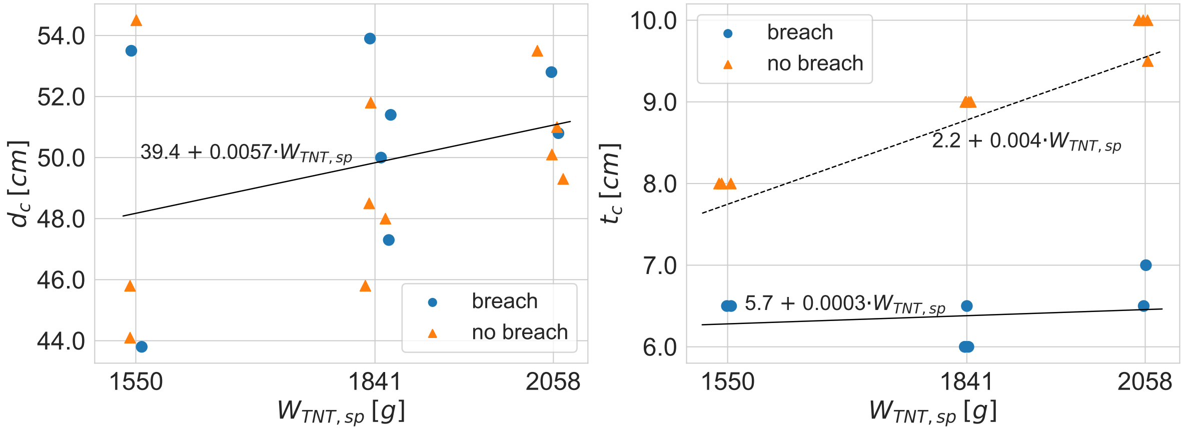

Figure 4.11.: Crushing crater diameter (left) and depth (right) over TNT and spherical equivalent explosive mass

As expected, the average crushing crater diameter increases with increasing explosive mass. For smaller explosive masses, there is a greater variation between the corresponding tests, which decreases with increasing explosive mass. A dependence of the crushing crater diameter on the occurrence of a breach (circles or triangles) cannot be identified.

The crushing crater depths in figure 4.11 (right) can be grouped into two different situations. For all cases without a breach (triangles), the crushing crater depth increases linearly with increasing TNT and spherical equivalent explosive mass $W_{TNT,sp}$ (dashed line).

When a breach occurs, the crushing crater depth is defined as the distance from the surface of the concrete slab to the location of the narrowest opening between the crushing crater and the spalling crater. It is therefore also influenced by the size of the spalling crater. In the tests presented, the location of the breach, and therefore the depth of the crushing crater, is in all cases at a depth of approximately 6.5 cm from the loaded surface of the concrete slab.

The location of the breach is likely to be influenced by the position of the rebar layer on the detonation side. In order to be able to make reliable statements about the influence of the rebar layer, additional tests with a variation of the rebar layer position are required.

4.5.2. Breach

An important factor for the secondary debris is whether or not the concrete slab is breached by the detonation. As this is a very characteristic feature of the damage from a contact detonation, it is well suited for a comparison between different test series.

Figure 4.12 shows the occurrence of a breach in dependence on the spherical equivalent explosive mass $W_{TNT,sp}$ and the concrete slab thickness T. The tests with a breach are marked as dots and the tests without a breach are marked as triangles. The different lines mark threshold curves from the literature for the occurrence of a breach, which will be illustrated in the following.

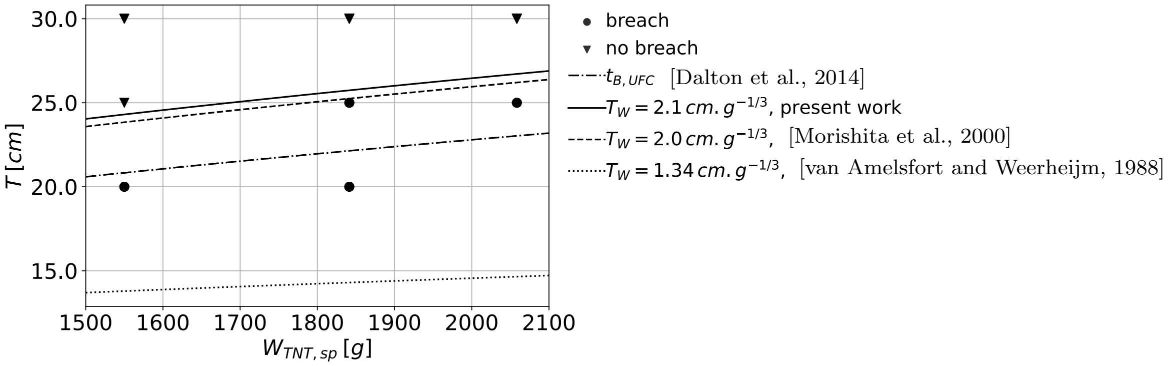

Figure 4.12.: Occurrence of a breach for tests without steel fibers including threshold curves

In the present series of tests, a scaled concrete slab thickness of $T_W = 2.1\,\mathrm{cm\,g^{-1/3}}$ proves to be a well suited threshold for the occurrence of a breach. For all tests with a scaled thickness $T_W < 2.1\,\mathrm{cm\,g^{-1/3}}$, a breach can be observed. For the tests with a scaled thickness $T_W > 2.1\,\mathrm{cm\,g^{-1/3}}$, there is no breach and only spalling on the protective side of the concrete slab. This threshold is shown as a solid line in figure 4.12.

The criterion of a scaled concrete slab thickness as threshold for a breach has also been employed by [Morishita et al., 2000] and [van Amelsfort and Weerheijm, 1988].

[Morishita et al., 2000] proposes a breach threshold scaled thickness of $T_W = 2.0\,\mathrm{cm\,g^{-1/3}}$ based on contact detonation tests on 10 cm thick normal strength concrete slabs with a reinforcement ratio of $47.1\,\mathrm{cm^2/m^2}$. The explosive charges were cylinders with explosive masses of 111 g and 435 g of Pentolite (50 %TNT and 50 % PETN by mass). The given threshold is already given in terms of a TNT equivalent explosive mass. The explosive charges were attached flush with one of their flat surfaces to the surface of the concrete slabs and had a L/D ratio of 1.0. This L/D ratio results in a spherical equivalence factor of 1.03 based on the energy equivalent impulse in section 3.3. The resulting threshold curve including the equivalence factor for the L/D ratio is shown as a dashed line in figure 4.12.

[van Amelsfort and Weerheijm, 1988] proposes a breach threshold scaled thickness of $T_W = 1.35\,\mathrm{cm\,g^{-1/3}}$ based on a series of contact detonation tests on normal strength concrete slabs with a thickness of 6 cm and a reinforcement ratio of $195\,\mathrm{cm^2/m^2}$. The explosives were hemispherical charges with their flat surface attached to the surface of the concrete slabs. The charges had masses between 70 g and 90 g of PETN (80 %). To relate this explosive to TNT [Jeremic and Bajic, 2006] gives a TNT equivalency factor of 1.08 for PETN (80 %) based on the heat of detonation.

For a comparison with the test series in this work, an equivalence factor for the charge geometry is derived analogous to the procedure described in section 3. This factor relates the spherical charges to equivalent hemispherical charges on the basis of the energy equivalent impulse. In the tests of [van Amelsfort and Weerheijm, 1988], no information is given on how and where the explosive charges were initiated. Therefore, it is assumed that the hemispherical charges were initiated at the point on the surface of the explosive charge furthest from the concrete slab. The derived equivalence factor can be found in the appendix section G.2. The resulting curve for the threshold criterion $T_W = 1.35\,\mathrm{cm\,g^{-1/3}}$ using an energy equivalent hemispherical charge and the TNT equivalency factor for PETN is shown as a dotted line in figure 4.12.

UFC 3-340-02 [Dalton et al., 2014] provides a threshold thickness $t_{\mathrm{B,UFC}}$ for the occurrence of a breach, calculated from a spalling parameter Ψ and the distance R between the surface of the concrete slab and the center of the explosive charge. The associated empirical equations (4.3) - (4.5) refer to imperial units.

$$t_{\mathrm{B,UFC}} = \frac{R}{a + b\,\Psi + c\,\Psi^2} \tag{4.3}$$

Where $a = 0.028\,205$, $b = 0.144\,308$, $c = 0.049\,265$ are dimensionless parameters and R is the distance between the center of the explosive charge and the surface of the concrete slab. For the presented comparison R is chosen as the radius of the equivalent spherical charge.

The spalling parameter Ψ for contact charges is given by:

$$\Psi = 0.527\, R^{0.972}\, f_c^{0.308}\, W_{adj}^{-0.341} \tag{4.4}$$

Where f_c is the unconfined compressive strength (cylinder) of the concrete and W_{adj} is the TNT equivalent mass of a hemispherical surface charge giving an equivalent total impulse. This equivalent hemispherical charge is oriented with its flat surface perpendicular to the surface of the concrete slab and can be calculated by:

$$W_{adj} = B_f\, C_f\, W_{\text{TNT}} \tag{4.5}$$

In this, the burst configuration factor B_f corrects the explosive mass to that of an equivalent surface burst. For the presented comparison this factor is set to 0.5.

The cylindrical charge factor C_f is used to account for the L/D ratio of a cylindrical charge, which is oriented side-on to the concrete surface. Since the charges in the presented test series are oriented end-on to the concrete surface, this factor is set to $C_f = 1.0$, which is the suggested value for *all other cases* in [Dalton et al., 2014]. The resulting threshold curve is shown as dash-dotted line in figure 4.12.

When comparing the different threshold curves, it can be seen that the threshold curve of [Morishita et al., 2000] agrees very well with the presented test series. This is due to the fact that although the explosive mass and the thickness of the concrete slabs are slightly smaller when compared to the presented test, the orientation and geometry of the explosive charge as well as the reinforcement ratio are very similar to the presented tests.

The threshold curve of [van Amelsfort and Weerheijm, 1988] significantly underestimates the required thickness of a concrete slab to avoid breaching when compared to the presented tests. A possible reason for this is that although the type and geometry of the explosive charge are taken into account by the respective equivalence factors, the explosive mass and concrete slab thickness are much smaller than in the presented test. In addition, the reinforcement ratio is more than four times that of the presented test series. Therefore, tests with different reinforcement ratios and charge geometries are required for a thorough analysis.

The threshold curve of [Dalton et al., 2014] slightly underestimates the required thickness of a concrete slab to avoid breaching when compared to the presented tests. Probably the most important influence for this deviation is the different shape of the explosive charge. With an increased factor $C_f = 1.5$, the threshold curve of [Dalton et al., 2014] is almost identical to the presented threshold of $T_W = 2.1\,\mathrm{cm\,g^{-1/3}}$.

4.5.3. Spalling crater

Figure 4.13 shows the **diameter** of the spalling crater d_s for the tests without steel fibers over the scaled concrete slab thickness T_W. The shape of the markers indicates the TNT and spherical equivalent mass of the explosive, and the color indicates the thickness of the concrete slab. This representation was chosen because it reflects the explosive mass and the thickness of the concrete slab in relation to the threshold for a breach ($T_W = 2.1\,\mathrm{cm\,g^{-1/3}}$).

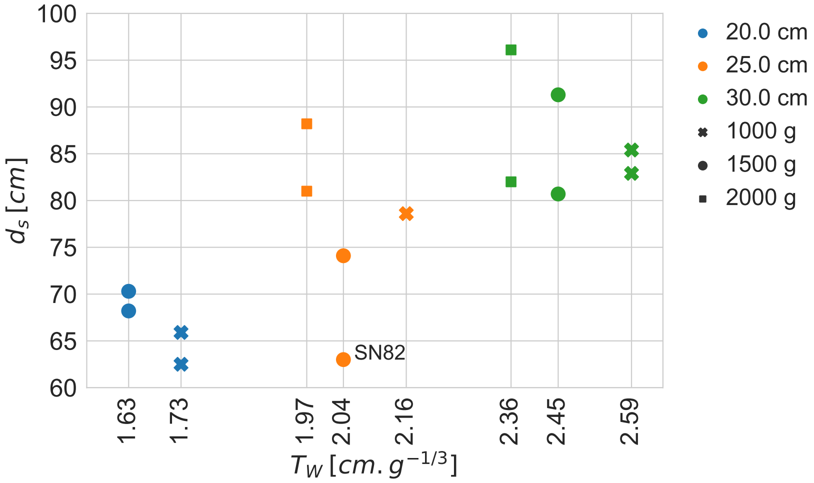

Figure 4.13.: Diameter of the spalling crater d_s over scale thickness T_W of the concrete slabs

An increasing spalling crater diameter d_s with increasing scaled thickness of the concrete slab T_W can be observed in figure 4.13. This increase of the damaged area with increasing scaled thickness seems contradictory at first, but is due to the fact that the pressure wave can spread over a larger area when propagating through a thicker concrete slab. Therefore, the dominant influence on the diameter of the spalling crater is the thickness of the concrete slab and not the explosive mass.

When the groups of tests with the same concrete slab thickness are analyzed separately, a decreasing trend of the spalling diameter can be observed as the scaled thickness increases. This effect is caused by the influence of the explosive mass, since a smaller explosive mass results in a greater scaled thickness. However, for the range tested, the influence of the explosive mass on the spalling diameter is small compared to the influence of the concrete slab thickness.

Test SN82 has a smaller diameter than would be expected when compared to the other tests. One reason for this could be the proximity to the breach threshold $T_W = 2.1\,\mathrm{cm\,g^{-1/3}}$, which leads to more pronounced variations in the dimensions of the spalling crater. Another reason could be that this concrete slab was part of the pretest series and was produced by a different manufacturer. It is unclear how this could affect the resulting shape of the spalling crater as the parameters of the concrete are very similar to the other tests. However, it is important to note that the concrete slabs in the pretest series had a much shorter curing time compared to the concrete slabs in the main test series (appendix figure A.1).

To evaluate the **shape and depth** of the spalling crater, figure 4.14 shows the rotationally symmetric shapes of the spalling craters for the different scaled concrete slab thicknesses. On the left are the tests with a breach and on the right the tests without a breach.

These shapes were determined using the procedure described in section 4.4.1 and averaged over the tests of the same type in order to reduce the influence of experimental variations. Test SN82 was excluded from this averaging, because it shows a strongly deviating shape for which the reason could not be clearly determined. An overview of all tests is given in the appendix section B.2.

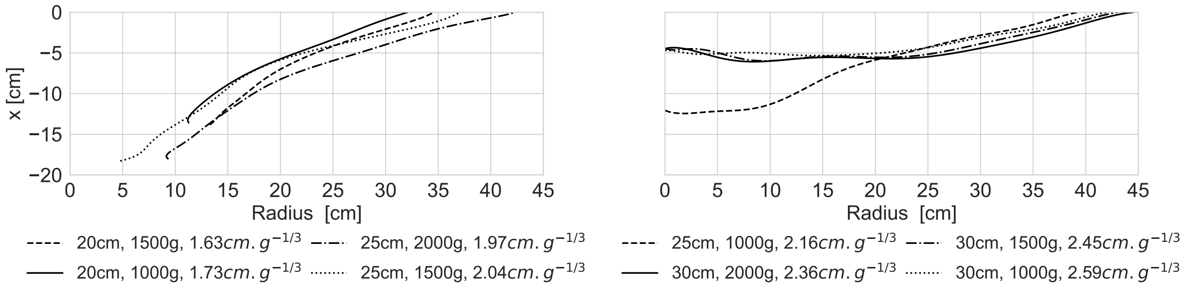

Figure 4.14.: Rotationally symmetric shapes of the spalling craters without steel fibers

The tests performed give a good representation of the development of the spalling crater with increasing scaled thickness. The shape of the spalling crater is almost straight for a scaled thickness of $T_W = 1.63\,\mathrm{cm\,g^{-1/3}}$. As the scaled thickness increases, the influence of the rebar becomes more dominant, resulting in a flatter shape of the spalling crater above the rebar layer ($x \gtrsim -4.5\,\mathrm{cm}$).

In this context, a comparison between the tests with an explosive mass of 1500 g and a breach shows the influence of the scaled thickness very well (figure 4.14, left). Between the two cases ($t = 20\,\mathrm{cm}$ dashed line and $t = 25\,\mathrm{cm}$ dotted line), the radius of the spalling crater above the rebar layer ($x \gtrsim -4.5\,\mathrm{cm}$) increases with increasing concrete slab thickness. At the same time, the radius of the breach decreases with increasing scaled thickness and the shape of the spalling crater approaches the shape without a breach (figure 4.14, right: $T_W = 2.16\,\mathrm{cm\,g^{-1/3}}$).

The threshold for a breach is reached between the scaled thickness of $2.04\,\mathrm{cm\,g^{-1/3}}$ and $2.16\,\mathrm{cm\,g^{-1/3}}$. For all tests without a breach (figure 4.14, right) the slope of the spalling crater above the rebar layer is very similar with an average angle of about 18° against the surface of the concrete slab.

In almost all cases without a breach, the depth of the spalling crater is limited by the position of the rebar relative to the surface of the concrete slab. The only exception is the test with a scaled thickness of $T_W = 2.16\,\mathrm{cm\,g^{-1/3}}$ (only one test available), which is slightly above the breach threshold of $T_W = 2.1\,\mathrm{cm\,g^{-1/3}}$. This test shows a greater depth of the spalling crater below the rebar layer. However, as can be seen in figure 4.15, most of the concrete below the rebar was retained by the rebar during the detonation test and only fell out afterwards.

Although this effect is more pronounced near the breach threshold of $T_W = 2.1\,\mathrm{cm\,g^{-1/3}}$, cracked but still attached concrete below the rebar layer can also be found at larger scaled thicknesses. However, this concrete is not relevant for the secondary debris, as in cases without a breach the secondary debris consists mainly of concrete fragments from above the rebar layer.

Figure 4.15.: Protective side of test SN175 ($T_W = 2.16\,\mathrm{cm\,g^{-1/3}}$) directly after the tests and after removal of loose parts

4.5.4. Damage mechanism

To better analyze the underlying damage mechanism, some concrete slabs were cut along their horizontal centerline (z-axis). Figure 4.16 shows the resulting cross-sections of two concrete slabs, representing the situations with a breach (SN130, top) and without a breach (SN131, bottom). The corresponding sections from the 3D scans (without rotationally symmetric approximation) are included as red lines.

For the case without a breach (SN131, bottom), the section from the 3D scan of test SN175 (figure 4.15) is added as a blue line. Tests SN131 and SN175 were both loaded with 1000 g of SEMTEX10, but have a different concrete slab thicknesses (SN130: 30 cm, SN175: 25 cm).

Figure 4.16 shows that the concrete is more damaged than can be seen from the surface. This effect is much more pronounced in the region of tensile failure (spalling crater), which is particularly evident in the situation without a breach (SN131, bottom). The area of compressive failure directly beneath the explosive (crushing crater) is almost exclusively confined to the damaged area visible from the surface.

Between the crushing crater and the spalling crater is a region of visually intact concrete. In order to assess the properties of the concrete in this region, a drill core was taken from this region in the center of the reinforced concrete slab. This revealed that although the concrete in the center of the reinforced concrete slab appears visually intact, the concrete

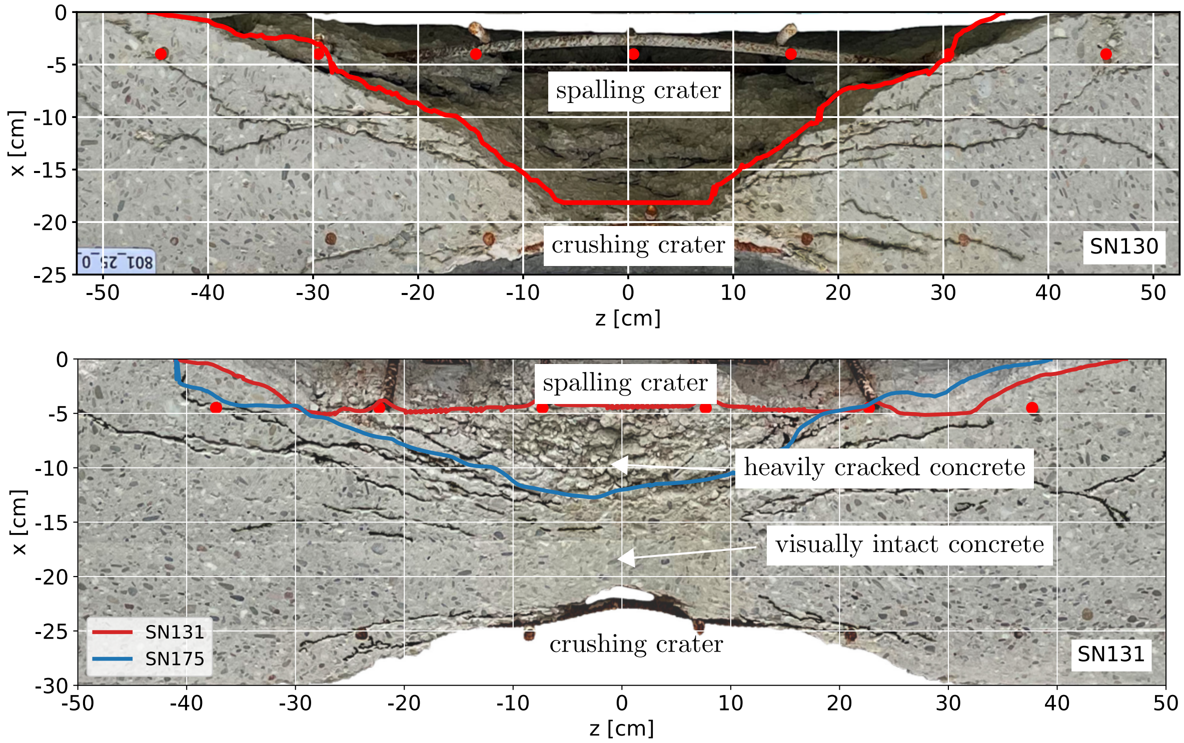

Figure 4.16.: Horizontal cross section of test SN130 (top, no breach) and test SN131 (bottom, with breach) including measurements from 3D scans

structure was permanently damaged by the detonation. It was not possible to determine the static parameters from the existing drill core as it had largely disintegrated into individual parts during drilling. Whether the damage in this area was caused by the initiated shock wave or by the reflected tensile wave cannot be readily determined.

In both cases, with a breach (SN130, top) and without a breach (SN131, bottom), there are cracks starting from the lower part of the spalling crater and propagating outwards. The propagation of these cracks appears to be influenced by the location of the rebars, which represent a weakening of the concrete structure.

In the case without a breach (SN131, bottom), there is an area of heavily cracked concrete directly below the rebar layer that extends up to a depth of about -15 cm. This region correlates well with the shape of the spalling crater of test SN175 (blue line), in which most of the cracked concrete below the rebar fell out when the concrete slab was removed from the test setup (figure4.16). As mentioned before, test SN175 was loaded by the same explosive mass but the concrete slab has a thickness of 25 cm instead of 30 cm.

It is expected that most of the cracked concrete in the region below the rebar layer would have detached without the rebars resulting in a similar spalling crater for both situations. The retaining effect of the rebar layer can be explained by the development of a vault-like structure in the damaged concrete, which can still carry some load under compression while being supported by the rebar.

The shape of the spalling crater, including the crushed concrete below the rebar, is very similar in the tests loaded with the same explosive mass but with different concrete slab thicknesses (SN131 and SN175). This indicates that the explosive mass is the determining factor for the depth of the spalling crater. Unfortunately, not enough concrete slabs were cut in this series of tests to make reliable statements about this.

4.5.5. Mass and size-distribution of the secondary debris

For a more thorough evaluation of the dependence of the spalling crater on the explosive mass, figure 4.17 (left) shows the total mass of the secondary debris over the TNT and spherical equivalent explosive mass separately for each test. As explained in section 4.4.4, the total mass of the secondary debris is determined from the 3D scans and therefore includes some of the concrete retained by the rebar layer. However, as can be seen from the cross-section of test SN131 in figure 4.16, in most cases only a small proportion of the retained concrete was identified as loose prior to the 3D scans.

Figure 4.17 (right) shows the size distribution of the collected secondary debris from the protective side of the concrete slab in context with the occurrence of a breach.

In cases with a breach, almost all of the damaged concrete is propelled away from the concrete slab in the form of secondary debris. This is reflected by a significant increase in the total mass of the secondary debris as the explosive mass increases.

In the tests with 1500 g of SEMTEX10 ($W_{TNT,sp} = 1841\,\text{g}$), the total mass of the secondary debris is very similar for the concrete slab thicknesses of 20 cm and 25 cm (with breach). This again indicates, that the total mass of the secondary debris in cases with a breach is mainly dependent on the explosive mass and less on the concrete slab thickness.

In case of no breach the increase in the total mass of secondary debris with increasing explosive mass is not as pronounced. This is mainly attributed to the retaining effect of the rebar layer. For the tested range, the depth of the spalling crater relevant for the

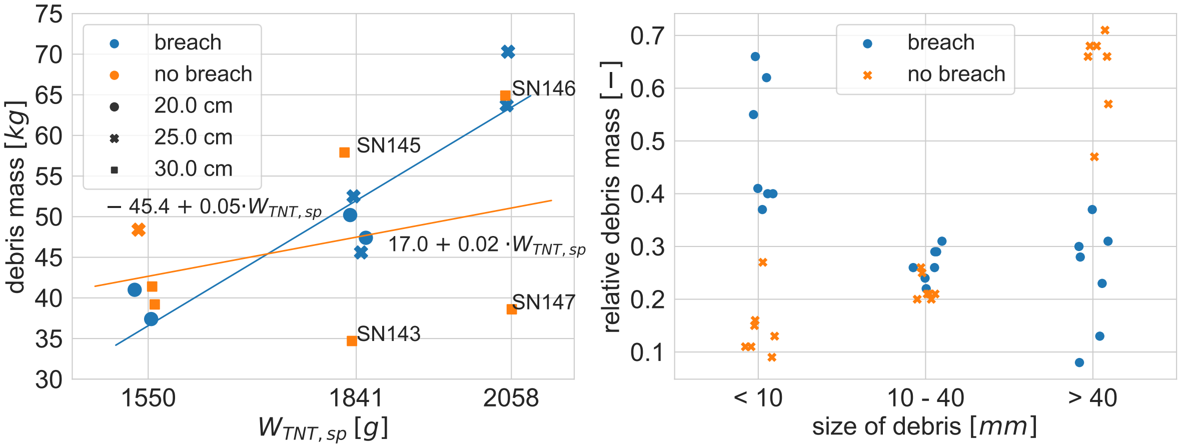

Figure 4.17.: Mass of secondary debris from spalling crater over the TNT and spherical equivalent explosive mass (left), size distribution of the secondary debris on the protective side of the concrete slab (right)

secondary debris is always limited by the rebar layer in cases without a breach.

The diameter of the spalling crater in the tested range is much more dependent on the thickness of the concrete slab than on the explosive mass. Also, all the tests without a breach, but SN175 (25 cm, 1000 g), are 30 cm thick concrete slabs. Therefore, the tests without a breach show a very similar diameter of the spalling crater, which is reflected in a similar total volume/mass of the secondary debris.

Following the principle of conservation of energy, the different explosive masses must be reflected in the damaged volume below the rebar and/or in the velocity of the secondary debris. It is expected that the mass of the secondary debris, including the damaged concrete below the rebar, will have a similar dependence on the explosive mass as in the cases with a breach. Further testing is required to confirm this conclusion.

The influence of the rebar is apparent in the relatively large variation of the total secondary debris mass in the tests SN143 and SN145, as well as SN146 and SN147. In these tests, the concrete cover deviates from the planned 35 mm, which is reflected by the total mass of the secondary debris. In test SN143 the concrete cover is 5 mm too small and in tests SN145 and SN146 it is 10 mm too large.

From figure 4.17 (right) it can be seen, that the size-distribution of the secondary debris changes completely depending on the occurrence of a breach. Without a breach, ∼60 % of the secondary debris consists of fragments larger than 40 mm and only ∼15 % has a size smaller than 10 mm. With a breach, this relation flips, and ~50 % of the debris is smaller than 10 mm, while only ~25 % consists of fragments larger than 40 mm.

It is concluded that the rebar has a very strong influence on the total mass of the secondary debris as long as no breach occurs. If a breach occurs, the concrete is so heavily fragmented that the rebar can no longer retain the concrete and therefore loses most of its influence.

4.5.6. Summary

In cases without a breach the depth of the spalling crater increases linearly with increasing TNT and spherical equivalent explosive mass. When the concrete slab is breached by the detonation, this location is at a depth of approximately 6.5 cm from the loaded surface of the concrete slab in the tests presented.

The experimental results show that a scaled thickness of $T_W = 2.1\,\mathrm{cm\,g^{-1/3}}$ is a well suited threshold for the occurrence of a breach. This threshold is compared with other test series from the literature. A good agreement can be found with the breach threshold by [Morishita et al., 2000], which is based on a test series with parameters very similar to the presented tests. The breach thresholds by [van Amelsfort and Weerheijm, 1988] and [Dalton et al., 2014] underestimate the required thickness of the concrete slab compared to the presented tests. This is probably due to a different shape and arrangement of the explosive charges and a much larger reinforcement ratio. Further experimental tests with a variation of the reinforcement ratio and the charge geometry are required for a thorough analysis of the respective influences.

The tests presented show that the diameter of the spalling crater is more dependent on the thickness of the concrete slab. The depth of the spalling crater, including the crushed concrete below the rebar layer, is more dependent on the explosive mass.

The influence of the rebar layer on the shape of the spalling crater increases with increasing scaled thickness. This results in a flattened shape of the spalling crater above the rebar layer. For all tests without a breach, the average slope of the spalling crater against the surface of the concrete slab is approximately 18°.

The depth of the spalling crater relevant for the secondary debris is limited by the rebar layer in all tests without a breach. Therefore, the damage below the rebar layer is only relevant for the secondary debris if a breach occurs.

The size distribution of the secondary debris fragments is flipped as soon as a breach occurs. With a breach, more of the secondary debris consists of small fragments, whereas in cases without a breach, the larger fragments have a greater proportion by mass.

4.6. Velocity of the secondary debris

To evaluate the velocity of the secondary debris, figure 4.18 shows the HS recordings from the side (HS camera 1+2) for selected tests. The blue dots mark the locations of the tracked features. The red dots mark the features whose mean x-velocity is given in the upper right corner of each image. The time step shown represents the end of the tracking performed and is given in the bottom right corner of the corresponding image.

Especially for larger scaled thicknesses, the trajectory of the tracked features is affected by the rotation of larger debris fragments. As a result, the tracked features move slower than the center of mass of the associated debris fragments, which can even result in an apparent backward motion. Tests where this behavior is very pronounced are not well suited to represent the x-velocity, especially in the outer regions of the debris cloud.

The tests shown in figure 4.21 have been selected to give a good representation of the series of tests, and the associated HS recordings allow very complete tracking without too much interference from rotating fragments. The upper two images show tests including a breach in the concrete slab, and the lower two images show tests where only spalling occurred without a breach. The same tests are used throughout this section to illustrate the behavior of the entire test series. An overview of the HS recordings for tracking of all tests can be found in the appendix section C.

There is less secondary debris as the scaled thickness of the concrete slab increases. At the same time, the individual debris fragments become larger and the maximum x-velocity at the tip of the debris cloud decreases with increasing scaled thickness. These effects are evaluated quantitatively below.

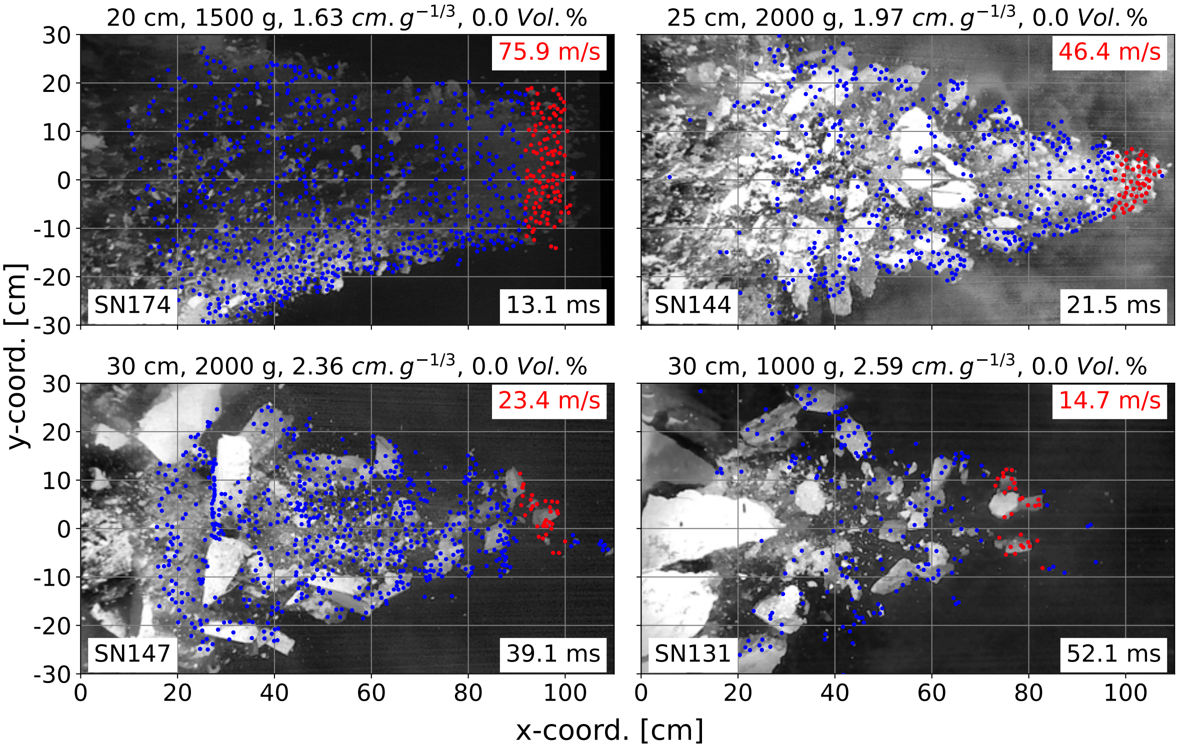

Figure 4.18.: Secondary debris for selected tests

4.6.1. Velocity in y-direction / radial direction

To obtain information about the direction of flight of the secondary debris, figure 4.19 (left) shows the angle of the resulting velocity $(v_x + v_y)$ relative to the x-axis along with a linear regression line for SN174. Figure 4.19 (right) shows analogue regression lines for all tests including an averaged regression line.

This shows that the motion of the debris is dominant in the x-direction, as the majority of the debris moves at an angle less than 20° relative to the x-axis. This trend is very similar for all tests with an increasing angle of the resulting velocity with increasing radial distance from the center. The following evaluations will focus on the x-velocity of the secondary debris as it is the decisive factor in terms of the impact on people and technical installations on the protective side of a concrete slab.

The tests SN130 and SN132 show significantly smaller and larger angles of the resulting velocities. This is due to the rotation of larger debris fragments, which strongly influenced the tracking in these tests.

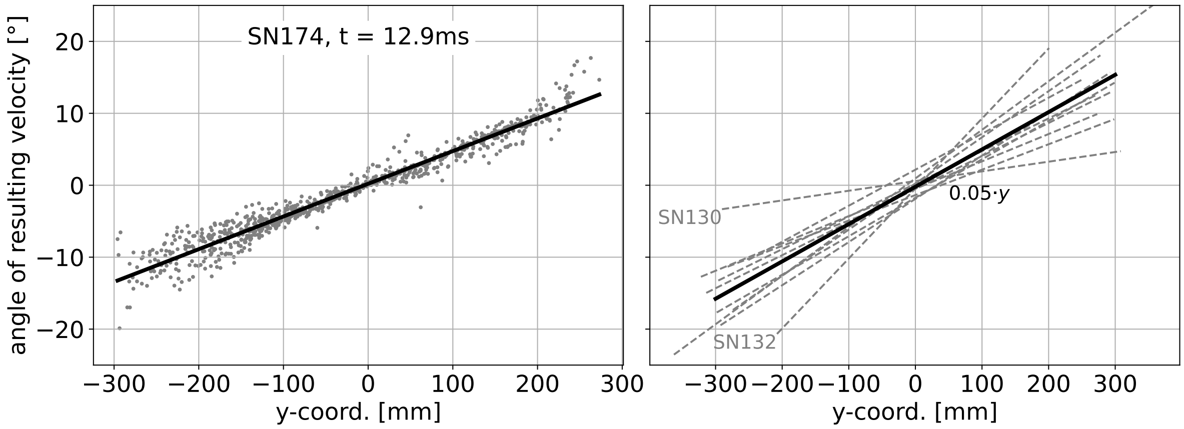

Figure 4.19.: Angle of resulting velocity ($v_x + v_y$): measured values including regression line for SN142, t = 14.9 ms (left) and regression lines for all shots (right)

4.6.2. Maximum x-velocity

Figure 4.20 shows the maximum x-velocity $v_{x,max}$ of the tracked debris fragments over the inverse of the scaled thickness T_W for the tests without steel fibers. The color of the markers indicates the concrete slab thickness, and the shape of the markers indicates the TNT and spherical equivalent explosive mass.

The maximum x-velocity is calculated as the average x-velocity of all tracked debris fragments that are within an x-distance of 100 mm from the tip of the debris cloud at the end of tracking (red dots in figure 4.18).

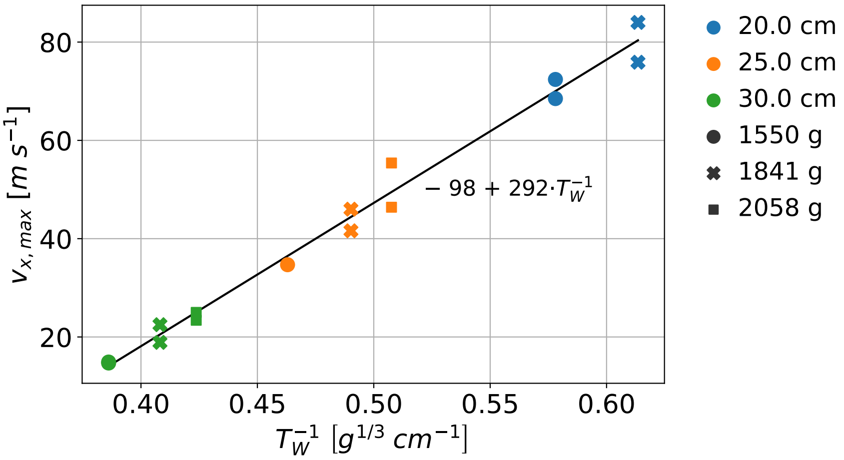

Figure 4.20.: Maximum x-velocity for tests without steel fibers

The inverse of the scaled thickness, including the influence of the L/D ratio of the explosive charge (see section 3.3), provides a useful linear relation with respect to the maximum x-velocity of the secondary debris measured in the experimental tests. The resulting coefficient of determination R^2 between this linear approximation and the measured velocities is $R^2 = 0.99$. A representation without the introduced scaling factor can be found in section 3.3.

The variation in the measured maximum x-velocities between analogue tests is small compared to the dimensions of the damaged areas. This indicates that the maximum x-velocity is less affected by the material inhomogeneity and the rebar location than the resulting damage.

4.6.3. Spatial x-velocity distribution

The secondary debris is not just a single fragment, but a cloud of multiple fragments with different velocities. To get an idea of the spatial x-velocity distribution within the debris cloud, figure 4.21 shows the x-velocities of the tracked features over the y-coordinate. The y-coordinate from the HS recordings can also be interpreted as the radial coordinate r, assuming rotational symmetry.

The horizontal axis in figure 4.21 represents the original y-coordinate of the features in the concrete slab prior to the detonation. This coordinate is determined by tracing each feature back to an x-coordinate of zero. For this, it is assumed that the velocity in x-direction is constant (no drag) and only gravity changes the trajectory of each feature in the vertical y-direction. However, the influence of gravity is only marginal for the time frame observed.

As explained in section 4.4.2, the tracked x-velocity is only correct for fragments at the outer edge of the recorded debris cloud, since the associated features are close to the calibrated target plane. To evaluate the spatial x-velocity distribution, it is approximated by an enveloping curve. The basis for this curve is given by the pseudo-Voigt function $V(r)$, which is a bell-shaped curve resulting from a linear combination of the Gaussian distribution $G(r)$ and the Lorentzian distribution $L(r)$. These curves are given as a function of the radial distance r from the center of the spalling crater, which for the tracked features is given by the y-coordinate.

$$V(r) = \Lambda \cdot (\eta \cdot L(r) + (1-\eta) \cdot G(r)) \tag{4.6}$$

with:

$$L(r) = \frac{\Gamma^2}{\Gamma^2 + r^2} \tag{4.7}$$
$$G(r) = e^{-r^2/(2\sigma^2)} \tag{4.8}$$

Here Λ is the peak height of the curve given by the maximum x-velocity and η specifies the ratio of both functions set to $eta = 0.25$. The shape parameter σ controls the width of the Gaussian part and is determined based on the width w of the point cloud at half of the peak height (maximum x-velocity):

$$\sigma = \frac{w}{2 \cdot (2 \ln 2)^{1/2}} \tag{4.9}$$

For the present approximation, the width w is determined by the difference between the maximum and minimum y-coordinate of the tracked velocities within a region of $\pm\,5\,\%$ around $\Lambda/2$. This region is marked in figure 4.21 by a gray box with width w. The width Γ of the Lorentzian part $L(r)$ is calculated as $\Gamma = \sigma/2$ to give the resulting curve a more pointed shape.

To validate the approximated spatial x-velocity distribution it is compared to the fragmentation process in section 4.7. For this purpose, two characteristic points are marked on the velocity distributions in figure 4.21. The red points mark the radii of the averaged spalling craters determined from the 3D scans (figure 4.13). The average x-velocity at these points in the conducted test is $1.0\,\mathrm{m\,s^{-1}}$.

The blue dots in figure 4.21 are the locations of the maximum curvatures of the deformations calculated according to equation (4.10). The deformations are approximated based on the derived velocity distributions and the time steps shown in figure 4.23, which are selected to show a complete fracture pattern of the respective test.

$$\kappa = \frac{d^2u}{dr^2} \cdot \left(1 + \left(\frac{du}{dr}\right)^2\right)^{-3/2} \tag{4.10}$$

As described in [Gensichen, 2006], the calculation of a curvature is only meaningful if the two axes defining the curve have the same physical units. Therefore, the locations of the maximum curvatures are determined from the resulting deformations and not directly from the velocity distributions shown in figure 4.21. For the selected time frame, the deformations are small compared to the radial dimensions of the spalling craters. As a result, the radial locations of the maximum curvatures of the deformations and the maxima of the second derivatives of the velocity distributions are very similar. Because the axes in figure 4.21 are scaled for better visualization, this location appears shifted.

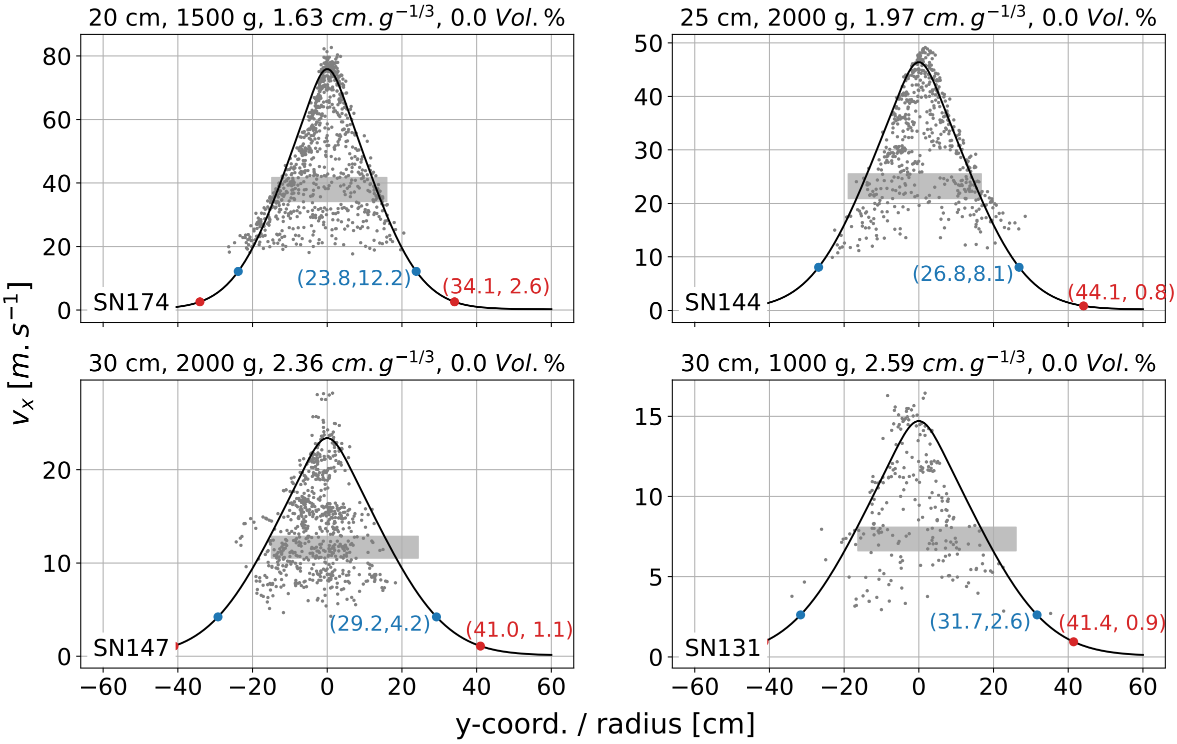

Figure 4.21.: Approximated distribution of the x-velocity

The fitted x-velocity distribution depends on the maximum x-velocity and the parameter σ for the width of the distribution at half of the maximum x-velocity in equation (4.9). To make predictions for similar situations, the maximum x-velocity as a function of the scaled thickness T_w can be determined from the regression line in figure 4.20. To derive a similar dependence for σ, this parameter is plotted against the scaled thickness of the concrete slab in figure 4.22 for the tests without steel fibers.

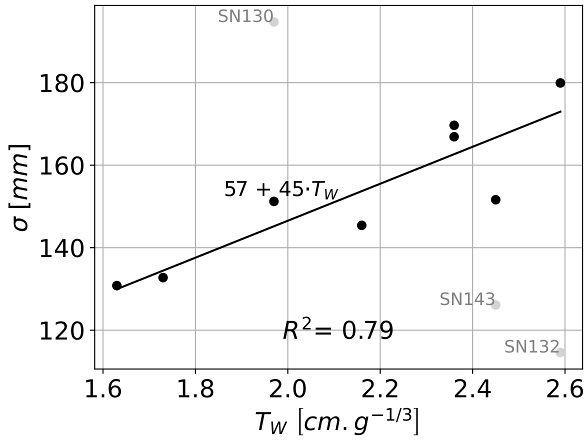

Figure 4.22.: Parameter σ for velocity distribution over scaled thickness of concrete slabs

The tests marked in gray are excluded from the calculation of the regression line. In these tests, the tracking was too disturbed by larger rotating debris fragments, leading to incorrect x-velocities, especially in the outer regions of the debris cloud. The agreement between the measured values for σ and the approximated regression line is considered satisfactory for the following evaluations.

The current tests indicate that the parameter σ is influenced by the concrete cover of the rebar. However, there is not enough data available to quantify this influence.

Plots for all tests with the approximated x-velocity distributions can be found in the appendix section C. In this, the approximated x-velocity distributions are calculated based on the derived regression lines for the width σ in figure 4.22 and the maximum x-velocity in figure 4.20.

4.6.4. Summary

The velocity of the secondary debris was determined to be dominant in the x-direction, since the majority of the secondary debris moves at angles less than 20°.

A linear relation was found between the maximum x-velocity of the secondary debris and the scaled thickness. This relation allows a simplified assessment of the impact of the secondary debris on people and technical installations.

The spatial x-velocity distribution of the secondary debris in the radial direction was approximated by an enveloping curve. This allows a better description of x-velocity for further evaluations.

The parameters of this spatial x-velocity distribution are the maximum x-velocity and the width of the spatial x-velocity distribution at half of the maximum x-velocity. The maximum x-velocity can be approximated by the linear relation in dependence on the scaled thickness derived in section 4.6.2. For the width parameter σ, a similar linear relation based on the scaled thickness was derived for further use.

4.7. Fragmentation process of the secondary debris

To validate the determined spatial x-velocity distributions from figure 4.21, they are compared with the fragmentation process of the secondary debris. For this purpose, figure 4.23 shows the HS recordings of the protective surfaces of the concrete slabs in the corresponding tests. Again, the upper two images show tests with a breach and the lower two images show tests without a breach. The time steps are chosen to show a complete fracture pattern with a central deformation in the x-direction of about 15 cm. The red circles correspond to the measured diameters of the spalling craters. The blue circles are the locations of the maximum curvatures of the displacements approximated from the velocity distributions and the time steps shown in figure 4.23.

The tips of the debris clouds are slightly shifted to the right and up in figure 4.23. This is due to the perspective of the HS camera relative to the concrete slabs. Using the method described in section 4.4.2, the resulting distortion is compensated so that the distances on the surface of the concrete slab are accurately represented.

It can be seen from figure 4.23, that there are two distinct regions in the formation of the secondary debris. These two regions are separated by an additional circumferential crack that correlates well with the location of the maximum curvature of the deformation derived from the x-velocity distribution (blue circle). In all cases, the center of the debris cloud with the fastest x-velocity consists of heavily fragmented small concrete pieces. Outside of this central region, there is a steep velocity gradient in the radial direction

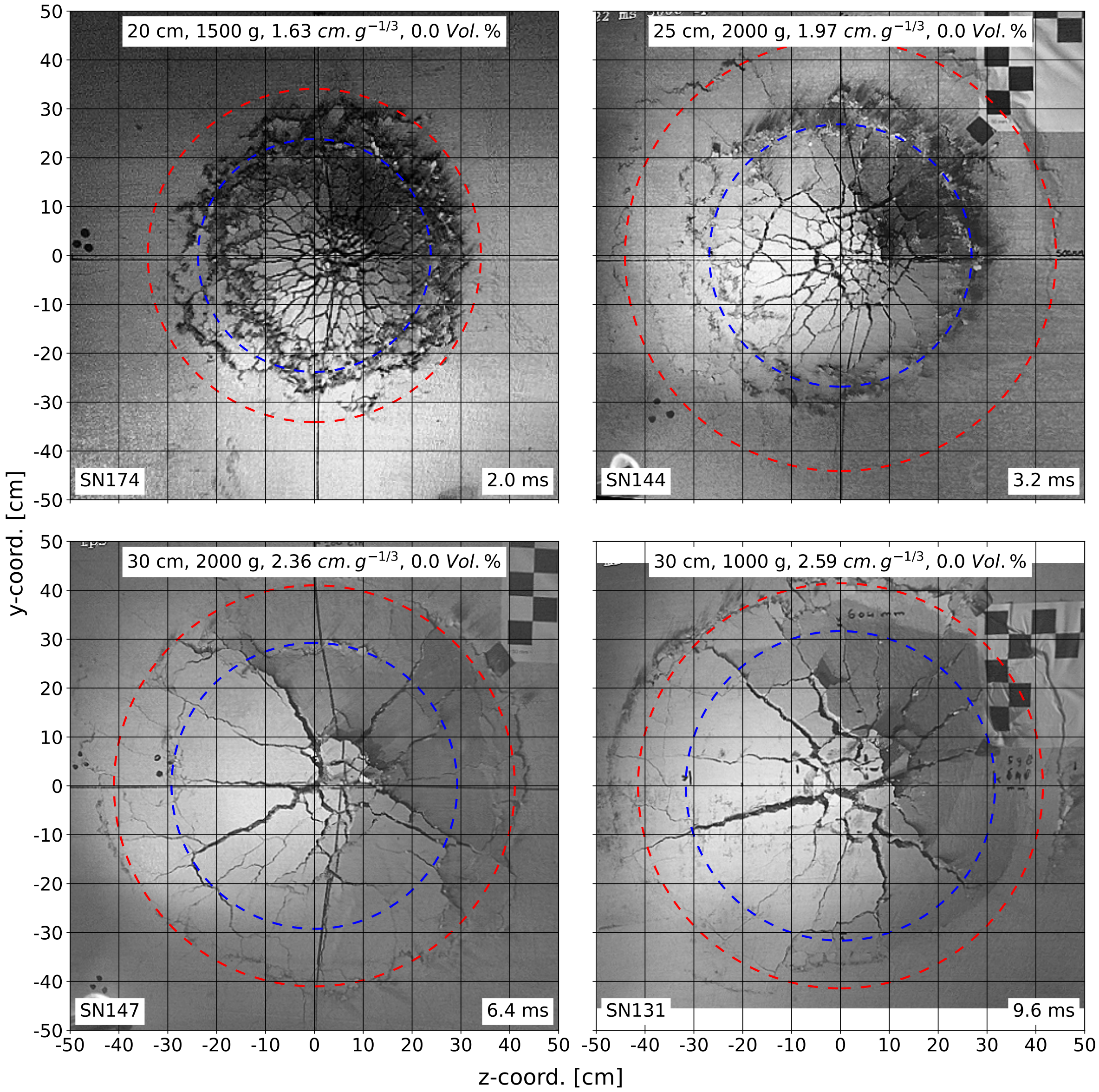

Figure 4.23.: Fragmentation process of the secondary debris

up to the blue circle.

In cases with a breach ($T_w < 2.1\,\mathrm{cm\,g^{-1/3}}$) the region inside the blue circle consists of small fragments that become larger with an increasing scaled thickness. In cases without a breach ($T_w > 2.1\,\mathrm{cm\,g^{-1/3}}$) the debris fragments are much larger with only a few radial cracks. These radial cracks are mainly caused by the different deformations resulting from the x-velocity gradient between the inner and outer regions of the spalled region.

These different deformations cause circumferential tensile stresses in the spalled secondary debris and thus radial cracking. The resulting larger secondary debris fragments fly away while rotating around their center of mass due to the velocity gradient between the inner and outer regions.

The two different regions are most pronounced in case of the scaled thickness $T_w = 1.97\,\mathrm{cm\,g^{-1/3}}$ with a breach. While the additional circumferential crack (blue circle) is still visible in the case of the scaled thickness $T_w = 2.36\,\mathrm{cm\,g^{-1/3}}$, it is hardly noticeable in the case of the largest scaled thickness $T_w = 2.59\,\mathrm{cm\,g^{-1/3}}$. This indicates a more uniform distribution of the x-velocity in the radial direction. It is also reflected by the continuous approach of the maximum curvature (blue circle) with the outer diameter of the spalling crater (red circle) with increasing scaled thickness.

In the region outside the blue circle, the x-velocity is slower than inside the blue circle and the concrete is significantly less fragmented. The tests performed indicate a correlation between the location of the additional circumferential crack (blue circle) and the position of the rebar layer relative to the surface of the concrete slab. To illustrate this correlation figure 4.24 shows the corresponding spalling craters after the test together with the location of the maximum curvature.

The location of the maximum curvature (blue circle) is almost identical to the location where the surface of the spalling crater intersects the rebar layer. It is expected that a variation of the concrete cover has an influence on the fracture process in the region of the spalling crater and therefore on the size of the individual fragments (see section 4.5.5).

The concrete cover was kept approximately constant throughout the test series. Only the tests with the retrofit layer have a significantly greater concrete cover due to the manufacturing process. This allows a first evaluation of the influence of a varying concrete cover. This influence will be discussed together with the DIC recordings of the retrofit layer in the section 4.10.

It is concluded that the distribution according to equation (4.6) can approximate the radial x-velocity distribution of the experimental tests very well. A comparison with the DIC measurements from the tests with steel fiber reinforcement can be found in section 4.10.

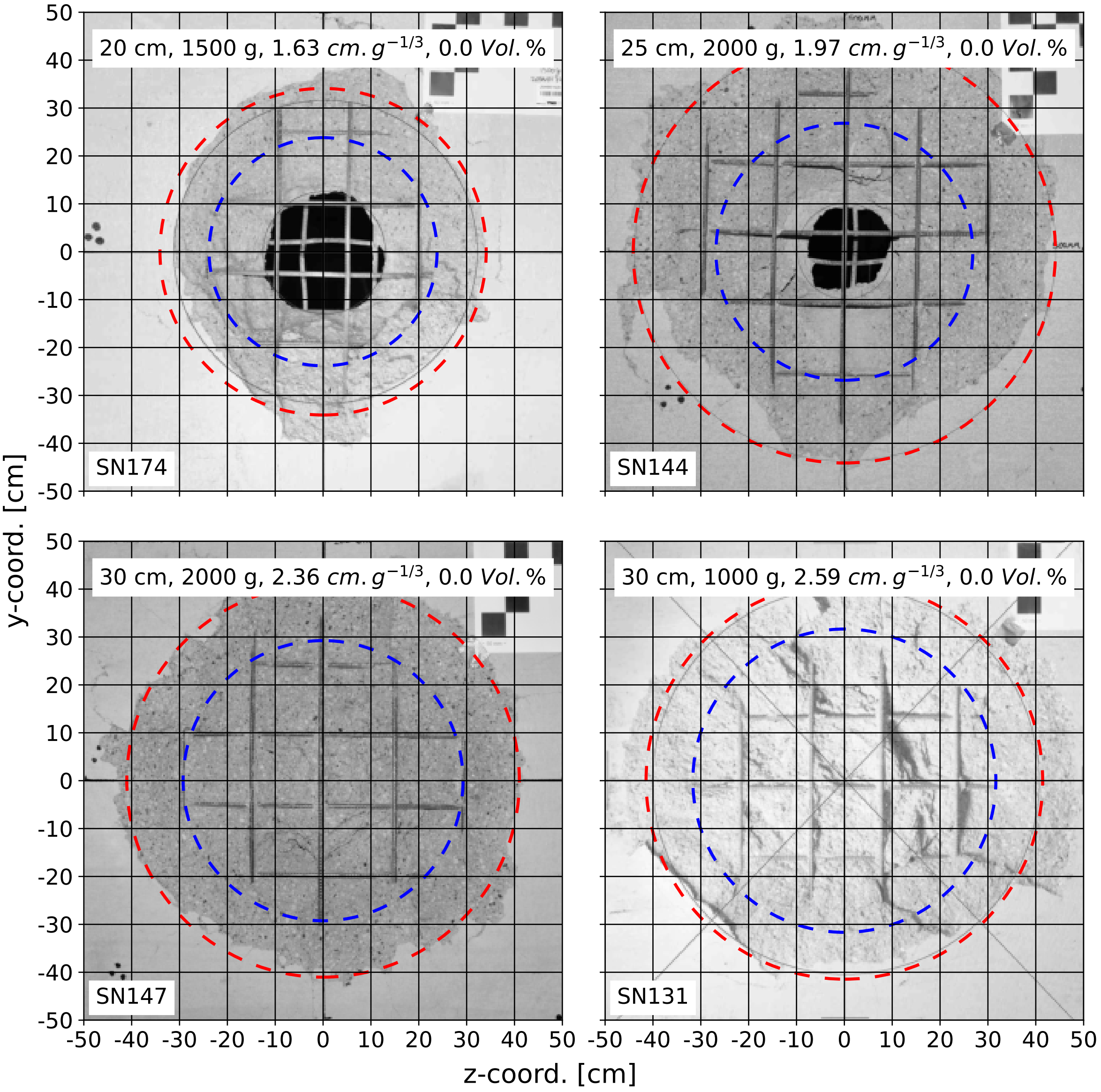

Figure 4.24.: Influence of rebar on fragmentation and x-velocity distribution

4.7.1. Summary

The fragmentation process was compared with the x-velocity distribution derived in section 4.6.3. Two regions were identified with a circumferential crack in between them. This crack was shown to correlate with the maximum curvature derived from the approximated x-velocity distribution.

The first region identified in the center of the spalling crater shows heavily crushed concrete with a steep outward x-velocity gradient of the secondary debris fragments. The concrete in this region has predominantly radial cracks and the size of the individual fragments increases with increasing scaled thickness. The origin of these cracks has been attributed to the steep x-velocity gradient and the resulting deformation of the spalled concrete.

The second region identified at the border of the spalling crater has lower x-velocities than in the first region and the concrete is significantly less fragmented. In this region the surface of the spalling crater is completely above the rebar layer.

The experimental tests indicate that the transition between these two regions is correlated with the location of the rebar layer in the concrete slab. Further experiments are required to quantify this relation.

4.8. Kinetic energy of the secondary debris

The total kinetic energy of the entire secondary debris cloud can be derived from the approximation of the spatial x-velocity distribution according to equation (4.6) and the shapes of the spalling craters in figure 4.14. For this purpose, it is assumed that the x-velocity is constant in the depth direction of the concrete slab.

While the assumption of a constant x-velocity in the depth direction of the concrete slab is considered well suited for situations without a breach, a decrease in velocity below the rebar layer is expected for situations with a breach. Since the velocity distribution in the depth direction cannot be determined experimentally, it is further discussed together with the numerical simulations in chapter 5.

An example of the resulting x-velocity distribution over the rotationally symmetric shape of the spalling crater is shown for test SN144 in figure 4.25 (right). The total kinetic energy is then calculated by numerical integration of the rotationally symmetric x-velocity distribution over the volume of the spalling crater according to equation (4.11).

$$E_{kin} = \int_0^R \int_0^{x(r)} 2\, r\, \pi \left(\frac{1}{2}\, \rho\, v_x(r,x)^2 \right) dx\, dr \tag{4.11}$$

Where ρ is the density of the concrete, r is the location in radial direction, x is the location in depth direction, and $v_x(r, x)$ is the x-velocity at the respective locations. The integral is calculated from the center of the spalling crater up to the maximum radius R and the corresponding depths $x(r)$ according to the rotational symmetric approximated shapes of the spalling craters (figure 4.14).

The resulting total kinetic energy in dependence on the scaled thickness is shown in figure 4.25 (left) separately for all tests without steel fibers.

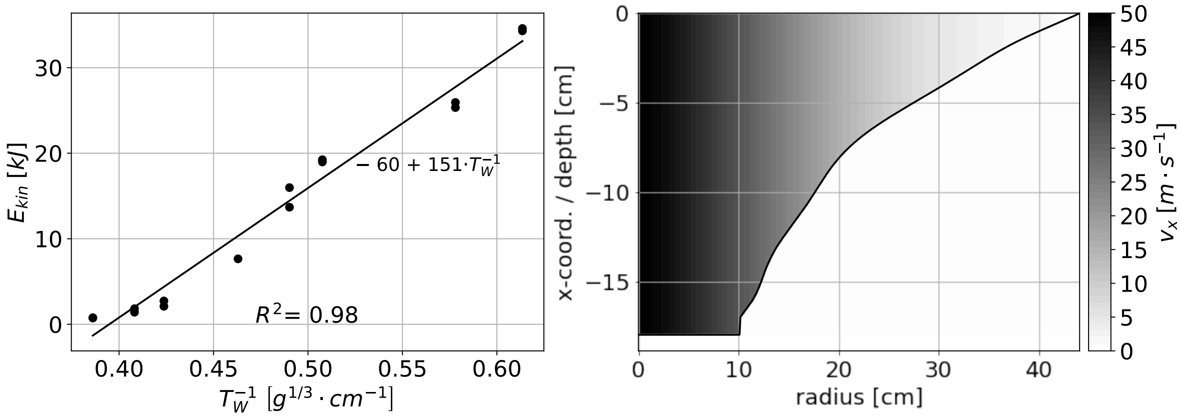

Figure 4.25.: Total kinetic energy over scaled thickness (left), velocity distribution SN144 (right)

The kinetic energy can be compared to the impacting explosive load using the energy equivalent impulse described in section 3.3. For this, the energy equivalent impulses of the explosive charges $I_{Ek,Expl.}$ and the resulting secondary debris $I_{Ek,Deb.}$ are calculated according to equation (3.13). The resulting ratios of the corresponding energy equivalent impulses for all experimental tests without steel fibers are shown in figure 4.26.

It is important to keep in mind that the load from the explosive is based on the reflection at a perfectly rigid surface (see section 3.3) and the energy equivalent impulse of the secondary debris is based on the assumption of a constant spatial x-velocity distribution in the depth direction of the concrete slab.

From figure 4.26 it can be seen that for the 20 cm thick concrete slabs almost all of the energy transferred from the explosive charge to the concrete slab is contained in the resulting secondary debris. This ratio decreases with increasing scaled thickness down to a reduction of approximately 20 % for the 30 cm thick concrete slabs.

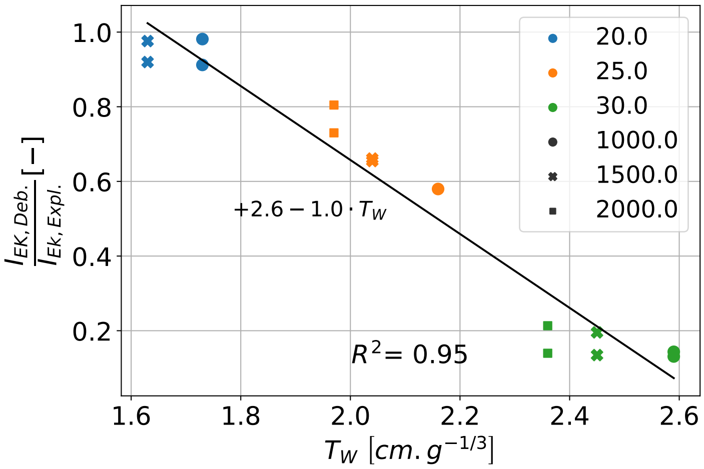

Figure 4.26.: Relative energy equivalent impulse

According to the included regression line, a scaled thickness of $T_W = 2.6\,\mathrm{cm\,g^{-1/3}}$ would result in no secondary debris. This threshold is quite similar to the threshold of $T_W = 3.0\,\mathrm{cm\,g^{-1/3}}$ determined from the regression line for the maximum x-velocity in figure 4.20 (see also appendix section G.1).

Based on the observed influence of the rebar layer on the secondary debris, a small concrete cover reduces the depth of the spalling crater but widens the region with high velocities. The fastest velocities are in the center of the spalling crater, and velocity has a much greater influence (quadratic) on the kinetic energy of the secondary debris than the mass (linear). Therefore, reducing the depth of the spalling crater at its center by reducing the concrete cover is expected to be beneficial in reducing the kinetic energy of the secondary debris. Further experiments are required to quantify this relation.

The derived kinetic energy can be used to quantify the impact of the entire secondary debris cloud on humans and technical installations, which will be discussed in chapter 6. In the following section, the kinetic energy is used to quantitatively assess the influence of the steel fibers on the secondary debris.

4.9. Influence of steel fibers

4.9.1. Damage and fracturing

This section evaluates the influence of steel fibers in the concrete on the resulting secondary debris. For a first qualitative assessment, figure 4.27 shows the damage at the protective surface of steel fiber reinforced concrete slabs that have been loaded with 2000 g of SEMTEX10. The red lines indicate area equivalent circles of the areas surrounded by the outermost circumferential cracks. Analogous plots for the other tests can be found in the appendix section B.

Figure 4.27 shows that the outer dimension of the spalling crater visible from the surface decreases continuously up to a steel fiber content of 1.0 Vol % in case of 2000 g of SEMTEX10. A further increase of the steel fiber content to 2.0 Vol % has no effect on the outer dimension of the spalling crater. This limiting diameter for steel fiber contents of 1.0 Vol % and 2.0 Vol % (lower two images in figure 4.27) is very similar to the region where the depth of the spalling crater is limited by the rebar layer in the case without steel fibers (upper left in figure 4.27).

As the steel fiber content increases, more and more concrete within the spalling crater is retained by the steel fibers. Consequently, the important quantity for the secondary debris is not the outer dimension of the spalling crater, but the total amount of secondary debris detached from the concrete slab.

For a quantitative assessment, figure 4.28 (left) shows the relative reduction of the spalling crater diameter d_S in dependence on the steel fiber content for the two tested explosive masses (1500 g and 2000 g).

In order to evaluate the total amount of secondary debris retained by the steel fibers, figure 4.28 (right) shows the relative total mass of the secondary debris. This mass consists of the secondary debris collected after the detonation tests. Therefore, it only includes fragments that detached from the concrete slab and not the visually loose fragments that were removed prior to the 3D scans.

The data points in the graphs represent the mean masses of the corresponding tests, with a vertical line indicating the results of each individual test. All values are normalized by the corresponding masses of the tests without steel fibers.

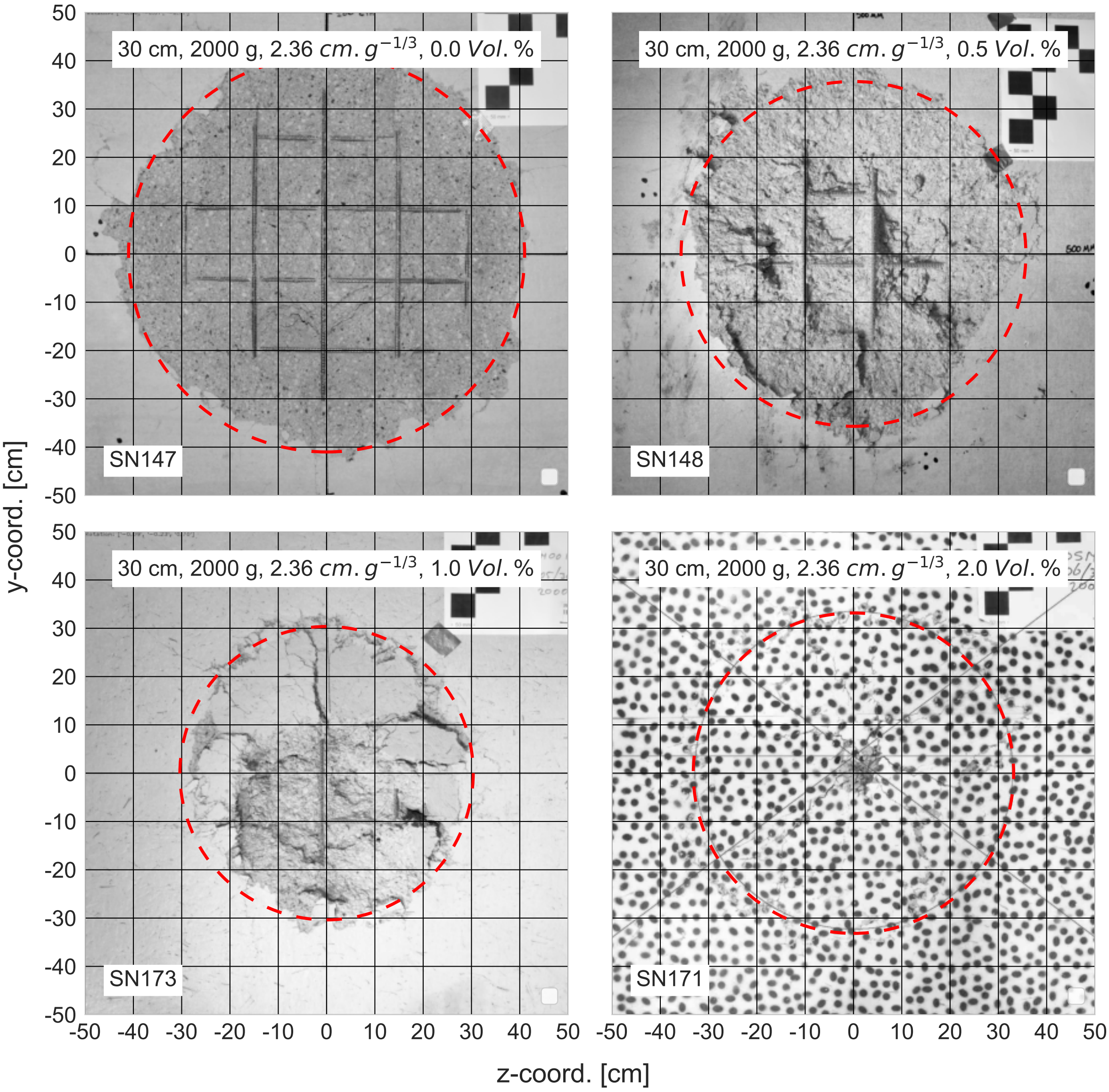

Figure 4.27.: Influence of steel fibers on spalling crater

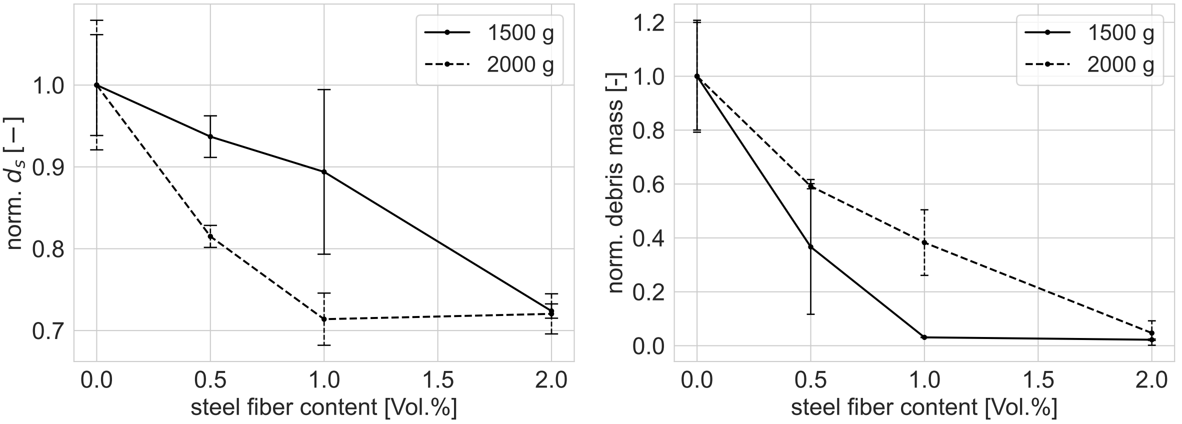

Figure 4.28.: Normalized spalling crater diameters (left) and normalized total secondary debris mass (right) over the steel fiber content

For both explosive masses, the outer diameter of the spalling crater decreases continuously down to a diameter that is about 70 % of the spalling crater without steel fibers (figure 4.28, left). As mentioned above, this reduction correlates with the region where the depth of the spalling crater is limited by the rebar layer. In the case of 2000 g of SEMTEX10, the limiting reduction of 70 % is reached earlier, at a steel fiber content of 1.0 Vol %. With an explosive mass of 1500 g, a similar reduction of the spalling crater is only achieved with a steel fiber content of 2.0 Vol %.

When the maximum reduction of 70 % is reached, the spalling crater no longer has a circular shape, but is reduced to single cracks. This is particularly relevant for 1500 g of SEMTEX10 with steel fiber contents of 1.0 Vol % and 2.0 Vol %. Here, the outer dimensions of the spalling craters are vague and difficult to determine by visual inspection from the surface (see appendix section B). This is also reflected in the comparatively large variation between the individual tests in the case of 1500 g of SEMTEX10 and a steel fiber content of 1.0 Vol %.

At the same time, the total mass of the secondary debris decreases continuously as the steel fiber content increases. Already the addition of 0.5 % of steel fibers reduces the total mass of the secondary debris by 50 % on average of the two explosive masses. With an explosive mass of 1500 g, a steel fiber content of 1.0 % retained almost all of the secondary debris. With a steel fiber content of 2.0 %, the secondary debris in both cases is reduced to only a few small fragments from the center of the spalling crater.

In order to evaluate the effect of the steel fibers in more detail, figure 4.29 shows a horizontal cross section of the concrete slab with 1.0 Vol % of steel fibers (SN173) that has been cut along its centerline (z-axis). The section from the 3D scans of an analogue test without steel fibers (SN147) is included as a red line.

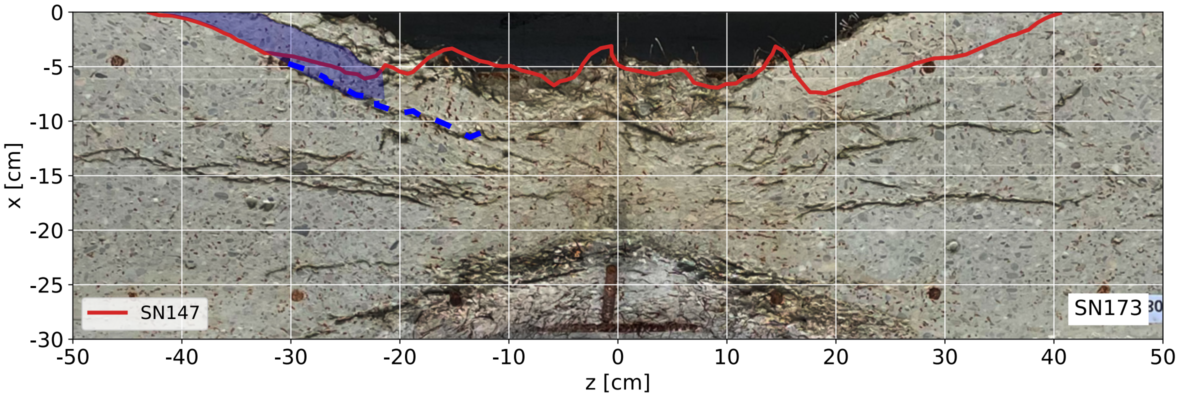

Figure 4.29.: Horizontal cross section of test SN173 including measurements from 3D scans for test SN147 ($T_W = 2.36\,\mathrm{cm\,g^{-1/3}}$)

The concrete fragment marked in blue shows a characteristic shape of the secondary debris, starting at the surface of the concrete slab and pointing inwards at an angle. This shape was common in the collected secondary debris and could be allocated to the outer area of the spalling crater. In the situation with 1.0 Vol % of steel fibers (SN173) the blue fragment is still attached to the concrete slab. A crack can be seen starting from the center of the concrete slab and extending outwards (blue dashed line). This crack would have separated the blue concrete fragment if it had propagated further. However, the propagation of the crack was stopped by the additional steel fibers, preventing a larger spalling crater.

The influence of the steel fibers on the fracture process can be seen more clearly in a direct comparison of the HS recordings. For this purpose, figure 4.30 shows the protective surface of the concrete slabs for the different steel fiber contents at 6.5 ms. In the case of test SN171 (2.0 Vol %), the time step shown is 4.4 ms because there is no relevant deformation afterwards. The outer diameter of the spalling crater (red circle) and the location of the maximum curvature (blue circle), both from the test without steel fibers, are included in all images.

It can be seen that the overall behavior is very similar in all cases. There is a heavily

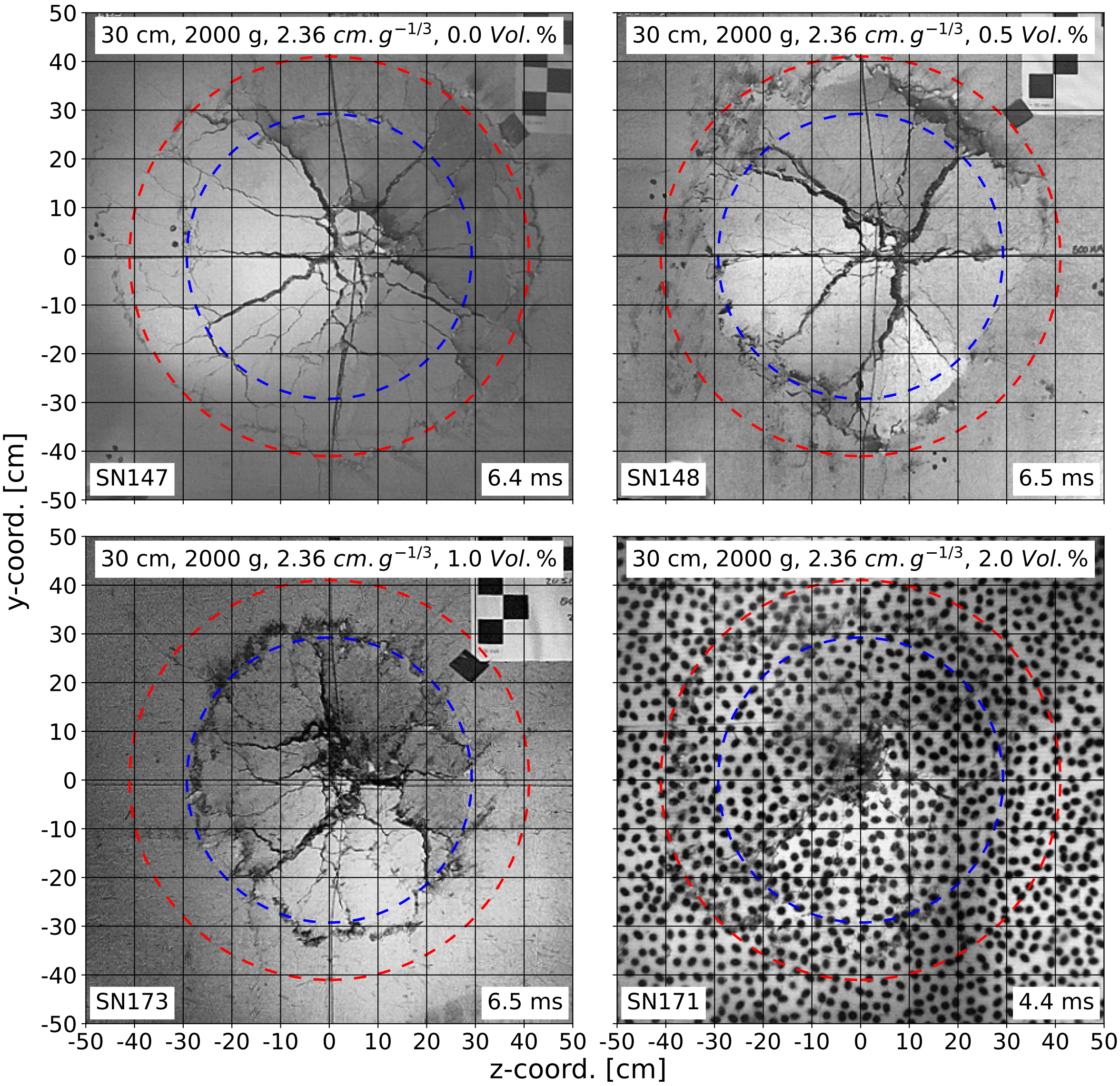

Figure 4.30.: Influence of steel fibers on fragmentation of spalling crater

crushed region in the center of the spalling crater with radial cracks pointing outwards and separating larger debris fragments. As described in section 4.7, the spalled fragments in the case without steel fibers (SN147) (figure 4.30, upper left) show an additional circumferential crack (blue circle) that separates the spalled debris into two distinct regions.

In the case of test SN148 with a steel fiber content of 0.5 Vol % there is still detached concrete outside the blue circle, but the fragmentation begins to localize inside the blue circle. With 1.0 Vol % of steel fibers (SN173), the fragmented region corresponds to the blue circle. Due to the DIC pattern, the circumferential crack around the spalling crater is difficult to identify in the test SN171 with 2.0 Vol % of steel fibers. However, also in this case, the outer dimension of the spalling crater corresponds to the blue circle.

The blue circle correlates with the location where the depth of the spalling crater is limited by the rebar layer. As can be seen in figure 4.29 the cracks separating the secondary debris fragments from the concrete slab in the region outside the blue circle start in the center and propagate outward at an angle. Since the failure in this outer region involves mainly individual cracks separating larger debris fragments, the bond between the steel fibers and the concrete is expected to be less affected than in the central region. In addition, the initial velocity of the secondary debris in the outer region is much smaller, resulting in less energy available to pull the steel fibers out of the concrete. This explains the continuous reduction of the spalling crater by the steel fibers from the outer regions inwards.

It is concluded that the overall damage mechanism of the concrete prior to initial cracking is independent of the steel fiber content. It is only after initial cracking that the steel fibers provide additional resistance through the work required to pull them out of the concrete matrix. Since the steel fibers also stop crack propagation, the extent of the damaged region is reduced starting from the outer regions and not just held together by the steel fibers. In the central region of the spalling crater, the retained concrete below the rebar is severely damaged. This impairs the bond between the concrete and the steel fibers, resulting in a reduced influence of the steel fibers in this region (limiting diameter). Consequently, the steel fibers are expected to have a significantly reduced impact on secondary debris in cases where the concrete slab would already be breached by the detonation without the steel fibers.

4.9.2. Velocity and kinetic energy

To evaluate the influence of the steel fibers on the velocity of the secondary debris, figure 4.31 shows the HS recordings at 38 ms for different steel fiber contents. The tests shown are 30 cm thick concrete slabs loaded with 2000 g of SEMTEX10 with steel fiber contents between 0.0 Vol % and 2.0 Vol %.

Analogous to the tests without steel fibers (figure 4.20), the blue dots mark the locations of the tracked features and the red dots mark the features whose mean x-velocity is given in the upper right corner of each image.

In the tests with steel fiber reinforcement, there are always small debris fragments that are not or only minimally affected by the steel fibers. These debris fragments are either too small to be anchored by the steel fibers, consist of the included aggregates, or originate from regions of an uneven steel fiber distribution. These unaffected or minimally affected debris fragments are propelled away from the concrete slab at a velocity similar to that in the case without steel fibers.

To evaluate the influence of the steel fibers on the velocity of the secondary debris, the features for the maximum x-velocity (red dots) are selected to correspond to the fastest debris fragments that are expected to represent the behavior of the steel fiber reinforcement.

In the case of 2.0 Vol % of steel fibers (SN171), the tracking algorithm is too much disturbed by the DIC pattern on the surface of the concrete slab. Therefore, the x-velocity of the debris fragment at about 15 cm is approximated by its x-location and the current time step. The resulting x-velocity is $4.0\,\mathrm{m\,s^{-1}}$.

As the steel fiber content increases, the amount and x-velocity of the secondary debris is continuously reduced. In addition, the size distribution of the secondary debris changes. Especially in case of 0.5 Vol % of steel fibers (figure 4.31, top right) it becomes obvious, that large debris fragments are held together by the steel fibers while flying away from the concrete slab. In the situation without steel fibers these fragments are fractured into several smaller pieces.

Due to large rotating debris fragments and small debris fragments that are not or only minimally affected by the steel fibers, it is not possible to derive a velocity distribution for the tests with steel fibers in the same way as without steel fibers in section 4.6.3. Therefore, the influence of the steel fibers on the secondary debris is evaluated based on the total kinetic energy of the secondary debris derived in section 4.8.

This is done by reducing the kinetic energy of the concrete without steel fibers $E_{kin,0}$ by the difference of the specific fracture energies of the concrete with $G_{F,A,0}$ and without $G_{F,A,pc}$ steel fibers (table 4.3), multiplied by the surface of the spalling crater S_0.

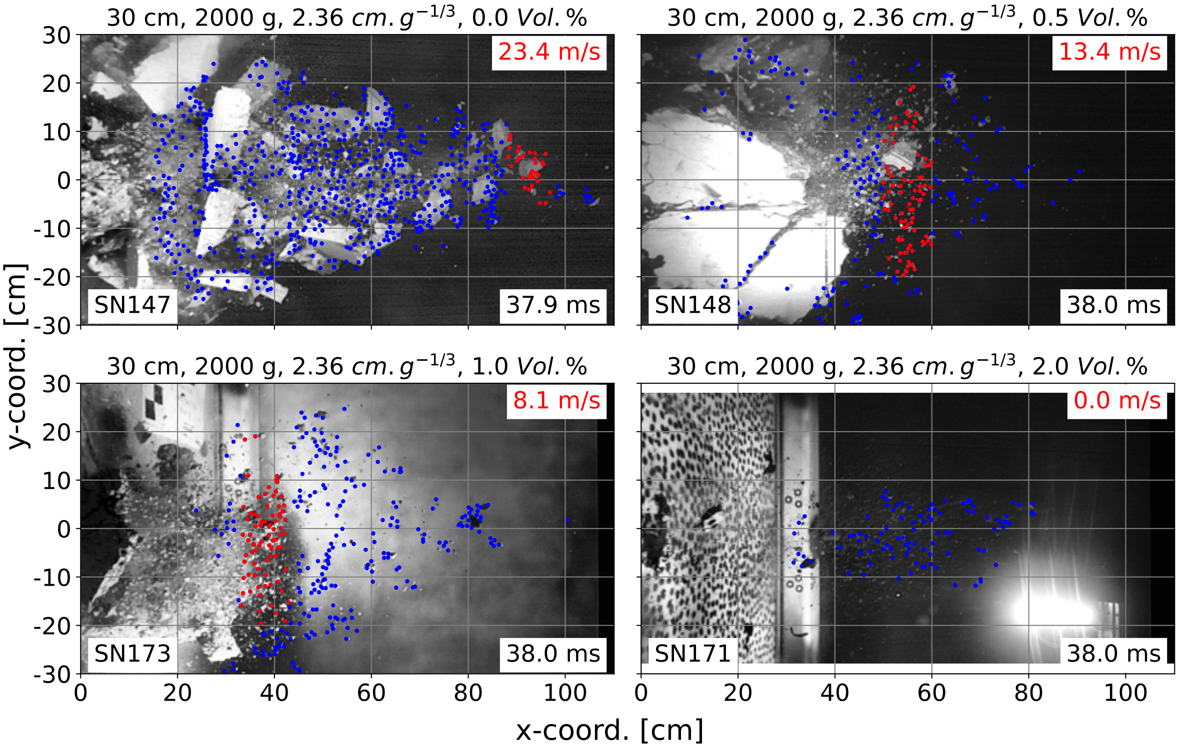

Figure 4.31.: HS Tracking - Influence of steel fibers on the the secondary debris fragments

$$E_{kin,pc} = E_{kin,0} - (G_{F,A,pc} - G_{F,A,0})\, S_0\, f \tag{4.12}$$

In this $E_{kin,0}$ and $G_{F,A,0}$ are the kinetic energy and the fracture energy for the case without steel fibers and the index pc indicates the same values for the different steel fiber contents. The surface S_0 is calculated by rotational integration of the averaged shape of the spalling crater from the 3D-scans in figure 4.14.

Based on this, the x-velocity distribution for the case with steel fibers is estimated by varying the maximum x-velocity in equation (4.6) such that the kinetic energy from the resulting velocity distribution matches the expected kinetic energy $E_{kin,pc}$ for the steel fiber content pc.

By varying the additional factor f, the resulting x-velocity distribution is fitted to the experimentally measured maximum x-velocity of the secondary debris fragments and the measured diameter of the spalling crater. The criterion for the diameter of the spalling crater from the approximation is a threshold x-velocity of $1.0\,\mathrm{m\,s^{-1}}$ as derived from the experimental tests without steel fibers shown in figure 4.21.

For the present case, the factor f is set to f =1.45. A reason for this factor could be that the fractured surface is 45 % larger than the surface of the spalling crater and/or that there are additional load bearing mechanisms. It can be seen from the collected secondary debris that, except for the heavily fractured central area of the spalling crater, the larger secondary debris fragments in cases without a breach cracked mainly at the rebar layer, with only sporadic spalling layers in between. According to the HS recordings in figure 4.30 the increased resistance could be attributed to the additional radial cracks and an associated membrane action of the spalled fragments similar to the retrofit layer (see section 4.9.3).

Another reason for the factor f =1.45 could be an influence of the strain rate on the fracture energy. Unfortunately, there is no conclusive explanation in the literature as to how the fracture energy is affected by the strain rate, especially at the extremely high strain rates caused by a contact detonation. Since the difference in fracture energy is used to calculate the velocity distribution with steel fibers, the effect of the strain rate would have to be greater in cases with steel fibers than without steel fibers. However, since the same factor can be used to describe all tested steel fiber contents loaded with different explosive masses, the effect must be constant between the different steel fiber contents.

The resulting x-velocity distribution (left) and the relative total energy (right), both in dependence on the steel fiber content, are shown in figure 4.32 for an explosive mass of 2000 g.

In the presented case of a 30 cm thick concrete slab loaded with 2000 g of SEMTEX10, the total kinetic energy of the secondary debris decreases approximately linearly with increasing steel fiber content between 0.0 Vol % and 1.0 Vol % until it almost vanishes for 2.0 Vol % of steel fibers.

With a steel fiber content of 1.0 Vol %, the total kinetic energy is already significantly reduced by almost than 90 %. To properly evaluate the influence of 2.0 Vol% of steel fibers, a higher explosive mass would be required. However, at a steel fiber content of 2.0 Vol % it becomes increasingly difficult to achieve a homogeneous distribution of the steel fibers in the concrete. This is particularly evident in the Split-Hopkinson-Bar tests to determine the specific fracture energy described in [Mosig et al., 2021].

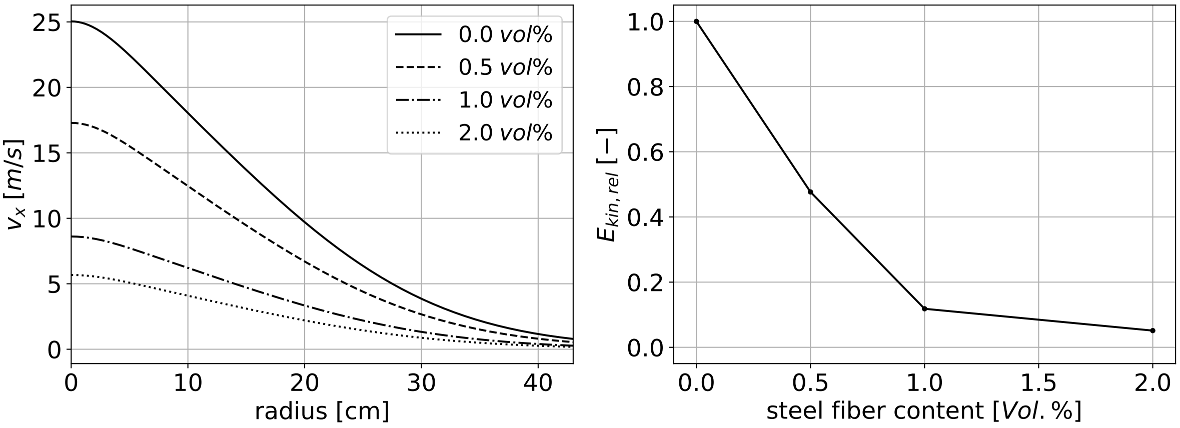

Figure 4.32.: Velocity distribution (left) and relative total kinetic energy (right) of secondary debris for varying steel fibers content

For a comparison of the approximated x-velocity distribution (solid line) with the experimental measurements (dashed line), figure 4.33 shows the maximum x-velocity of the spalled debris for both tested explosive masses. The dashed lines represent the respective mean values and the vertical lines the individual measurements from the corresponding tests.

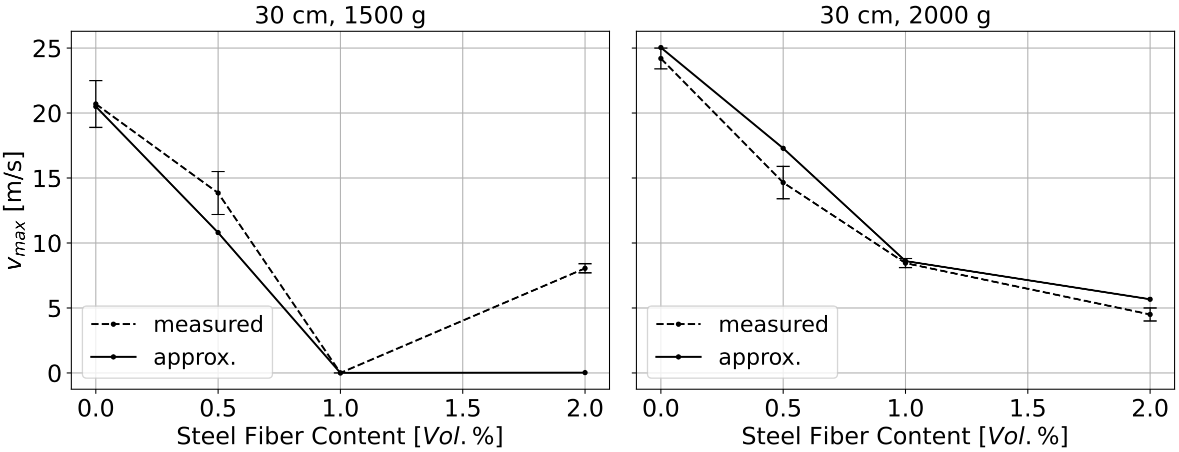

Figure 4.33.: Comparison of measured and approximated maximum x-velocity

The agreement between the approximation and the experimental measurements is considered satisfactory for the tests presented. Due to the comparatively low kinetic energy in the cases of 1.0 Vol % and 2.0 Vol% of steel fibers, the results in this range are extremely sensitive to even small changes of the input parameters.

To compare the approximated diameters (blue lines) of the spalling craters with the experimental measurements (red lines) they are plotted in figure 4.34 together with photos of the spalling craters. The criterion for the diameters of the spalling craters is a threshold x-velocity of 1.0 m s^{-1} as derived from the experimental tests without steel fibers shown in figure 4.21.

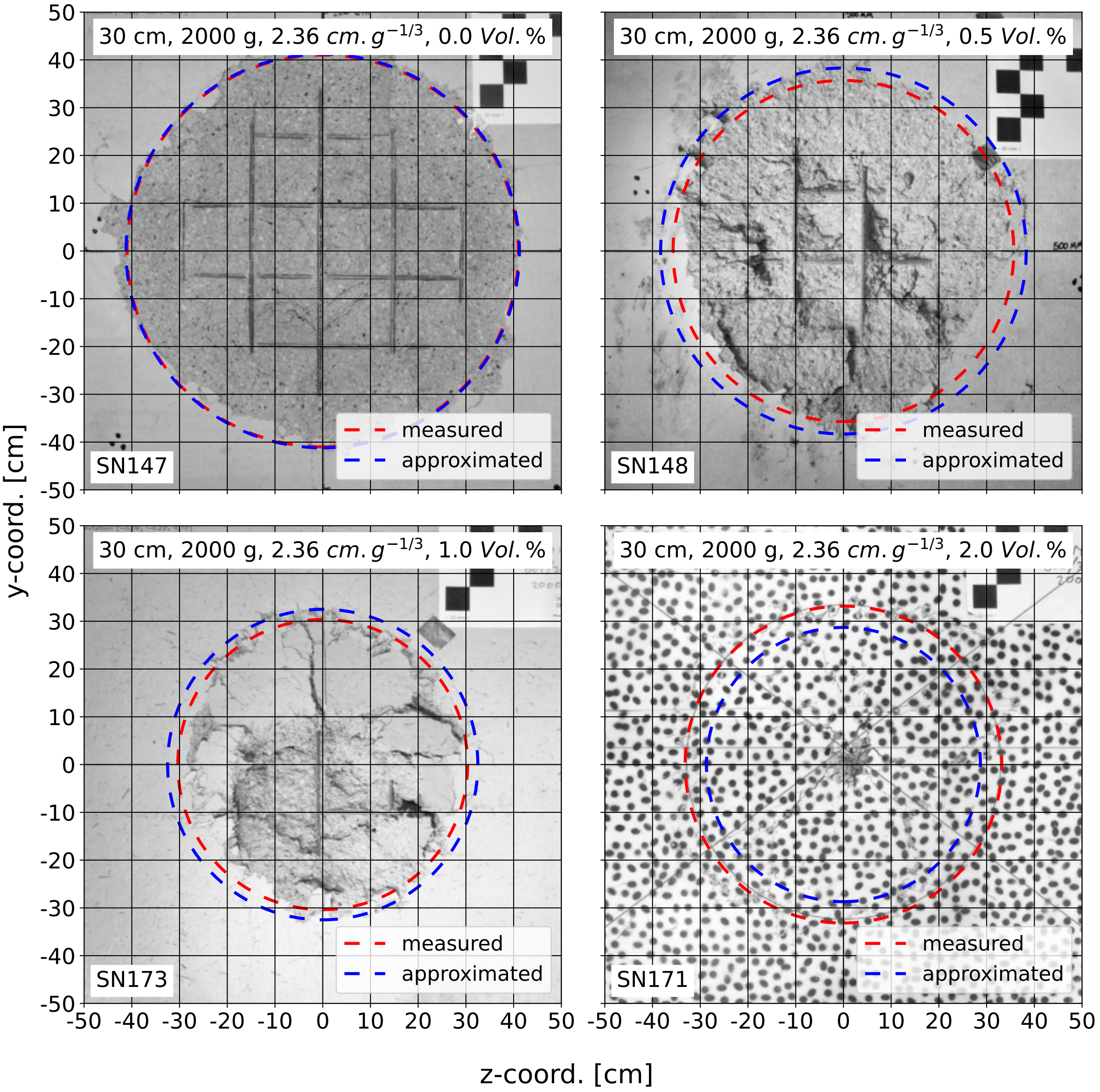

Figure 4.34.: Resulting spalling crater for different steel fiber contents including measured (red circle) and approximated (blue circle) diameter of spalled debris

For 0.0 Vol % and 0.5 Vol % the agreement between the measured and approximated values is well within the expected deviations for the presented tests.

For 1.0 Vol % of steel fibers, the approximation encloses the spalling crater, but there are debris fragments within this area that did not detach from the concrete slab. In the analogue test, the secondary debris in this region was not retained by the steel fibers but flew away at a low x-velocity. Consequently, the combination of load and resistance in this case appears to be close to a threshold for which the approximation gives a conservative prediction.

In the case of 2.0 Vol % of steel fibers, almost all of the secondary debris was retained by the steel fibers. The analogue test shows some detached debris fragments, but these mostly fell down directly in front of the concrete slab. After the test, the debris in this region could be easily removed from the concrete slab and the resulting spalling crater is very similar to the case with 1.0 Vol % of steel fibers. As mentioned above, the residual kinetic energy in this case is very low and even an increase in fracture energy of less than 1.0 % would result in no predicted secondary debris.

Therefore, the proposed approximation of the influence of the steel fibers is considered to be well suited to represent the experimental measurements. It enables a quantitative evaluation of the influence of the steel fibers and allows predictions for similar situations when the associated fracture energy is known.

4.9.3. Retrofit layer of steel fiber reinforced concrete

As a measure for already existing concrete structures, concrete slabs can be retrofitted with a layer of steel fiber reinforced concrete on the protective side. The retrofit in the present series of tests consists of a 5 cm thick layer of fiber reinforced concrete with 2.0 Vol % of steel fibers applied to an existing 25 cm thick concrete slab. The retrofit was applied to the protective side of the concrete slab as this side is predominantly subjected to tensile loading and the main purpose of the addition of steel fibers is to increase the tensile strength of the concrete.

Figure 4.35 shows the protective surface of a retrofitted concrete slab after the detonation test. The retrofitted concrete slab has a total thickness of 30 cm and was loaded with 2000 g of SEMTEX10. The area equivalent circle of the spalling crater is shown as a red dashed circle. The diameter of the spalling crater for an analogue test without steel fibers but with the same total concrete slab thickness is added as a blue dashed circle.

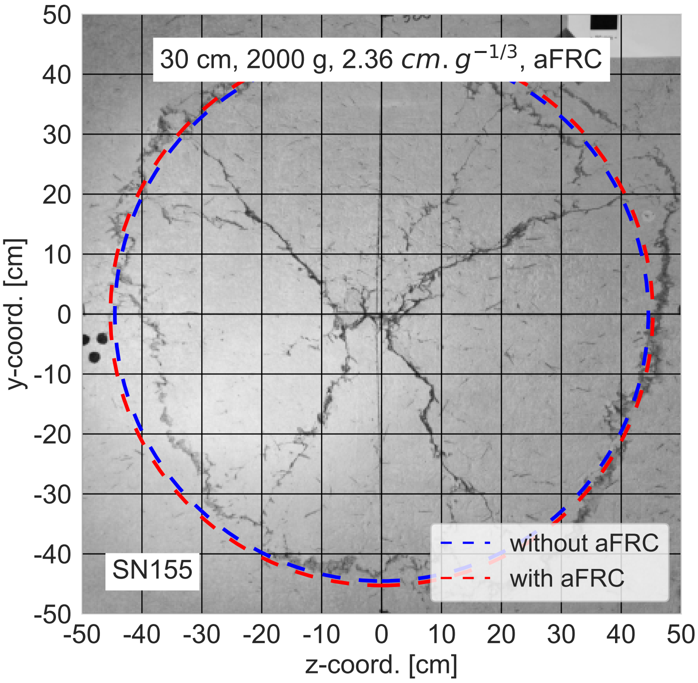

Figure 4.35.: Protective surface of the concrete slab with an additional layer of fiber reinforced concrete

The test with a retrofit layer shows the same expansion of the spalling crater at the surface as an analogue test with the same total concrete slab thickness but without steel fibers. There is no reduction in spalling diameter as with fully fiber reinforced concrete slabs. At the same time, almost no fragments detached from the concrete slab but were retained by the retrofit layer. This is also reflected in a reduction of the secondary debris to near zero, similar to the concrete slabs with 2.0 Vol % full steel fiber reinforcement in figure 4.30.

For a more thorough evaluation of the damage mechanism, figure 4.36 shows a horizontal cross section of the same concrete slab after the removal of the still attached but visually loose concrete fragments. For comparison, the section derived from the 3D scan of an analogue test without steel fibers and with the same total concrete slab thickness is added as a red line. The transition between the conventional concrete and the layer of fiber reinforced concrete is marked with a black dashed line. The locations of the cut rebar are marked by red dots.

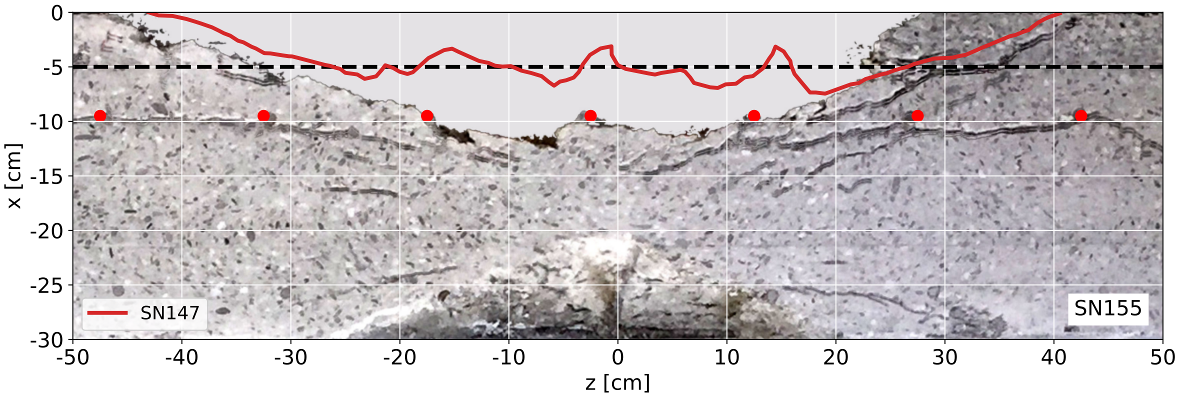

Figure 4.36.: Horizontal cross section of test SN155 including measurements from 3D scans for SN147

As in the tests without the retrofit layer, the depth of the spalling crater is limited by the rebar in the original concrete slab (red dots). The retrofitted concrete slab was originally a 25 cm thick concrete slab that was retrofitted with an additional 5 cm thick layer of fiber reinforced concrete. As a result, the total concrete cover from the surface of the retrofitted concrete slab to the rebar layer in the original concrete slab is 8.5 cm.

Comparing the spalling crater from the retrofitted test with a test without steel fibers and the same total concrete slab thickness (SN147, red line in figure 4.36), the resulting shape of the spalling crater is deeper and more uniformly shaped in the case of the retrofitted slab. In addition, there is no crushed concrete beneath the rebar as in the analogue test without retrofit layer in figure 4.16. This indicates that the rebar layer at this depth does not have much influence on the shape of the spalling crater.

In the case of fully fiber reinforced concrete slabs, the spalled debris is retained primarily by the steel fibers anchored in the concrete in the direction of loading. In the case of retrofitted concrete slabs, the spalling crater extends below the retrofit layer. As a result, most of the spalling crater is not directly influenced by the steel fibers, but only indirectly by a support with the retrofit layer. This support is primarily due to the membrane action of the retrofit layer rather than the steel fibers being pulled out over the entire failure surface of the spalling crater. A graphical representation of the identified failure mechanism is shown in figure 4.37.

The spalled, but still attached, secondary debris was much easier to remove after the tests than in the case of the fully fiber reinforced concrete slabs. Consequently, a less

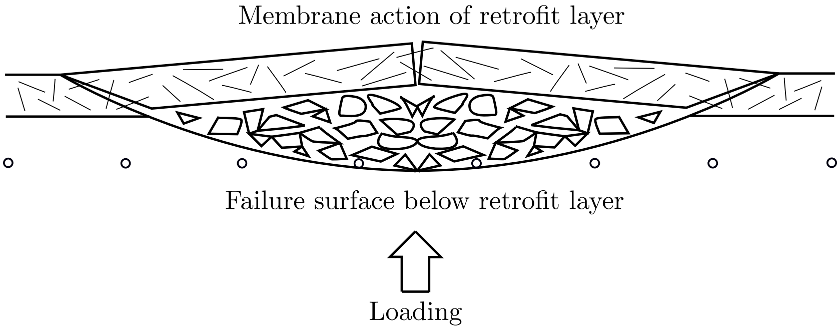

Figure 4.37.: Membrane action of retrofit layer

ductile failure of this layer is expected once the membrane action fails, as most of the fragmented concrete is only retained by the retrofit layer and not by the rebar at the greater depth. The fragmented but retained concrete becomes secondary debris once the retrofit layer fails. However, the resulting secondary debris fragments are expected to have a lower velocity and consequently a lower resulting kinetic energy than in the case without retrofit.

4.9.4. Summary

The diameter of the region with spalled but retained concrete reduces to about 70 % before only single cracks can be found. The tests indicate that this reduction is correlated with the concrete cover of the rebar. For a better understanding of this influence, an extended series of tests with a variation of the concrete cover is required.

The influence of the steel fibers is also reflected in the total mass of secondary debris. An almost complete reduction of the secondary debris can be achieved with 1.0 Vol % of steel fibers for the explosive mass of 1500 g and with 2.0 Vol % of steel fibers for the explosive mass of 2000 g.

Observations on cut test specimens show that the damage mechanism prior to an initial cracking is independent of the steel fibers. It is only after an initial cracking that the steel fibers start to act. They inhibit crack propagation and prevent complete spalling of concrete fragments. The inhibited crack propagation also results in a reduced expansion of the the spalling crater in radial direction. However, there are always a few fragments from a heavily crushed region in the center of the spalling crater that are too small to be influenced by the steel fibers. These fragments fly away at a similar velocity as in the case without steel fibers.

In cases where a concrete slab without steel fibers would already be breached by the detonation, the steel fibers are expected to have a significantly reduced impact on secondary debris. This assumption is caused by the fact, that in cases with a breach the steel fibers cannot anchor into the concrete in the loading direction.

A new methodology was presented that allows a quantitative evaluation of the influence of the steel fibers on the secondary debris. This methodology derives the x-velocity distribution and kinetic energy of the secondary debris from steel fiber reinforced concrete slabs. This derivation is based on the x-velocity distribution without steel fibers and the difference between the specific fracture energies of the concrete with and without steel fibers.

In the present series of tests a steel fiber content of 1.0 Vol % was found to be the most efficient. It reduced the total kinetic energy of the secondary debris by more than 90 %. A further increase in the steel fiber content to 2.0 Vol % did not show a similar reduction. This is consistent with the fracture energy of the concrete measured in [Mosig et al., 2021] and is largely attributed to an increasingly uneven distribution of the steel fibers in the concrete with increasing steel fiber content. However, tests with a larger explosive load are required to fully investigate the potential of higher steel fiber contents.

Retrofit layers of steel fiber reinforced concrete can be used to significantly reduce the effect of secondary debris from existing structures. In the present series of tests, the reduction is similar that of fully steel fiber reinforced concrete slabs with the same steel fiber content of 2.0 Vol %.

Because of the identified failure mechanism, the retrofit layer is expected to fail less ductile than a fully steel fiber reinforced concrete slab. Due to the greater concrete cover of the rebar in the original concrete slab, more secondary debris is expected once the retrofit layer fails, but with a lower x-velocity.

4.10. DIC measurements

It becomes increasingly difficult for the developed tracking algorithm to determine the velocity when there is only little secondary debris. This is particularly true as the steel fiber content increases. Therefore, in some tests where little secondary debris was expected, DIC measurements were taken from the protective surface of the concrete slabs.

4.10.1. Validation of the x-velocity distribution

Figure 4.38 (right) shows the x-velocity distribution of test SN171 (2000 g, 2.0 Vol %) along a section through the center of the protective concrete surface. The coordinate on the abscissa is given in terms of the radial distance from the center on the concrete surface. The changing gray values of the lines indicate the different time steps.

The DIC measurements can be used to validate the x-velocity distribution approximated by equation (4.6). This velocity distribution for a steel fiber content of 0.0 Vol % is shown in figure 4.38 (right) as a red dashed line. In addition, the blue dashed line shows the x-velocity distribution for a steel fiber content of 2.0 Vol %, determined on the basis of the energy principle introduced in section 4.9.2. The maximum x-velocity and the parameter σ for the width of the distribution are calculated from the approximated polynomials in figures 4.20 and 4.22.

To evaluate the evolution of the x-velocity over the time, figure 4.38 (left) shows the x-velocity at selected locations. These locations are evenly spaced in radial direction from the center of the spalling crater at $r = 0.0\,\mathrm{cm}$ to the edge of the spalling crater at $r = -33.2\,\mathrm{cm}$.

Starting from the time-step of 1.4 ms, the DIC pattern in the center ($-5.0\,\mathrm{cm} \leq r \leq 5.0\,\mathrm{cm}$) is too disturbed by the fracture of the concrete to make further DIC measurements in this region.

The velocity at the protective surface of the concrete slab is the result of the reflection of the incoming compressive wave at this surface. Due to the large difference in impedance between the concrete and the surrounding air, the compressive wave is converted into a tensile wave upon reflection. This tensile wave propagates in the direction opposite to the original compressive wave. As soon as the superposition of the incoming compressive wave and the reflected tensile wave leads to a tensile stress above the dynamic strength of the concrete, cracks are formed (spalling). The velocity of the secondary debris then results from the momentum trapped in the spalled concrete minus the energy required

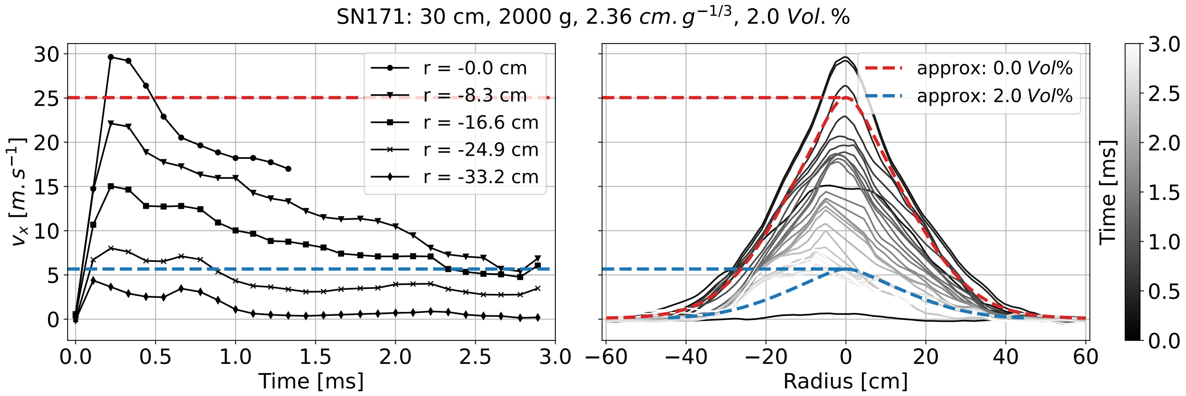

Figure 4.38.: Velocity over time from DIC measurement for SN171

for the fracture.

As a result of the incoming compressive wave and the associated particle velocity, the x-velocity of the concrete at the protective surface of the concrete slab increases rapidly between 0.0 ms and 0.2 ms. This brief velocity peak is followed by a velocity drop during which the fracture of the concrete takes place. The DIC measurements in this test series were not performed on reinforced concrete slabs without steel fibers. Therefore, it cannot be clearly determined which part of this velocity drop is due to the fracture of the concrete and when the influence of the steel fibers begins.

According to [Hartmann, 2009], who determined the shock velocity - particle velocity relationship for concrete using numerical simulations of the mesoscopic structure, no influence of the steel fibers on the surface velocity can be found before fracture of the concrete. This is attributed to the proportionally very low share of the steel fibers ($\leq$2.0 Vol %). It is only after an initial cracking that the steel fibers begin to have an effect by inhibiting crack propagation and reducing the velocity of the secondary debris.

At 0.4 ms, the shape of the x-velocity distribution approximated by equation (4.6) (red dashed line) shows a good agreement with the x-velocity distribution determined from the DIC measurement for 2.0 Vol % of steel fibers. It is therefore assumed that the fracture of the concrete itself is complete at this time step and the subsequent reduction in x-velocity is caused by the influence of the steel fibers. The velocity distribution for a steel fiber content of 2.0 Vol %, that has been approximated by the energy principle in section 4.9.2 (blue dashed line), also agrees well with the DIC measurements.

Unfortunately, the frame rate of the present DIC recordings is too low to analyze the initial fracture process before 0.5 ms in more detail. For future test series, a much higher frame rate of the DIC recordings could help to gain a better understanding of the underlying processes. Based on the numerical simulations in chapter 5, the required frame rate is estimated to be $>1 \times 10^5\,\mathrm{s}^{-1}$ to properly capture the fragmentation process of the concrete.

4.10.2. Validation of the load bearing mechanism

While the fragments are propelled away at a constant velocity in the case without steel fibers, they are partially or fully retained by the additional steel fibers and the retrofit layer.

Figure 4.39 shows the x-velocity in dependence on the time (left) for 30 cm thick concrete slabs subjected to 1500 g of SEMTEX10 at equally spaced locations across the surface of the spalling crater. The situation with 2.0 Vol % full steel fiber reinforcement is shown as an orange dash-dotted line, the situation with a retrofit layer is shown as a blue solid line. The respective curves are calculated by averaging the two analogue tests to minimize the influence of experimental variations. The measurements at a radial location of $r = 0.0\,\mathrm{cm}$ end at a time step of 1.0 ms due to the fragmentation of the concrete, which prevents further DIC measurements in this region.

For a better visual comparison of the different load bearing mechanisms, figure 4.39 (right, dashed) shows the situation at 1.0 ms in dependence on the radial location. The approximated spatial x-velocity distribution for the case without steel fibers according to equation (4.6) is added as a red dashed line.

An analysis of the x-velocity profile in dependence on the time shows that the behavior of the two reinforced cases (full steel fiber reinforcement and retrofit layer) is very similar up to about 0.3 ms. Thereafter, the full steel fiber reinforced concrete slab (orange) exhibit a strong reduction in x-velocity due to the resistance of the steel fibers. For most of the spalled concrete, this results in a complete stop at a time step of latest 2.0 ms. Only in the center of the spalling crater there are some concrete fragments that are so heavily fragmented that they cannot be anchored by the steel fibers. As a result, they fly away at a similar velocity as in the case without steel fibers.

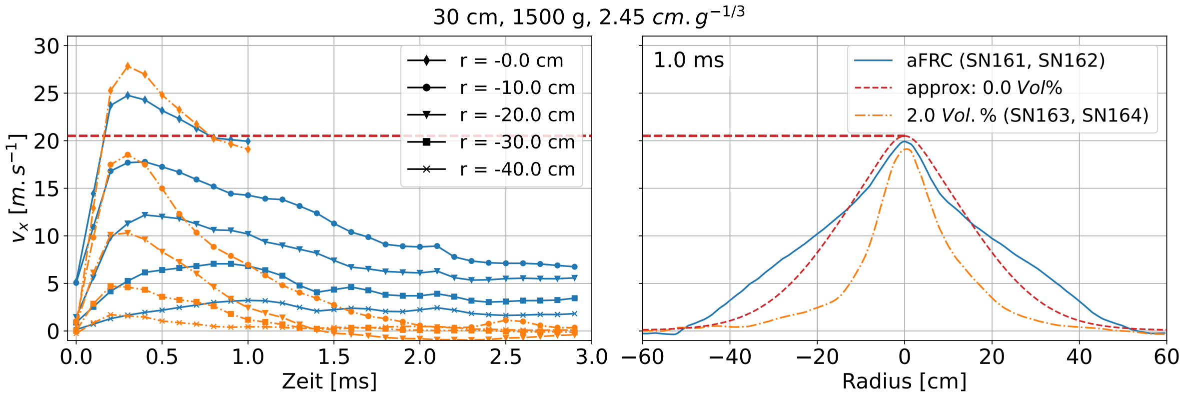

Figure 4.39.: Velocity over time from DIC measurement

As can be seen in figure 4.39 (left), the retrofit layer (blue) reduces the velocity of the concrete at the protective surface below that of the case without steel fibers (red). However, this reduction occurs at a much smaller rate than in the case of full steel fiber reinforcement (orange). At the same time, the concrete in the outer region ($|r| \geq 30.0\,\mathrm{cm}$) is accelerated even further until about 1.0 ms. This is a result of the membrane action of the retrofit layer (section 4.9.3), which equalizes the x-velocity across the entire spalled retrofit layer. This results in a more linear x-velocity distribution in the radial direction, which is reflected by the absence of an additional circumferential crack that can be seen in the case without steel fibers (section 4.9.3). The extent to which this effect is also influenced by the greater concrete cover of the rebar layer cannot be assessed with the tests presented.

The full steel fiber reinforcement (figure 4.39, right, orange) reduces the velocity of the secondary debris especially in the less fragmented outer regions of the spalling crater, where the steel fibers can better anchor into the surrounding concrete. However, there is a small region in the center that is only minimally affected because the concrete in this region is so heavily fragmented that the steel fibers cannot anchor properly.

4.10.3. Summary

The spatial x-velocity distribution of the secondary debris from the DIC measurements is used to validate the introduced approximation according to equation (4.6) and the influence of the steel fibers according to the energy principle as described in section 4.9.2.

Overall, a good agreement can be found.

The load bearing mechanism of the retrofit layer and the full steel fibers reinforcement described in section 4.9.1 show a good correlation with the spatial x-velocity distribution on the protective surface of the concrete slab from the DIC measurements.

4.11. Summary

Damage The shock wave introduced into the concrete crushes the concrete directly behind the explosive charge, creating a crushing crater. The remaining damage to the concrete is almost entirely due to the reflected tensile wave, resulting in a spalling crater.

The dimensions of the spalling crater were measured using 3D scans. A new method was introduced to average the geometry of the spalling crater assuming rotational symmetry. This method unifies the irregular geometry of the spalling crater and thus allows a better comparison between different tests.

It has been shown that the thickness of the concrete slab is the determining factor for the diameter of the spalling crater, while the depth of the spalling crater is more influenced by the mass of the explosive. This is due to the expansion of the blast wave, which spreads over an increasing area as it propagates through the concrete slab. The depth of the spalling crater, on the other hand, depends more on the length of the blast wave, which in turn depends on the mass of the explosive.

Based on the experimental results, a scaled thickness of $T_W = 2.1\,\mathrm{cm\,g^{-1/3}}$ proves to be a good measure as a threshold for the occurrence of a breach. This threshold agrees very well with the tests of [Morishita et al., 2000]. However, other tests with a different geometry of the explosive charge and a different reinforcement ratio of the concrete slabs underestimated the thickness required to prevent breaching compared to the presented test. For a thorough analysis, further tests are needed to analyze the influence of the charge geometry and the reinforcement ratio in more detail.

Especially in cases without a breach the rebar layer has a strong influence on the total amount of secondary debris. Although the spalling crater extends below the rebar layer in the tests without a breach, most of the damaged concrete below the rebar layer is retained by the rebar layer, resulting in less secondary debris. Therefore, a small concrete cover of the rebar layer is considered beneficial to reduce the amount of secondary debris.

Velocity A tracking algorithm was developed to measure the trajectory and velocity of the secondary debris fragments from the HS recordings. Based on this, the trajectory of the secondary debris fragments was found to be dominant in the x-direction, with most fragments moving at angles less than 20°.

A linear relation was found between the maximum x-velocity of the secondary debris and the inverse of the scaled thickness of the concrete slab. This relation is well suited to make predictions about similar situations.

It has been shown that the velocity and size of the secondary debris fragments are strongly influenced by the occurrence of a breach in the concrete slab. With smaller, faster fragments in the presence of a breach and larger, slower fragments in the absence of a breach.

The spatial x-velocity distribution in the radial direction of the spalling crater was approximated by an enveloping curve. The parameters for this curve are the maximum x-velocity of the secondary debris and the width of the velocity distribution. Linear approximations depending on the scaled thickness of the concrete slab were determined for both parameters.

The approximated spatial x-velocity distribution of the secondary debris was compared with the fracture pattern of the concrete and shows good agreement. The results indicate a strong influence of the rebar layer. Based on the present tests, reducing the concrete cover of the rebar layer is considered beneficial to reduce the impact of the secondary debris. However, further testing is required to quantify the influence of the rebar layer.

Kinetic energy Based on the rotationally symmetric averaged shape of the spalling crater and the approximated spatial x-velocity distribution of the secondary debris, the total kinetic energy of the secondary debris was derived. This total kinetic energy is a well suited parameter to evaluate the impact of secondary debris on people and technical installations on the protective side of a concrete slab. A discussion of this impact is presented in chapter 6.

Steel fibers The influence of the steel fiber reinforcement was evaluated in terms of its ability to reduce the impact of secondary debris. In addition to a visual inspection of the damaged regions, a method based on the kinetic energy of the secondary debris and the fracture energy of the concrete was used to quantitatively evaluate the influence of the different steel fiber contents. This method shows a good agreement with the measurements of the spalling crater size and the velocity of the secondary debris.

The additional steel fibers continuously reduce the amount and velocity of secondary debris as the steel fiber content increases. A decreasing efficiency of the steel fibers was observed with increasing steel fiber content. This is particularly relevant at a steel fiber content of 2.0 Vol% and is caused by a deterioration in the workability of the fiber reinforced concrete with increasing steel fiber content, resulting in an uneven distribution of the steel fibers. A steel fiber content of 1.0 Vol % was found to be the most efficient, reducing the kinetic energy of the secondary debris by more than 90 %. However, experimental testing with higher explosive loads is required to fully investigate the potential of higher steel fiber contents.

There are always fragments that are minimally affected by the different reinforcements (full steel fiber reinforcement and retrofit). However, these are only very few, small fragments resulting from a heavily crushed region in the center of the spalling crater.

The steel fibers reduce the size of the spalling crater and the velocity of the secondary debris from the outer regions inwards. The damage mechanism prior to an initial cracking of the concrete is independent of the steel fiber content. It is only after the initial cracking that the steel fibers begin to have an effect by inhibiting crack propagation and preventing complete spalling of concrete fragments. In this context, the results again indicate an influence of the concrete cover of the rebar layer which retains some of the damaged concrete. However, since the retained concrete is damaged, it is expected that the bond between the steel fibers and the concrete is comprised, especially in the central region of the spalling crater. Consequently, the steel fibers are expected to have a significantly reduced impact on secondary debris in cases where a concrete slab without steel fibers would be breached by the detonation.

The load bearing mechanism of the retrofit layer was found to be mainly based on a membrane action of the retrofit layer. In the present tests, the retrofit layer can reduce the resulting secondary debris to a similar extent as a full steel fiber reinforcement with 2.0 Vol% of steel fibers. Due to the identified failure mechanism, the retrofit layer is expected to fail less ductile than a full steel fiber reinforced concrete slab. As a result of the greater concrete cover of the rebar in the original concrete slab, more secondary debris is expected once the retrofit layer fails.

It is concluded that steel fibers can significantly reduce the impact of secondary debris from concrete slabs. A retrofit layer of steel fiber reinforced concrete on the protective side of the concrete slab is considered to be well suited to protect against secondary debris in already existing structures.

DIC The DIC measurements were compared with the approximated spatial x-velocity distributions as well as the identified failure mechanisms of the steel fiber reinforced concrete slabs and the retrofit layer. Good agreement can be observed.

5. Numerical simulation of secondary debris

Validated numerical simulations can help to gain a deeper insight into the underlying physical processes and thus improve the understanding of the related phenomena. In the following, numerical simulations are performed to validate their ability to simulate the secondary debris caused by contact detonations on concrete slabs. This information can then be used to gain a better understanding of the relevant parameters and the spatial velocity distribution in the depth direction of the concrete slab.

Concrete is a highly heterogeneous material whose behavior is strongly influenced by its underlying mesostructure. This mesostructure consists of coarse aggregates and a mortar matrix, which in turn consists of cement, fine aggregates and individual pores. Direct modeling of this mesostructure down to the coarse aggregates has been employed by several authors, e.g. [Riedel, 2000], [Zhou and Hao, 2009], [Gebbeken and Hartmann, 2010], [Grunwald, 2023]. However, due to the immense computational requirements of such a representation, for most applications the material behavior is described by homogeneous material models. Homogeneous material models describe the resulting phenomenological behavior of the mesostructure by assuming a homogeneous continuum on the macroscopic scale.

The nonlinear stress-strain relation of concrete is influenced by the development of cracks throughout the material. In normal strength concrete, these cracks occur primarily in the mortar matrix between the coarse aggregates, and especially at the mortar/aggregate interface [van Mier, 1984]. In plasticity models, the development of cracks and the resulting influence on the stress-strain relation until failure is typically accounted for by a damage parameter. This damage parameter describes the degradation of the material strength as a function of the effective plastic strain.

This chapter compares two established and well-documented plasticity models for their ability to describe the behavior of concrete subjected to a contact detonation. Emphasis is placed on the formation and velocity of the secondary debris. The material models compared are the Karagozian & Case model (KCC) [Crawford et al., 2012], and the Riedel, Hiermaier, and Thoma model (RHT) [Riedel, 2000], [Grunwald et al., 2017], both as implemented in LS-Dyna.

Both material models have a variety of different parameters, but also provide the ability to automatically generate these parameters based on the uniaxial compressive strength of the concrete. While the automatically generated parameters provide a good starting point for the intended studies, they need to be calibrated against available data to ensure good agreement with the experimental results. This is particularly relevant for the parameters related to the damage behavior, as they are strongly dependent on the size of the spatial discretization.

The main objective of the following calibration is to obtain a similar description of the concrete from both material models in order to gain a better insight into their respective advantages and potential for further development. For further information, the reader is referred to the relevant literature ([Lsdyna, 2021], [Grunwald et al., 2017], [Crawford et al., 2012], [Riedel, 2000]).

5.1. Deviatoric strength model

The theoretical background of deviatoric strength models has already been given in section 2.4.3. Therefore, the following descriptions focus on the implementation in both material models.

The strength model in both material models is based on three surfaces defined in the principal stress space. These surfaces describe the locations of the elastic limit Y_e, the maximum strength Y_m and the residual strength after failure Y_r. For both material models these surfaces are given by a pressure depended polynomial of the respective compressive meridian.

The shapes of the compressive meridians start at the point of hydrostatic tensile failure (Y_m, Y_e) or at zero (Y_r) and widen with decreasing gradient in the direction of increasing pressure. Failure from purely hydrostatic compressive loading is initially not described by the strength model.

The shape in the deviatoric plane is derived from the compressive meridian depending on the third invariant of the stress tensor. This shape is given in both material models by the Willam-Warnke formulation [Willam, K.J. and Warnke, E.P., 1974], which describes the different behavior in compression, shear and tension by a continuous transition.

5.1.1. RHT model

In the RHT model, the maximum strength surface Y_m is described based on the compressive meridian of the concrete Y_{TXC} (triaxial compression), which in turn is based on a polynomial description that includes the influence of the third invariant $R_3(\theta)$ (Willam-Warnke) and the influence of the strain rate $F_R(\dot{\varepsilon})$.

$$Y_m(p, \theta, \dot{\varepsilon}) = Y_{TXC}(p) R_3(\theta) F_R(\dot{\varepsilon}) \tag{5.1}$$

$$Y_{TXC}(p) = A_0 + A \left(\frac{p - p_t}{f_c} \right)^{n_f} \tag{5.2}$$

Where the hydrostatic pressure p and the hydrostatic tensile limit p_t are normalized by the uniaxial compressive strength of the concrete f_c (cylinder). The parameters A and n_f can be adjusted by the user to fit the meridian of the maximum strength surface to available experimental data. The parameter A_0 is determined by the program from continuity requirements.

In addition to this polynomial description, the meridian of the maximum strength surface is described by a linear interpolation in the range $p \leq f_c/3$ to better fit experimental measurements of the shear strength f_s and the tensile strength f_t (see e.g. [Grunwald et al., 2017]).

The elastic limit Y_e is derived from the maximum strength surface Y_m as a function of the parameters g_c and g_t. In addition, the RHT model adds a cap F_{cap} to the elastic limit surface that describes the onset of plastic deformation for hydrostatic pressure greater than the pore crush pressure p_{el}.

$$Y_e(p, \theta, \dot{\varepsilon}) = Y_m(p, \theta, \dot{\varepsilon}) F_e(p, g_c, g_t) F_{cap}(p, p_{el}) \tag{5.3}$$

The surface describing the residual strength after failure Y_r under hydrostatic confinement is given by a polynomial description independent on the strain rate and the third invariant.

$$Y_r(p) = B \left(\frac{p}{f_c} \right)^{n_r} \tag{5.4}$$

For the present calibration, the maximum strength surface is fitted directly to experimental measurements from the literature.

Analogous to the default parameters, the parameters of the residual strength surface are the same as those of the maximum strength surface. This ensures, that the residual strength surface approaches the maximum strength surface with increasing pressure ($p \to \infty$).

The parameters of the elastic limit are chosen to satisfy the default criterion of the KCC model. This criterion defines the elastic limit Y_e at about 45 % of the maximum strength Y_m [Crawford et al., 2012] according to:

$$Y_e(p^*) = 0.45\, Y_m(p) \tag{5.5}$$

$$p^* = p - 0.55\, Y_m/3 \tag{5.6}$$

Figure 5.1 shows the compressive meridians of the three RHT model strength surfaces with default parameters (gray lines) and with calibrated parameters (black lines).

The derived parameters of the strength surfaces are given in table 5.1. An overview of all parameters used for the simulation of the contact detonations can be found in the appendix section E.

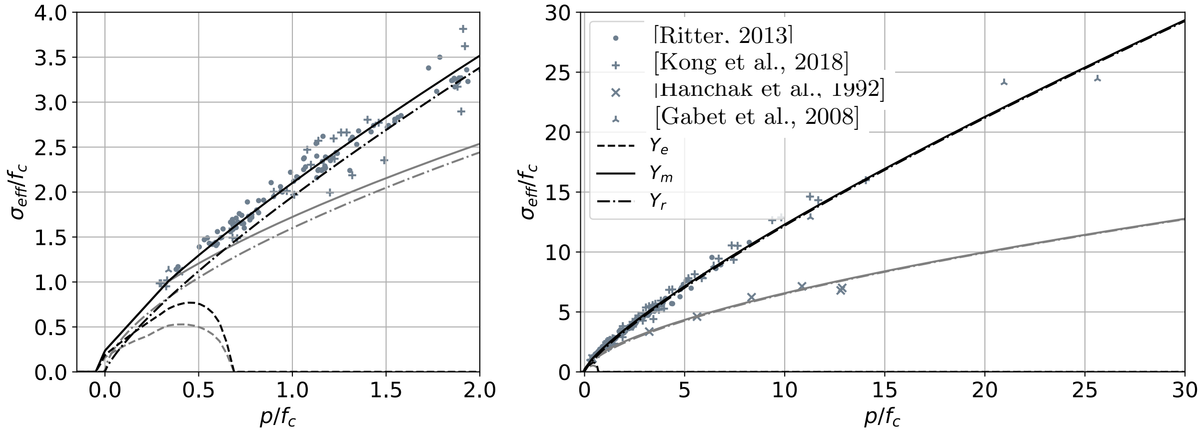

Figure 5.1.: Compressive meridians of the RHT model strength surfaces (gray lines: default parameters, black lines: new calibration

Table 5.1.: Parameters of the RHT model strength surfaces

	Y_m		Y_e		Y_r	
	A	n_f	g_c	g_t	B	n_r
default	1.6	0.61	0.53	0.7	1.6	0.61
fitted	1.95	0.80	0.67	0.9	1.95	0.80

5.1.2. KCC model

In the KCC model, the compressive meridians of the different surfaces $Y_{XTC,j}$ are all defined by the same functional, depending on three parameters a_{ij} each:

$$Y_{TXC,j}(p) = a_{0j} + \frac{p}{a_{1j} + a_{2j}\,p} \tag{5.7}$$

Where the index j represents the different surfaces for the elastic limit (e), the maximum strength (m) and the residual strength (r). The different parameters a_{ij} can be interpreted as:

$$a_{0j} = Y_{TXC,j}|_{p=0} \tag{5.8}$$

$$a_{1j} = \left(\frac{dY_{TXC,j}}{dp} \bigg|_{p=0} \right)^{-1} \tag{5.9}$$

$$a_{2j} = (\lim_{p \to \infty} Y_{TXC,j} - a_{0j})^{-1} \tag{5.10}$$

The parameters of the maximum strength surface are determined by a fitting of the associated curve to experimental values from the literature.

Since there is no residual strength without a confining pressure, the first parameter of the residual strength surface is $a_{0r} = 0$. As suggested by [Yin et al., 2023], the third parameter of the residual strength surface a_{2r} is calculated so that it approaches the maximum strength surface with increasing pressure ($p \to \infty$):

$$a_{2r} = (0.99\,(a_{0m} + a_{2m}^{-1}))^{-1} \tag{5.11}$$

The second parameter of the residual strength surface a_{1r} is chosen so that it does not intersecting the maximum strength surface at high pressures.

The parameters of the elastic limit are chosen to satisfy the default criterion of the KCC model. This criterion defines the elastic limit Y_e at about 45 % of the maximum strength Y_m [Crawford et al., 2012] according to equation (5.5). In contrast to the RHT model, the KCC model does not give an option to limit the elastic limit surface with a cap for hydrostatic pressure greater than the pore cursh pressure.

Similar to the RHT model, for $p/f_c \leq 1/3$ the maximum strength surface and the elastic limit surface are linearly interpolated to better fit the experimental measurements of the shear strength f_s and the tensile strength f_t (see e.g. [Crawford et al., 2012]).

Analogous to the RHT model, the three strength surfaces are defined based on the associated compressive meridians from equation (5.7) and a description including the influence of the third invariant (Willam-Warnke) and the influence of the strain rate. A detailed description of the strength surfaces in the KCC model can be found in [Crawford et al., 2012].

Figure 5.1 shows the three strength surfaces of the KCC model with default parameters (gray lines) and with calibrated parameters (black lines).

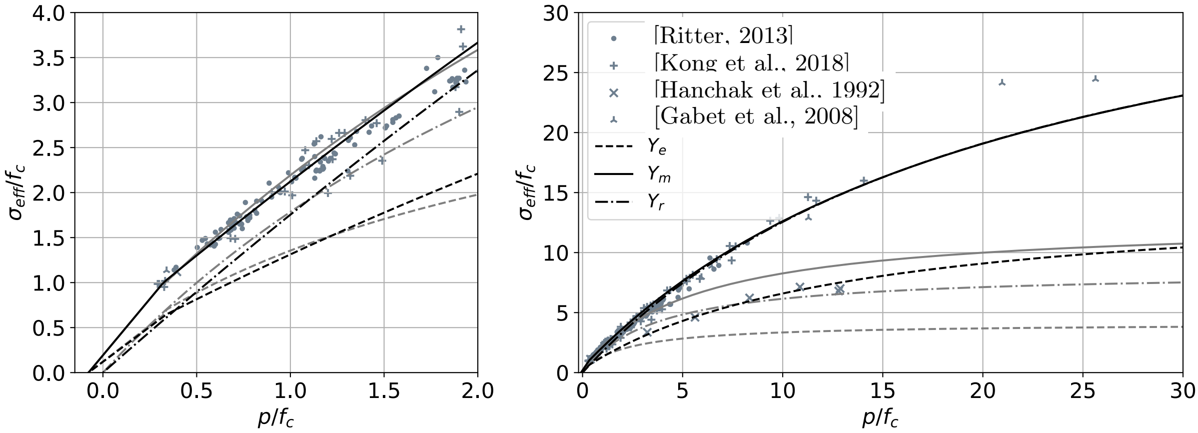

Figure 5.2.: Compressive meridians of the KCC model strength surface (gray lines: default parameters, black lines: new calibration)

For a pressure greater than $p > 15\ f_c$, the maximum strength surface of the KCC model describes a lower maximum deviatoric strength than the RHT model. This is due to the formulation of the curve according to equation (5.7), which does not allow for a good fit over the entire range.

Although the pressure from the contact detonation is extremely high immediately behind the explosive, it attenuates rapidly as the shock wave propagates through the concrete. In the region of the concrete slab relevant for the description of the secondary debris, the pressure in the experimental tests is below $p/f_c < 15$. Therefore, a good fit below $p/f_c < 15$ is considered more important than a mediocre fit over the entire pressure range.

The resulting parameters of the strength surfaces are given in table 5.2. An overview of all parameters used for the simulation of the contact detonations can be found in the appendix section E.

Table 5.2.: Parameters for the KCC model strength surfaces

	Y_m			Y_e			Y_r		
	a_{0m}	a_{1m}	a_{2m}	a_{0e}	a_{1e}	a_{2e}	a_{0r}	a_{1r}	a_{2r}
default	$0.296\,f_c$	0.446	$0.081/f_c$	$0.223\,f_c$	0.625	$0.258/f_c$	0	0.442	$0.118/f_c$
fitted	$0.39\,f_c$	0.54	$0.032/f_c$	$0.26\,f_c$	0.92	$0.078/f_c$	0	0.515	$0.032/f_c$

5.2. Hardening, softening and damage

The hardening and softening/damage behavior described by the material models is strongly correlated with the size of the spatial discretization. In the following, the main points of the corresponding descriptions implemented in both material models are given and calibrated on the basis of empirical curves available in the literature.

Inspired by the work of various authors ([Tu and Lu, 2009], [Crawford et al., 2012], [Kong et al., 2017], [Hong et al., 2017], [Kucewicz et al., 2022], [Yin et al., 2023]), the calibration of the material models is performed using single-element simulations to analyze their behavior under triaxial compression and uniaxial tension. The elements used for these simulations are under-integrated solid elements with a side length of 24 mm. This element size was chosen based on the extent of the fracture process zone for concrete, which according to [Bažant and Oh, 1983] is approximately three times the diameter of the largest aggregate.

To model the confinement in the triaxial compression tests, three surfaces of the solid element are provided with symmetry conditions, while the confining pressure is gradually applied to the remaining three surfaces over the first 50 ms of the simulation. The uniaxial load is subsequently applied to one of these surfaces at a constant nodal velocity of $1 \times 10^{-3}\,\mathrm{m\,s^{-1}}$. To eliminate strain rate effects, the corresponding factors are switched off in both material models. A sketch of the associated numerical model is shown in figure 5.3.

The **compressive behavior** of the concrete is compared to empirical curves introduced by [Samani and Attard, 2010] as *New Model for Stress Strain Relationship*. This model describes the compressive hardening and softening of the concrete under confined and unconfined conditions. The hardening part of the model is given by a fractional curve according to equation (5.12).

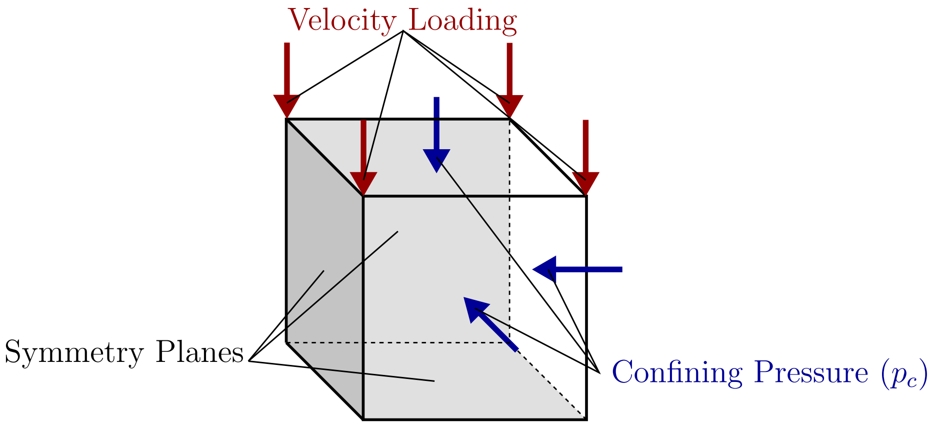

Figure 5.3.: Numerical model for single-element simulations

$$\frac{\sigma}{f_0} = \frac{AX + BX^2}{1 + (A-2)X + (B+1)X^2} \qquad X = \frac{\varepsilon}{\varepsilon_0},\ 0 \leq \varepsilon \leq \varepsilon_0,\ 0 \leq f \leq f_0 \tag{5.12}$$

Where the parameters A and B depend on the compressive strength f_c and elastic stiffness E_c of the concrete (see [Samani and Attard, 2010]), while the softening part of the model is described by a power function according to equation (5.13).

$$\frac{\sigma}{f_0} = \frac{f_r}{f_0} + \left(1 - \frac{f_r}{f_0}\right)\left(\frac{f_i}{f_c}\right)^{\left(\frac{\varepsilon-\varepsilon_0}{\varepsilon_i-\varepsilon_0}\right)^2} \qquad \varepsilon \geq \varepsilon_0 \tag{5.13}$$

Here the indices of the strain ε and the compressive strength f describe the peak strength under confinement 0, the inflection point i and the residual strength r of the concrete as shown in figure 5.4. This curve has been validated by [Samani and Attard, 2010] using experimental results with a hydrostatic confinement of $p/f_c \leq 1.0$.

The **tensile softening** of the concrete is compared with an empirical curve introduced by [Hordijk, 1991]. This curve describes the softening of the concrete by expressing the tensile stress in the concrete in terms of the crack opening w and a critical crack opening w_c.

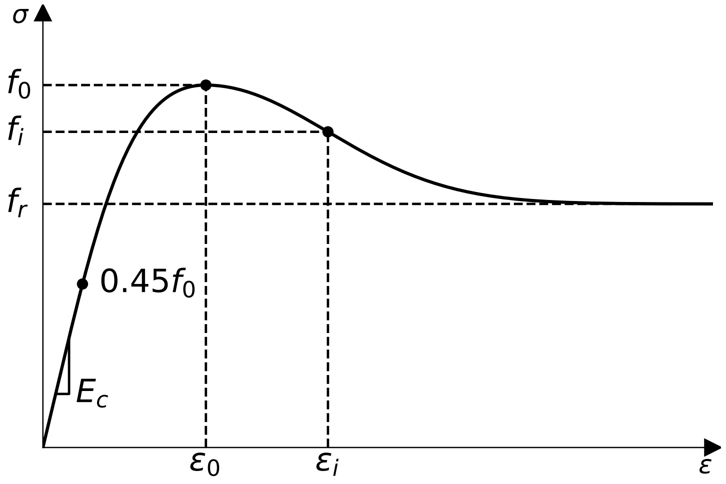

Figure 5.4.: Empirical compressive stress-strain-relation for confined concrete [Samani and Attard, 2010]

$$\frac{\sigma}{f_t} = \left[1 + \left(c_1 \frac{w}{w_c}\right)^3\right] \exp\left(-c_2 \frac{w}{w_c}\right) - \frac{w}{w_c}\left(1 + c_1^3\right) \exp\left(-c_2\right) \tag{5.14}$$

The shape of this curve is controlled by the parameters c_1 and c_2, for which [Hordijk, 1991] determined the best fit in the case of static loading conditions with $c_1 = 3$ and $c_2 = 6.93$. The critical crack opening w_c can be approximated from the fracture energy of the concrete G_f according to:

$$w_c = 5.14 \frac{G_f}{f_t} \tag{5.15}$$

For the following evaluation, the static tensile strength $f_t = f_{ctm}$ and fracture energy G_f of the concrete are calculated according to [fib, 2013]. For this, the characteristic compressive strength f_{ck} of the concrete is related to the mean compressive strength f_{cm} measured on the test specimens by $f_{cm} = f_{ck}{+}8\,\mathrm{MPa}$.

$$f_{ctm} = 0.3\, f_{ck}^{2/3} \tag{5.16}$$

$$G_f = 73\, f_{cm}^{0.18} \tag{5.17}$$

To compare the tensile softening curve according to equation (5.14) with numerical simulations, the crack opening w is described in terms of the plastic strain $\varepsilon_p = w/l_c$ for which the reference length is given by the size of the fracture process zone l_c.

As explained in section 2.4.5, the size of the spatial discretization can lead to a non-objective behavior of the numerical simulations, especially if it is smaller than the respective fracture process zone.

According to [Schuler, 2004], the crack band model, which localizes the total fracture energy in each element, is well suited to describe the energy dissipated by the fracture of the concrete. While this reduces the effect of strain localization within a single layer of elements, it overestimates the total fracture energy of a structure when the element size is smaller than the fracture process zone.

An alternative representation is to assign each element a fracture energy that is proportional to the fraction of the fracture process zone that the element represents. Thus, multiple elements spanning the fracture process zone add up to the total fracture energy.

To investigate the influence of the spatial distribution of the fracture energy in the numerical model on the velocity of the secondary debris, both methods are compared in section 5.6.1 with respect to the x-velocity at the protective concrete surface.

5.2.1. RHT model

Hardening in the RHT model is described by a linear interpolation between the elastic limit and the maximum strength surface based on the effective plastic strain ε_p.

$$Y_{em} = Y_e + \frac{\varepsilon_p}{\varepsilon_{p,hard}}(Y_m - Y_e) \qquad \text{with} \quad \varepsilon_{p,hard} = \frac{Y_m - Y_e}{3G_p} \tag{5.18}$$

Where G_p is the plastic shear modulus, which is related to the elastic shear modulus G of the concrete by $G_p = \xi G$. With $\xi = 0.5$ being the default input parameter of the RHT model. For the following simulations, the elastic shear modulus $G = 12\,962\,\mathrm{MPa}$ of the concrete is calculated from a Young's modulus of $E = 31\,108\,\mathrm{MPa}$ determined in the SHB tests (table 4.3, [Mosig et al., 2021]) together with an assumed Poisson ratio of $\nu = 0.2$.

$$G = \frac{E}{2(1+\nu)} \tag{5.19}$$

After reaching the maximum strength surface, the RHT model uses a **damage description** introduced by [Holmquist et al., 1993], which describes the damage D by relating the incremental plastic strain $d\varepsilon_p$ to a plastic strain at failure ε_p^f. The resulting damage variable D then ranges from $D = 0$ for no damage below the maximum strength to $D = 1$ when the residual strength surface is reached.

$$D = \int_0^{\varepsilon_p} \frac{1}{\varepsilon_p^f}\, d\varepsilon_p \tag{5.20}$$

The effective plastic strain at failure ε_p^f is controlled by two failure parameters d_1 and d_2 as well as the hydrostatic tensile cutoff p_t. In addition, it is constrained by a minimum plastic strain ε_p^{min} to avoid fracture caused by low magnitude tensile waves [Grunwald et al., 2017].

$$\varepsilon_p^f = d_1 \left(\frac{p}{f_c} - (1-D)\frac{p_t}{f_c} \right)^{d_2} \geq \varepsilon_p^{min} \tag{5.21}$$

Softening in the RHT model is described by a linear interpolation between the maximum strength surface and the residual strength surface based on the damage parameter D.

$$Y_{mr} = Y_m + D(Y_r - Y_m) \tag{5.22}$$

The direction of plastic flow with respect to the current yield surface is given in the RHT model by a non-associative flow rule perpendicular to the hydrostatic axis. This continues the strict separation of the hydrostatic and deviatoric components of the stress tensor and avoids the need for additional iterations due to an interaction of the plastic flow with the equation of state. As a consequence, shear dilatation is not represented by the RHT model.

The slope of the softening part in compression can be controlled by the damage parameter d_1, which is the dominant influence for compressive loading in equation (5.21).

For the present case, the parameter $d_1 = 1.5 \times 10^{-2}$ and the parameter d_2 is left at the default value ($d_2 = 1.0$). These parameters agree with the calibration presented by [Tu and Lu, 2009].

Figure 5.5 shows the **compressive stress-strain relation** from single-element simulations for different confining pressures. For a comparison, the dotted lines show the empirical curves which have been calculated according to equations (5.12) and (5.13). The dashed lines show the result of the simulations with the default parameters for a concrete with a compressive strength of $f_{cm} = 35\,\text{MPa}$. The solid lines show the results of simulations with the newly adjusted parameters.

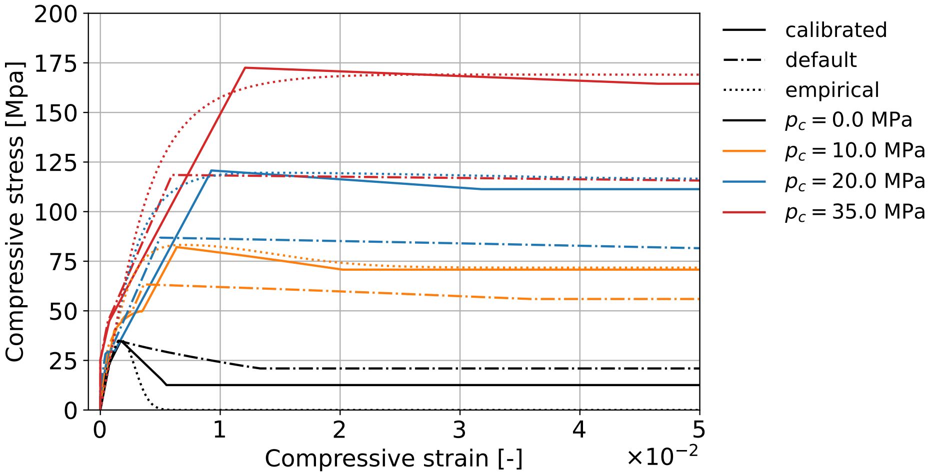

Figure 5.5.: Stress-strain-relation for triaxial compression with confinement (RHT model)

Comparing the different curves in figure 5.5, the default parameters significantly underestimate the compressive strength of the concrete as described by [Samani and Attard, 2010]. This is mainly influenced by the lower compressive meridians of the default parameters shown in figure 5.1. With the calibrated parameters, a much better fit can be obtained.

The different shape during hardening is caused by the linear interpolation between the elastic limit and the maximum strength surface. A particularly noticeable effect is that there is still a residual compressive strength of the concrete without any additional confinement (curves with $p_c = 0.0\,\text{MPa}$).

Figure 5.6 shows the **tensile stress-strain relation** from the single-element simulations. As before, the dashed line shows the results from the simulation with default parameters and the solid line shows the results with newly adjusted parameters. For comparison, the dotted line shows the empirical curve calculated according to equation (5.14).

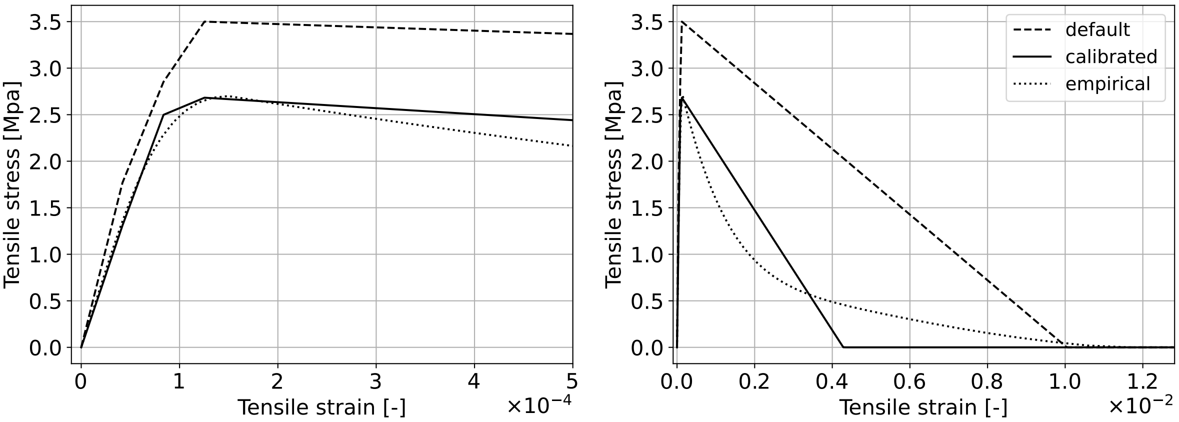

Figure 5.6.: Stress-strain-relation for uniaxial tension (RHT model)

As explained by [Tu and Lu, 2009], the term in parentheses in equation (5.21) becomes small in case of tensile loading and the minimum strain ε_p^{min} is the governing parameter for the tensile softening behavior. On the basis of equation (2.38) and the linear softening behavior of the RHT model, ε_p^{min} can be calibrated to represent the desired fracture energy G_f for a given size of the fracture process zone l_c according to equation (5.23).

$$\varepsilon_p^{min} = \frac{2G_f}{l_c f_t} \tag{5.23}$$

For a size of the fracture process zone equal to the element size $l_e = l_c = 24\,\mathrm{mm}$, a fracture energy $G_f = 138\,\mathrm{J\,m^{-2}}$ according to equation (5.17), and a tensile strength $f_t = 2.7\,\mathrm{MPa}$ according to equation (5.16) this results in $\varepsilon_p^{min} = 4.3 \times 10^{-3}$.

The higher peak value of the default fit in figure 5.6 is caused by a normalized tensile strength of $f_t/f_c = 1 \times 10^{-1}$ as opposed to $f_t/f_c = 7.5 \times 10^{-2}$ for the new calibration based on equation (5.16). Together with the greater default minimum strain ε_p^{min} this causes the simulation with default parameters to considerably overestimate the fracture energy for the given element size with $G_f = 416\,\mathrm{J\,m^{-2}}$.

5.2.2. KCC model

In the KCC model, hardening and softening are described by an interpolation between the different surfaces based on the parameter η, which is given by a user-defined λ-η relation. The parameter λ is in turn defined by equation (5.24).

$$\lambda = \begin{cases} \displaystyle\int_0^{\varepsilon_p} \frac{1}{(1+p/f_t)^{b_1}}\, d\varepsilon_p & , p \geq 0 \\ \displaystyle\int_0^{\varepsilon_p} \frac{1}{(1+p/f_t)^{b_2}}\, d\varepsilon_p & p < 0 \end{cases} \tag{5.24}$$

The description of the parameter λ is similar to the damage parameter D of the RHT model in equation (5.20), but with an option to account for a different evolution in compression and tension based on the parameters b_1 and b_2.

The parameter η increases from 0 to 1 between the elastic limit ($\lambda = 0$) and the maximum strength surface ($\lambda = \lambda_m$), describing the hardening of the concrete. Subsequent softening between the maximum strength and the residual strength is described by a decreasing η back to 0 as λ increases.

The default λ-η relation has been calibrated for an element size of $l_e = 101.6\,\mathrm{mm}$ ($4.0\,$inches) with the intention of being applicable to a wide range of element sizes and aggregate sizes [Crawford et al., 2012]. To account for element sizes that differ from the calibrated size, [Crawford et al., 2012] gives an equation for the compressive damage exponent b_1 as a function of the element size l_e:

$$b_1 = 0.0135\, l_e + 0.79 \qquad l_e[mm] \tag{5.25}$$

To account for the influence of different compressive strengths and aggregate sizes on the tensile behavior of the concrete, [Crawford et al., 2012] provides a means to calibrate the tensile exponent b_2 as a function of the aggregate size d_a and the compressive strength f_c of the concrete.

$$\begin{aligned} b_2 = (1.4 \times 10^{-4}\,(3\,d_a)^2 - 3.86 \times 10^{-2}\,(3\,d_a) + 3.06)\cdot \\ \cdot\,(1 - 8.41 \times 10^{-5}\,f_c^2 + d\,f_c - 0.484) \qquad d_a\,[mm],\ f_c\,[MPa] \end{aligned} \tag{5.26}$$

In addition, release III of the KCC model includes an automatic adjustment of the tensile softening behavior based on the input parameter w_{loc}, which is related to the element size and controls its influence on the fracture energy [Crawford et al., 2012]. While this relation can give a good description of the concrete behavior for many situations, it proves to be problematic in the case of small element sizes [Crawford et al., 2012].

This is especially relevant in the case of the present simulations of contact detonations. Therefore, the parameter w_{loc} is set to a value much smaller than the element size $w_{loc} \ll l_e$ to exclude the automatic adjustment [Kucewicz et al., 2022]. For the simulations with default parameters the parameter w_{loc} is set to the size of the fracture process zone $w_{loc} = l_c$ together with the suggested parameters b_1 and b_2 according to equations (5.25) and (5.26).

The present calibration uses a new λ-η relation based on modified versions of equation (5.12) for hardening ($\lambda \leq \lambda_m$) and equation (5.14) for softening ($\lambda > \lambda_m$):

$$\eta(\lambda) = \begin{cases} \dfrac{AX_1 + BX_1^2}{1 + (A-2)X_1 + (B+1)X_1^2}, & \lambda \leq \lambda_m \\ \left[1 + (c_1 X_2)^3\right] \exp(-c_2 X_2) - X_2\,(1 + c_1^3)\exp(-c_2), & \lambda > \lambda_m \end{cases} \tag{5.27}$$

$$X_1 = \frac{\lambda}{\lambda_m},\ X_2 = \frac{\lambda - \lambda_m}{\lambda_r - \lambda_m}$$

Where $\lambda_m = 1 \times 10^{-4}$ is the location of the peak of the λ-η relation at $\eta = 1$, which is reached at the maximum strength surface and defines the transition from hardening to softening. $\lambda_r = 2.5 \times 10^{-3}$ is the point where η returns to 0, defining the arrival at the residual strength surface. The parameter $A = 8$ controls the initial slope of the λ-η relation in the elastic region and B the curvature in the plastic hardening region starting at $\xi = f_{pl}/f_c = 0.45$ [Samani and Attard, 2010]. These parameters were calibrated using single-element simulations for triaxial compression and uniaxial tension.

$$B = \frac{(A-1)^2}{1-\xi} - 1 \tag{5.28}$$

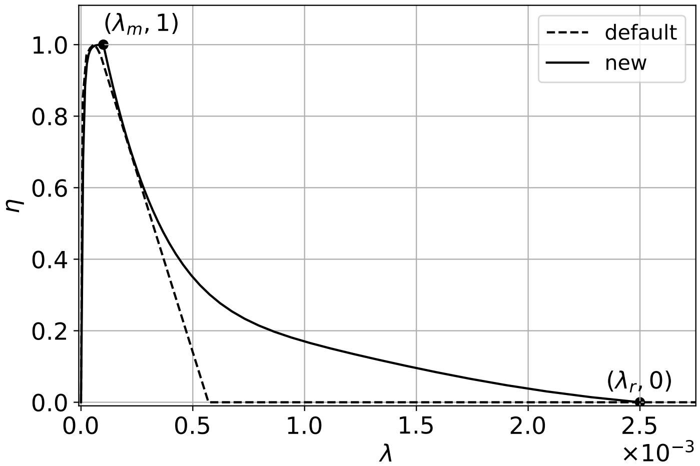

Figure 5.7.: Default (dashed) and calibrated (solid) λ-η relation

The λ-η relation is a single curve that describes the compressive and tensile behavior of the concrete. To account for different behavior in compression and tension, the compressive exponent in equation (5.24) is set to $b_1 = 1.35$ and the tensile exponent is set to $b_2 = 1.0$.

The damage parameter D is defined to range from 0 to 1 for hardening between the elastic limit and the maximum strength surface, and from 1 to 2 for softening between the maximum strength surface and the residual strength surface. Therefore, when comparing the two material models, the damage parameter in the range between 1 and 2 from the KCC model must be compared with the damage parameter in the range between 0 and 1 from the RHT model.

$$D = \frac{2\lambda}{\lambda + \lambda_m} \tag{5.29}$$

The direction of the plastic flow relative to the current yield surface can be varied in the KCC model based on the parameter ω. $\omega = 0$ describes non-associative flow perpendicular to the hydrostatic axis similar to the RHT model, and $\omega = 1.0$ gives a fully associative description of the plastic flow perpendicular to the current yield surface. The default value is $\omega = 0.5$, while [Crawford et al., 2012] suggests a range between

$\omega = 0.5$ and $\omega = 0.9$ for concrete with fine aggregates.

Figure 5.8 shows the **compressive stress-strain relation** from the single-element simulations for different confining pressures. For a comparison, the dotted lines show the empirical curves which have been calculated according to equations (5.12) and (5.13). The dashed lines show the result of the simulations with the default parameters for concrete with a compressive strength of f_c =35 MPa. The solid lines show the results of the simulations with the newly calibrated parameters.

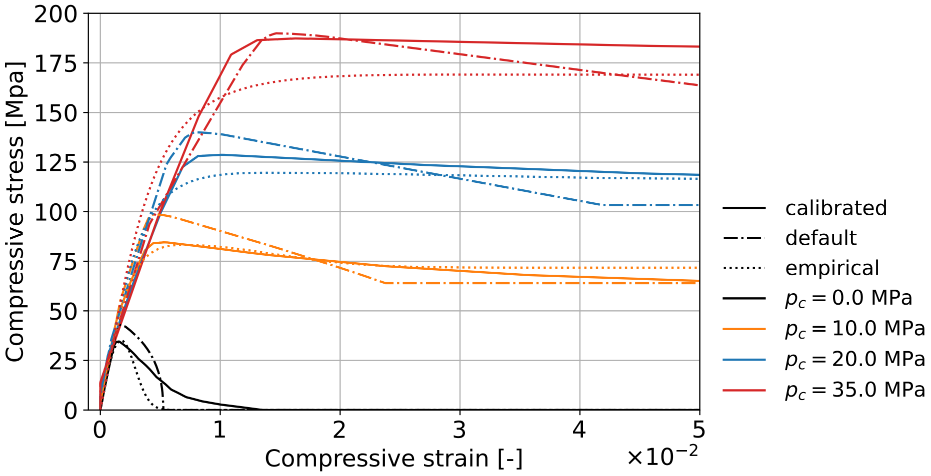

Figure 5.8.: Stress-strain relation for triaxial compression with confinement (KCC model)

Already the simulations with the default parameters are in good agreement with the empirical predictions according to [Samani and Attard, 2010]. However, the calibrated parameters give a slightly better agreement.

Figure 5.6 shows the **tensile stress-strain relation** from the single-element simulations. As before, the dashed line shows the results from the simulation with default parameters and the solid line shows the results with the calibrated parameters. For comparison, the dotted line shows the empirical curve calculated according to equation (5.14).

In case of the tensile softening, the calibrated parameters are in much better agreement with the shape of the empirical curve than the description using the default parameters. While the default parameters underestimate the empirical fracture energy with $G_f = 67\,\mathrm{J\,m^{-2}}$, the calibrated parameters give a fracture energy of $G_f = 135\,\mathrm{J\,m^{-2}}$,

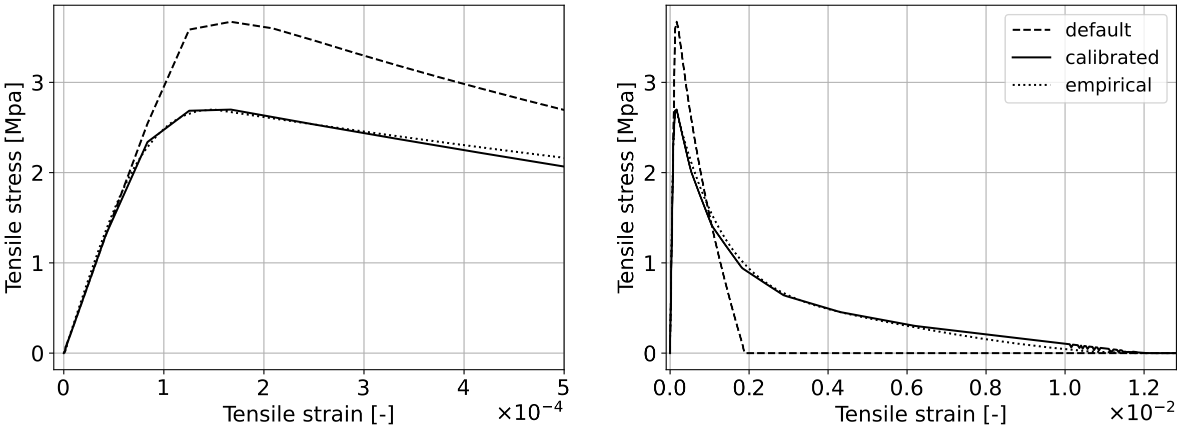

Figure 5.9.: Stress-strain relation for uniaxial tension (KCC model)

which agrees with the fracture energy according to equation (5.17).

5.3. Influence of the strain rate

Both material models describe the influence of the strain rate on the deviatoric strength by a dynamic increase factor (DIF) separately for compression and tension. The effects relevant for the strength increase with increasing strain rate have already been discussed in section 2.4.6. Therefore, only the implementation of these factors in both material models are given below.

The RHT model describes the dynamic strength increase in dependence on the plastic strain rate $\dot{\varepsilon_p}$ separately for compression (c) and tension (t):

$$DIF_{c,t} = \begin{cases} \left(\dfrac{\dot{\varepsilon_p}}{\dot{\varepsilon_0}^{c,t}}\right)^{\beta^{c,t}} & \dot{\varepsilon_p}^{c,t} \geq \dot{\varepsilon_p} \\ \gamma^{c,t}\, \dot{\varepsilon_p}^{1/3} & \dot{\varepsilon_p} > \dot{\varepsilon_p}^{c,t} \end{cases} \tag{5.30}$$

with:

$$\beta^c = (5 + 3/4 f_{cm})^{-1} \tag{5.31}$$

$$\beta^t = (10 + 1/2 f_{cm})^{-1} \tag{5.32}$$

Where f_{cm} is the mean compressive strength of the concrete and $\gamma^{c,t}$ is determined by the program from continuity requirements so that the function has a monotonically increasing shape. The exponents $\beta^{c,t}$ of the first part of the curves are calculated by the program according to the equations (5.31) and (5.32), but can also be entered directly by the user. The default reference strain rates correspond to [Comite Euro-International du Beton, 1993] $\dot{\varepsilon_0}^{c,t} = 30 \times 10^{-6}\,\mathrm{s}^{-1}$. The threshold between the different regions is set by default to a plastic strain rate of $\dot{\varepsilon_p}^{c,t} = 1 \times 10^{22}\,\mathrm{s}^{-1}$, which excludes the second steeper part of the strength increase.

In case of the KCC model, the strain rate increase factor is included by a simple user-defined input of enhancement factors in dependence on the strain rate, also separately in compression and tension.

Figure 5.10 shows the relative increase in concrete strength under compressive and tensile loading with increasing strain rate for both material models. The gray dots mark measurements from different authors which have been collected by [Xu and Wen, 2013]. The gray rectangles represent the increase in tensile strength of the concrete used in the present test series, determined from the Split Hopkinson Bar (SHB) tests of [Mosig et al., 2021]. For this, the dynamic tensile strength determined in the SHB tests is compared to the quasi-static tensile strength according to equation (5.16).

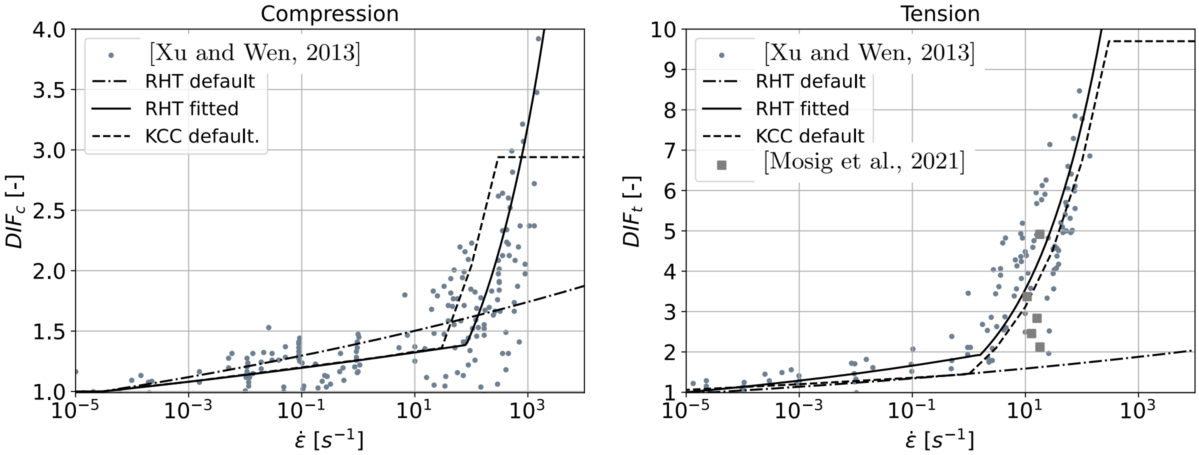

Figure 5.10.: Dynamic strain rate increase factor in tension (left) and compression (right)

The following simulations use the description of the RHT model with slightly modified input parameters. These are the quasi-static reference strain rates in compression and tension of $\dot{\varepsilon_0}^{c,t} = 30 \times 10^{-6}\,\mathrm{s}^{-1}$ as well as the beginning of the second steeper part of the curves for plastic strain rates in compression $\dot{\varepsilon_p}^c = 80\,\mathrm{s}^{-1}$ and tension $\dot{\varepsilon_p}^t = 1.5\,\mathrm{s}^{-1}$. In addition, the exponents for the first part of both curves are set to $\beta^c = 2.2 \times 10^{-2}$ and $\beta^t = 5.5 \times 10^{-2}$ to match their respective slopes to the experimental measurements. The resulting fitted curves are shown as solid lines in figure 5.10.

The fitted curve of the RHT model is also used for the KCC model, with the difference that, similar to the default parameters of the KCC model, both curves are limited by a maximum strain rate increase factor of $DIF_{c,t} \leq 10$. Whilst this is not expected to have a major effect on the simulation results, it is necessary to define a dynamic increase factor over the wide range of possible strain rates using the tabular input.

To investigate the effect of the strain rate on the tensile softening behavior of the material models, figure 5.11 shows the tensile stress-strain relation of both material models for different strain rates. Unlike the simulations in the last section, these simulations include the dynamic strain rate increase factors according to figure 5.10.

The red dotted lines show the expected shapes of the tensile softening behavior based on the respective descriptions of the material models. For this, the strain at the maximum strength is estimated from the dynamic tensile strength together with a Young's modulus of $E = 31\,108\,\text{MPa}$ determined in the SHB tests (table 4.3, [Mosig et al., 2021]). The softening part of the curves is calculated by equation (5.14) for the KCC model and by a linear interpolation between the maximum strength and a plastic failure strain of $\varepsilon_p^{min} = 4.3 \times 10^{-3}$ for the RHT model. The higher maximum strength of the RHT model at a strain rate of $10^3\,\text{s}^{-1}$ is due to the fact that, unlike the curve for the KCC model, the RHT model does not limit the DIF with a threshold.

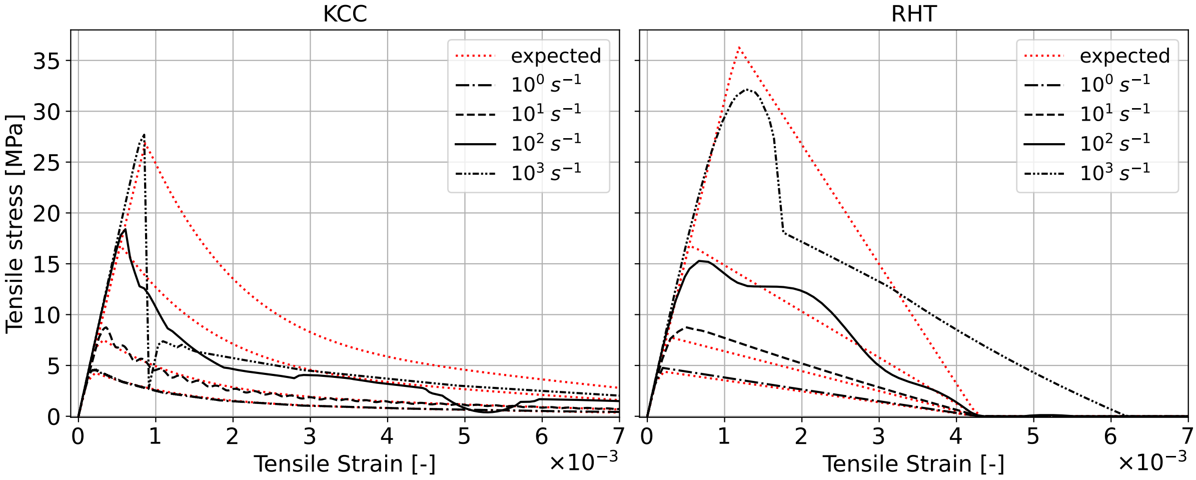

Figure 5.11.: Influence of the strain rate on the tensile stress-strain relation, KCC (left) and RHT (right)

Up to a strain rate of $1\,\text{s}^{-1}$, the simulation results of both material models agree quite well with the expected shape of the the tensile softening behavior. For a strain rate of $10^1\,\text{s}^{-1}$, the KCC model shows some oscillations, but overall the agreement between the simulation and the expected shape is good for both material models.

Starting from a strain rate of $10^2\,\text{s}^{-1}$, the simulation results begin to deviate from the expected shape of the softening behavior. In the case of the KCC model, this results in a slightly faster decrease in tensile stress with increasing strain rate when compared to the expected shape, while the RHT model shows strong oscillations. The reason for the larger maximum strain in the case of the RHT model at a strain rate of $10^3\,\text{s}^{-1}$ is that ε_p^{min} is no longer the dominant parameter in equation (5.21) at this strain rate.

Similar simulations with a layer of multiple elements instead of a single element show that the oscillations can be damped by the neighboring elements. However, the overall behavior is still similar, with a faster decay of strength during softening at higher strain rates. This behavior of the softening at high strain rates, and therefore of the fracture energy, is considered one of the main issues for the numerical simulations. Experimental results of [Weerheijm and Vegt, 2010] even suggest a more linear shape of the softening with increasing strain rate.

In order to analyze the effect of the deviating shapes of the softening behavior on the fracture energy, the fracture energies are calculated according to equation (2.38) for an extension of the fracture process zone of $l_c = 24\,\mathrm{mm}$. It is important to note that the calculated curves were not designed to quantify the increase in fracture energy with increasing strain rate, but to describe the softening behavior of the concrete in a quasi-static case. Nevertheless, the material models have been calibrated in this way and therefore the expected curves should represent the numerical results for the fracture energy with increasing strain rate. The resulting fracture energies for the different strain rates are shown in figure 5.12 as black lines, including reference values from the literature (gray dots) and the values resulting from the expected shape (red dotted lines).

The influence of the strain rate on the fracture energy is still part of the ongoing discussion (e.g. [Schuler et al., 2006], [Weerheijm and Vegt, 2010], [Rey-de Pedraza et al., 2018]). Here the results from the simulations are shown to compare the differences in both material models and set them in context with the experimental measurements.

The fracture energies from both material models agree quite well with the expected values up to a strain rate of $10^1\,\mathrm{s}^{-1}$. After that, the fracture energies from the simulations are much lower than what would be expected from the underlying definitions.

A possible reason for this is described in [Schwer, 2009b]. Although the tensile stress is only applied in one direction, there are also stresses and strains in the lateral directions which are dictated by the Poisson ratio. Due to the mass associated with the nodes of the finite elements, these nodes do not react immediately, but are subject to inertial effects. This introduces additional stresses into the material, which lead to a deviating behavior at high strain rates. However, as described in section 2.4.6, according to [Lu and Li, 2011] and [Xu and Wen, 2013], the strength increase due to lateral inertia is only considered relevant in the case of the compressive strength.

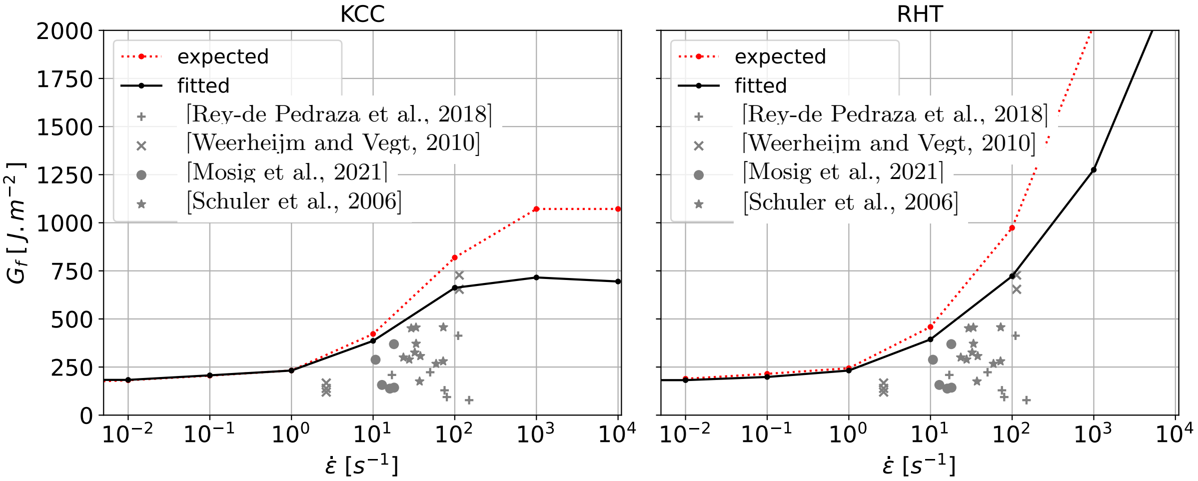

Figure 5.12.: Specific fracture energy in dependence on strain rate, KCC (left) and RHT (right)

Test simulations show, that reducing the density or the Poisson's ratio of the concrete significantly reduces the deviating softening behavior, which supports the explanation of [Schwer, 2009b]. The extent to which this is a true physical effect or a numerical problem cannot be conclusively determined within the scope of this work.

This behavior can be influenced by the time step scale factor $tsfac$, which reduces the time step of the calculation to a fraction of the value resulting from the Courant-Friedrichs-Lewy criterion. While this does not solve the problem, it can reduce its effect to some extent. This is particularly relevant for strain rates of $10^3\,s^{-1}$ and above. The present single-element simulations were performed with a value of $tsfac = 0.01$. Therefore, a time step scale factor of $tsfac = 0.01$ will also be used for the simulation of the experimental tests.

5.4. Equation of state

The equation of state, describing the hydrostatic part of the material model, is given by a simple tabular input in case of the KCC model. The RHT model uses a polynomial description of the EOS for the solid matrix material with p-α-compaction to include the influence of the porosity. The essential parts of this description have already been introduced in section 2.3. The following section describes the calibration process of the

EOS with experimental measurements from the literature.

Unlike the original implementation of the RHT model in Autodyn, the LS-Dyna implementation does not derive the slope of the EOS below the elastic limit directly from the porous sound velocity $dp/d\rho = c_{B,0}^2$ [Grunwald et al., 2017]. Instead, the bulk modulus in the elastic region K_0 is linked to the bulk modulus of the compacted material A_1 via the initial porosity $\alpha_0 = \rho_c/\rho_0$.

$$A_1 = \frac{dp}{d\rho}\rho_c = K_0\ \alpha_0 \tag{5.33}$$

The elastic bulk modulus $K_0 = 17\,355\,\mathrm{MPa}$ and the associated bulk wave velocity $c_{B,0} = 2796\,\mathrm{m\,s^{-1}}$ in the elastic region ($\rho_0 = 2.22\,\mathrm{g\,cm^{-3}}$) are derived from the longitudinal wave velocity $c_{L,0} = 3751\,\mathrm{m\,s^{-1}}$ determined in the SHB tests (table 4.3, [Mosig et al., 2021]) together with an assumed Poisson ratio for the concrete of $\nu = 0.2$.

$$K_0 = \frac{E}{3-6\nu} = \frac{c_{L,0}^2\ \rho_0}{3-6\nu} = c_{B,0}^2\ \rho_0 \tag{5.34}$$

Comparing equations (5.33) and (5.34) with the approximation by equation (2.19), the bulk wave velocities of the compacted material $c_{B,c}$ and the porous material $c_{B,0}$ are proportional to the initial porosity α_0 in the implementation of the RHT model in LS-Dyna:

$$\frac{c_{B,c}^2}{c_{B,0}^2} = \alpha_0 \tag{5.35}$$

The crucial variable for fitting the EOS is therefore the initial porosity α_0 of the concrete, which determines the length of the compaction path and thus the amount of the dissipated energy.

In the following, a simple volume-based mixing rule is used to determine the initial porosity of the concrete. The corresponding proportions of the concrete are shown in table 5.3.

The calculation of the densities of the porous and compacted cement stone is based on experimental data of [Duric, 2018], who determined the densities of cement stone with

Table 5.3.: Components of the wet concrete (see appendix figure A.4)

	aggregates	water	cement	fly ash
mass [kg]	m_G =1888	m_W =137	m_Z =280	m_A =70
density $[kg.m^{-3}]$	ρ_G =2640	ρ_W =1000	ρ_Z =3100	ρ_A =2200
volume fraction [-]	v_G =0.76	v_W =0.13	v_Z =0.09	v_A =0.03

and without pores for different water/cement (w/c) ratios. For the present concrete with a w/c ratio of 0.49 (fly ash neglected), a porous density of $\rho_{ZS,0}$ =1552 kg m^{-3} and a density of the compacted matrix material of the cement stone without pores of $\rho_{ZS,c}$ =2633 kg m^{-3} are obtained. Thus, the densities of the porous concrete ρ_0 and the compacted concrete ρ_c can be calculated as follows:

$$\rho_0 = v_G\rho_G + v_A\rho_A + (v_Z + v_W)(\rho_{ZS,0} + 0.5\ \alpha_{ZS,0}\ \rho_W) \tag{5.36}$$

$$\rho_c = v_G\rho_G + v_A\rho_A + (v_Z + v_W)\rho_{ZS,c} \tag{5.37}$$

It is assumed that the compaction of the concrete takes place only within the cement stone and that the aggregate does not undergo any change in density. Furthermore, the volume fraction of cement stone in the hardened concrete is derived from the volume fractions of water and cement in the wet concrete. Analogous to [Gebbeken and Hartmann, 2010], it is assumed that 50 % of the pores in the hardened cement stone are filled with water and the initial porosity of the cement stone is given by:

$$\alpha_{ZS,0} = \left(1 - \frac{\rho_{ZS,0}}{\rho_{ZS,c}}\right) \tag{5.38}$$

Using the data from table 5.3, the density of the porous concrete is ρ_0 = 2422 kg m^{-3} and the density of the compacted concrete is ρ_c =2624 kg m^{-3}.

Comparing the calculated density of ρ_0 = 2422 kg m^{-3} with the experimentally measured density of the concrete in this test series ρ_0 = 2220 kg m^{-3}, it can be seen that the calculated density of the porous concrete is about 10 % too high. The author considers that the most likely cause of this discrepancy is a deviation in the density of the aggregate from the manufacturer's specifications. Therefore, the density of the aggregate is reduced so that the density of the porous concrete calculated by equation (5.36) matches with the corresponding experimentally measured density. The adjusted aggregate density of $\rho_G = 2350\,\mathrm{kg\,m^{-3}}$ is within the normative limits of $2000\,\mathrm{kg\,m^{-3}} \leq \rho_G \leq 3000\,\mathrm{kg\,m^{-3}}$ [Thienel, 2018] for a normal aggregate.

Using the resulting initial porosity of $\alpha_0 = 1.08$, the bulk wave velocity of the compacted concrete $c_{B,c}$ $=2905\,\mathrm{m\,s^{-1}}$ is calculated according to equations (5.35) and (5.34) to ensure that the slope of the EOS in the elastic region matches the elastic bulk modulus K_0 $=17\,355$ determined from the SHB tests (equation (5.34)).

The slope S $=1.38$ of the u_s-u_p relation is determined by a linear fit to the corresponding experimental measurements from the literature shown in figure 5.13. In agreement with [Neel, 2018] and [Hall et al., 1999] it is assumed that the concrete is fully compacted at a particle velocity of $u_p = 500\,\mathrm{m\,s^{-1}}$. With the density of the compacted concrete of ρ_c $=2406\,\mathrm{kg\,m^{-3}}$ this gives a compaction pressure of $p_c = 4308\,\mathrm{MPa}$ according to equation (2.4).

The regression line is then fitted to the experimental measurements with $u_p \geq 500\,\mathrm{m\,s^{-1}}$ and the determined bulk wave velocity of the compacted concrete $c_{B,c}$ $=2905\,\mathrm{m\,s^{-1}}$ as the u_s-axis intercept (see figure 5.13).

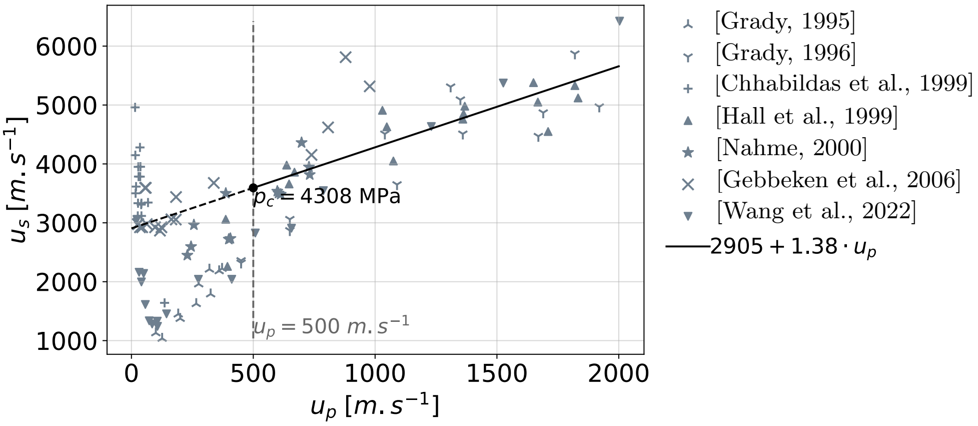

Figure 5.13.: u_s-u_p relations from literature including linear approximation for the employed calibration

Figure 5.14 shows the equations of state with default and fitted parameters in the $\rho/\rho_0 - p$ space, including experimental results from the literature.

The newly calibrated equation of state resembles the default equation of state of the

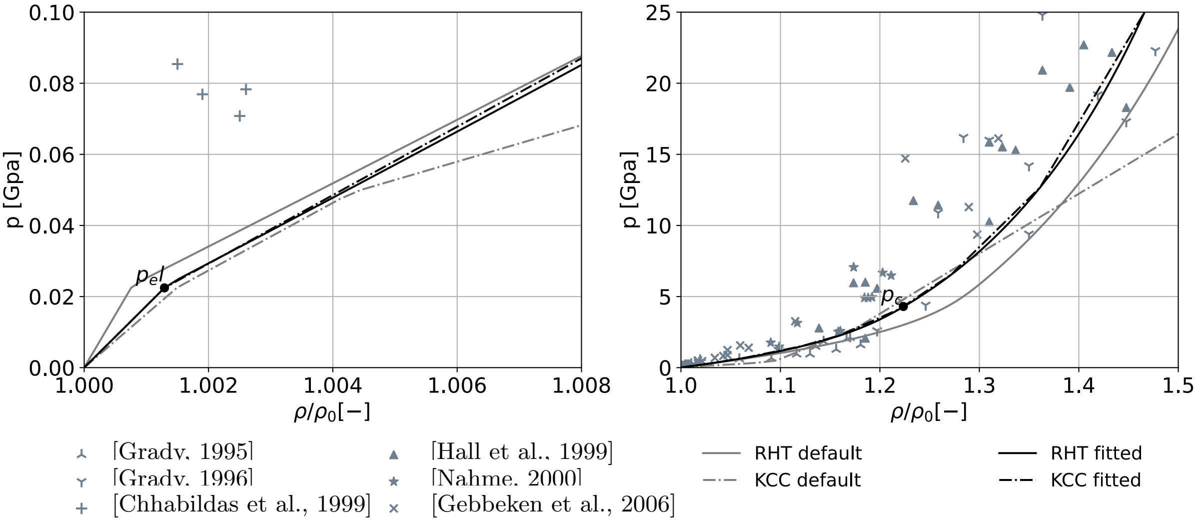

Figure 5.14.: Equation of state for RHT model and KCC model

KCC model up to a compaction of $\rho/\rho_0 = 1.004$. At high pressure, the shape is qualitatively similar to the default equation of state of the RHT model, with a slightly shorter compaction path. This results from the lower initial porosity α_0 compared to the default parameters, which is mainly due to the higher proportion of aggregates in the present concrete compared to that used to derive the default EOS. In addition, a mass-based mixing rule was used to derive the default parameters [Riedel, 2000], while a volume-based mixing rule is used in the present work, analogous to [Hartmann, 2009].

Compared to the default EOS, the newly calibrated EOS of the RHT model has a smaller slope in the elastic region of $K_0 = 17\,321\,\mathrm{MPa}$, which is in better agreement with the bulk elastic modulus of $K_0 = 17\,282\,\mathrm{MPa}$ calculated according to equation (5.34).

The KCC model uses a simple tabular description of the EOS which is included by *EOS_TABULATED_COMPACTION. For this, the pressures p and the bulk modulus K are each described by 10 discrete values as a function of the volumetric strain ε_V. The default EOS of the KCC model is only defined down to a volumetric strain of $\varepsilon_V = -0.21$. Below this compaction, the program linearly extrapolates the pressure with respect to the volumetric strain.

The p-ε_V relation for the following calculations are chosen so that the EOS of the KCC model is congruent with the EOS of the RHT model. In the absence of other information, the associated bulk modulus K is estimated from the derivative of the pressure p with respect to the volumetric strain ε_V, with a lower bound given by the elastic bulk modulus

K_0 according to equation (5.34):

$$K = -\frac{dp}{d\varepsilon_V} \geq K_0 \tag{5.39}$$

To account for the compaction of the concrete, the bulk modulus is linearly interpolated between the elastic limit and the onset of full compaction p_c. Figure 5.15 shows the resulting equation of state (left) and the associated bulk modulus (right) both as a function of the volumetric strain.

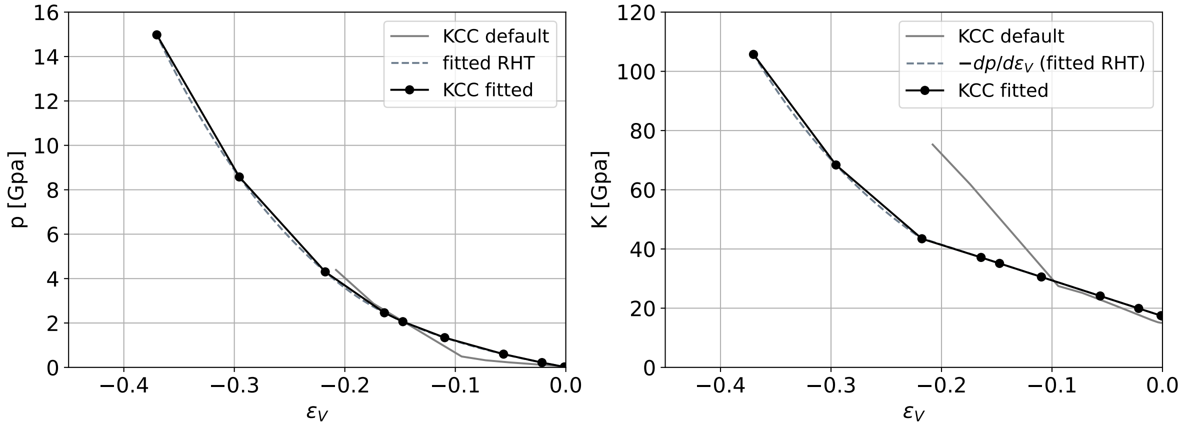

Figure 5.15.: Tabular equation of state (left) and bulk modulus (right) for the KCC model

To compare the assumed bulk modulus for the KCC model with the description of the RHT model, figure 5.16 shows the unloading path for both material models following different hydrostatic pressures (1.0 GPa - 6.0 GPa).

A significant difference between the two material models can be seen. In the KCC model, the bulk modulus and thus the remaining plastic volume change increases continuously with increasing pressure. While the plastic volume change at lower hydrostatic pressures (1.0 GPa, 2.0 GPa) from the RHT model is similar to the results from the KCC model, the behavior changes significantly at high hydrostatic pressures. Mainly due to the determined slope S of the u_s-u_p relation, the elastic capacity of the RHT model increases again with increasing compression, which is reflected in a smaller residual volume change after unloading. Although no experimental measurements are available to validate this behavior, it does not seem physically reasonable to the author, especially for concrete that has been fully compacted to the granular structure ($p \geq p_c$).

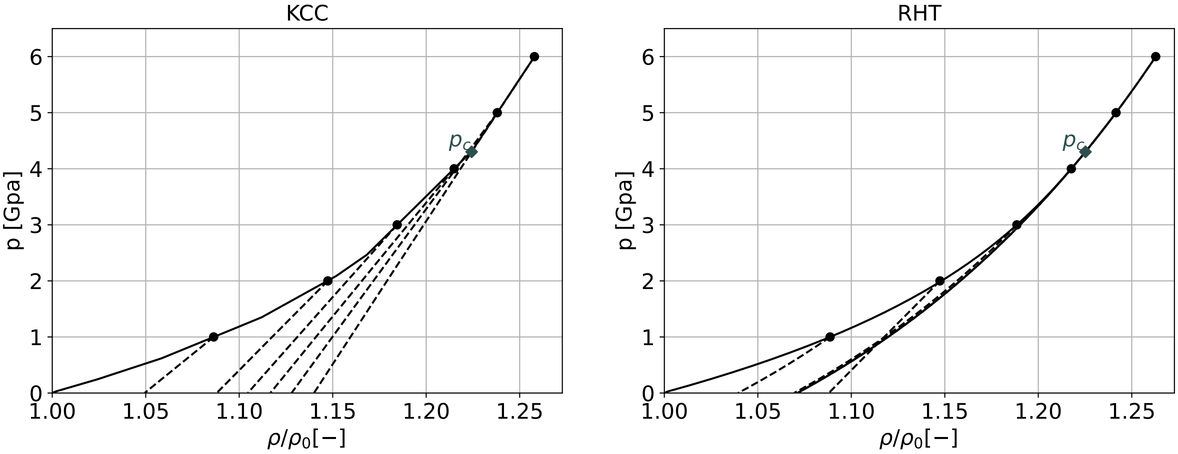

Figure 5.16.: Hydrostatic unloading KCC model (left) and RHT model (right)

Both material models have been calibrated to give a very similar representation of the concrete. A complete set of the input parameters for both material models can be found in the appendix section E

5.5. Reinforcing steel

The reinforcing steel is modeled using the simplified Johnson-Cook material model [Ls-dyna, 2021], [Johnson and Cook, 1983]. This material model is able to represent strain-rate dependent material behavior. In contrast to the original Johnson-Cook material model, thermal effects and damage are neglected. The resulting yield stress is calculated as:

$$\sigma = \left(A + B\varepsilon_{pl}^{n}\right)\left(1 + C\ln\frac{\dot{\varepsilon}}{\dot{\varepsilon}_0}\right) \tag{5.40}$$

In this ε_{pl}^{n} is the plastic strain, $\dot{\varepsilon}$ the strain rate and $\dot{\varepsilon}_0 = 1.0\,\mathrm{s}^{-1}$ the quasi-static threshold strain rate below which no strain adjustment is necessary.

Failure of the reinforcing steel could only be observed in very few experimental tests directly behind the explosive and is not considered relevant for the behavior of the secondary debris. Consequently a failure criterion is not included for the reinforcement to reduce the influence of eroded elements from the simulations.

The material parameters for the high ductility reinforcement steel B500B are taken from [Cadoni and Forni, 2015] and are shown in table 5.4.

Table 5.4.: Material parameters Johnson-Cook

A [MPa]	B [MPa]	n [-]	C [-]	ρ [g mm^{-3}]	E [MPa]	ν [-]
571	643	0.72	2.14×10^{-2}	7.85×10^{-3}	205×10^{3}	0.29

5.6. Numerical model

For the numerical simulation of the concrete structure, the symmetry of the test setup is utilized and only a quarter of the setup is modeled with symmetric boundary conditions. The L-shaped steel supports of the concrete slab are not modeled directly. Instead, the displacement of the nodes in the area of the supports is fixed in the direction perpendicular to the surface of the concrete slab.

The concrete structure is discretized using under-integrated Lagrangian hexahedral elements (ELFORM = 1). For the spatial discretization of the structure, fully integrated elements would allow a coarser discretization, but can also lead to a stiffer element behavior than under-integrated elements (shear locking). This is especially relevant in the context of the large deformations present in the simulations performed. Also, the computation time for fully integrated elements is much higher than for under-integrated elements [Lsdyna, 2019]. Since very fine meshing is required anyway to model the propagation of the shock front, under-integrated elements with constant stress are well suited to discretize the structure. To avoid non-physical hourglass deformations that can occur in under-integrated elements, Flanagan-Belytschko viscous damping (IHQ=3) is added.

The rebar is modeled using Hughes-Liu beam elements (ELFORM = 1) with a circular cross section. The coupling between the concrete and the rebar is defined by *CONSTRAINED_BEAM_IN_SOLID_PENALTY using the default penalty factor of 0.1.

The ALE domain for the explosive extends up to 500 mm from the symmetry planes in the directions perpendicular to the normal vector of the concrete surface (y- and z-direction). In the loading direction (x-direction), the ALE domain (air and explosive) overlaps with the the Lagrangian domain (concrete) by 100 mm. In the opposite direction, the ALE domain extends up to a distance of 200 mm from the loaded surface of the concrete slab.

The element size for the ALE domain of 2.5 mm is selected based on the convergence study in section 3.2. The resulting total momentum transmitted from the explosive to the structure is within 5 % of the estimated "exact" solution according to Richardsons extrapolation [Richardson and Gaunt, 1927].

The interaction between the explosive and the concrete structure is modeled using the penalty-based contact algorithm *ALE_STRUCTURED_FSI. The penalty factor is given by a linear description based on the suggestions of [Chen, 2020]. This description is defined by the origin (0,0) and the point $(0.1\, l_e,\, p_{max})$, where $l_e = 2.5\,\text{mm}$ is the element size of the ALE mesh and $p_{max} = 1.2 \times 10^4\,\text{MPa}$ is the maximum pressure determined by repeated calculations.

After 0.1 ms, the simulation of the explosive is terminated as there is no relevant interaction with the concrete structure afterwards. The lateral dimensions of the ALE domain include the entire expansion of the explosive along the surface of the concrete slab during this time.

Figure 5.17 shows an example of the numerical model for a 30 cm thick concrete slab loaded with 2000 g of explosive. To illustrate the rebar, parts of the concrete are blanked out.

5.6.1. Regularization of the fracture energy and spatial discretization

As described in section 5.2, different mesh sizes affect the concrete softening behavior described by the material model. To adjust the calibrated λ-η relation from the KCC model for an alternative element size, [Yin et al., 2023] gives a regularization method according to equation (5.41). This method scales the tensile softening part of the λ-η relation ($\lambda > \lambda_m$) for a given element size l_e depending on the calibrated element size l_e^{ref} (here $l_e^{ref} = 24\,\text{mm}$). A similar effect can be achieved by scaling λ_r in equation (5.27) with l_e/l_e^{ref}.

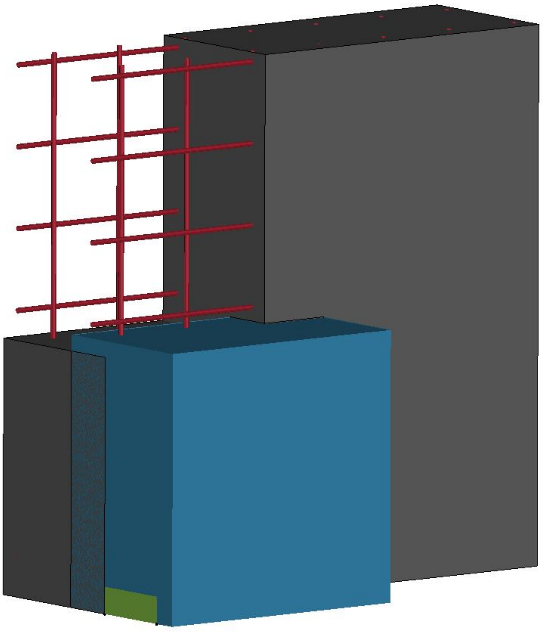

Figure 5.17.: Example of the numerical model for a 30 cm thick concrete slab loaded with 2000 g of SEMTEX10

$$\lambda_i^{l_e} = \begin{cases} \lambda_i & i \leq m \\ \lambda_m + (\lambda_i - \lambda_m)\, l_e / l_e^{ref} & i > m \end{cases} \tag{5.41}$$

As explained in section 5.2, the fracture energy is defined by the integral under the stress-strain relation multiplied by the size of the fracture process zone according to equation (2.38). To calculate the fracture energy dissipated by one element, the integral under the stress-strain relation is multiplied by the characteristic size of that element.

To compare the different regularization methods, figure 5.18 shows the resulting fracture energies dissipated by one element for different element sizes with and without regularization for both material models. The associated tensile stress-strain relations can be found in the appendix section G.3.

As can be seen in figure 5.18, the fracture energies of the two material models agree very well for different element sizes.

In case of the KCC model without fracture energy regularization, the fracture strain

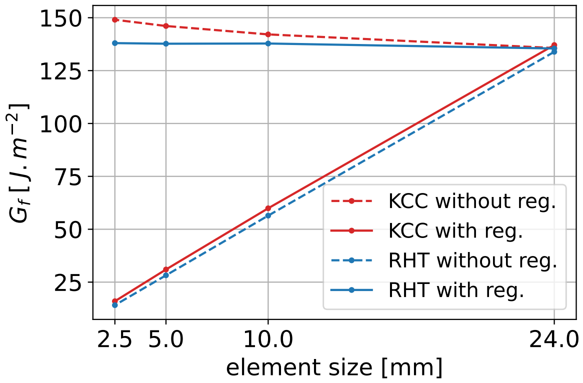

Figure 5.18.: Fracture energy dissipated by one element for different element sizes for the RHT model and the KCC model with and without regularization

increases with decreasing element size, so that the fracture energy of one element remains constant for the different element sizes. Therefore, the total fracture energy of a structure increases with a decreasing element size because multiple elements span the entire fracture process zone.

With fracture energy regularization according to equation (5.41), the stress-strain relation from the KCC model becomes independent of the element size. This ensures, that each element dissipates only the fracture energy associated with the region it represents, rather than the total fracture energy of the entire fracture process zone.

In case of the RHT model, the fracture energy regularization works exactly the opposite way. As explained in section 5.2, the minimum plastic strain in equation (5.21) dominates the tensile softening behavior and can therefore be used to calibrate the fracture energy. A constant failure strain leads to a decreasing fracture energy with decreasing element size. Consequently, a regularization of the fracture energy according to equation (5.23) leads to a constant fracture energy for different element sizes.

As discussed in section 5.2, the decision on which description is correct to describe the secondary debris depends on whether the numerical fracture localizes within a single layer of elements or distributes over the entire fracture process zone. To investigate the influence of the fracture energy regularization on the velocity of secondary debris, the x-velocity of the concrete at the protective surface of a 30 cm thick concrete slab loaded with 2000 g SEMTEX10 is compared below. The simulations are performed with different element sizes, both with and without fracture energy regularization for both material models.

To reduce the total number of elements, the respective mesh size is implemented only within the inner 500 mm from the center of the concrete slab in the directions normal to the symmetry surfaces. The concrete outside of this central region is not considered relevant for the simulation of the secondary debris, but is necessary to allow the different waves to propagate out of the relevant central region. Therefore, the mesh size in the outer region is continuously increased up to four times of the mesh size in the center. As a result, the fracture energy in this outer region is not correctly represented. The mesh size in the thickness direction of the concrete slab is kept constant throughout the whole concrete structure. The reinforcement was not included for this comparison of the influence of the fracture energy in order to avoid additional variables.

Figure 5.19 (left) shows the evolution of the maximum x-velocity with time at the center of the concrete slab for the KCC model. Figure 5.19 (right) shows the distribution of the x-velocity at 1.0 ms over the radial coordinate for the KCC model. To minimize the influence of boundary effects, the radial coordinate is defined along the diagonal of the numerical model. Both plots show the respective x-velocities for the different mesh sizes with (red) and without (blue) fracture energy regularization. Figure 5.20 shows the same information as figure 5.19 but from the simulations with the RHT model.

At this point, only the behavior of the two material models regarding the respective fracture energy regularization is examined. A comparison of the two material models and a discussion of the causes for the different velocities of the concrete at the protective surface is given in section 5.7.

From figures 5.19 and 5.20 (left) it can be seen that the initial x-velocity increase before 0.1 ms is not affected by either the element size or the fracture energy regularization. This initial x-velocity increase marks the arrival of the shock wave at the protective surface before any tensile damage has occurred due to the reflected tensile wave. Therefore, it is mainly influenced by the equation of state and less by the fracture properties of the material.

With the onset of tensile damage, the influence of the fracture energy becomes apparent in the further change in x-velocity with time. The influence of the fracture energy regularization is analogous to the single-element simulations in figure 5.18. In case of the KCC model the drop of the x-velocity after the initial peak is hardly affected by the

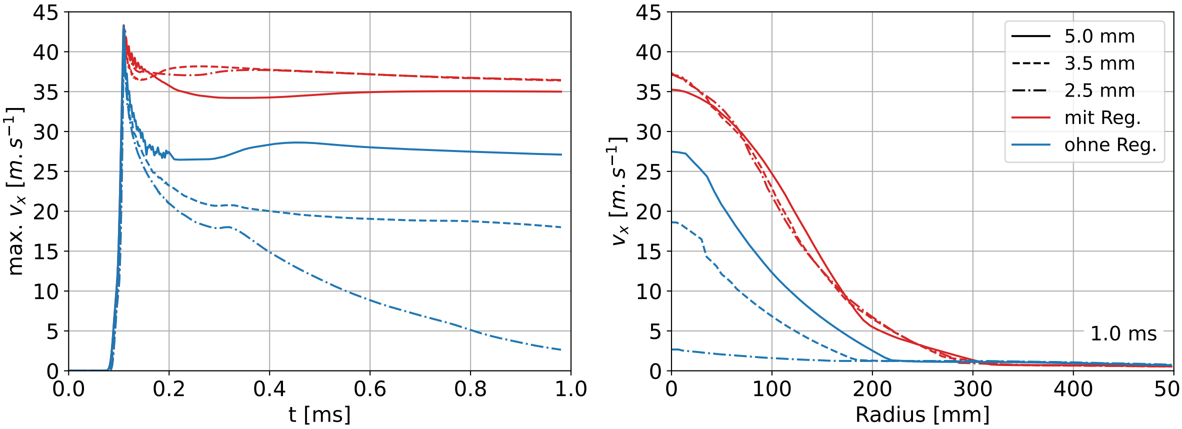

Figure 5.19.: KCC: Velocity at protective surface of concrete slab with (red) and without (blue) fracture energy regularization (T=30 cm, W=2000 g)

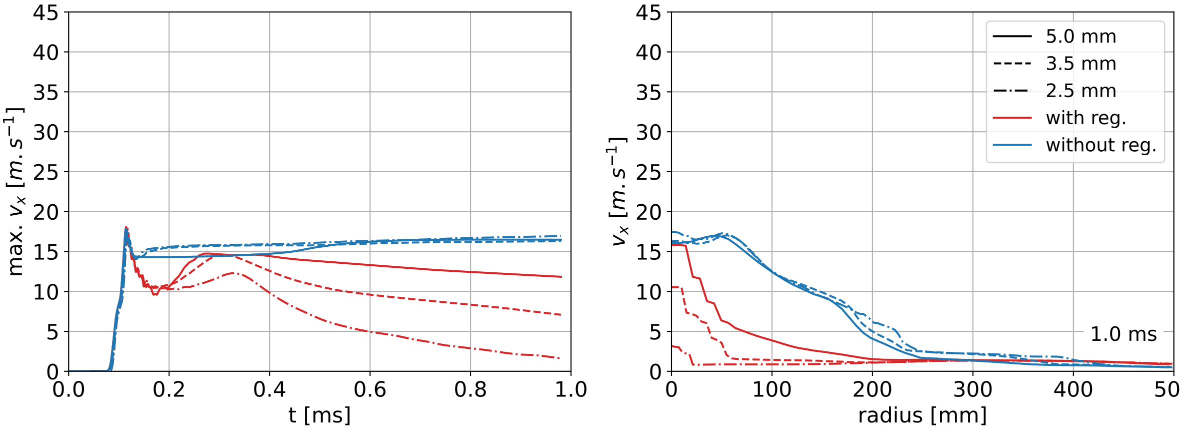

Figure 5.20.: RHT: Velocity at protective surface of concrete slab with (red) and without (blue) fracture energy regularization (T=30 cm, W=2000 g)

variation of the element size with the presented regularization. Without regularization the x-velocity drop increases with decreasing element size. Like in the single-element simulations its exactly the opposite way in the case of the RHT model.

In both material models, the variant that leads to a similar x-velocity for different element sizes is the one that distributes the fracture energy over the fracture process zone rather than localizing it within a single layer of elements (RHT without regularization, KCC with regularization). This shows that the energy dissipation during the fracture process relevant for spalling is not localized within a single element layer, but is distributed over a larger fracture process zone.

A possible explanation for this could be that, unlike a uniaxial tensile test where the stress is initially more or less uniformly distributed throughout the structure, the load from the reflected tensile wave is not as uniformly distributed. Therefore, the location of failure is more dependent on the shape of the tensile wave and localization to the weakest link is less likely.

Figures 5.19 and 5.20 (right) show that the influence of the fracture energy regularization is present over the entire radius of the spalling crater. Therefore, a correct calibration of the fracture energy is very important for the material model to reproduce the velocity of the secondary debris.

On average, refining the element size from 5.0 mm to 2.5 mm increases the required computation time by a factor of 13. This increase is similar for both material models, but the RHT model takes about 3.5 times longer for the simulation than the KCC model. The reason for this are probably the additional iterations required for the more complex definition of the EOS in the case of the RHT model.

The KCC model has some numerical problems that can lead to blow-ups of single elements mainly on the protective surface and especially when simulating tests without breach. The exact reason for these blow-ups could not be resolved, but it seems to be related to the oscillating softening behavior at higher strain rates (see section 5.3). It becomes more problematic for smaller element sizes and can be partially counteracted by reducing the timestep scale factor $tsfac$ or varying damping factors related to dynamic viscosity and hourglassing.

The following simulations are performed with a mesh size of 5.0 mmm for the concrete structure. For the KCC model with fracture energy regularization and for the RHT model without fracture energy regularization. Although this mesh size is required to adequately represent the propagation of the shock wave, it is already well below the minimum mesh size for which the assumption of homogenization of the material properties is valid according to [Bažant and Oh, 1983] (see section 5.2).

5.7. Simulation of the experimental tests

In the following, the simulations with both material models are compared with the experimental tests. The focus is on the geometry of the spalling crater and the velocity of the secondary debris.

In order to consider the different failure mechanisms, the evaluation is performed for two experimental constellations of concrete slab thickness and explosive mass. One with a breach in the concrete slab (20 cm, 1000 g) and one without a breach in the concrete slab (30 cm, 1000 g). The constellations are selected so that cut concrete slabs are available from the test series in order to compare the damage along the cross sections of the concrete slabs.

5.7.1. Test with a breach in the concrete slab (20 cm, 1000 g)

For the situation with a breach in the concrete slab, figure 5.21 shows the protective surface of a 20 cm thick reinforced concrete slab loaded by 1000 g of SEMTEX10 after 3.0 ms. On the left is the damage prediction of the RHT model, on the right the damage prediction of the KCC model and in the center an image of the HS recording from test SN142.

As explained in section 5.2, the damage parameter of the RHT model between 0 and 1 describes the interpolation between the maximum strength and the residual strength. The corresponding quantity in the KCC model is given by the associated damage parameter between 1 and 2. Therefore, when comparing the two material models, one must compare the damage parameter in the range between 0 and 1 from the RHT model with the damage parameter in the range between 1 and 2 from the KCC model.

The comparisons between the numerical simulations and the experimental tests refer

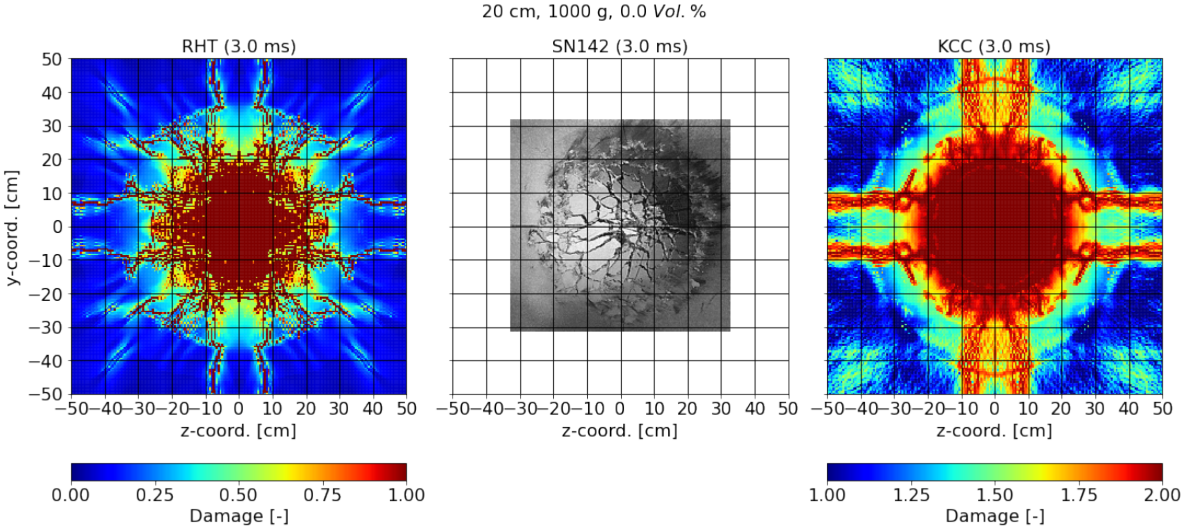

Figure 5.21.: Damage at the protective surface of the concrete slab, with a breach (T=20 cm, W=1000 g)

mainly to the fully damaged areas from the numerical simulations (dark red), as partially damaged concrete is difficult to identify visually in the experimental test.

Both material models describe a completely damaged area in the center of the reinforced concrete slab with ”cracks” propagating in radial direction. Note that the propagation of the ”cracks” in the numerical simulation is influenced by the layout of the spatial discretization, which in the presented cases is dominant in horizontal and vertical directions.

In both material models, the area with completely damaged concrete (dark red) has a diameter of about 40 cm, which is in good agreement with the experimental test. Outside the central region, the damage predicted by the KCC model is slightly greater than that predicted by the RHT model.

A representation of the crack pattern with individual fragments cannot be achieved with either material model. As explained earlier, modeling of the individual aggregates on the mesoscopic scale would improve the assumption of a homogenized material description for the required element size. As a result, a better representation of cracks with individual fragments is expected. For a 3D discretization of the investigated concrete slabs, an element size of ≤ 1.0 mm, which is the minimum requirement to model the individual aggregates, would result in an extremely large number of more than 10^8 elements. Such

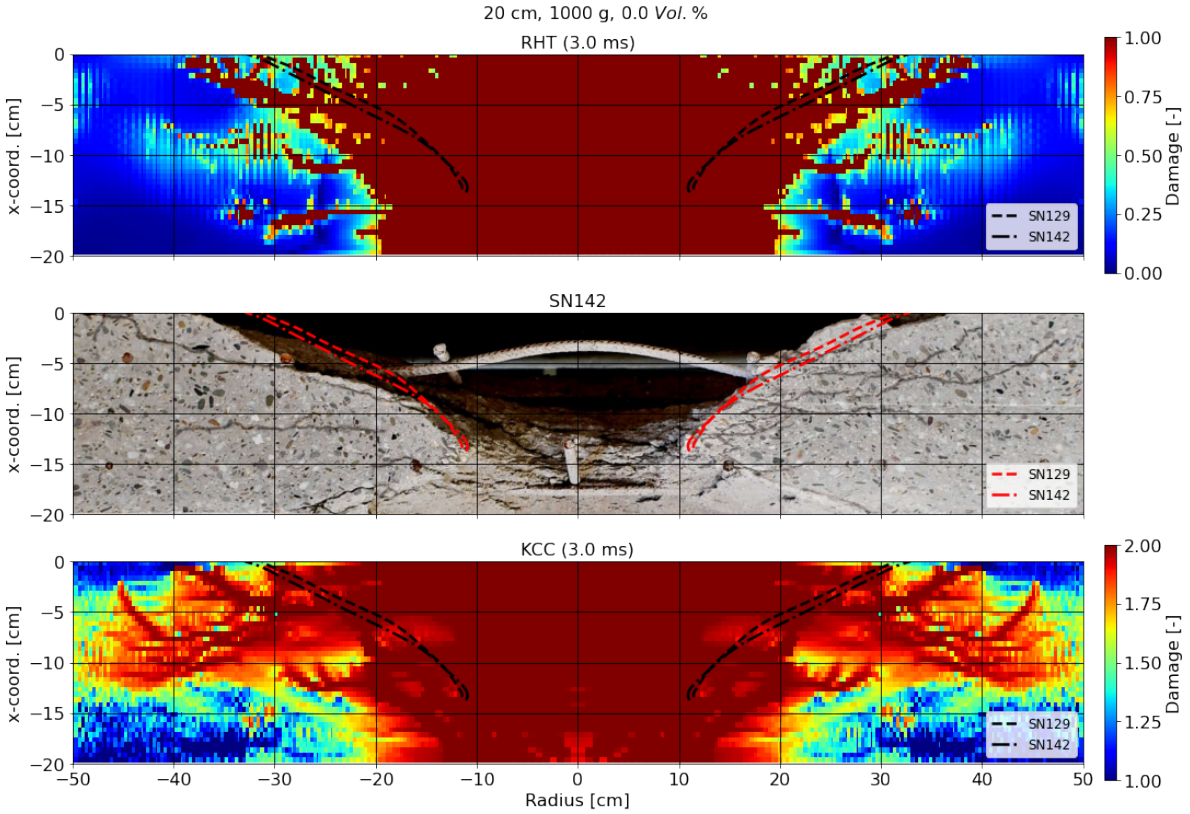

Figure 5.22.: Damage in the cross-section of the concrete slab, with breach (T=20 cm, W=1000 g)

simulations are therefore not feasible with the available IT infrastructure.

Figure 5.22 shows the damage in the cross-section of the reinforced concrete slab for the same constellation as in figure 5.21. On the top the RHT model, on the bottom the KCC model, and a photo of the cut reinforced concrete slab from test SN142 in the middle. The included lines show the rotationally symmetric approximated geometry of the spalling craters from both associated tests (see section 4.4.1). The damage plots from the numerical simulations represent a section along the main diagonal of the numerical model to minimize the influence of the boundary conditions along the symmetry borders.

The predicted damage from both material models is qualitatively similar with a completely damaged central region and ”cracks” propagating in radial directions. Especially in the region of the spalling crater ($x \geq -5.0\,\text{cm}$) corresponding cracks can also be found in the experimental test. In this region, the agreement with the experimental test is considered slightly better for the RHT model than for the KCC model.

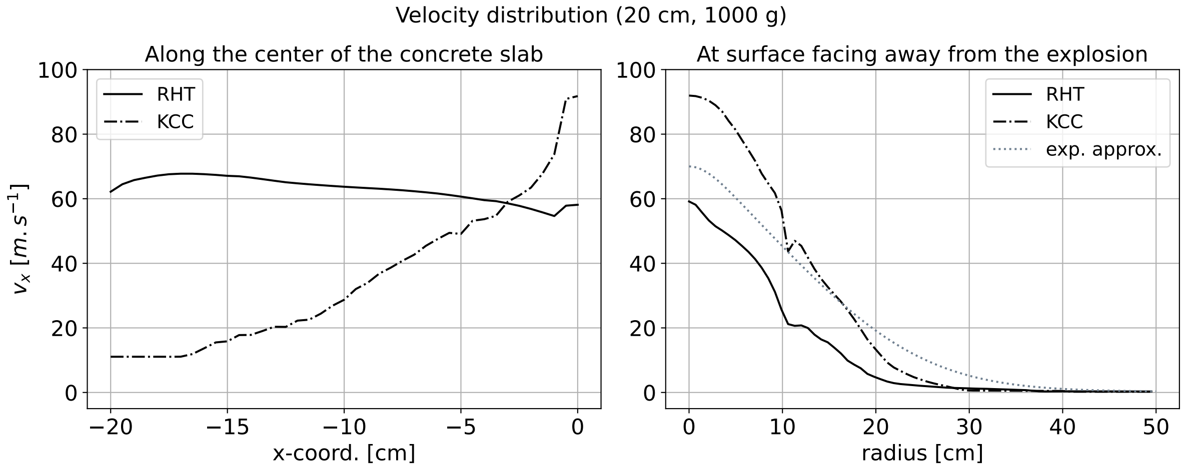

Figure 5.23.: Velocity distribution, with breach (T=20 cm, W=1000 g)

In the central region of the reinforced concrete slab ($-5.0\,\mathrm{cm} \geq x \geq -15.0\,\mathrm{cm}$), the damaged region is wider for both material models than in the experimental test. In this region the agreement with the experimental test is considered slightly better for the KCC model than for the RHT model.

To compare the x-velocity of the secondary debris calculated by the material models with the experimental test, figure 5.23 shows the spatial x-velocity distributions at the protective surface of the reinforced concrete in dependence on the radial coordinate (right) and the depth coordinate (x-coord.) along the center of the reinforced concrete slab (left).

The x-velocity distribution along the protective surface of the concrete slab (figure 5.23, right) from both material models qualitatively agrees with the experimental test. However, the x-velocity of the KCC model is too high, especially in the center of the concrete slab surface, and the velocity of the RHT model is too low.

The velocity distribution in the depth direction of the reinforced concrete slab (figure 5.23, left) differs significantly between the two material models. While the KCC model gives an approximately linear reduction of the x-velocity in the depth direction, the velocity distribution of the RHT model is almost constant over the thickness of the reinforced concrete slab.

The velocity distribution in the depth direction of the reinforced concrete slab cannot be measured experimentally. However, the depth of about 15 cm where the x-velocity

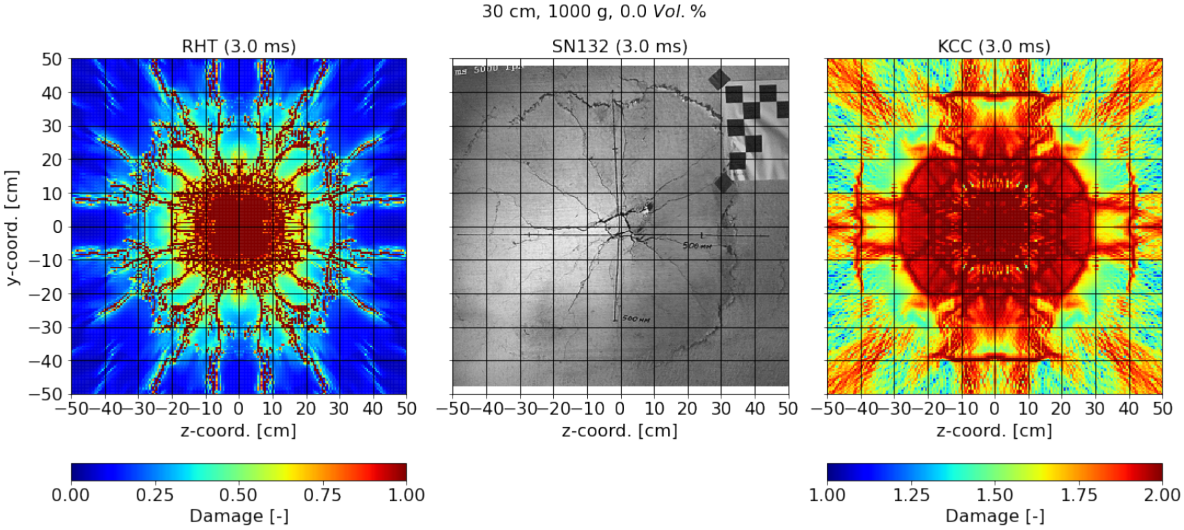

Figure 5.24.: Damage at the protective surface of the concrete slab, without breach (T=30 cm, W=1000 g)

in the KCC model reaches its minimum agrees well with the location of the breach (see figure 5.22). Therefore, the x-velocity distribution of the KCC model is qualitatively considered to give a better representation of the reality.

5.7.2. Test without a breach in the concrete slab (30 cm, 1000 g)

For the situation without a breach of the concrete slab, figure 5.24 shows the protective surface of a 30 cm thick reinforced concrete slab loaded by 1000 g of SEMTEX10 after 3.0 ms. On the left is the damage prediction of the RHT model, on the right the damage prediction of the KCC model and in the center an image of the HS recording from test SN131.

Similar to the situation with a breach, both material models describe a completely damaged region in the center of the concrete slab with "cracks" propagating in radial direction. An additional circumferential "crack" can be identified in case of both material models. This circumferential "crack" corresponds to the edge of the spalling crater in the experimental test. For both material models, the damage of the concrete at the surface is significantly more pronounced than in the experimental test. This is particularly relevant for the KCC model, which predicts partially damaged concrete along the entire surface of the concrete slab. In the experimental tests, relatively large fragments separated by individual radial cracks fly off from the concrete slab.

Figure 5.25 shows the damage in cross-section of the reinforced concrete slab for the same constellation as in figure 5.24. On top the RHT model, on the bottom the KCC model and in the middle a photo of the cut reinforced concrete slab from test SN131. The included lines show the rotational symmetric approximated geometry of the spalling craters from both associated tests (see section4.4.1).

Similar to the situation with a breach, both material models describe a severely damaged central region with "cracks" in radial direction. These radial "cracks" correspond well with the experimental test, especially in case of the RHT model in the region of the spalling crater.

In both material models there is no region with intact concrete between the spalling crater and the crushing crater. While the KCC model shows slightly less damage in the center of the concrete slab, the RHT model predicts completely damaged concrete over the entire thickness of the concrete slab.

As outlined in section 4.5.3, the structure of the visually intact concrete in the center of the reinforced concrete slab is damaged, although there is no breach. Therefore, the damage description of the KCC model is considered acceptable in the context of the tests performed. The RHT model is not capable to represent situations without a breach since it always predicts completely damaged concrete throughout the total thickness of the concrete slab.

To compare the secondary debris velocity from the numerical simulation with the experimental test, figure 5.26 shows the spatial x-velocity distribution at the protective surface of the reinforced concrete slab in dependence on the radial coordinate (right) and the depth coordinate (x-coord.) along the center of the reinforced concrete slab (left).

Similar to the situation with a breach, the spatial x-velocity distribution along the protective surface of the reinforced concrete slab (figure 5.26, right) qualitatively agrees with the experiment. While the maximum x-velocity in the center of the reinforced concrete slab according to the RHT model is almost identical to the experimental test, it is clearly too high in case of the KCC model.

Similar to the situation with a breach, the x-velocity according to the KCC model decreases in the direction of the depth of the reinforced concrete slab, while the RHT

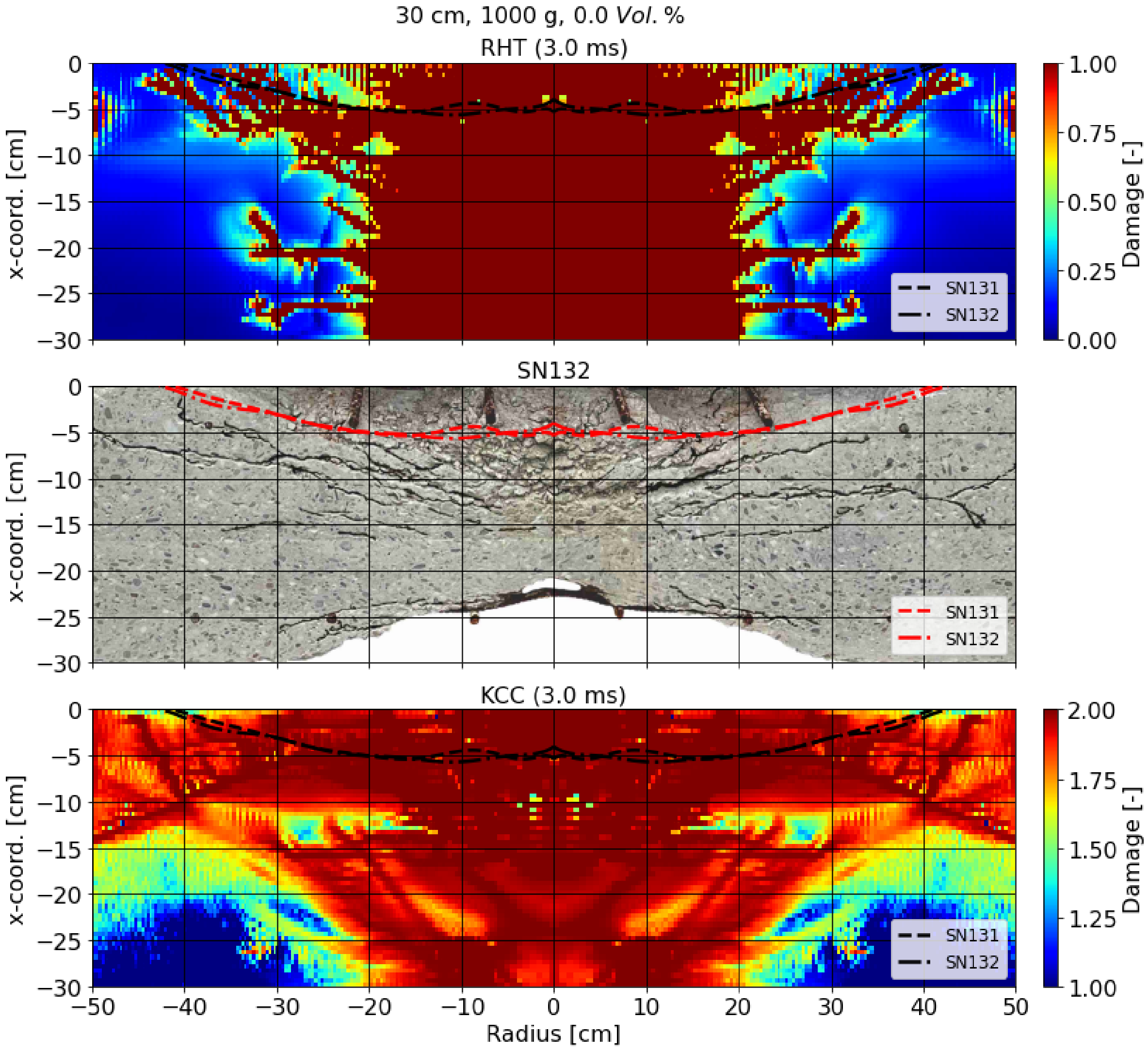

Figure 5.25.: Damage in the cross-section of the concrete slab, without breach (T=30 cm, W=1000 g)

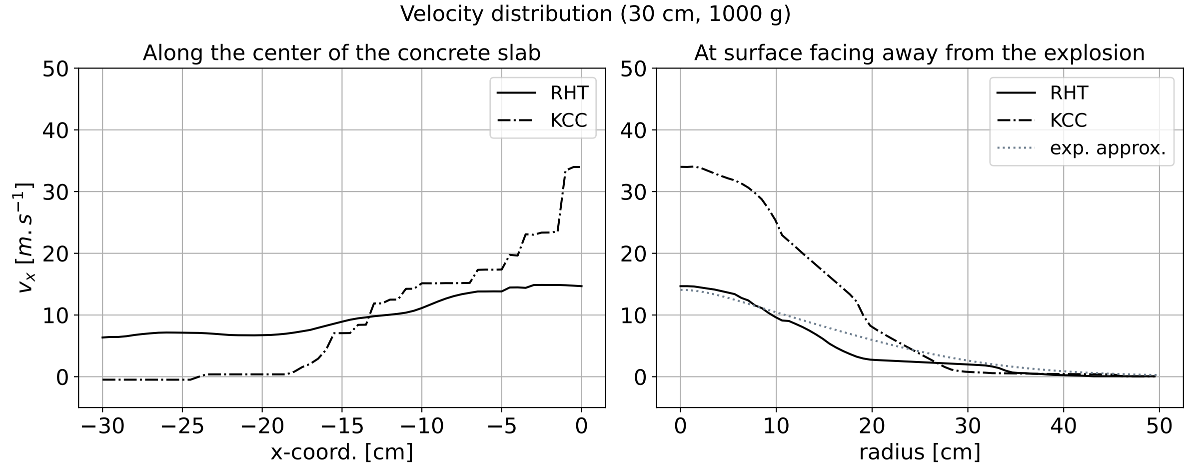

Figure 5.26.: Velocity distribution, with breach (T=30 cm, W=1000 g)

model gives a more constant x-velocity distribution. In case of the KCC model, a drop in x-velocity can be seen at approximately $x = -15.0\,\text{cm}$. This x-velocity drop corresponds with the depth in the reinforced concrete slab up to which damaged concrete can be detected in the cross section from the experimental test (figure 5.25).

5.7.3. Influence of the flow rule

An essential difference between the two material models is the direction of the plastic flow. While the RHT model uses a purely non-associative flow rule perpendicular to the hydrostatic axis, the KCC model allows the flow rule to be varied using the parameter ω. For this, $\omega = 0$ corresponds to a non-associative flow rule perpendicular to the hydrostatic axis (analogous to the RHT model) and $\omega = 1$ corresponds to a fully associative flow rule perpendicular to the current yield surface.

To investigate the influence of the flow rule on the simulated material behavior, figure 5.27 shows the spatial pressure distribution in the x-direction along the center of the reinforced concrete slab for different values of ω. The time step shown is chosen to show the situation just before the reflection of the pressure wave at the protective surface of the concrete slab. The analog result of the RHT model is shown as a blue line.

As can be seen in figure 5.27, the flow rule has a significant influence on the propagation of the pressure wave in the concrete. With a non-associative flow rule ($\omega = 1$), the KCC

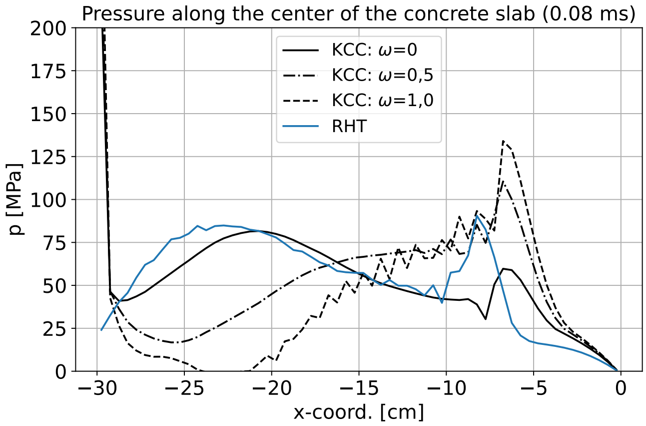

Figure 5.27.: Pressure distribution in the x-direction along the center of the reinforced concrete slab for different values of ω (T=30 cm, W=1000 g)

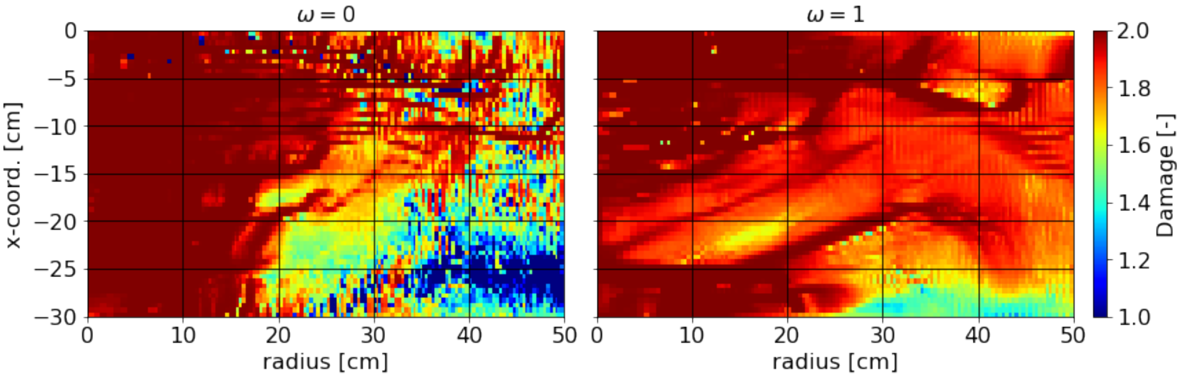

Figure 5.28.: Damage in the cross-section of the concrete slab from KCC model with $\omega = 0$ (left) and $\omega = 1$ (right)

model shows a pressure distribution that is very similar to the RHT model after the initial peak pressure. In this case, the pressure wave is characterized by an increasing pressure after the initial shock front. With increasing ω, the energy of the pressure wave shifts more towards the location of the shock front with a greater peak pressure and fast faster decay afterwards.

Since the tensile damage is a direct result of the reflection of this incoming compressive wave, the different shapes of these waves are expected to have a significant influence on the resulting damage. To investigate this influence, figure 5.28 shows the damage in the cross-section of the reinforced concrete slab from the KCC model for $\omega = 0$ (left) and $\omega = 1$ (right). The corresponding damage for $\omega = 0.5$ can be taken from figure 5.25.

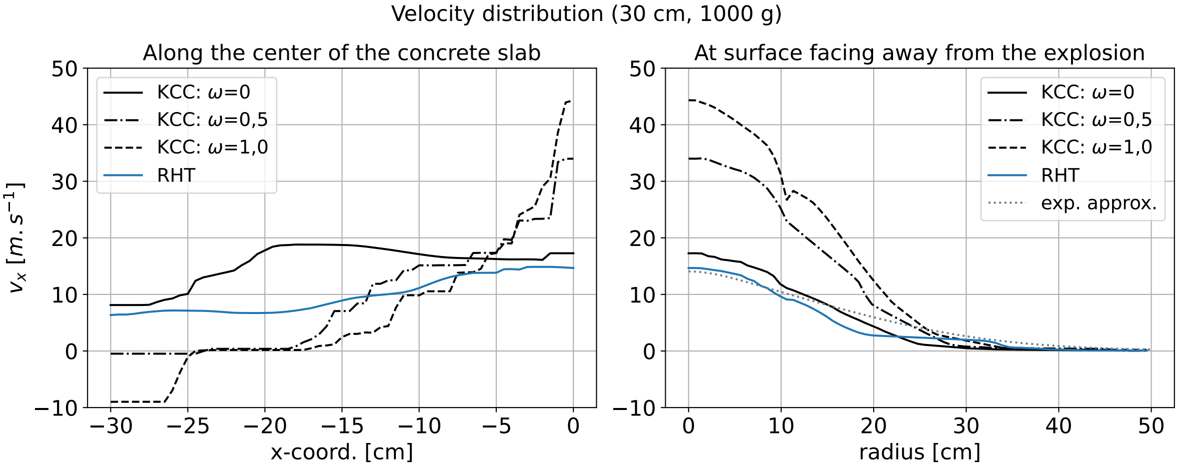

Figure 5.29.: Influence of the flow rule on the spatial x-velocity distribution (T=30 cm, W=1000 g)

Figure 5.28 shows that the damage of the concrete slab with the KCC model is more uniformly distributed across the cross-section with a non-associative flow rule ($\omega = 0$, left), similar to the RHT model. The damage, especially in the center of the concrete slab, occurs only after the arrival of the second pressure peak shown in figure 5.28. With an associative flow rule ($\omega = 1$, right), the damage is localized more along the surfaces of the concrete slab, which is in better agreement with the experimental test.

To investigate the influence of the flow rule on the spatial x-velocity distribution of the secondary debris, figure 5.29 shows the spatial x-velocity distribution in the depth direction (left) and along the protective concrete surface in radial direction (right).

The effect of the flow rule on the x-velocity is similar to that observed for the damage prediction. For $\omega = 1$, the x-velocity is more uniformly distributed across the cross-section of the reinforced concrete slab similar to the RHT model. As ω increases, the x-velocity distribution shifts toward the protective concrete surface resulting in a larger maximum x-velocity. Thus, the spatial x-velocity distribution along the protective concrete surface is in better agreement with the experimental test for $\omega = 0$, while this is the case for the damage of the reinforced concrete slab for $\omega = 1$.

To evaluate the influence of the flow rule on the strain rate of the concrete, figure 5.30 shows the strain rate along the protective surface of the concrete slab for the KCC model with different values of ω and the RHT model. The strain rate shown is evaluated along

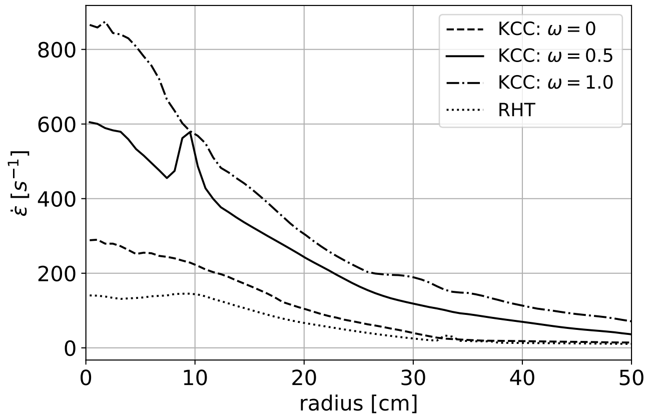

Figure 5.30.: Influence of the flow rule on the strain rate on the protective side of the concrete slab (T=30 cm, W=1000 g)

the diagonal of the protective surface of the concrete slab and has been averaged over the first five element layers (25 mm) in the depth direction. This region was chosen for averaging because it is representative of the estimated size of the fracture process zone. Within this region, the strain rate shows a strong variation in between different element layers, which is attributed to a localization of the strain. However, as discussed in section 5.6.1, this localization is not represented by the x-velocity.

As can be seen, the flow rule has a large influence on the strain rate at the protective surface. For a flow rule perpendicular to the hydrostatic axis (KCC: $\omega = 0$ and RHT), the maximum strain rate in the center of the protective surface is about $200\,\mathrm{s}^{-1}$. With increasing ω the strain rate increases continuously, resulting in a maximum strain rate of more than $800\,\mathrm{s}^{-1}$ for a fully associative flow rule perpendicular to the current yield surface. This range of the strain rate is consistent with data from [Riedel and Forquin, 2013] on the strain rate within the spalling region of a concrete slab subjected to a contact detonation.

Comparing the strain rate with the influence on the fracture energy discussed in section 5.6.1, it becomes apparent that the concrete behavior is influenced by the reduced fracture energy at high strain rates. This could be an explanation for the higher velocity from the numerical simulation when compared to the experimental tests.

Further investigation of the effect described in section 5.6.1 is necessary to make reliable statements about this relation. From an experimental point of view, DIC recordings of the protective surface with a much higher frame rate (compared to the presented tests) could help to gain a better understanding. Based on the numerical simulations, a frame rate of $> 10^5\,\mathrm{s}^{-1}$ is required to capture the initial velocity increase before $\sim 0.2\,\mathrm{ms}$, which can then be used to derive the actual strain rate of the concrete.

5.7.4. Influence of the strain rate

As described by [Ožbolt and Riedel, 2013], especially at high strain rates the influence of inertia on the macroscopic scale is the dominant influence on the strength increase of the concrete, leading to the second steeper part of the DIF in figure 5.10. According to [Ožbolt and Riedel, 2013], this strength increase should not be included into the constitutive model, but result from the dynamic analysis on the macroscopic scale.

The homogenized description of the concrete using the employed plasticity-based material models allows only for a limited consideration of the inertia effects on the macroscopic scale. However, it is unclear how much of the strength increase is already accounted for by the numerical model and how much needs to be accounted for by an additional DIF. Therefore, to investigate the influence of the strength increase at high strain rates, simulations are performed without the second steeper part of the DIF from figure 5.10.

Figure 5.31 shows the damage prediction of both material models for a 30 cm thick concrete slab loaded by 1000 g of SEMTEX10. The only difference to the simulation presented in section 5.7.2 is the missing steep part of the strength increase from figure 5.10.

Overall, the extension of the damaged region is similar to the simulation including the steep part of the strength increase. But, the predicted damage is much more localized in the simulations without the steep part of the strength increase, resulting in more individual "cracks" rather than a smeared damaged region. This becomes especially apparent from the damage plots of the protective concrete surface (figure 5.31, upper two images).

Figure 5.32 shows the resulting x-velocity distribution along the protective surface (right) and along the center of the concrete slab (left) for both material models with (gray) and without (black, mod.DIF) the steep part of the strength increase.

From figure 5.32 it can be seen that the influence of the DIF on the spatial x-velocity distribution is not as severe as for the damage prediction with only a slight increase of

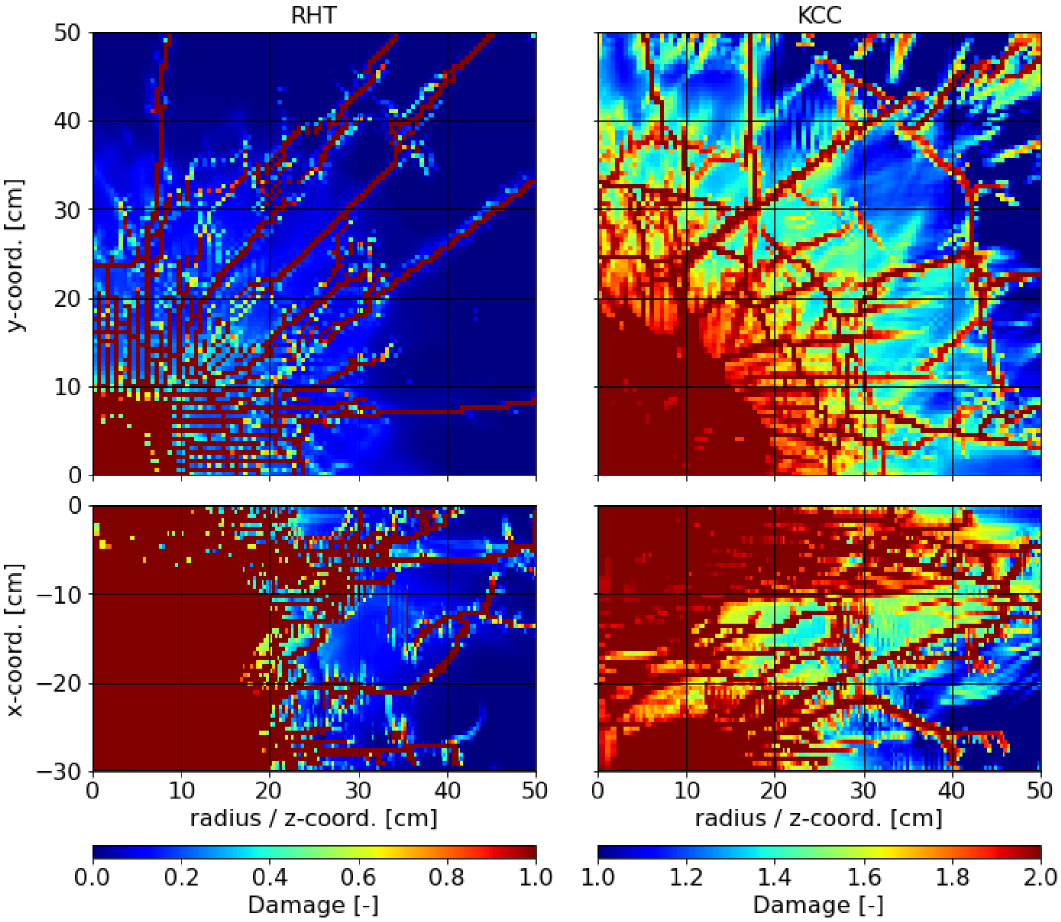

Figure 5.31.: Influence of DIF on the damage prediction (T=30 cm, W=1000 g)

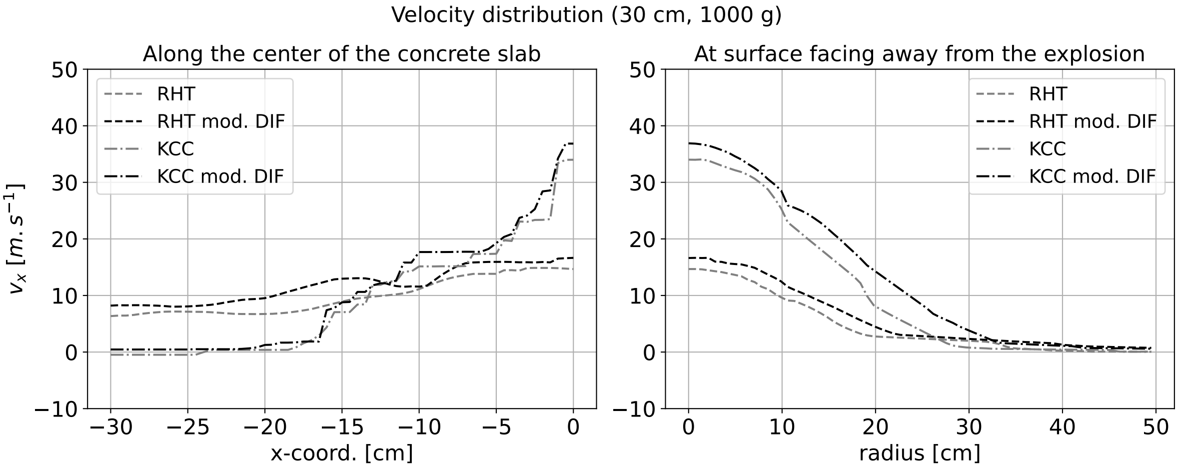

Figure 5.32.: Influence of DIF on the spatial x-velocity distribution (T=30 cm, W=1000 g)

the x-velocity over the whole region of the spalling crater.

Qualitatively, the simulations without the steep part of the strength increase are considered to be a better representation of reality. However, the realistic representation is probably somewhere in between these two extreme scenarios with a DIF that has a reduced slope in the second region. In addition, there is still the deviating behavior of the fracture energy described in section 5.6.1, which is considered to be the main reason for the overestimated velocity from the numerical simulation compared to the experimental tests. Therefore, further numerical and experimental research is required for a conclusive explanation.

5.7.5. Influence of element erosion

An often employed technique is to represent the damage of a structure due to explosive loading by eroding elements based on a selected failure criterion (e.g. [Xu and Lu, 2006], [Tu and Lu, 2009], [Hong et al., 2017], [Kong et al., 2018], [Wu et al., 2020], [Wang et al., 2021], [Yin et al., 2023]). This allows a geometrical representation of the damage and can avoid numerical problems due to large deformations. In addition, the erosion of elements creates new surfaces within the structure on which the existing waves can be reflected.

Although this practice has proven useful in representing experimental results, it is an irreversible process and the energy associated with the eroded elements is lost from the simulation. Therefore, erosion criteria must be carefully selected based on the simulated problem and with physics-based reasoning.

Most of the erosion criteria used are based on strain, stress or damage. Damage-based criteria probably have the best physical justification for the erosion of the associated elements because they directly reflect the behavior of the material as simulated by the material model. However, none of the investigated material models include a damage-based erosion criterion.

Stress-based criteria, such as a maximum tensile stress, provide a very simple criterion for the erosion of elements. However, since the elements are eroded once this maximum or minimum value is reached, the subsequent softening behavior and therefore the associated fracture energy are removed from the simulation.

Strain-based erosion criteria can be correlated quite well with physical processes and also include the softening behavior of the simulated material. However, like the softening behavior, strain-based erosion criteria are mesh dependent, which has to be considered when setting up a numerical model.

For the presented simulations, an erosion criterion based on the maximum principal strain is selected, since tensile failure is considered to be the most important mechanism for the secondary debris. This erosion criterion is implemented using the keyword *MAT_ADD_EROSION and the associated parameter MXEPS. The respective erosion strain for both material models is set to the fracture strain from the calibrated softening behavior due to uniaxial tension presented in section 5.2. This allows the fracture energy in tension to be correctly represented before the element is removed from the simulation. For the RHT model MXEPS $= 4.3 \times 10^{-3}$ (figure 5.6) and for the KCC model MXEPS $= 1.1 \times 10^{-2}$ (figure 5.9).

Figure 5.33 shows the damage predicted by the RHT model (left) and the KCC model (right) using the maximum principal strain as the erosion criterion. The black regions mark eroded elements.

The eroded elements in figure 5.33 correspond well with the locations where the concrete is completely damaged (KCC: damage=2.0, RHT damage=1.0). This indicates, that the selected erosion criterion is in principle suited to describe the occurring processes.

At the same time, the damaged region is much smaller than in the case without erosion, which is especially obvious in the case of the RHT model (see figures 5.24, 5.25). This effect is caused by the fact, that a significant amount of the explosive energy is already eroded during the interaction of the explosive with the concrete. Although the erosion criterion is a tensile strain, it is also relevant in the region of the crushing crater because Poisson related deformations due to compressive loading can result in tensile strains greater than the erosion limit. In addition, numerical oscillations due to the interaction of the material with the shock wave can lead to nonphysical tensile strains.

To quantify the influence of the erosion, figure 5.34 shows the total energy transferred from the explosive to the concrete slab on the left and the velocity at the protective surface of the concrete slab on the right. Here E_{tot} is the total energy and $E_{erod.}$ the eroded energy, both in the concrete part of the numerical model.

Figure 5.34 (left) shows, that the total energy transferred from the explosive to the

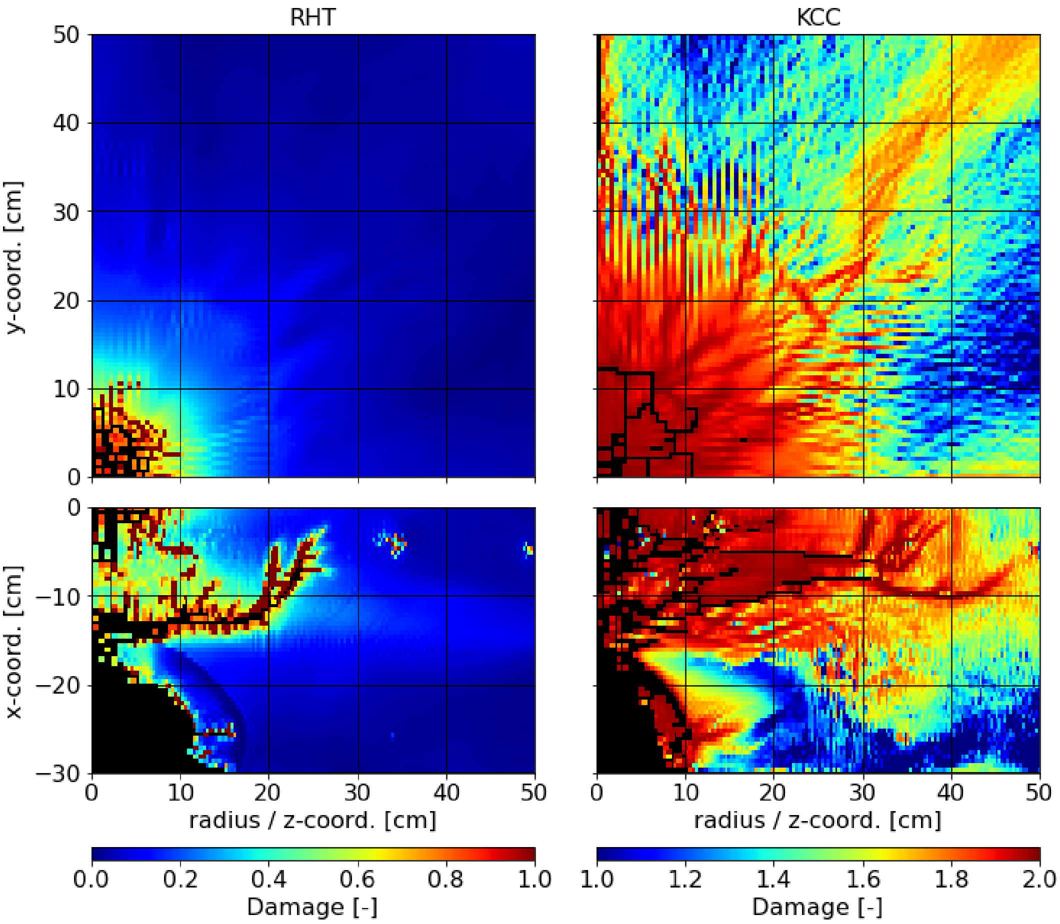

Figure 5.33.: Influence of erosion on predicted damage: RHT left and KCC right, (T=30 cm, W=1000 g)

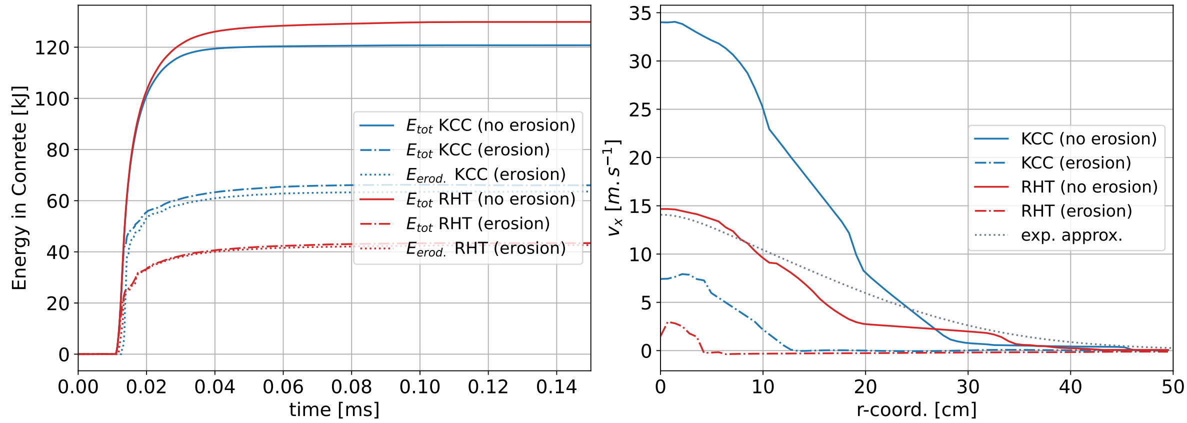

Figure 5.34.: Influence of erosion on the energy in the concrete (left) and the velocity at the protective surface of the concrete slab

concrete slab is reduced to 54 % in case of the KCC model and to 33 % in case of the RHT model compared to the simulation without erosion. About 99 % of this erosion occurs well before 0.02 ms. This shows, that the relevant erosion takes place during the interaction of the explosive with the concrete, since the arrival of the shock wave at the surface of the concrete slab facing away from the explosion is only at about 0.8 ms.

As a result, a considerable amount of the energy from the explosive is removed from the simulation before its interaction with the concrete is complete. This is also reflected by the x-velocity at the protective surface of the concrete slab, which is significantly reduced due to the erosion (figure 5.34, right).

It is concluded that erosion alters the simulation of a contact detonation too much to be considered representative of the experimental test. Alternative strain-based erosion criteria, such as the maximum shear strain, show a similar effect. Therefore, erosion should be avoided when simulating a contact detonation.

5.8. Summary

In this chapter, two well-established material models have been calibrated to provide a similar representation of concrete. In addition to the strength surfaces and the dynamic increase factor, this calibration includes the derivation of a new set of parameters for the equation of state using a volume-based mixing rule. It was found that the hydrostatic unloading from the RHT model, using the derived slope of the u_s-u_p relation, exhibits a behavior that is considered physically unreasonable.

The focus of the calibration is on the softening behavior and the associated fracture energy of the concrete, as it is a critical factor for the velocity of the secondary debris. In this context, identified problems of the softening behavior at high strain rates could not be solved within this work.

To investigate the influence of different mesh sizes and whether the fracture energy is localized within a single layer of element, a convergence study was performed regarding the x-velocity at the protective surface of the concrete slab. In contrast to uniaxial tensile tests, where the fracture energy usually localizes within a single layer of elements, a similar effect could not be observed with respect to the velocity of the secondary debris.

The determined mesh size necessary to describe the propagation of the shock wave in the concrete is well below the minimum mesh size for the assumption of a homogeneous material behavior according to [Bažant and Oh, 1983]. Simulations with discrete modeling of the individual aggregates could help to improve the underlying assumptions. However, due to the immense number of elements required for a three-dimensional discretization of the concrete slabs in this test series, this type of representation is not yet possible with the available IT infrastructure.

A comparison of the numerical simulations with the experimental tests showed that both material models can only predict the damage caused by a contact detonation to a limited extend. This is especially relevant in the case of situations without a breach in the concrete slab. Here, the KCC model does show a region with reduced damage in the center of the concrete slab, while the RHT model always predicts completely damaged concrete across the whole thickness of the concrete slab.

It was shown that the direction of the plastic flow (flow rule) has an important influence on the shape of the compressive wave inside the concrete and therefore the predicted damage as well as the velocity of the secondary debris. With increasing associativity of the flow rule, the damage and the velocity distribution shift more towards the protective surface of the concrete slab. This is considered to be a shortcoming of the RHT model, as it does not allow for variation of the flow rule analogous to the KCC model.

It was not possible to correctly represent the velocity of the secondary debris with the numerical simulations. In this context, the issues related to the softening behavior at high strain rates are considered to be an important factor. However, further investigations are required to provide a conclusive explanation. For this, additional experimental tests with a much higher frame rate for the DIC recordings of the protective surface fo the concrete slab could help to improve the understanding of the underlying mechanisms.

Since it is an often employed technique in the literature, the effect of erosion on the numerical results was analyzed. It was shown that already during the initial interaction of the explosive with the concrete, a large part of the induced energy is eroded from the simulation. Therefore, it is concluded that erosion should be avoided when simulating a contact detonation.

6. Impact of secondary debris

Based on the relationships derived in chapter 4, a demonstrator is presented below. This demonstrator estimates the spatial mass and velocity distributions of the secondary debris from the input variables for the concrete slab thickness, the explosive mass and the steel fiber content. The derived distributions can then be used to determine the impact of the secondary debris on people and technical installations on the protective side of a concrete slab.

6.1. Approximation of the secondary debris

The basis for the empirical demonstrator is the rotationally symmetric x-velocity distribution of the secondary debris introduced in chapter 4. To obtain a similar description for the dimensions of the spalling crater, characteristic points of the velocity distribution are used to approximate the associated geometry. These points are the outer diameter of the spalling crater r_s at a velocity of $1.0\,\mathrm{m\,s^{-1}}$ (with breach $2.0\,\mathrm{m\,s^{-1}}$) and the intersection of the spalling crater with the reinforcement layer at the location of the maximum curvature of the velocity distribution r_k.

A scaled thickness of $2.1\,\mathrm{g\,cm^{-1/3}}$ is used as the criterion for the occurrence of a breach. When a breach occurs, its position is defined by the depth of the crushing crater $t_c = 6.5\,\mathrm{cm}$. In cases without breach, the depth of the spalling crater is limited by the reinforcement layer on the protective side of the concrete slab ($c_v + 2d = 5.5\,\mathrm{cm}$, c_v: concrete cover, d: diameter of the reinforcement).

Figure 6.1 shows the different regions for the approximation of the spalling crater in the case of a breach.

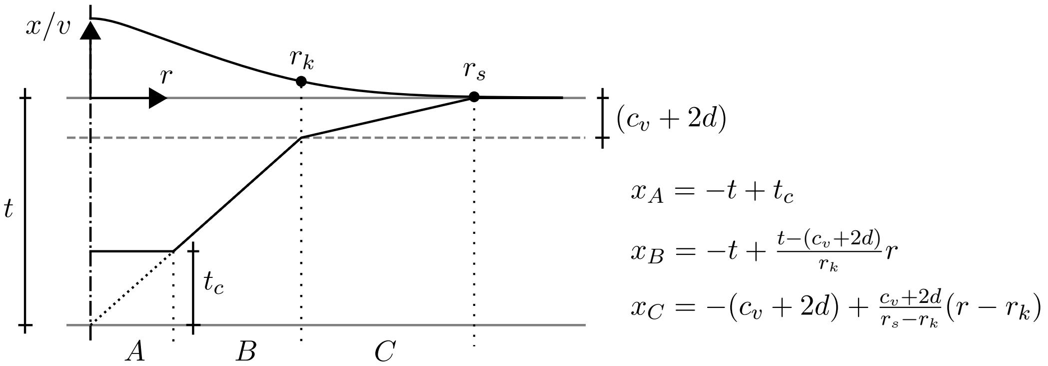

Figure 6.1.: Approximation of spalling crater with breach

Figure 6.2 shows the resulting approximated geometries of the spalling craters (black lines) without steel fibers, including the rotationally symmetric description of the experimental measurements (grey lines).

As can be seen in figure 6.2, the rotationally symmetric geometry of the spalling craters can be well represented using the introduced approximations. Only in the case of the test with a scaled thickness of $2.16\,\mathrm{g\,cm^{-1/3}}$, the region of the spalling crater below the reinforcement is not considered. However, as described in section 4.5.4, the concrete below the reinforcement in this test was initially retained by the reinforcement and only fell out after the test. It is therefore not relevant for the resulting secondary debris.

In order to make statements about the influence of steel fibers, the method described in section 4.9.2 is used to determine the influence of the steel fibers on the velocity distribution. The geometry of the spalling craters is determined analogously to the situation without steel fibers.

The geometry of the spalling crater is transformed into the third dimension by rotation and discretized by point masses with representative spacing. Since the size distribution of the secondary debris fragments can only be inferred to a limited extent from the experimental tests, the point masses are uniformly distributed with a spacing of 6.5 mm. This spacing assigns a mass to each discretization point that corresponds to the largest aggregate in the concrete. The effect of larger fragments is taken into account by summing the individual energies to evaluate the resulting impact.

The initial velocity of the point masses perpendicular to the surface of the concrete slab (x-axis) is defined on the basis of the approximated x-velocity distribution. Although

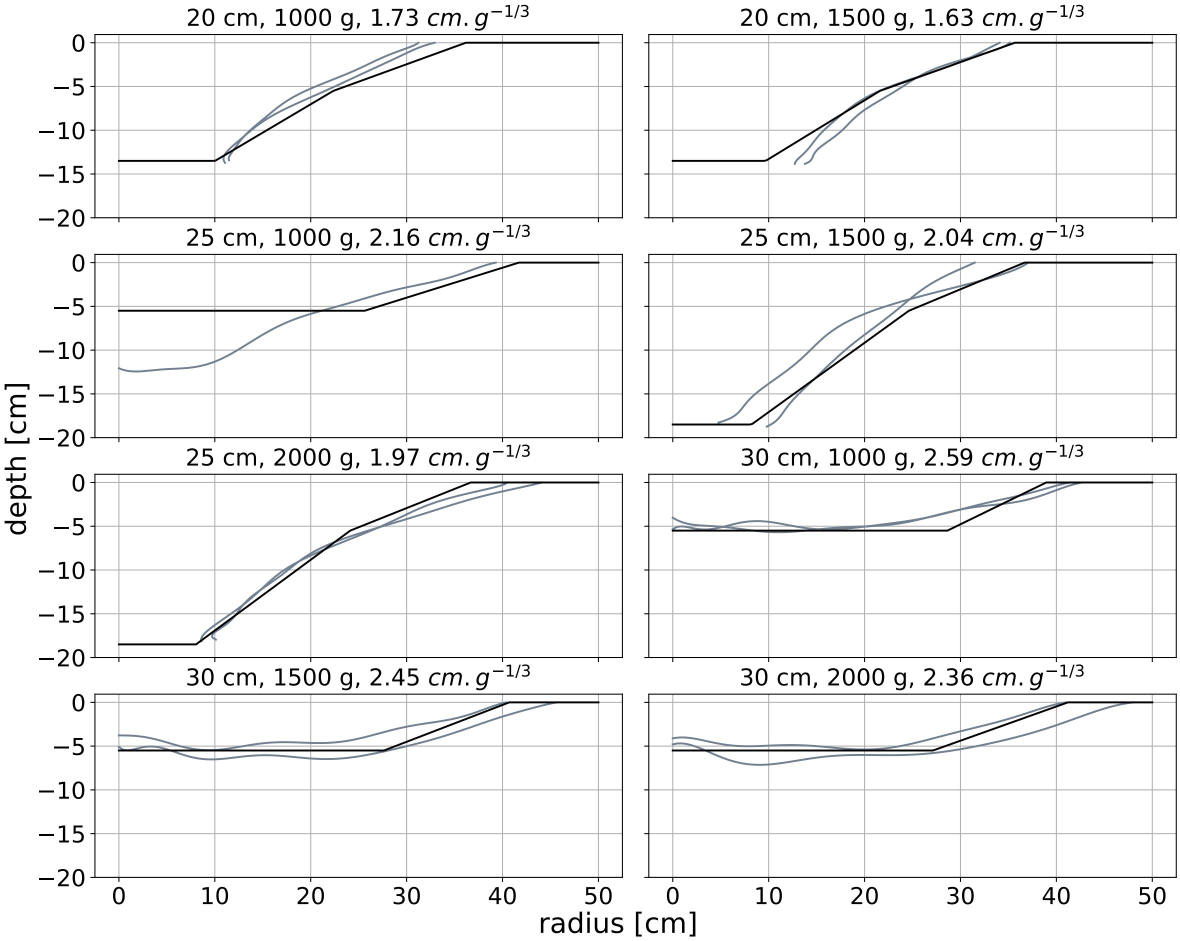

Figure 6.2.: Approximated geometries of the spalling craters (black lines), including the rotationally symmetric description of the experimental measurements (grey lines)

the numerical simulations suggest that the x-velocity decreases in the depth direction of the concrete slab, the exact characteristics of this could not be clearly determined. Therefore, for the empirical model of the demonstrator, a conservative assumption is made that the initial x-velocity of the point masses is constant in the depth direction of the concrete slab.

The initial radial velocity of the point masses is defined based on the relationship derived in section 4.6.1 with respect to the corresponding radial location and the x-velocity.

With the initial conditions defined, the trajectory of each point mass can be solved iteratively, taking into account gravity and neglecting air friction.

Figure 6.3 shows an exemplary comparison of the HS recording from test SN144 including the tracked points with the presented empirical model. Good agreement can be observed.

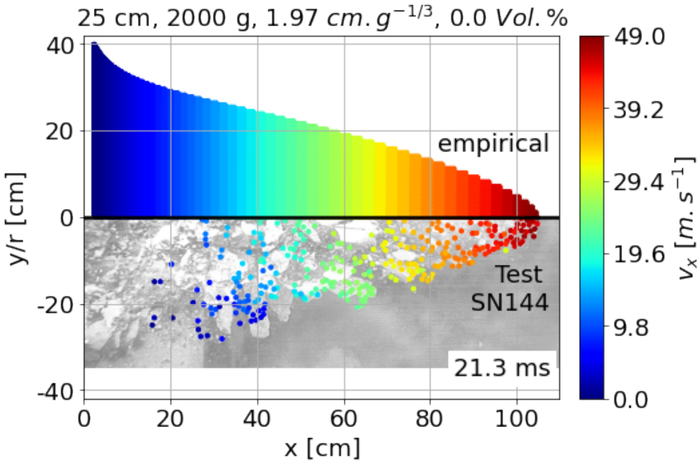

Figure 6.3.: Comparison of the empirical predictions with the experimental test SN144

6.2. Impact of secondary debris on people

An assessment of the impact of secondary debris on people on the protective side of a concrete slab is realized using a virtual witness panel. The witness panel stores the position, velocity and mass of each mass point at a defined distance from the protective surface of the concrete slab.

For the following evaluation, a grid size of the witness panel of 50 mm at a distance from the protective surface of the concrete slab of 1.0 m is selected. The stored values are then combined within each grid cell to derive the resulting impact. In addition to the kinetic energy, the probability of a lethal injury is of particular interest.

To determine the probability of a lethal injury from the impact of individual debris fragments, [Solomos et al., 2020] compares different models. It is important to note that due to the high complexity of the human body, these models can only provide rough approximations of possible injury scenarios. In reality, besides the parameters related to the impacting secondary debris fragment (mass, shape, velocity, ...), the point of impact on the human body is also of crucial importance. For example, an impact to the head is likely to result in significantly more severe injuries than an impact to the leg.

The simplest method for determining the effect of fragments on humans goes back to [Rohne, 1906] and describes that a person is incapacitated by the impact of a fragment with a kinetic energy greater than 80 J. This method does not specify the type of injury caused by the fragment, nor does it take into account the different geometries of the impacting fragments. Nevertheless, this reference value is still often used when assessing the impact of flying fragments on humans [Grisaro et al., 2021].

A more detailed empirical model has been developed by [Lewis et al., 1978]. This model uses complete penetration of the skin as the criterion for a dangerous injury. Based on experiments with goat skin, a logistic regression model (logit) was derived. This model uses the sigmoid function in equation (6.1) to map a continuous input parameter S to a probability distribution between the two binary states - suffering a lethal injury or not suffering a lethal injury.

$$P_L = \frac{1}{1 + e^{-Y}} \tag{6.1}$$

$$Y = -28.42 + 2.94 \ln S, \; S = \frac{mv^2}{A} \tag{6.2}$$

Where P_L is the probability of a lethal injury by complete penetration of the skin, m is the mass of a fragment in g, and v is the x-velocity at impact in m/s. The regression line Y was calibrated on tests without additional protective measures and with fragment masses of less than 5 g. As an additional parameter, the cross-sectional area A of the fragment is included in the calculation. For the present analysis, the concrete fragments are assumed to be spheres with radius r and a cross-sectional area of $A = r^2\pi$.

Another model for determining the impact of fragments on humans is given in the Greenbook [Roos, 1992]. This model is based on different injury scenarios depending on the mass of the fragment. Up to a fragment mass of 0.1 kg, the penetration of the fragment through the skin is decisive for the injury of a person. For fragments with a mass between 0.1 kg and 4.5 kg, the effect of internal organs being damaged by the kinetic impact energy even without complete penetration, is predominant. Above a fragment mass of 4.5 kg, a fracture of the skull due to the impact of the fragment on the head is decisive.

$$P_L = \frac{1}{(2\pi)^{1/2}} \int_{-\inf}^{Y} e^{-\frac{1}{2}(x-5)^2} dx \tag{6.3}$$

$$Y = \begin{cases} -29.15 + 2.1 \ln S & S = mv^{5.115} \quad 0.001\,\text{kg} \leq m < 0.1\,\text{kg} \\ -17.65 + 5.3 \ln S & S = \frac{1}{2}mv^2 \quad 0.1\,\text{kg} \leq m < 4.5\,\text{kg} \\ -13.19 + 10.54 \ln S & S = v \quad m > 4.5\,\text{kg} \end{cases} \tag{6.4}$$

The units for the mass m and the velocity v are kg and m/s. Unlike the model by [Lewis et al., 1978], the shape of the fragment is not taken into account.

The regression lines Y in equation (6.4) were fitted using a probit model [Solomos et al., 2020]. Analogous to the logistic regression model by Lewis, this allows the binary states - suffering a lethal injury (dead) or not suffering a lethal injury (alive) - to be associated with a continuous input variable S. Unlike the logistic distribution in equation 6.1, the probit model assumes that the probability of suffering a lethal injury is normal distributed with respect to the input variable S (mean = 5, standard deviation = 1).

To compare the two models, the underlying distributions are shown in figure 6.4. It can be seen that the cumulative standard normal distribution (CDF) in equation (6.3) describes the transition between the binary states (dead-alive) within a much smaller range than the logistic distribution (Sigmoid) in equation (6.1).

Figure 6.5 (right) shows the predictions of the two models for the probabilities of a lethal injury of $P_L = 0.01$ and $P_L = 0.99$ as a function of the fragment mass and the velocity at impact. The 80 J criterion according to [Rohne, 1906] is added as a blue line. To compare the influence of the two distributions, figure 6.5 (left) shows the probability of

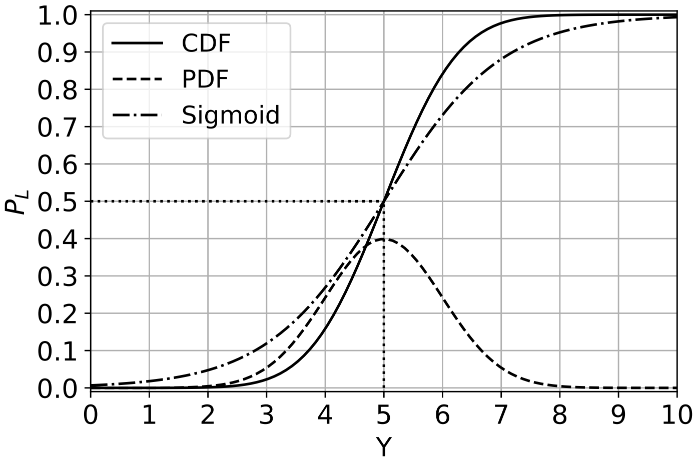

Figure 6.4.: Sigmoid function (Sigmoid), standard normal distribution (PDF), and cumulative standard normal distribution (CDF) around a mean of 5 to determine the probability of a lethal injury

a lethal injury as a function of the velocity at impact for a mass of 0.6 g corresponding to the largest aggregate ($D = 8$ mm) of the concrete.

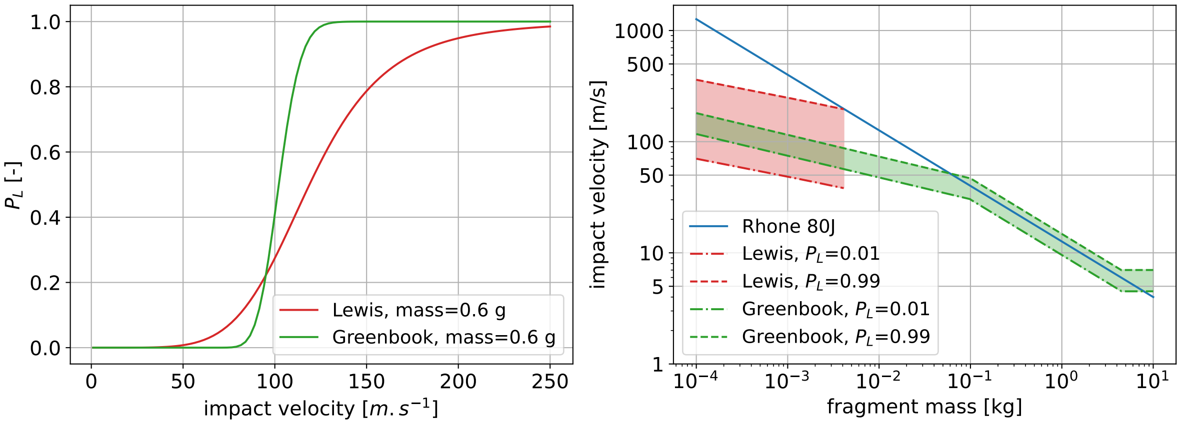

Figure 6.5.: Probability of a lethal injury according to the models of Lewis and the Greenbook as a function of the fragment mass and the velocity at impact (right) and for a fragment corresponding to the largest aggregate with a mass of 0.6 g as a function of impact velocity (left)

It is apparent that the 80 J criterion predicts a significantly higher velocity required for a lethal injury for fragment masses less than 0.1 kg compared to the models of [Lewis et al., 1978] and the Greenbook [Roos, 1992]. For fragment masses between 0.1 kg and 4.5 kg, the Greenbook model agrees very well with the 80 J criterion.

In the definition range of the Lewis model (fragment mass $< 5\,\mathrm{g}$), the predictions of the Lewis model and the Greenbook model are very similar. However, as described earlier, the assumption of a standard normal distribution in the Greenbook model results in a much narrower range of impact velocities for the transition of the probability of a lethal injury (figure 6.5, left) than with the logistic distribution in the Lewis model.

The probability of a lethal injury described by the two models refers to a single fragment. The probabilities of a lethal injury for each fragment are statistically independent of each other. Therefore, the associated total probability P_L of n fragments within a cell of the witness panel can be calculated by multiplying the individual inverse probabilities $(1 - P_{L,i})$ [Janser, 1982].

$$P_L = 1 - \prod_{i=1}^{n}(1 - P_{L,i}) \tag{6.5}$$

Figure 6.6 shows the virtual witness panel at a distance of 100 cm from the protective surface of a 25 cm thick concrete slab without steel fibers, which was loaded with 2000 g Semtex10 ($L/D = 1.4$). The specific kinetic energy (left) is determined by adding the individual energies of the point masses (0.6 g) within each cell of the witness panel and then dividing by the cell size of $(50\,\mathrm{mm})^2$. The probability of a lethal injury is calculated from the individual energies according to Lewis (equation (6.1) and subsequent combination within each cell of the witness panel according to equation 6.5.

Figure 6.6 shows that the impact of the secondary debris is strongly localized in the area behind the reinforced concrete slab. With a maximum in the center just behind the explosive charge and a rapid decrease in the radial direction.

To compare the two models in terms of the probability of a lethal injury as a function of the the fragment size, figure 6.7 shows horizontal sections through the respective witness panels ($y = 0$) for fragment masses of 0.6 g and 277.5 g. The fragment mass of 0.6 g corresponds to the size of the largest aggregate in the concrete and the fragment mass of 277.5 g represents fragments with a size corresponding to the depth of the reinforcement layer ($\approx$5 cm). Note that the fragment mass of 277.5 g is outside the definition range of the Lewis model.

Due to the discrete distribution of the individual mass points and their large mutual distances (277.5 g: 50 mm) compared to the cell size of the witness panel $(50\,\mathrm{mm})^2$,

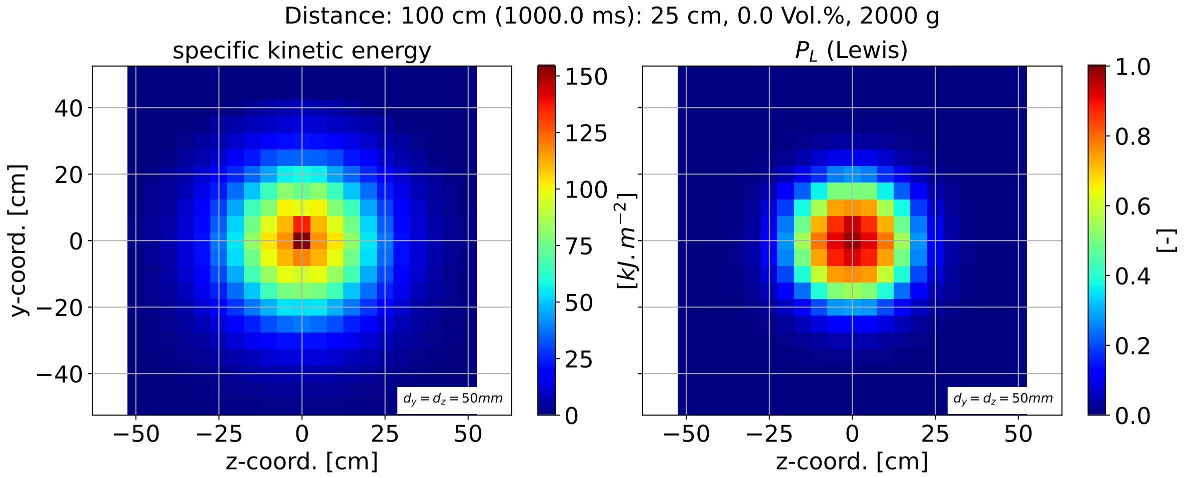

Figure 6.6.: Virtual witness panel at a distance of 100 cm behind a 25 cm thick reinforced concrete slab without steel fibers loaded with 2000 g Semtex10 ($L/D = 1.4$): specific kinetic energy (left) and probability of a lethal injury according to Lewis (right)

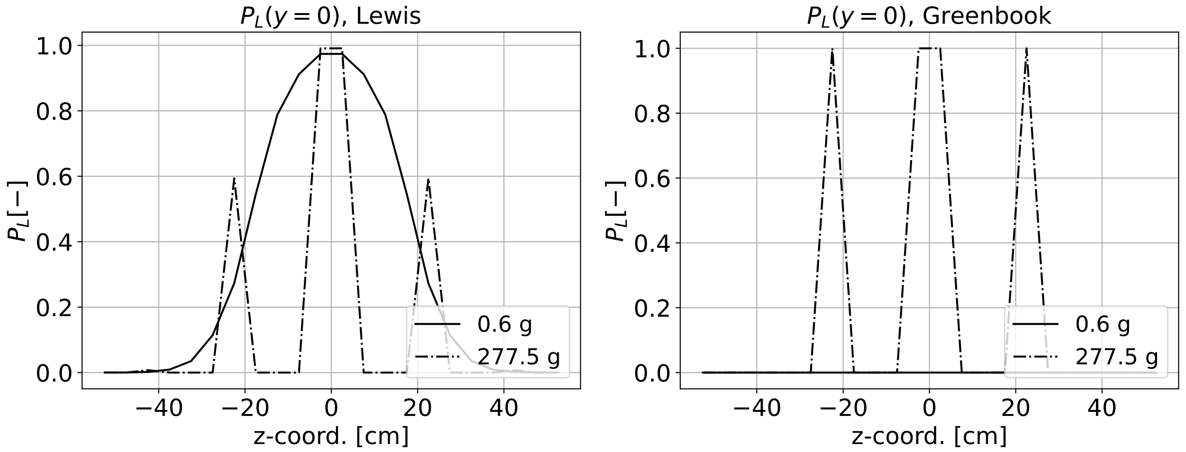

Figure 6.7.: Influence of fragment mass on the probability of a lethal injury: Lewis (left), Greenbook (right)

the probability for fragment masses of 277.5 g jumps between zero and the respective probability value. However, for a statement about the resulting hazard an enveloping curve is considered to be decisive.

Comparing the two models for a mass of 0.6 g again shows the influence of the different distribution functions. For the maximum velocity of the examined constellation of $50\,\mathrm{m\,s^{-1}}$, it can be seen in figure 6.5 (left) that the probability of a lethal injury from a fragment with a mass of 0.6 g is still equal to $P_L = 0$ in the Greenbook model, while the Lewis model predicts a low probability. The combination of the different fragments within the cells of the witness panel thus already leads to a relevant hazard in the Lewis model, while the Greenbook model does not yet predict any hazard.

The fastest fragments originate from a highly fragmented region in the center of the spalling crater. While the slower fragments in the outer regions of the spalling crater increase continuously in size without a breach (figure 4.23), with a breach 50 % the fragments are smaller than 10 mm (figure 4.17). Consequently, smaller fragment masses are decisive in the center of the spalling crater and larger fragment masses are decisive at the edges. However, for a conservative prediction of the resulting hazard, an enveloping curve of different fragment masses is best suited.

6.3. Summary

Based on the experimental results of the test series, a demonstrator was developed. This demonstrator allows conclusions to be drawn about the impact of secondary debris on objects and people on the protective side of a reinforced concrete slab, depending on the thickness of the concrete slab, the mass of the explosive, and the steel fiber content.

To assess the hazard of the secondary debris, two different models for determining the probability of a lethal injury were compared. It was shown that the impact of the secondary debris is strongly localized on the protective side of the concrete slab. With a maximum in the center just behind the explosive charge and a rapid decrease in the radial direction. Statements about the impact on humans are highly dependent on the underlying assumption of the probability distribution of a lethal injury from an impacting fragment.

7. Discussion

7.1. Summary

While there is a large quantity of research on the damage of concrete structures caused by explosive loading, the resulting secondary debris is an issue that has been rarely considered. The most important quantities in this context are the spatial mass and velocity distributions of the secondary debris, which can be used to make statements about the impact of the secondary debris on people and technical installations. In addition, an analysis of the preceding fragmentation can help to gain a better understanding of the underlying physical mechanisms.

This work addresses the topic of the secondary debris that results from a concrete slab loaded by a contact detonation. The basis for this research is an extensive test series that has been conducted together with the TNO in the Hague. A new test setup was developed for this purpose, which enables a detailed analysis of the protective side of the concrete slab regarding the fragmentation of the concrete as well as the resulting secondary debris. The evaluation of this test series in chapter 4 was compared to numerical simulations in chapter 5 and used for statements about the impact of the secondary debris in chapter 6.

After a brief introduction to the **theoretical background** in chapter 2, the influence of the **length to diameter ratio** of the cylindrical charges on the resulting load was investigated in chapter 3 using numerical simulations. Information about this influence allows a systematic evaluation of the concrete slab response based on the actual load rather than just the the explosive mass. The explosive mass, including the influence of the length to diameter ratio of the cylindrical charges, was used to scale the thickness of the concrete slabs. This **scaled thickness** showed to be a well suited parameter for the evaluation of the experimental tests in chapter 4.

The evaluation of the **spalling crater geometry** was performed using a rotationally symmetric approximation of the point clouds derived from 3D scans of the concrete slabs. This procedure unifies the irregular geometry of the spalling craters and allows a better comparison between different tests. It has been shown that the diameter of the spalling crater is more dependent on the thickness of the concrete slab, while the explosive mass is more decisive for the depth of the spalling crater. In this context, a **threshold for the occurrence of a breach** based on the scaled thickness of the concrete slab has been derived from the experimental tests and shows good agreement with similar tests from the literature.

The **position of the rebar** relative to the protective surface has an important influence on the secondary debris. Although the region of damaged concrete extends well below the rebar layer, especially in tests without a breach, most of the concrete from below the rebar was retained and is therefore not part of the resulting secondary debris.

A tracking algorithm was applied to the HS recordings from the protective side of the concrete slab, to determine the **velocity and the trajectory of the secondary debris**. The maximum velocity of the secondary debris shows a linear correlation with the scaled thickness of the concrete slabs, taking into account the influence of the length to diameter ratio of the cylindrical charges. Overall, the trajectory of the secondary debris is dominant in the direction perpendicular to the surface of the concrete slab, with the majority of the secondary debris moving at an angle of less than 20° relative to this dominant direction.

For a more detailed analysis, the **spatial velocity distribution** was approximated by a rotationally symmetric description. To validate this approximated velocity distribution, it was compared with the fracture process as well as with DIC measurements of the protective surface, showing a satisfactory agreement.

The **kinetic energy** of the secondary debris was derived from the rotationally symmetric descriptions of the spalling crater geometry and the spatial velocity distribution. The information about the kinetic energy of the secondary debris can help to make better informed statements about the impact of the secondary debris, but also allows a quantitative evaluation of reinforcing measures such as steel fibers in the concrete.

In the experimental tests involving **steel fiber reinforced concrete**, the kinetic energy of the secondary debris was continuously reduced, reaching a reduction of about 90 %

with a steel fiber content of 1.0 Vol %. A further increase of the steel fiber content up to 2.0 Vol % did not show a similar reduction. This is due to the fact that a further reduction beyond 90 % is difficult to achieve, but can also be attributed to an increasingly uneven distribution of the steel fibers in the concrete with increasing steel fiber content.

It has been shown, that **retrofit layers** of steel fiber reinforced concrete can achieve a similar reduction of the secondary debris as fully steel fiber reinforced concrete slabs. However, the identified failure mechanism suggests that the retrofit layer will fail less ductile than a fully steel fiber reinforced concrete slab. Furthermore, due to the increased concrete cover of the rebar in the case of a retrofit layer, it is expected that more secondary debris will be generated upon the failure of the retrofit layer, albeit at a lower x-velocity than in the unreinforced case.

To support the evaluation of the experimental tests, **numerical simulations** were compared with the experimental measurements. For this purpose, two well-established material models were calibrated to provide a similar description of the concrete. The intention was to gain insight into the quality of the predictions by comparing the differences between both material models, and thus to distinguish real physical effects from numerical artifacts.

In this context, the **fracture energy** and its distribution over the spatial discretization is a critical factor. Contrary to the uniaxial tensile tests, where the fracture is usually localized within a single layer of elements, a similar effect could not be observed with respect to the velocity of the secondary debris.

The conducted numerical simulations were performed with a mesh size of 5 mm, which is necessary to describe the propagation of the shock wave inside the concrete. However, it is important to note that this mesh size is well below the minimum mesh size for the assumption of a **homogeneous material behavior** according to [Bažant and Oh, 1983].

A comparison of the numerical simulations with the experimental tests revealed, that both material models cannot properly replicate the behavior of the concrete loaded by a contact detonation. This is especially relevant in cases without a breach in the concrete slab.

In this context, the direction of the **flow rule** has a critical influence on the shape of the shock wave and therefore the resulting damage and velocity of the secondary debris.

For a flow rule perpendicular to the hydrostatic axis the damage and the velocity are more evenly distributed throughout the thickness of the concrete slab. With increasing associativity of the flow rule the damage and the velocity shift more towards the surfaces of the concrete slab, which is considered important to represent situations without a breach. This is one shortcoming of the RHT model, since it does not allow a variation of the flow rule analogous to the KCC model.

An additional very important factor regarding the damage and especially the velocity of the secondary debris is the influence of the **strain rate** on the fracture energy of the concrete. Conducted single-element simulations revealed, that the increase of the fracture energy deviates from the expected values at strain rates above $10^2\,\mathrm{s}^{-1}$. A possible explanation for this are Poisson ratio related inertia effects, which according to [Schwer, 2009b] cause the steeper strength increase at high strain rates. Therefore, the steep part of the strength increase should automatically result from the numerical simulation and not be included as a material parameter in the form of a DIF [Ožbolt and Riedel, 2013]. However, according to [Lu and Li, 2011] and [Xu and Wen, 2013], the strength increase due to lateral inertia is only considered relevant in the case of the compressive strength.

To analyze the influence of the **dynamic increase factor** additional simulations are performed without the steep part of the strength increase. Qualitatively these simulations are considered to give a better representation of the reality. However, there is still the deviating behavior of the fracture energy at high strain rates ($\geq 10^2\,\mathrm{s}^{-1}$) which results in a overestimation of the velocity at the protective surface compared to the experimental tests.

It was shown, that **erosion** should be avoided when simulating a contact detonation, since a large portion of the induced energy is already lost during the interaction of the explosive with the concrete slab. Therefore, the subsequent reaction of the concrete slab is only caused by this reduced loading and not representative for the investigated situation.

Based on the experimental results of the test series, a demonstrator was developed which allows to make predictions about the **impact of the secondary debris**. The evaluation showed, that the impact of the secondary debris is strongly localized directly behind the explosive loading and decays rapidly in radial direction.

7.2. Outlook

Whilst this work provides an insight into the characteristics of secondary debris, there are still improvements that can be made to gain a better understanding of the underlying principles in the future.

The varied parameters of the experimental tests presented were the mass and length to diameter ratio of the explosive, the thickness of the concrete slabs, and the steel fiber content. For a systematic evaluation of these parameters, all alternative parameters such as concrete strength and rebar arrangement, as well as the geometry of the explosive charge, were kept constant. Based on the evaluations of the length to diameter ratio of the explosive charge in chapter 3, it is expected that the charge geometry has a large influence on the shape of the spatial velocity distribution of the secondary debris. Furthermore, from the evaluations in chapter 4, the type and position of the rebar is considered to be of particular interest for future investigations.

The test setup developed allowed, for the first time, a detailed analysis of the fragmentation and debris throw on the protective side of a reinforced concrete slab exposed to a contact detonation. As part of the test series, initial attempts were made to capture the secondary debris in three dimensions using high-speed stereo imaging. Unfortunately, these attempts were unsuccessful. Improvements that are considered helpful in this regard are increasing the resolution of the HS cameras and incorporating the armored glass protection of the HS cameras into the calibration process of the HS cameras.

The DIC measurements in this test series were performed on reinforced concrete slabs where a low level of fragmentation was expected in advance. Using the DIC measurements it was possible to successfully validate the determined spatial velocity distribution and the influence of the steel fibers. For future test series, the DIC measurements should be extended to a larger number of tests, also without steel fibers. In this context, it is necessary to significantly increase the frame rate of the HS recordings for DIC before the initial velocity peak on the protective concrete surface. This would enable a targeted recording of the surface deformation prior to complete fragmentation, from which valuable conclusions can be drawn about the concrete behavior. The frame rate required for HS recordings for DIC to properly capture the fragmentation of the concrete is estimated to be $>1 \times 10^5\,\mathrm{s}^{-1}$ based on the numerical simulations performed.

Based on the analysis of the numerical simulations, the direction of the plastic flow and the behavior of the fracture energy at high strain rates are considered to be critical parameters to represent the damage and velocity of a concrete slab when subjected to a contact detonation. To improve the agreement between the experimental tests and the numerical simulation, the softening behavior at strain rates above $10^2\,\mathrm{s}^{-1}$ needs to be considered in more detail.

In this context, simulations using a mesoscopic discretization of the concrete, as performed by [Grunwald, 2023], look promising, but have yet to be compared in detail with experimental results. The advantage of such a representation is that the assumption of homogeneous material behavior is no longer violated, since individual aggregates larger than the spatial discretizations are directly modeled.

In addition, methods that allow the simulation of individual cracks without the use of erosion could help to improve the agreement between the physical processes and the numerical simulation. This type of simulation can directly model inertia related effects of the crack propagation and introduce new surfaces into the model on which the occurring waves can be reflected. For conventional finite element simulations this feature can be added by introducing cohesive elements that separate the elements based on a failure criterion [Zhou et al., 2020]. Alternative methods using particle-based discretization are Peridynamics [Madenci and Oterkus, 2014] or the Smoothed Particle Galerkin method [Wu et al., 2016]. However, these types of representations are much more computationally demanding and there are currently no options available to the author to simulate the interaction with an explosive.

A. Material parameters

A.1. Concrete

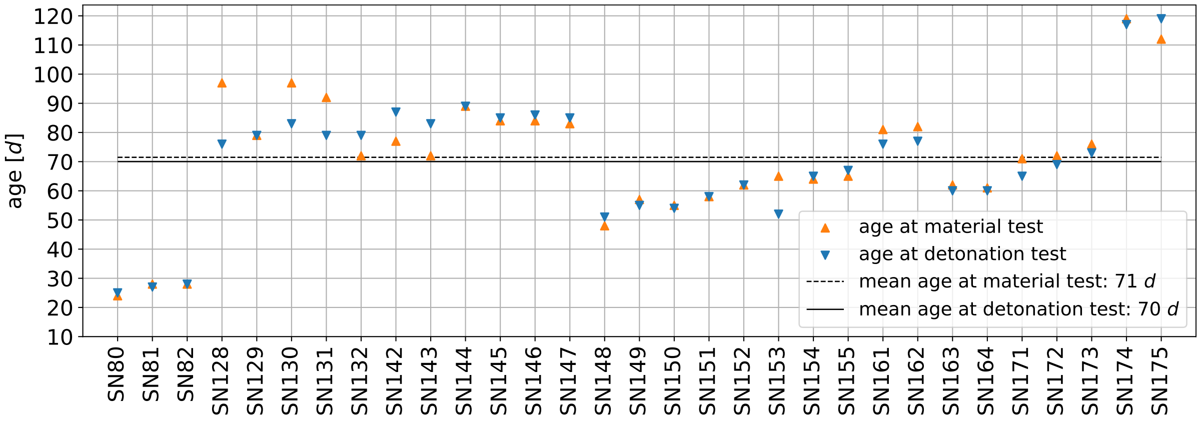

Figure A.1.: Concrete age at material test and detonation test

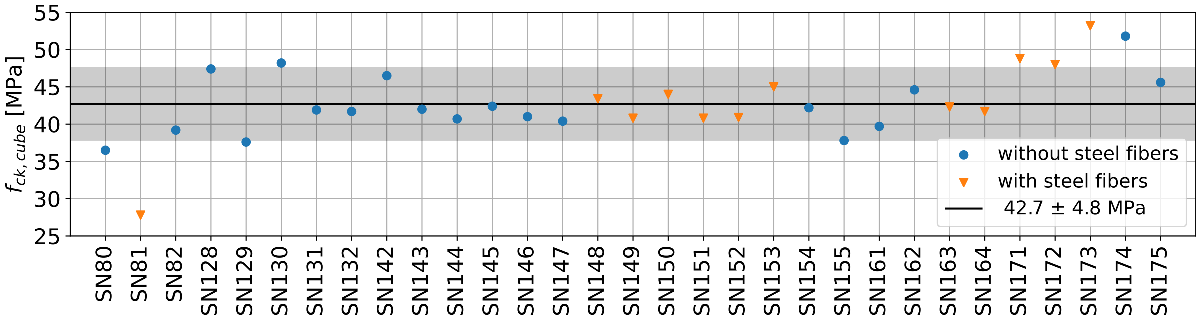

Figure A.2.: Concrete compressive strength

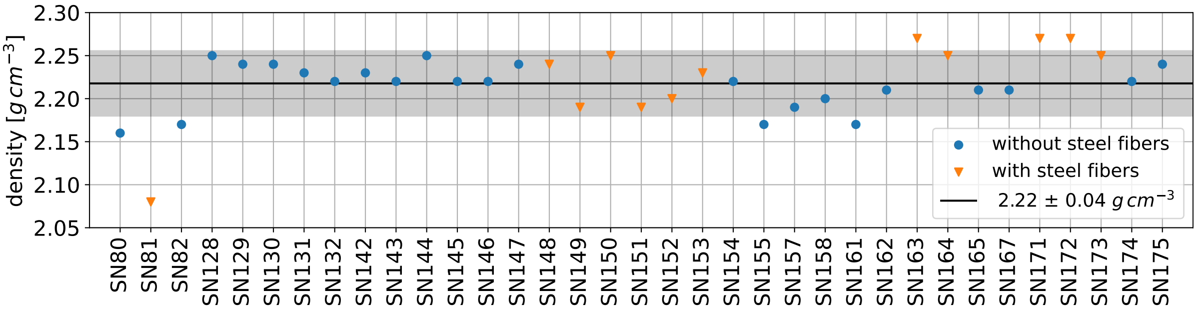

Figure A.3.: Concrete density

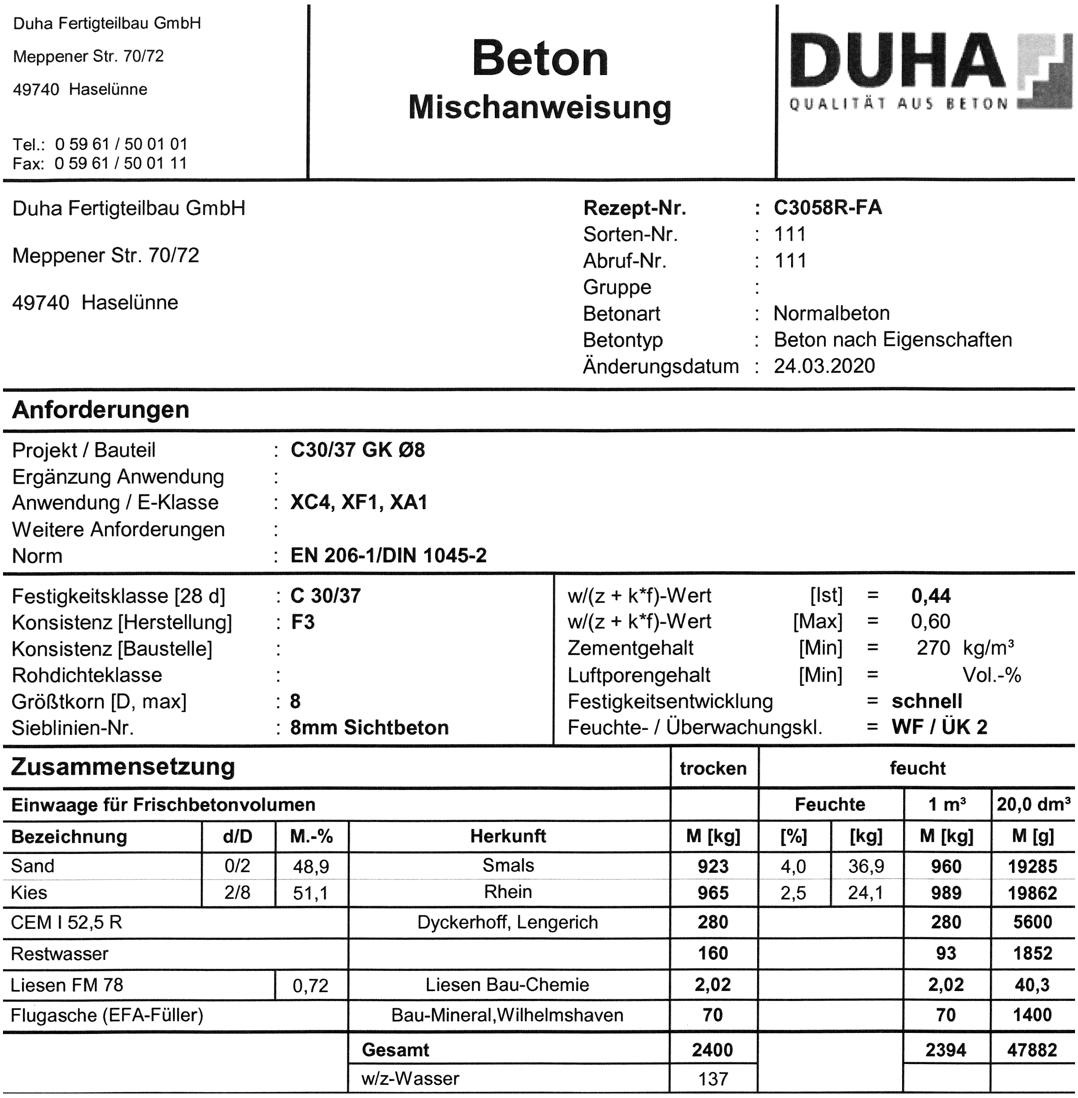

Duha Fertigteilbau GmbH
Meppener Str. 70/72
49740 Haselünne

Tel.: 0 59 61 / 50 01 01
Fax: 0 59 61 / 50 01 11

Beton
Mischanweisung

DUHA
QUALITÄT AUS BETON

Duha Fertigteilbau GmbH

Meppener Str. 70/72

49740 Haselünne

Rezept-Nr. : **C3058R-FA**
Sorten-Nr. : 111
Abruf-Nr. : 111
Gruppe :
Betonart : Normalbeton
Betontyp : Beton nach Eigenschaften
Änderungsdatum : 24.03.2020

Anforderungen

Projekt / Bauteil : **C30/37 GK Ø8**
Ergänzung Anwendung :
Anwendung / E-Klasse : **XC4, XF1, XA1**
Weitere Anforderungen :
Norm : **EN 206-1/DIN 1045-2**

Festigkeitsklasse [28 d] : **C 30/37**
Konsistenz [Herstellung] : **F3**
Konsistenz [Baustelle] :
Rohdichteklasse :
Größtkorn [D, max] : **8**
Sieblinien-Nr. : **8mm Sichtbeton**

w/(z + k*f)-Wert [Ist] = **0,44**
w/(z + k*f)-Wert [Max] = 0,60
Zementgehalt [Min] = 270 $\mathrm{kg/m^3}$
Luftporengehalt [Min] = Vol.-%
Festigkeitsentwicklung = **schnell**
Feuchte- / Überwachungskl. = **WF / ÜK 2**

Zusammensetzung				**trocken**	**feucht**			
Einwaage für Frischbetonvolumen					**Feuchte**		**1 $\mathrm{m^3}$**	**20,0 $\mathrm{dm^3}$**
Bezeichnung	**d/D**	**M.-%**	**Herkunft**	**M [kg]**	**[%]**	**[kg]**	**M [kg]**	**M [g]**
Sand	0/2	48,9	Smals	**923**	4,0	36,9	**960**	**19285**
Kies	2/8	51,1	Rhein	**965**	2,5	24,1	**989**	**19862**
CEM I 52,5 R			Dyckerhoff, Lengerich	**280**			**280**	**5600**
Restwasser				**160**			**93**	**1852**
Liesen FM 78		0,72	Liesen Bau-Chemie	**2,02**			**2,02**	**40,3**
Flugasche (EFA-Füller)			Bau-Mineral,Wilhelmshaven	**70**			**70**	**1400**
			Gesamt	**2400**			**2394**	**47882**
			w/z-Wasser	137				

Figure A.4.: Concrete mixture DUHA

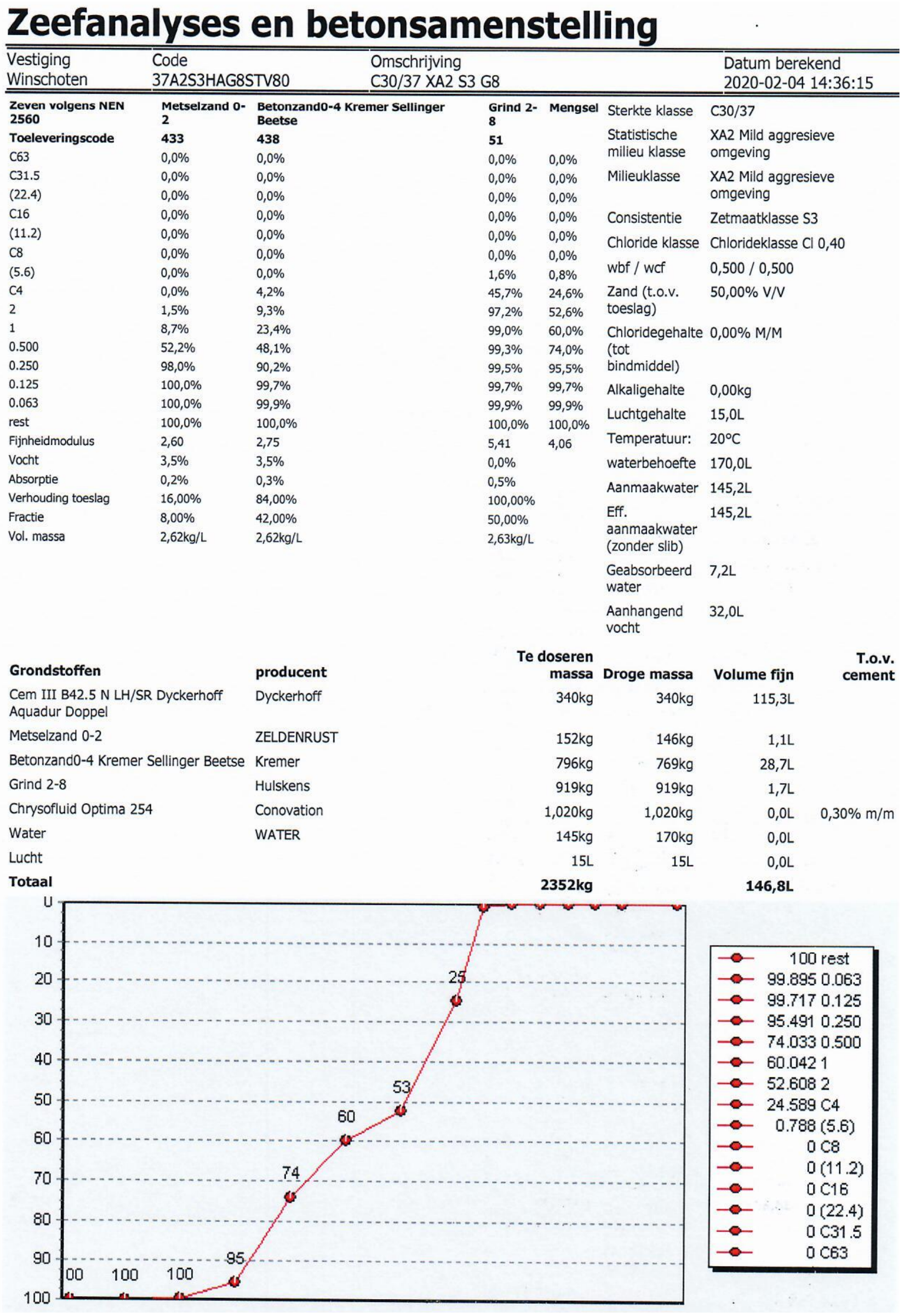

Zeefanalyses en betonsamenstelling

Vestiging	Code	Omschrijving	Datum berekend
Winschoten	37A2S3HAG8STV80	C30/37 XA2 S3 G8	2020-02-04 14:36:15

Zeven volgens NEN 2560	**Metselzand 0-2**	**Betonzand0-4 Kremer Sellinger Beetse**	**Grind 2-8**	**Mengsel**
Toeleveringscode	**433**	**438**	**51**	
C63	0,0%	0,0%	0,0%	0,0%
C31.5	0,0%	0,0%	0,0%	0,0%
(22.4)	0,0%	0,0%	0,0%	0,0%
C16	0,0%	0,0%	0,0%	0,0%
(11.2)	0,0%	0,0%	0,0%	0,0%
C8	0,0%	0,0%	0,0%	0,0%
(5.6)	0,0%	0,0%	1,6%	0,8%
C4	0,0%	4,2%	45,7%	24,6%
2	1,5%	9,3%	97,2%	52,6%
1	8,7%	23,4%	99,0%	60,0%
0.500	52,2%	48,1%	99,3%	74,0%
0.250	98,0%	90,2%	99,5%	95,5%
0.125	100,0%	99,7%	99,7%	99,7%
0.063	100,0%	99,9%	99,9%	99,9%
rest	100,0%	100,0%	100,0%	100,0%
Fijnheidmodulus	2,60	2,75	5,41	4,06
Vocht	3,5%	3,5%	0,0%	
Absorptie	0,2%	0,3%	0,5%	
Verhouding toeslag	16,00%	84,00%	100,00%	
Fractie	8,00%	42,00%	50,00%	
Vol. massa	2,62kg/L	2,62kg/L	2,63kg/L	

Sterkte klasse	C30/37
Statistische milieu klasse	XA2 Mild aggresieve omgeving
Milieuklasse	XA2 Mild aggresieve omgeving
Consistentie	Zetmaatklasse S3
Chloride klasse	Chlorideklasse Cl 0,40
wbf / wcf	0,500 / 0,500
Zand (t.o.v. toeslag)	50,00% V/V
Chloridegehalte (tot bindmiddel)	0,00% M/M
Alkaligehalte	0,00kg
Luchtgehalte	15,0L
Temperatuur:	20°C
waterbehoefte	170,0L
Aanmaakwater	145,2L
Eff. aanmaakwater (zonder slib)	145,2L
Geabsorbeerd water	7,2L
Aanhangend vocht	32,0L

Grondstoffen	**producent**	**Te doseren massa**	**Droge massa**	**Volume fijn**	**T.o.v. cement**
Cem III B42.5 N LH/SR Dyckerhoff Aquadur Doppel	Dyckerhoff	340kg	340kg	115,3L	
Metselzand 0-2	ZELDENRUST	152kg	146kg	1,1L	
Betonzand0-4 Kremer Sellinger Beetse	Kremer	796kg	769kg	28,7L	
Grind 2-8	Hulskens	919kg	919kg	1,7L	
Chrysofluid Optima 254	Conovation	1,020kg	1,020kg	0,0L	0,30% m/m
Water	WATER	145kg	170kg	0,0L	
Lucht		15L	15L	0,0L	
Totaal		**2352kg**		**146,8L**	

Figure A.5.: Concrete mixture Visser and Smith

A.2. Steel fibers

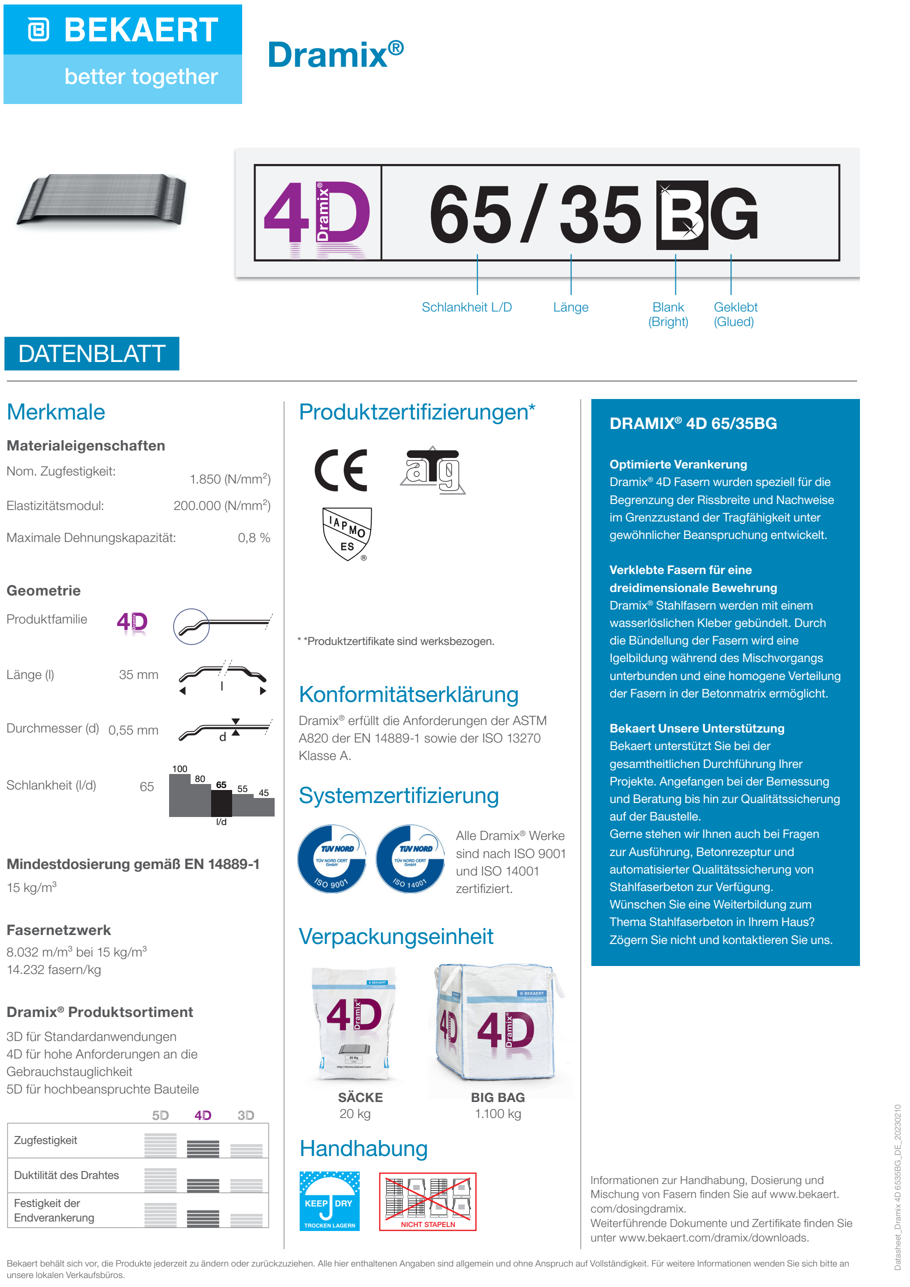

BEKAERT
better together

Dramix®

4D 65/35 BG

DATENBLATT

Merkmale

Materialeigenschaften

Nom. Zugfestigkeit:	1.850 (N/mm^2)
Elastizitätsmodul:	200.000 (N/mm^2)
Maximale Dehnungskapazität:	0,8 %

Geometrie

Produktfamilie	4D
Länge (l)	35 mm
Durchmesser (d)	0,55 mm
Schlankheit (l/d)	65

Mindestdosierung gemäß EN 14889-1
15 kg/m^3

Fasernetzwerk
8.032 m/m^3 bei 15 kg/m^3
14.232 fasern/kg

Dramix® Produktsortiment
3D für Standardanwendungen
4D für hohe Anforderungen an die Gebrauchstauglichkeit
5D für hochbeanspruchte Bauteile

	5D	4D	3D
Zugfestigkeit	▤	▤	▤
Duktilität des Drahtes	▤	▤	▤
Festigkeit der Endverankerung	▤	▤	▤

Produktzertifizierungen*

CE
atg
IAPMO ES®

* *Produktzertifikate sind werksbezogen.

Konformitätserklärung

Dramix® erfüllt die Anforderungen der ASTM A820 der EN 14889-1 sowie der ISO 13270 Klasse A.

Systemzertifizierung

TÜV NORD ISO 9001
TÜV NORD ISO 14001

Alle Dramix® Werke sind nach ISO 9001 und ISO 14001 zertifiziert.

Verpackungseinheit

SÄCKE
20 kg

BIG BAG
1.100 kg

Handhabung

KEEP DRY
TROCKEN LAGERN

NICHT STAPELN

DRAMIX® 4D 65/35BG

Optimierte Verankerung
Dramix® 4D Fasern wurden speziell für die Begrenzung der Rissbreite und Nachweise im Grenzzustand der Tragfähigkeit unter gewöhnlicher Beanspruchung entwickelt.

Verklebte Fasern für eine dreidimensionale Bewehrung
Dramix® Stahlfasern werden mit einem wasserlöslichen Kleber gebündelt. Durch die Bündellung der Fasern wird eine Igelbildung während des Mischvorgangs unterbunden und eine homogene Verteilung der Fasern in der Betonmatrix ermöglicht.

Bekaert Unsere Unterstützung
Bekaert unterstützt Sie bei der gesamtheitlichen Durchführung Ihrer Projekte. Angefangen bei der Bemessung und Beratung bis hin zur Qualitätssicherung auf der Baustelle.
Gerne stehen wir Ihnen auch bei Fragen zur Ausführung, Betonrezeptur und automatisierter Qualitätssicherung von Stahlfaserbeton zur Verfügung.
Wünschen Sie eine Weiterbildung zum Thema Stahlfaserbeton in Ihrem Haus? Zögern Sie nicht und kontaktieren Sie uns.

Informationen zur Handhabung, Dosierung und Mischung von Fasern finden Sie auf www.bekaert.com/dosingdramix.
Weiterführende Dokumente und Zertifikate finden Sie unter www.bekaert.com/dramix/downloads.

Datasheet_Dramix 4D 6535BG_DE_20230210

Figure A.6.: Dramix steel fibers 4D 65/35 BG

A.3. Explosive

```
Product library title: bkwc

Reactant library title: # Version 2.0 by P. Clark Souers


The composition:
Name      % wt.   % mol  % vol   Heat of     Mol.   TMD
                                formation    wt.    (g/cc)
                                (cal/mol)
petn       87.00  84.94  79.81  -125956   316.15     1.78 c5h8n4o12
dbp        12.00  13.31  18.73  -201004   278.34     1.04 c16h22o4
dmdnb       1.00   1.75   1.46   -74331   176.17     1.12 c6h12n2o4

Density  =  1.6311 g/cc   Mixture TMD =  1.6311 g/cc   % TMD = 100.0000


The C-J condition:
The pressure          =         22.62 GPa
The volume            =         0.461 cc/g
The density           =         2.170 g/cc
The energy            =          2.81 kJ/cc explosive
The temperature       =          3854 K
The shock velocity    =         7.474 mm/us
The particle velocity =         1.855 mm/us
The speed of sound    =         5.619 mm/us
Gamma                 =         3.029


Cylinder runs:              % of standards
  V/V0     Energy    TATB      PETN      HMX    CL-20   TRITON
 (rel.)   (kJ/cc)  1.83g/cc 1.76g/cc 1.89g/cc 2.04g/cc 1.70g/cc
   1.00    -0.87
   2.20    -4.87     100       77       65       54      112
   4.10    -5.97     103       77       67       57      108
   6.00    -6.38
   8.00    -6.63
  10.00    -6.79     104       78       69       59      103
  15.00    -7.04
  20.00    -7.19     105       78       71       61      100
  25.00    -7.30
  30.00    -7.38
  35.00    -7.44
  40.00    -7.49     105       79       71       62       97
  45.00    -7.54
  50.00    -7.58

Freezing occurred at T =     2145.0 K and relative V =   1.616
The mechanical energy of detonation =     -8.239 kJ/cc
The thermal energy of detonation    =     -0.000 kJ/cc
The total energy of detonation      =     -8.239 kJ/cc

JWL Fit results:
E0   =      -8.447 kJ/cc
A    =      671.10 GPa, B    =        9.37 GPa , C     =        1.65 GPa
R[1] =        4.91,     R[2] =        1.19,      omega =        0.40
RMS fitting error =   0.56 %
```

Figure A.7.: Semtex10 parameters from CHEETAH simulation [Fried and P., 1994]

B. Spalling crater

B.1. Photos

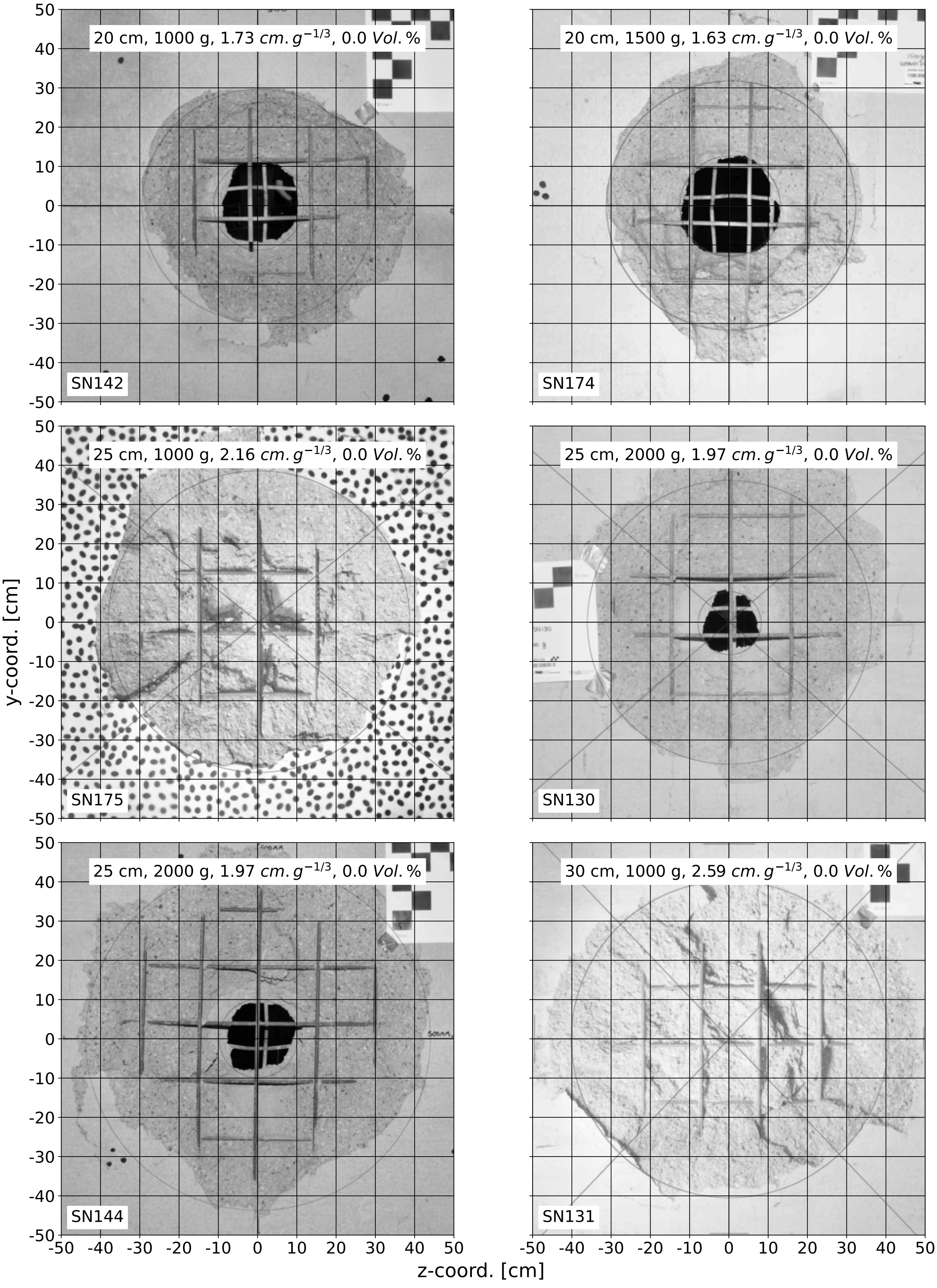

Figure B.1.: Spalling crater (without steel fibers, part 1)

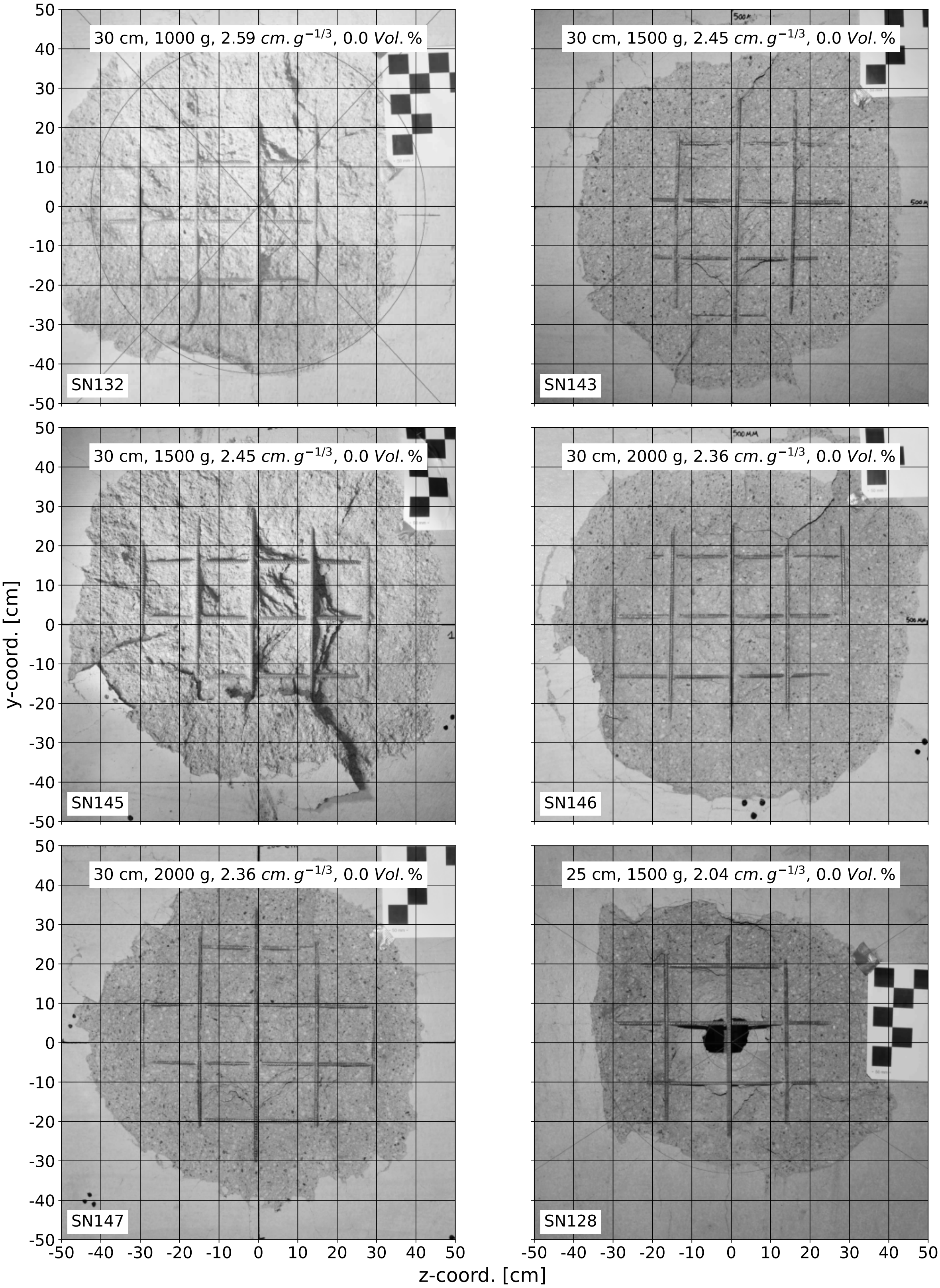

Figure B.2.: Spalling crater (without steel fibers, part 2)

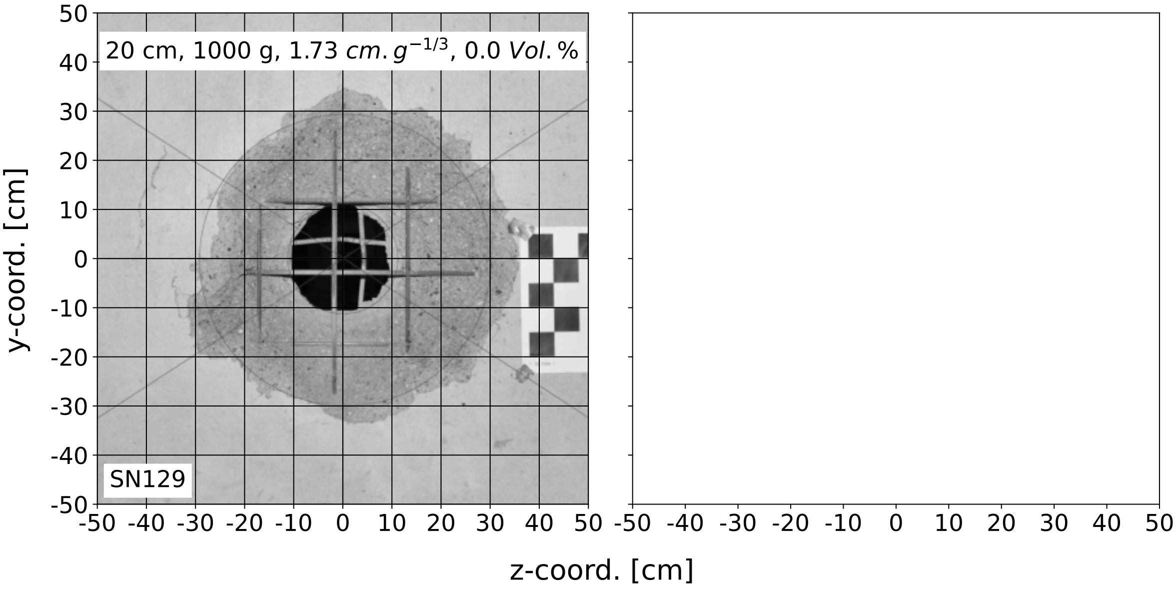

Figure B.3.: Spalling crater (without steel fibers, part 3)

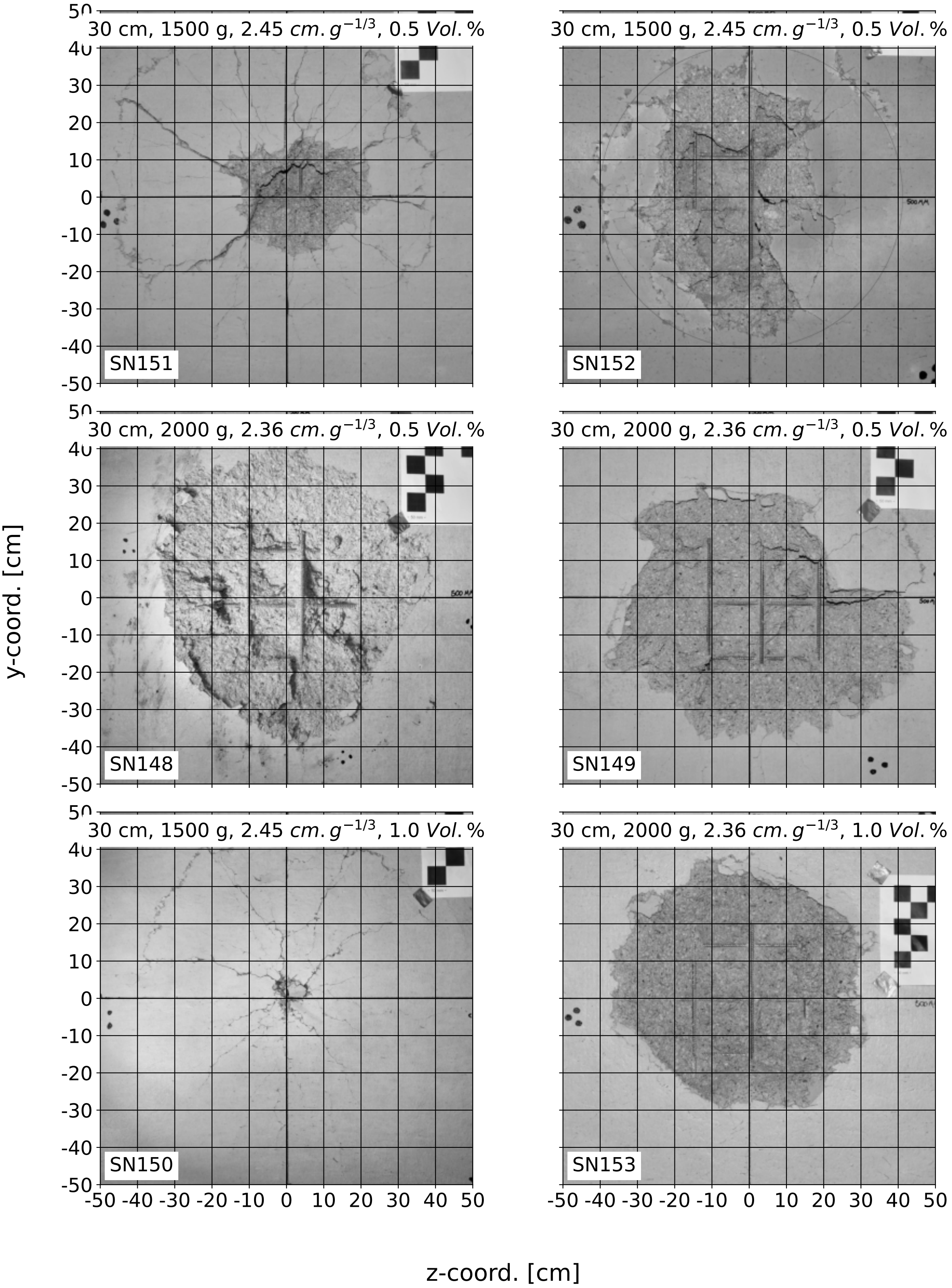

Figure B.4.: Spalling crater (with steel fibers, part 1)

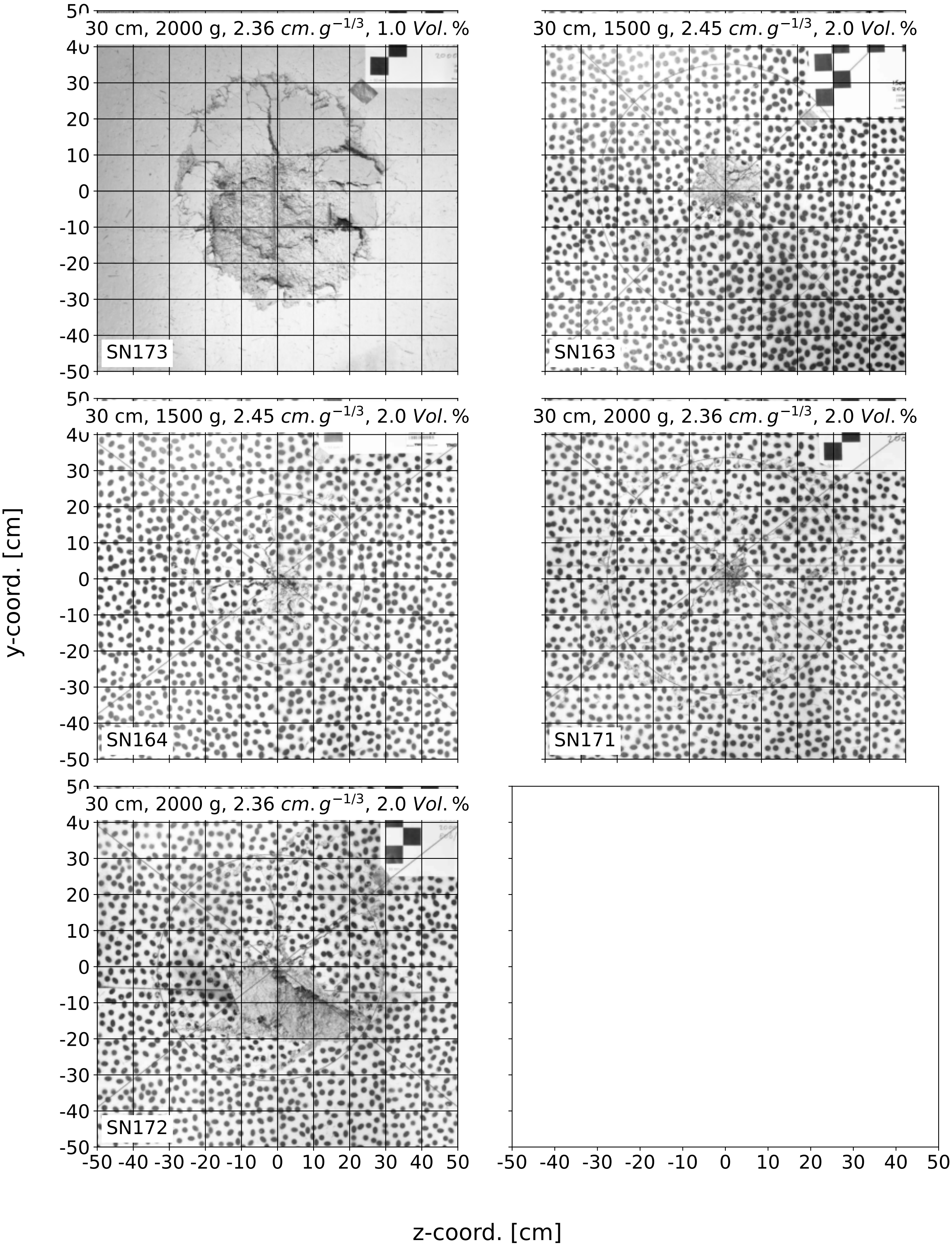

Figure B.5.: Spalling crater (with steel fibers, part 2)

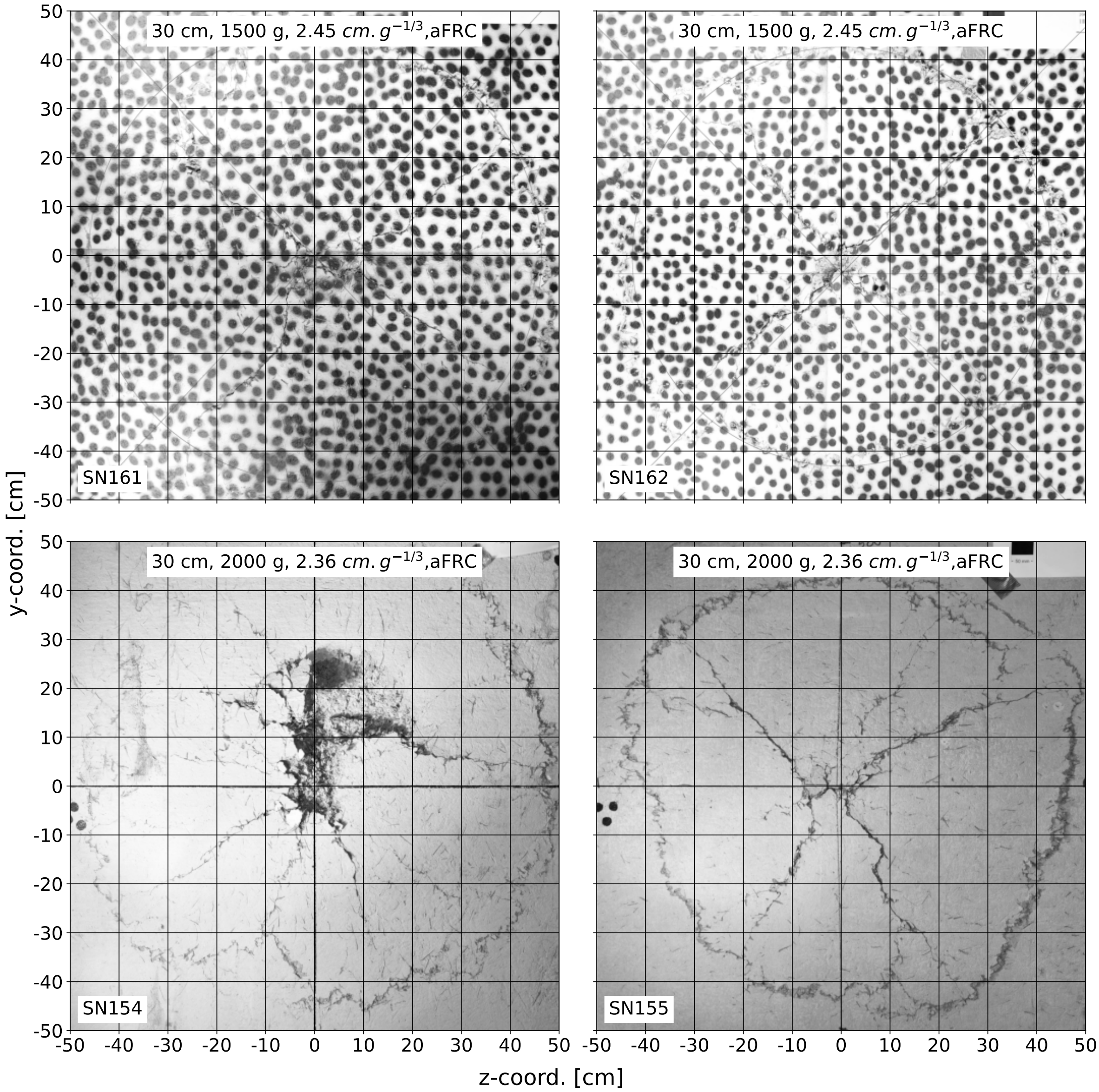

Figure B.6.: Spalling crater (with steel fibers, part 3)

B.2. 3D scans

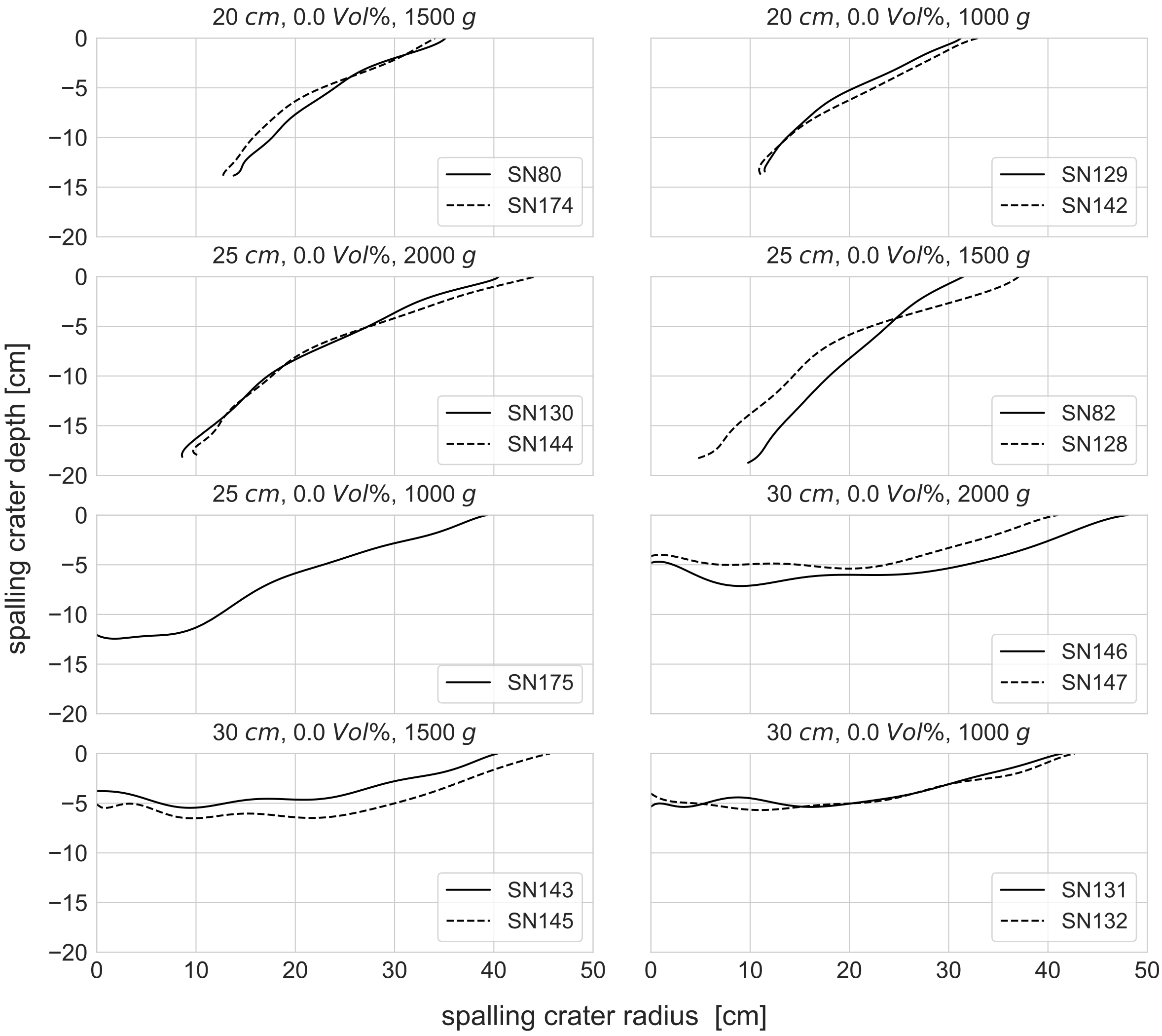

Figure B.7.: Averaged shapes of the spalling craters without steel fibers

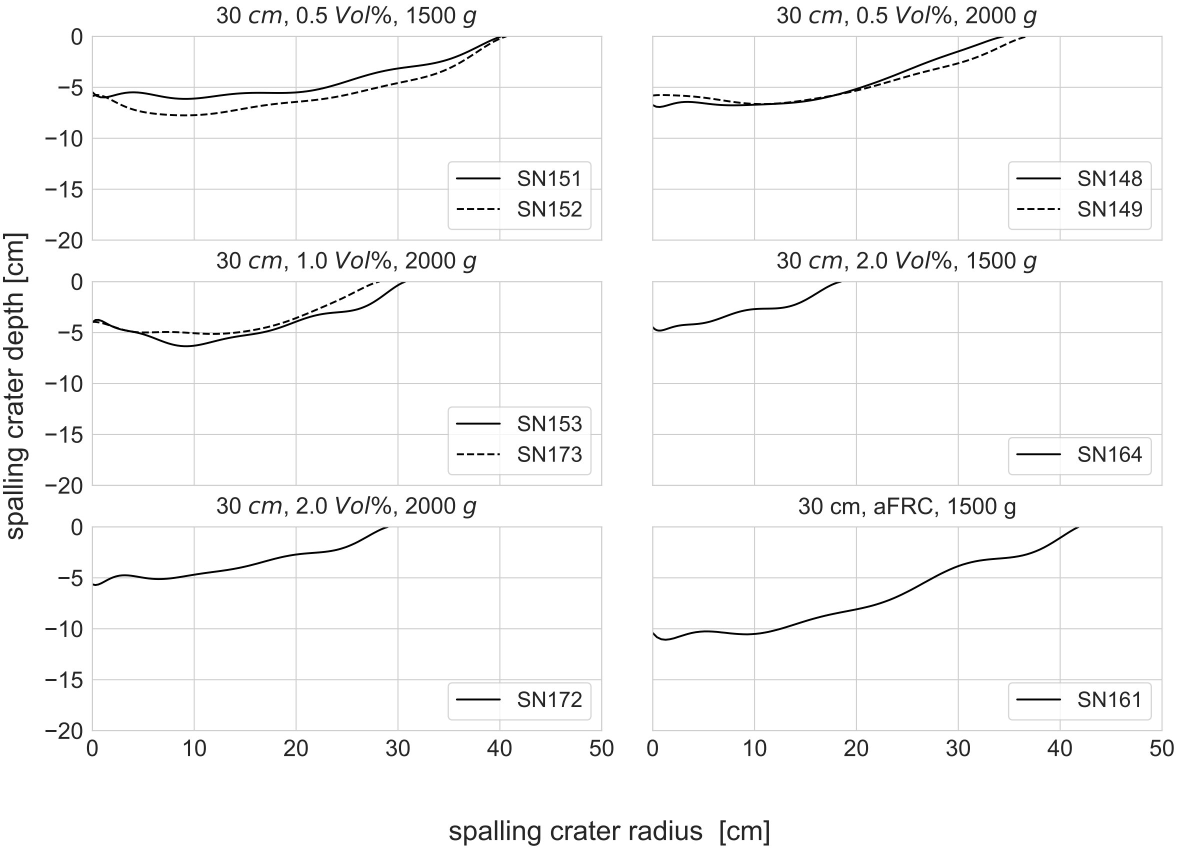

Figure B.8.: Averaged shapes of the spalling craters with steel fibers

B.3. Cross section SN164

Cross section from test SN164 together with the measurement from the 3D scan (red line). The section from the 3D scan of test SN143 without steel fibers is added as blue line for reference.

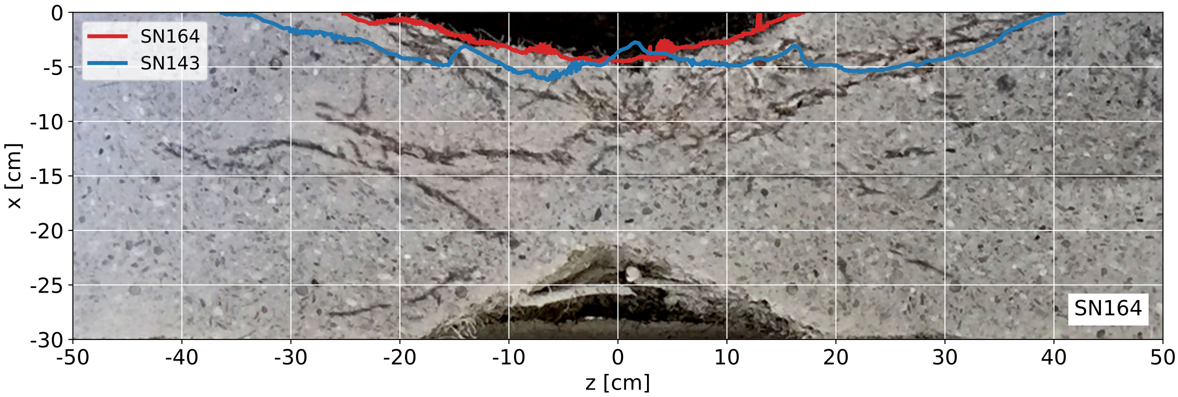

Figure B.9.: Horizontal cross section of test SN164 including measurements from 3D scans for tests SN146 and SN143

B.4. HS recording

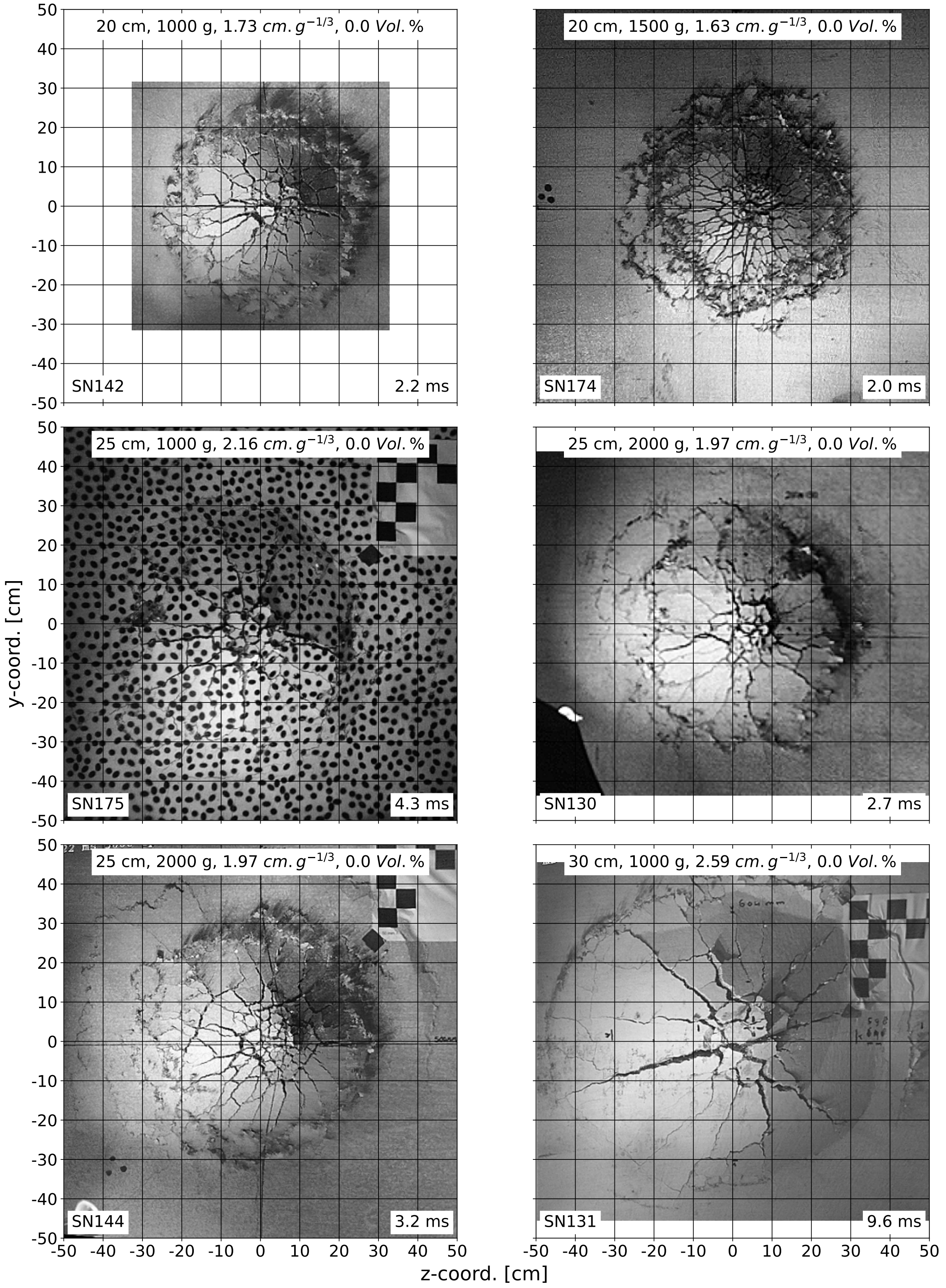

Figure B.10.: Spalling crater from HS recording (without steel fibers, part 1)

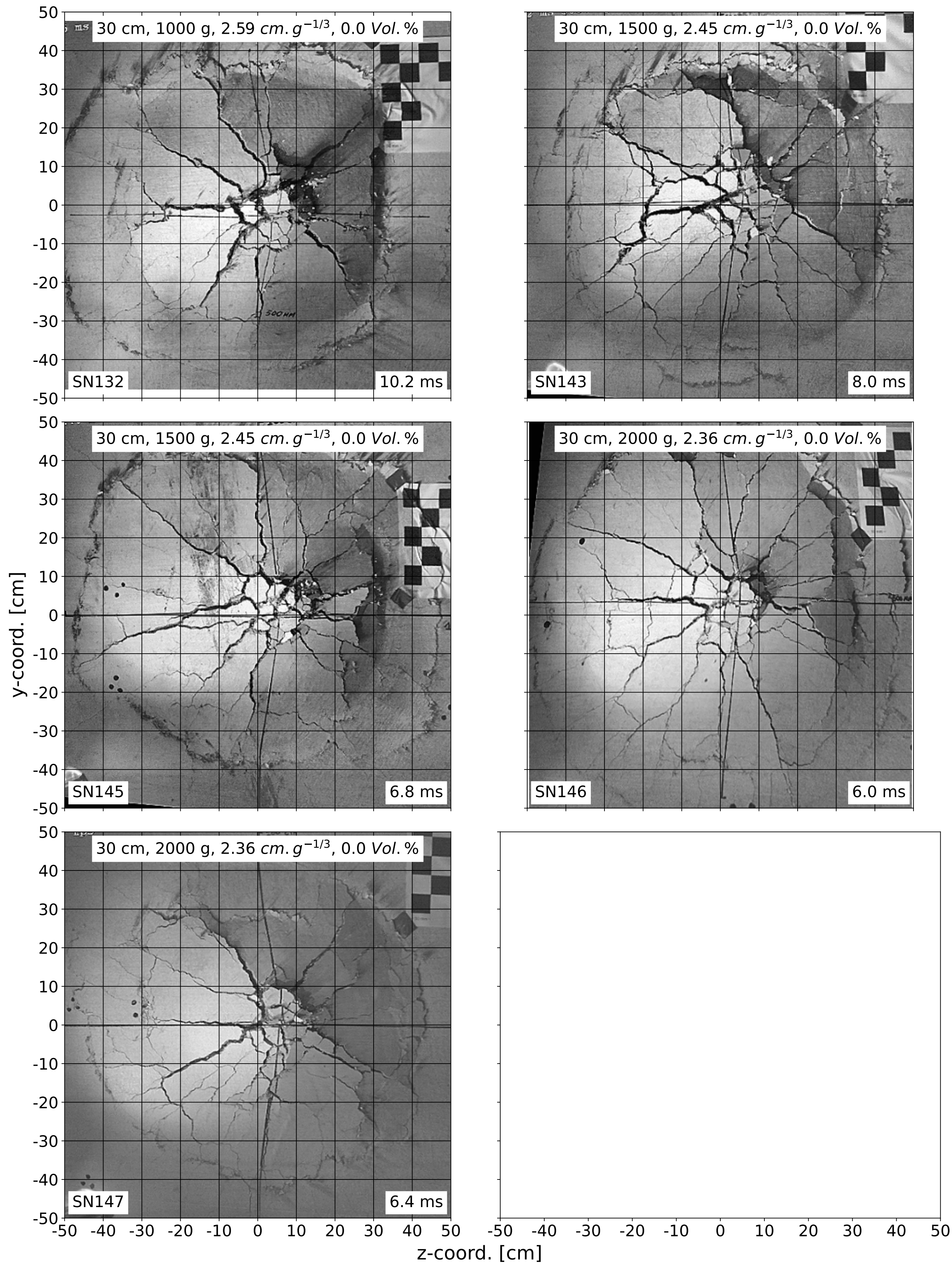

Figure B.11.: Spalling crater from HS recording (without steel fibers, part 2)

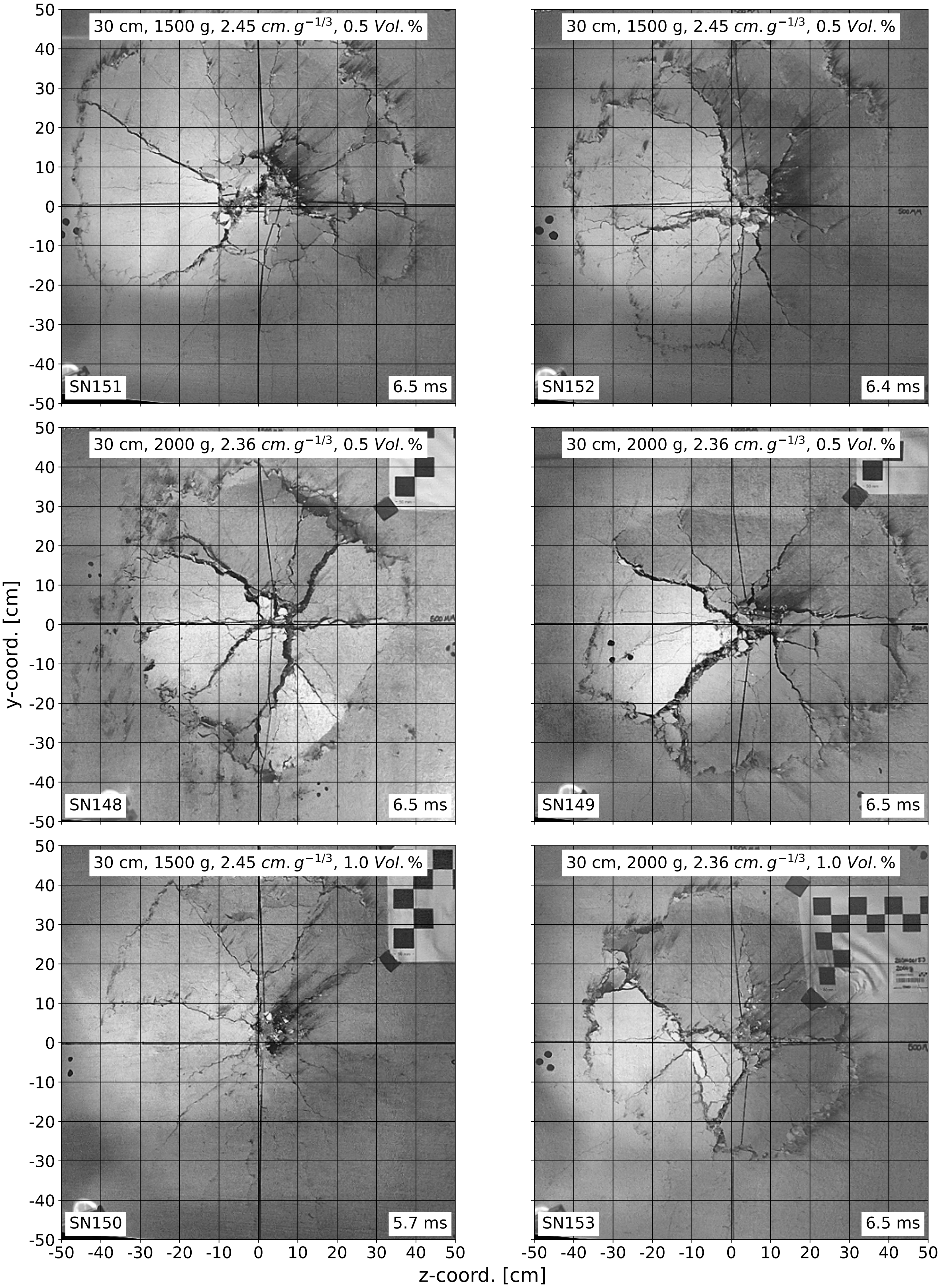

Figure B.12.: Spalling crater from HS recording (with steel fibers, part 1)

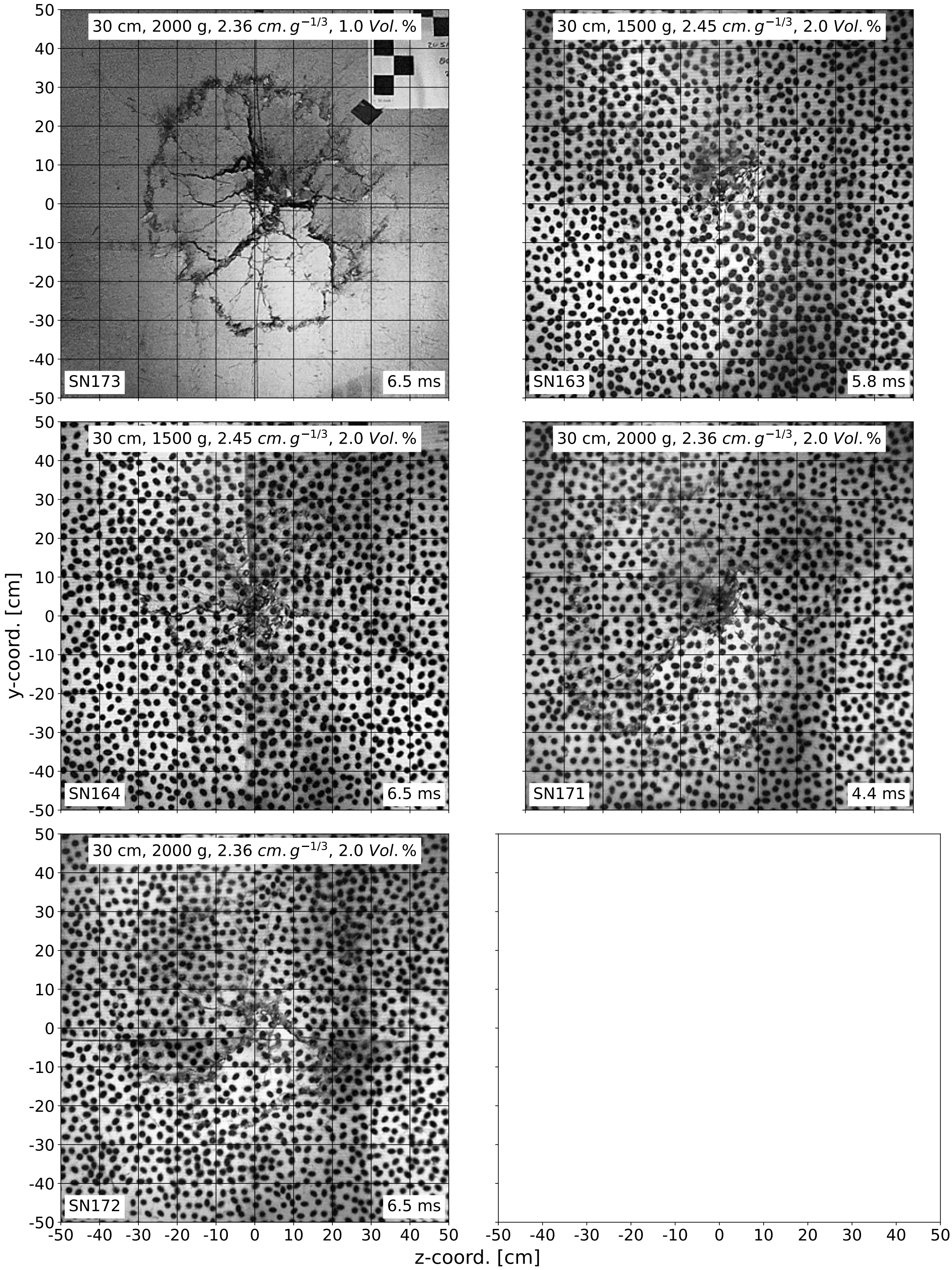

Figure B.13.: Spalling crater from HS recording (with steel fibers, part 2)

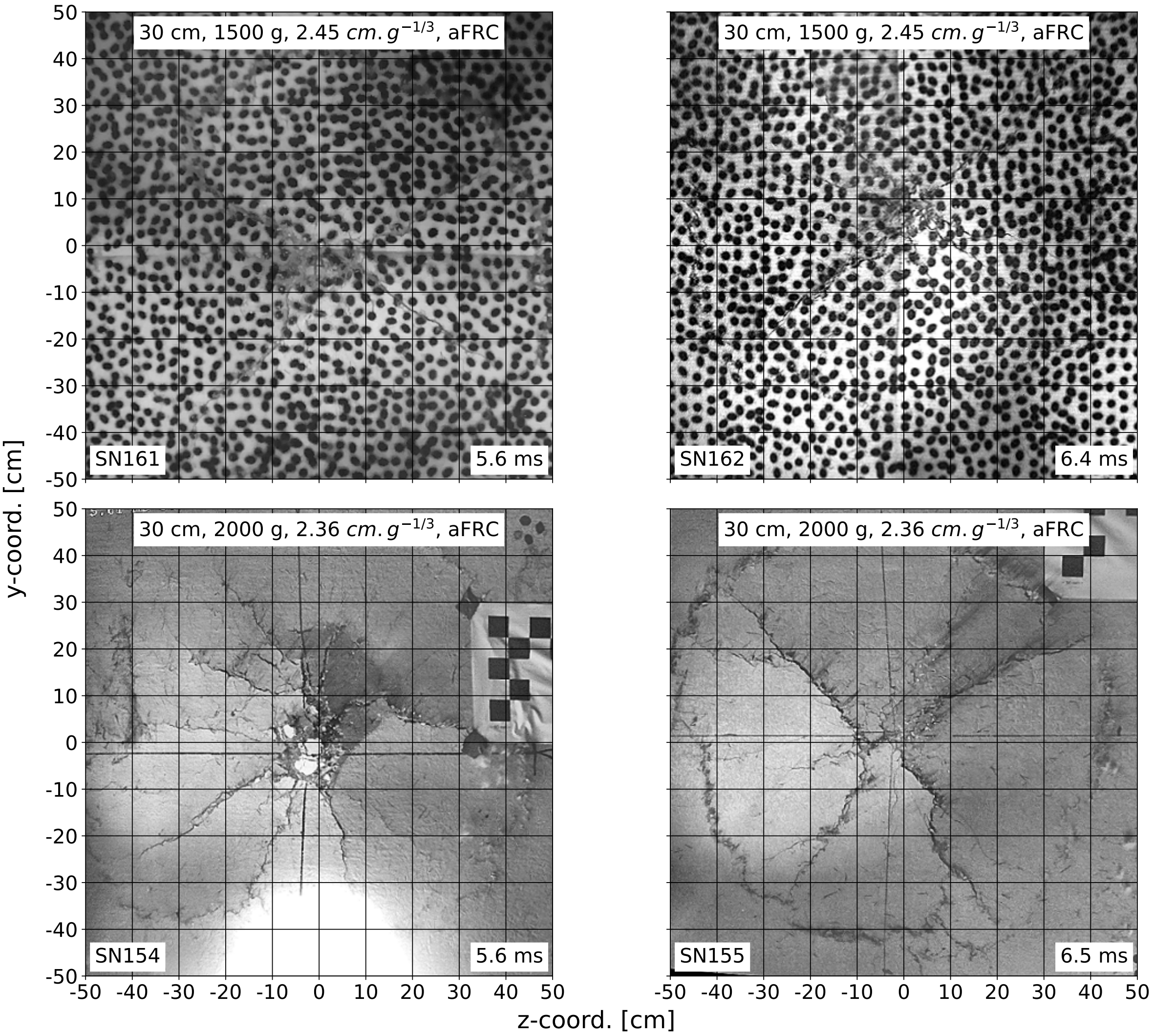

Figure B.14.: Spalling crater from HS recording (with steel fibers, part 3)

C. Tracking

C.1. HS recordings for tracking

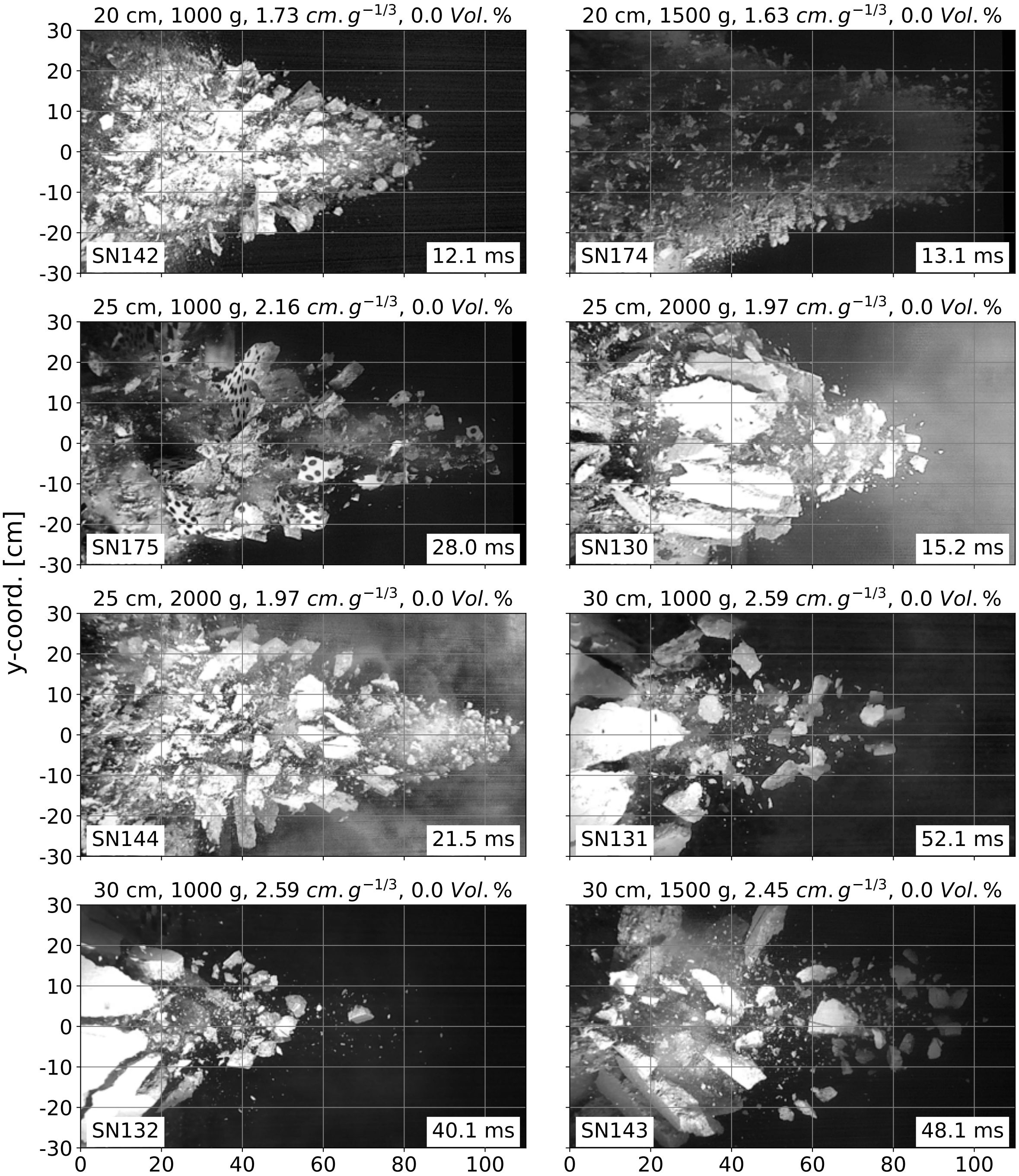

Figure C.1.: HS recordings for tracking part 1 (without steel fibers)

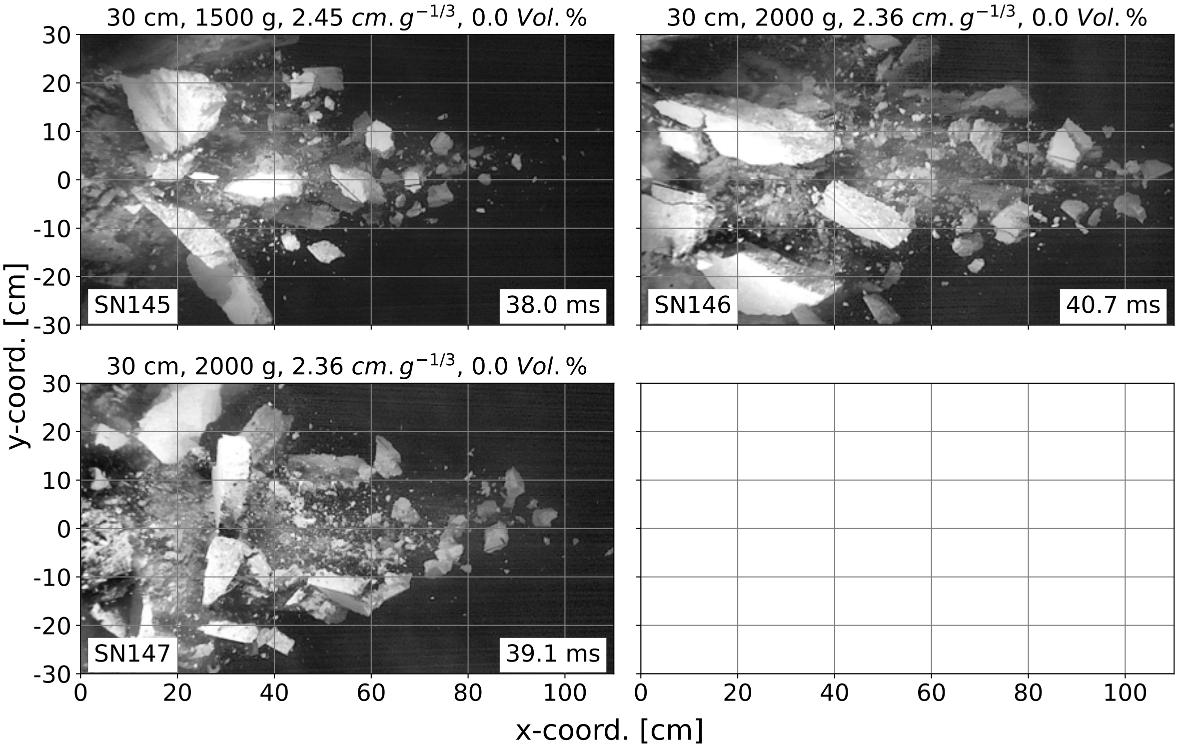

Figure C.2.: HS recordings for tracking part 2 (without steel fibers)

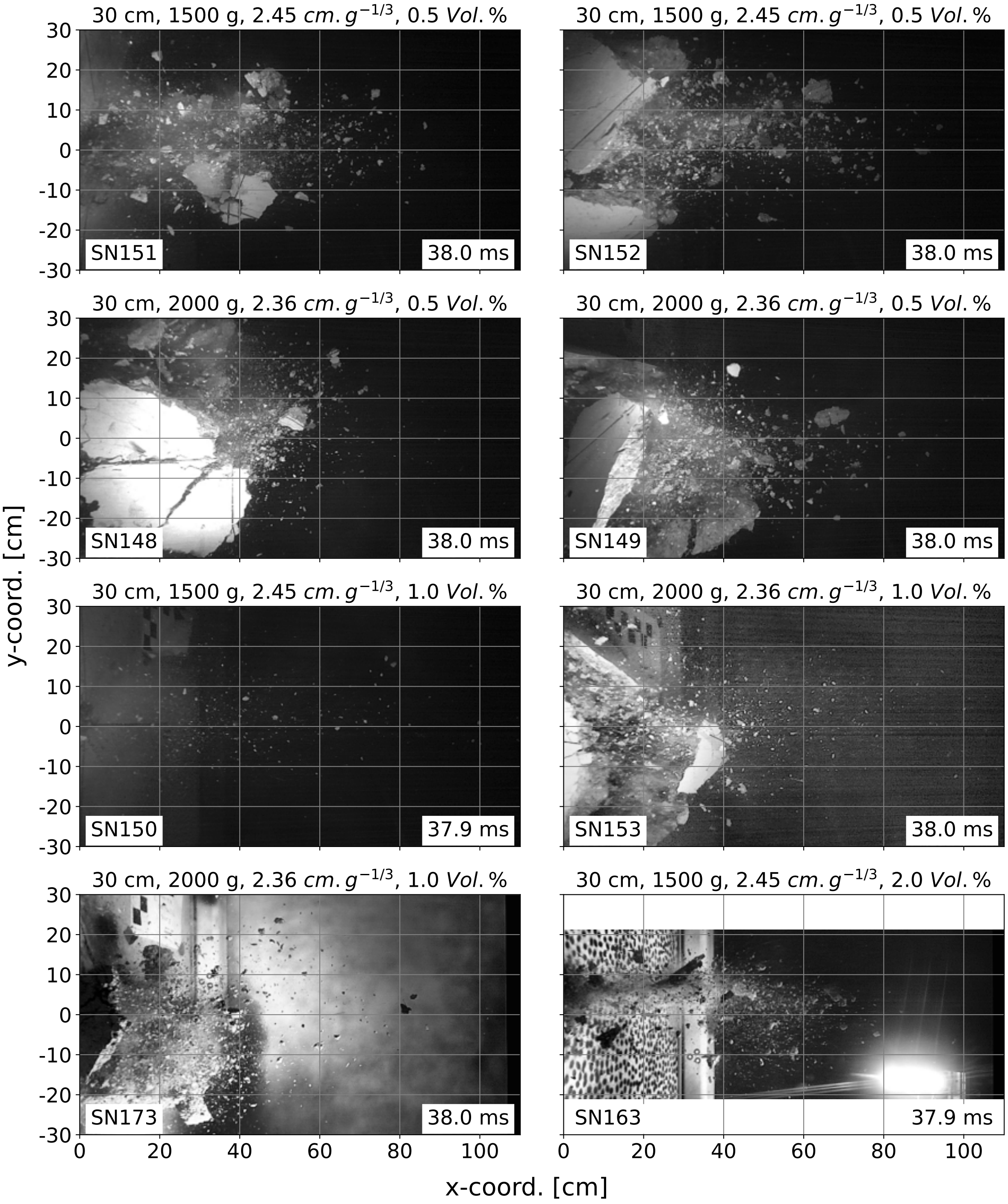

Figure C.3.: HS recordings for tracking part 3 (with steel fibers)

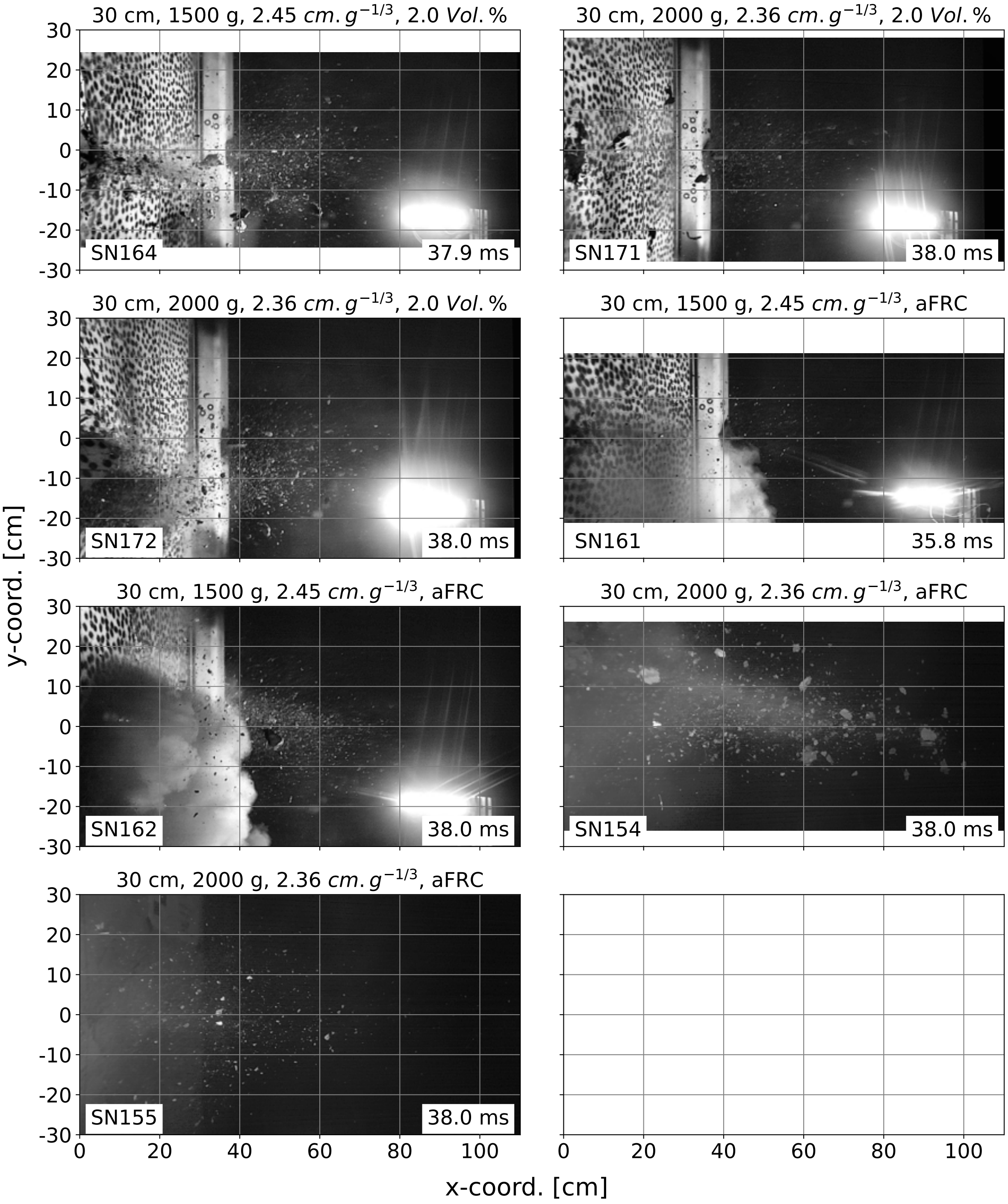

Figure C.4.: HS recordings for tracking part 4 (with steel fibers)

C.2. Velocity distributions

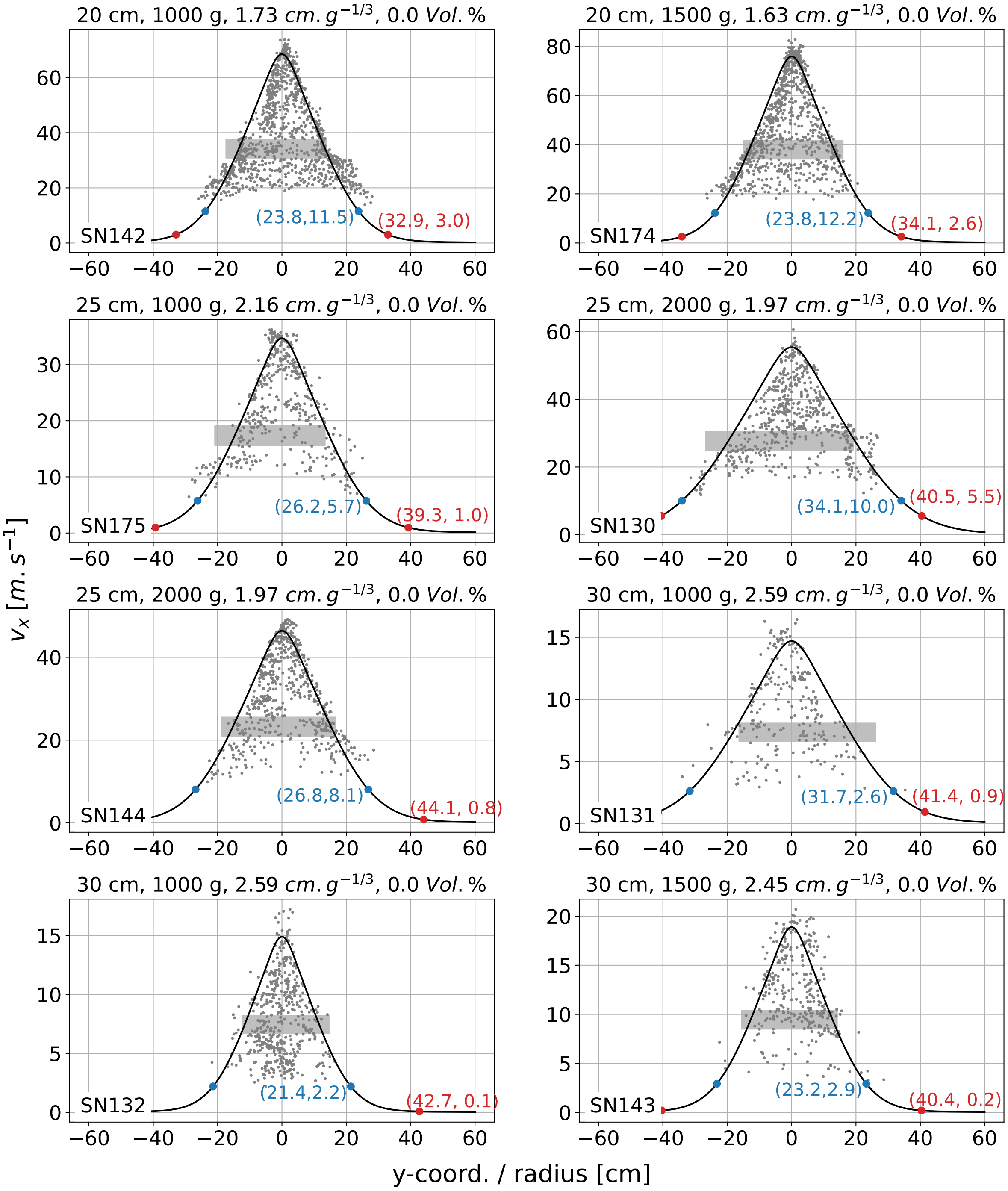
20 cm, 1000 g, 1.73 $cm.g^{-1/3}$, 0.0 $Vol.\%$

20 cm, 1500 g, 1.63 $cm.g^{-1/3}$, 0.0 $Vol.\%$

25 cm, 1000 g, 2.16 $cm.g^{-1/3}$, 0.0 $Vol.\%$

25 cm, 2000 g, 1.97 $cm.g^{-1/3}$, 0.0 $Vol.\%$

25 cm, 2000 g, 1.97 $cm.g^{-1/3}$, 0.0 $Vol.\%$

30 cm, 1000 g, 2.59 $cm.g^{-1/3}$, 0.0 $Vol.\%$

30 cm, 1000 g, 2.59 $cm.g^{-1/3}$, 0.0 $Vol.\%$

30 cm, 1500 g, 2.45 $cm.g^{-1/3}$, 0.0 $Vol.\%$

Figure C.5.: Approximated spatial x-velocity distribution part 1 (without steel fibers)

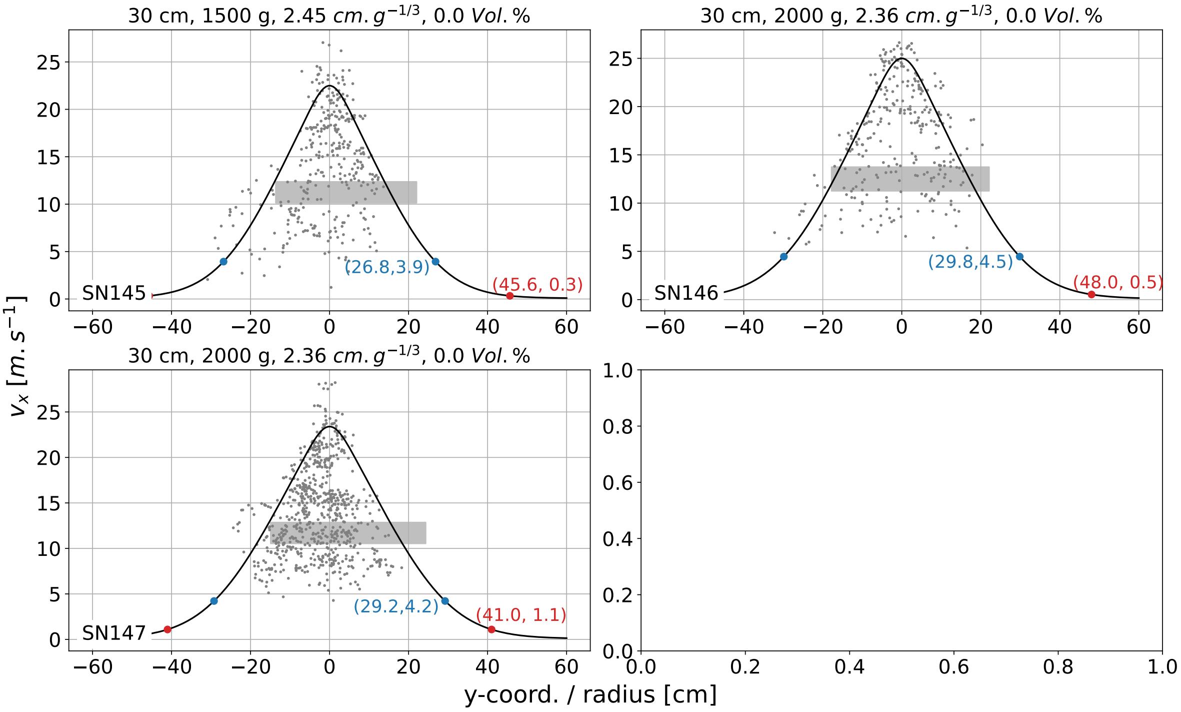

Figure C.6.: Approximated spatial x-velocity distribution part 2 (without steel fibers)

C.3. Flow chart for tracking algorithm

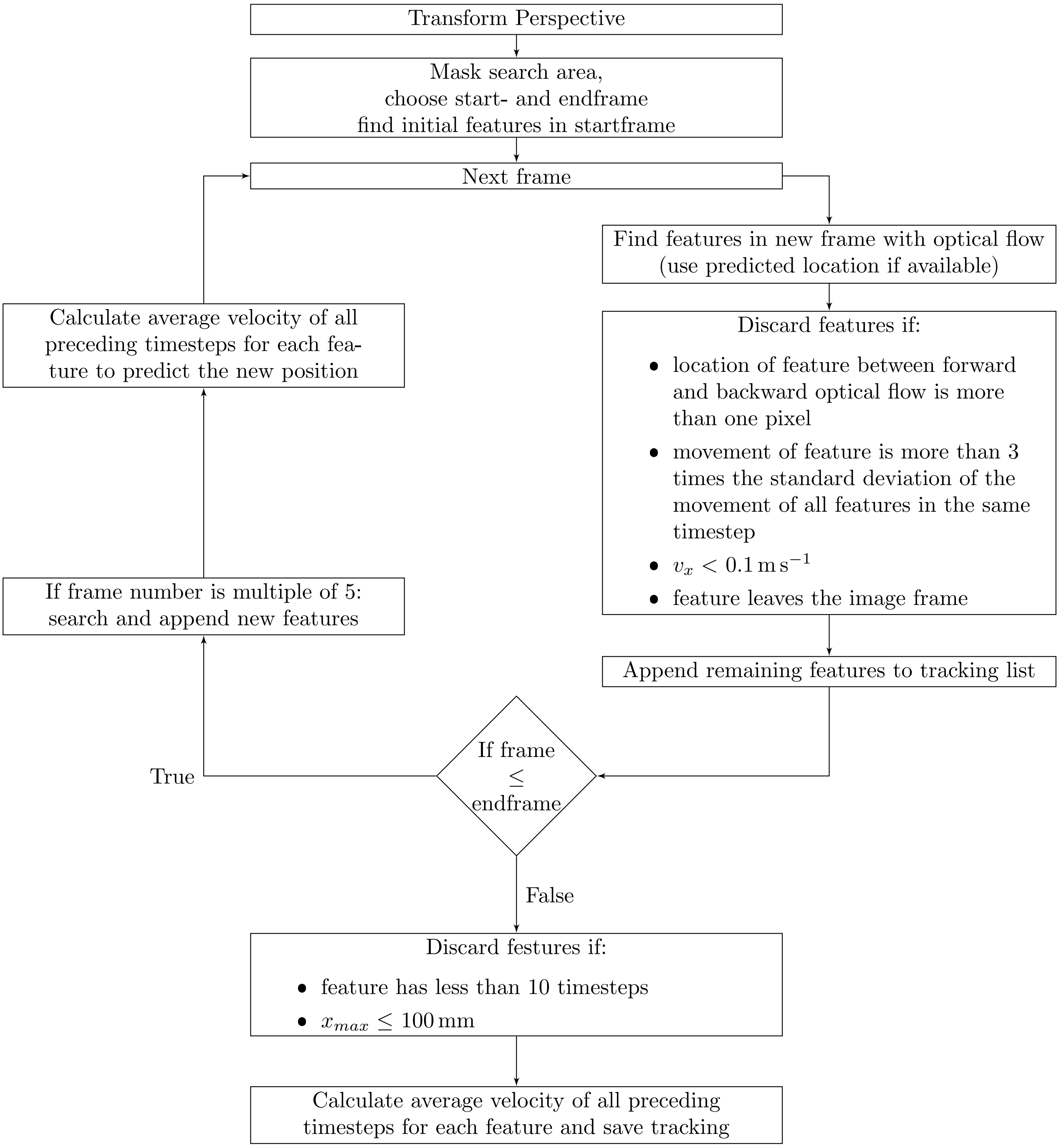

Figure C.7.: Flowchart for the tracking algorithm

D. DIC

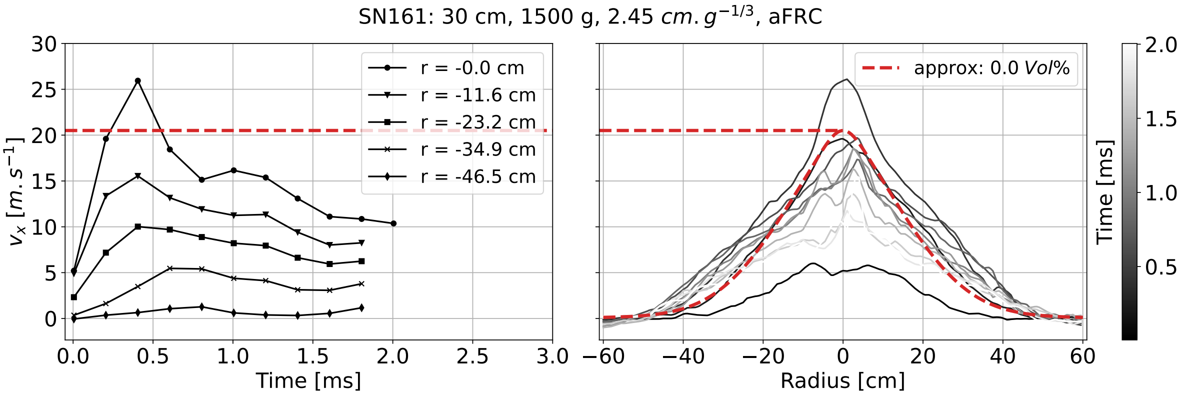

Figure D.1.: DIC velocity SN161

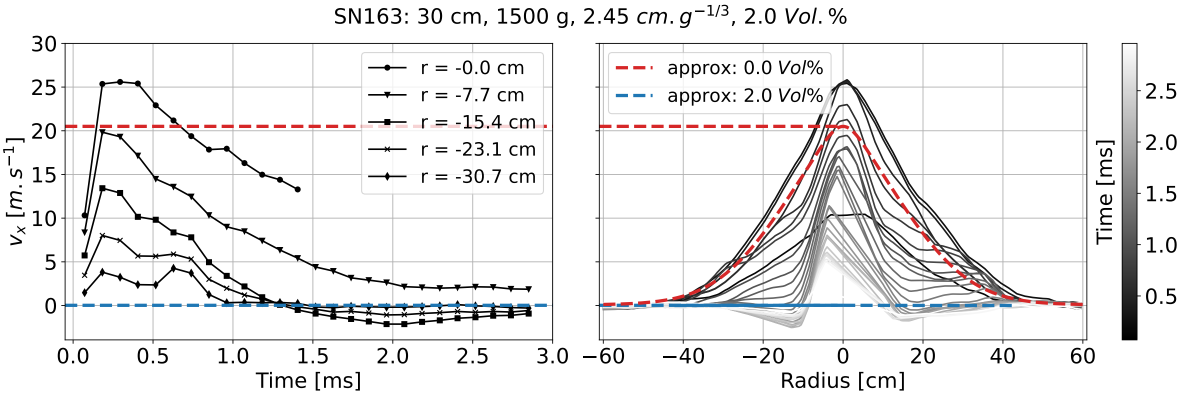

Figure D.2.: DIC x-velocity SN163

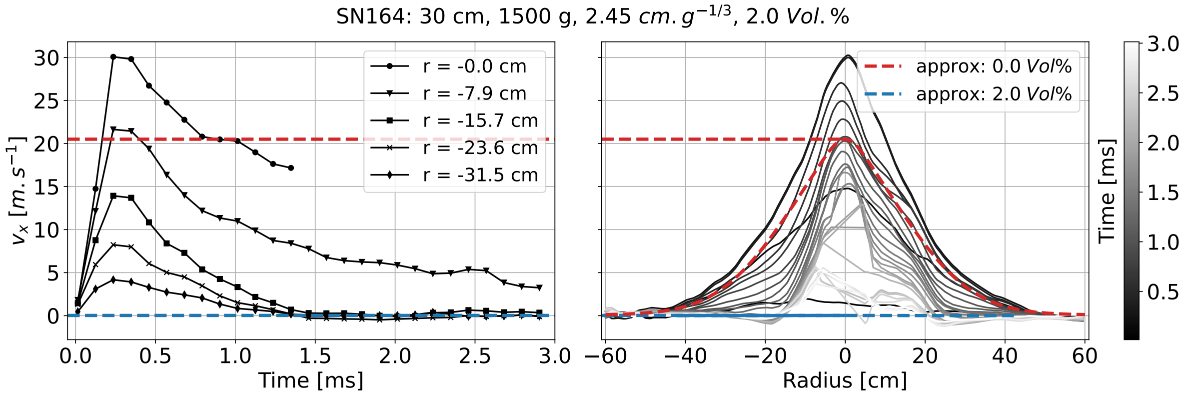

Figure D.3.: DIC x-velocity SN164

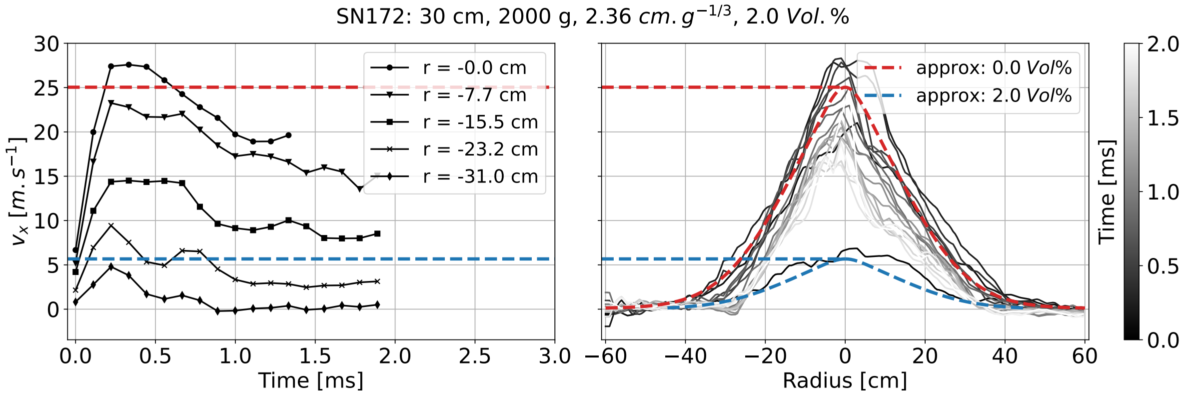

Figure D.4.: DIC x-velocity SN172

E. Parameters of the concrete material models

In the following sections, the parameters of the two material models used for the simulation of the experimental tests are given. The names of the individual parameters correspond to those used for the input in LS-Dyna [Lsdyna, 2021] and do not necessarily match those used for the description in chapter 5.

E.1. RHT model

Table E.1.: Parameters of the RHT model

name	value	unit
RO	2.22×10^{-3}	$\mathrm{g\,mm^{-3}}$
SHEAR	1.3×10^{4}	MPa
ONEMPA	-5.0	–
EPSF	10.0	–
B0	1.76	–
B1	1.76	–
T1 ($\alpha_0 = 1.08$)	1.87×10^{4}	MPa
A	1.95	–
N	7.97×10^{-1}	–
FC	35.0	MPa
FS*	1.8×10^{-1}	–
FT*	7.71×10^{-2}	–
Q0	6.81×10^{-1}	–
B	1.05×10^{-2}	–
T2	0.0	MPa
E0C	3.0×10^{-8}	$\mathrm{ms^{-1}}$
E0T	3.0×10^{-8}	$\mathrm{ms^{-1}}$
EC	8.0×10^{-2}	$\mathrm{ms^{-1}}$
ET	1.0×10^{-3}	$\mathrm{ms^{-1}}$
BETAC	2.2×10^{-2}	–
BETAT	3.64×10^{-2}	–
PTF	1.0×10^{-3}	–
GC*	6.7×10^{-1}	–
GT*	9.0×10^{-1}	–
XI	5.0×10^{-1}	–
D1	1.5×10^{-2}	–
D2	1.0	–
EPM (24 mm)	4.27×10^{-3}	–
AF	1.95	–
NF	7.97×10^{-1}	–
GAMMA	1.76	–
A1 ($\alpha_0 = 1.08$)	1.87×10^{4}	MPa
A2 ($\alpha_0 = 1.08$)	2.86×10^{4}	MPa
A3 ($\alpha_0 = 1.08$)	2.24×10^{4}	MPa
PEL	23.3	MPa
PC0 ($\alpha_0 = 1.08$)	4.31×10^{3}	MPa
NP	3	–
ALPHA ($\alpha_0 = 1.08$)	1.08	–

E.2. KCC model

Table E.2.: Parameters KCC of the model

name	value	unit
RO	2.22×10^{-3}	$\mathrm{g\,mm^{-3}}$
PR	2.0×10^{-1}	–
FT	2.7	MPa
A0	1.365×10^{1}	MPa
A1	5.4×10^{-1}	MPa
A2	9.134×10^{-4}	MPa
B1	1.35	–
OMEGA	5.0×10^{-1}	–
A1F	5.15×10^{-1}	–
Sλ	0	%
NOUT	2	–
RSIZE	3.937×10^{-2}	$\mathrm{mm\,in^{-1}}$
UCF	145.0	$\mathrm{MPa\,psi^{-1}}$
LCRATE	table E.4	–
LOCWID	1×10^{-1}	mm
NPTS	13	–
λ01 (24 mm)	0.0	–
λ02 (24 mm)	8.951×10^{-6}	–
λ03 (24 mm)	2.462×10^{-5}	–
λ04 (24 mm)	5.203×10^{-5}	–
λ05 (24 mm)	1.000×10^{-4}	–
λ06 (24 mm)	1.303×10^{-4}	–
λ07 (24 mm)	1.667×10^{-4}	–
λ08 (24 mm)	2.103×10^{-4}	–
λ09 (24 mm)	2.627×10^{-4}	–
λ10 (24 mm)	3.255×10^{-4}	–
λ11 (24 mm)	4.009×10^{-4}	–
λ12 (24 mm)	6.000×10^{-4}	–
λ13 (24 mm)	2.083×10^{9}	–
B3	1.0	–
A0Y	9.274	MPa
A1Y	9.208×10^{-1}	MPa
η01	0.0	–
η02	6.511×10^{-1}	–
η03	9.371×10^{-1}	–
η04	9.931×10^{-1}	–
η05	1.0	–
η06	6.593×10^{-1}	–
η07	4.187×10^{-1}	–
η08	2.736×10^{-1}	–
η09	1.935×10^{-1}	–
η10	1.403×10^{-1}	–
η11	8.984×10^{-2}	–
η12	0.0	–
η13	0.0	–
B2	1.0	–
A2F	9.121×10^{-4}	MPa
A2Y	2.162×10^{-3}	MPa

Table E.3.: Dynamic increase factor of the KCC model (compression positive, tension negative)

Strainrate [ms $^{-1}$]	DIF [-]
-1.00×10^{7}	1.00×10^{1}
-2.67×10^{-1}	9.98
-1.48×10^{-1}	8.19
-8.42×10^{-2}	6.79
-4.66×10^{-2}	5.58
-2.66×10^{-2}	4.63
-1.47×10^{-2}	3.80
-8.39×10^{-3}	3.15
-4.65×10^{-3}	2.59
-2.65×10^{-3}	2.14
-1.51×10^{-3}	1.78
-1.01×10^{-4}	1.56
-4.57×10^{-6}	1.32
-1.93×10^{-7}	1.11
-1.00×10^{-8}	1.00
0.00	1.00
1.00×10^{-8}	1.00
1.03×10^{-6}	1.08
1.01×10^{-4}	1.20
1.00×10^{-2}	1.32
7.94×10^{-2}	1.38
3.48×10^{-1}	2.25
1.53	3.68
6.69	6.03
3.02×10^{1}	9.97
1.00×10^{7}	1.00×10^{1}

Table E.4.: Equation of state of the KCC model (EOS_TABULATED_COMPACTION)

ε_V [−]	p [MPa]	K [MPa]
0.000	0.000	1.732×10^4
-1.291×10^{-3}	2.244×10^1	1.748×10^4
-2.158×10^{-2}	2.174×10^2	1.993×10^4
-5.635×10^{-2}	5.974×10^2	2.413×10^4
-1.096×10^{-1}	1.340×10^3	3.055×10^4
-1.475×10^{-1}	2.060×10^3	3.513×10^4
-1.642×10^{-1}	2.460×10^3	3.715×10^4
-2.177×10^{-1}	4.302×10^3	4.345×10^4
-2.955×10^{-1}	8.577×10^3	6.838×10^4
-3.701×10^{-1}	1.498×10^4	1.057×10^5

F. Perspective transformation

A camera projects objects in the 3-dimensional space onto a 2-dimensional image plane. A simple model to describe the basic principle of a camera is shown in figure F.1. The point $P(\tilde{X}, \tilde{Y}, \tilde{Z})$, which is given in a coordinate system aligned with the camera, is projected onto the image plane with its own coordinate system (x, y). This projection is performed along a line connecting the point P with the center of the projection. The distance between the center of the projection and the image plane is the projection distance, also called the focal length f. The line through the center of the projection and perpendicular to the image plane is called the principal axis. The point where the principal axis intersects the image plane is called the principal point. The projection $p(x, y, f)$ of the point $P(\tilde{X}, \tilde{Y}, \tilde{Z})$ onto the image plane can be calculated according to the rule of similar triangles as $x = f\tilde{X}\tilde{Z}^{-1}$, $y = f\tilde{Y}\tilde{Z}^{-1}$.

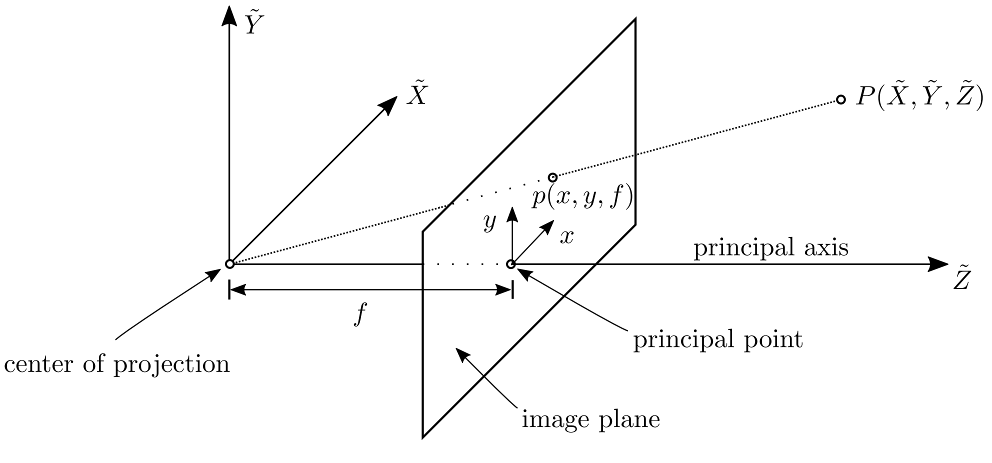

Figure F.1.: Principle of a camera

For a better description of the resulting projections and transformations, homogeneous coordinates, also called projective coordinates, are used. These allow a description of the transformations and projections by successive multiplication of the coordinates with the corresponding matrices.

Projective coordinates describe a point in the n-dimensional space by a (n+1)-dimensional vector. For example, (x, y) becomes (xw, yw, w). The additional parameter w can be understood as a scaling factor that describes multiple equivalent representations of the same point along a line in the projective space.

A transformation from the Euclidean space to the projective space can be achieved by adding $w = 1$ as a third coordinate. The inverse transformation from the projective space to the Euclidean space is computed by a division by w. This adds the possibility of describing the intersection of parallel lines at infinity in Euclidean space with $w = 0$ in projective coordinates.

The projection depicted in figure F.1 can be described by a matrix vector multiplication of the original coordinate with the so called intrinsic matrix $\boldsymbol{K}$ of the camera:

$$\begin{pmatrix} x \\ y \\ w \end{pmatrix} = \boldsymbol{K} \begin{pmatrix} \tilde{X} \\ \tilde{Y} \\ \tilde{Z} \end{pmatrix} \text{,with} \quad \boldsymbol{K} = \begin{bmatrix} f & 0 & c_x \\ 0 & f & c_y \\ 0 & 0 & 1 \end{bmatrix} \tag{F.1}$$

The intrinsic matrix contains the intrinsic parameters of the camera such as the focal length f and the position c_x and c_y of the principal points in terms of the image plane coordinates. The multiplication of the intrinsic matrix $\boldsymbol{K}$ with the coordinates $(\tilde{X}, \tilde{Y}, \tilde{Z})$ in the global camera coordinate system yields the additional parameter $w = \tilde{Z}$. The Euclidean coordinate can then be found by dividing the resulting projective coordinates (x, y, w) by the additional parameter $w = \tilde{Z}$.

Usually a point P is not given in terms of the camera coordinate system $(\tilde{X}, \tilde{Y}, \tilde{Z})$, but in a another global coordinate system $(\tilde{X}, \tilde{Y}, \tilde{Z})$. Therefore, the point P must first be transformed from the global coordinate system to the camera coordinate system. This is done using the so-called extrinsic matrix, which describes the transformation between the camera coordinate system and another global coordinate system. The extrinsic matrix consists of a rotation matrix $\boldsymbol{R}$ and a translation vector $\boldsymbol{t}$, which describes the relative orientation and position of the two coordinate systems. Due to the resulting 3x4 matrix, the point P must be described by projective coordinates.

$$\begin{pmatrix} x \\ y \\ w \end{pmatrix} = \boldsymbol{K} \left[\boldsymbol{R} \,|\, \boldsymbol{t} \right] \begin{pmatrix} X \\ Y \\ Z \\ 1 \end{pmatrix} \tag{F.2}$$

A single camera cannot provide information about the third dimension of the object space that can be drawn. Therefore, the information of interest is assumed to be in a common $X - Y$ plane and the corresponding Z coordinate is set to zero. As a consequence, the Z coordinate as well as the third column of the resulting transformation matrix can be excluded, resulting in a 3x3 matrix called the homography $\boldsymbol{H}$. The lower right entry in this homography is, analogous to the vector of projective coordinates, an arbitrary scaling factor, resulting in eight unknowns for a transformation between two perspectives. Therefore, the coordinates of four points with their respective X and Y coordinates are sufficient to solve the resulting system of equations.

Figure F.2 shows an example of an image from the test series performed that has been transformed to a view perpendicular to the surface of the concrete slab using the relative position of four known points on this surface. The red lines connecting these points with known relative coordinates are added to illustrate the transformation.

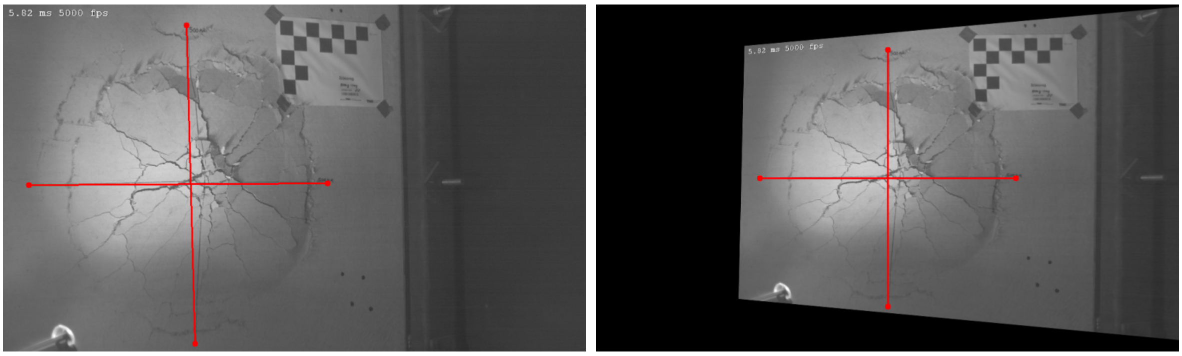

Figure F.2.: Example of a perspective transformation based on four points with known relative coordinates before (left) and after transformation (right)

Because of the assumption that the object space is reduced to the $X - Y$ plane, the tip of the debris cloud appears to be shifted to the right and up, because it is no longer in this calibrated plane. All distances in front of or behind this target plane will be displayed too long or too short according to the intercept theorem.

With the information about the intrinsic matrix, which can be obtained from a camera calibration, the rotation and translation of the transformation can be calculated from the determined homography. f Another useful application used in the context of this work is the rotation of the perspective with known information about the rotation and the intrinsic matrix. The resulting homography projects the image back into the camera coordinate system, rotates it by the given angle, and then projects it back into the image plane.

$$\boldsymbol{H}_R = \boldsymbol{K}\boldsymbol{R}\boldsymbol{K}^{-1} \tag{F.3}$$

G. Miscellaneous

G.1. Spalling threshold in dependence on the maximum x-velocity

From the determined regression line for the maximum x-velocity (figure 4.20), a required scaled thickness T_W can be extrapolated, for which a maximum x-velocity of $v_x = 0\,\mathrm{m\,s^{-1}}$ is expected. This scaled thickness of $T_W = 3.0\,\mathrm{cm\,g^{-1/3}}$, can be used to determine a threshold curve that gives the required concrete slab thickness T to prevent spalling in as a function of the explosive weight $W_{TNT,sp}$. For this purpose, it is assumed that a x-velocity of $v_x = 0\,\mathrm{m\,s^{-1}}$ is equivalent to no spalling.

The resulting threshold curve is plotted in figure G.1 as a solid line ($T_W = 3.0$). For comparison, the threshold curve from UFC-3-340-02 [Dalton et al., 2014], given by equation (G.1), is plotted in figure G.1 as a dashed line ($t_{s,UFC}$).

$$t_{\mathrm{s,UFC}} = \frac{R}{a + b\,\Psi^{2.5} + c\,\Psi^{0.5}} \tag{G.1}$$

In equation (G.1), Ψ is given by equation (4.4), R is the distance between the center of the spherical equivalent explosive charge and the surface of the concrete slab in $[ft]$, and $a = -0.02511$, $b = 0.01004$, and $c = 0.13613$ are dimensionless parameters.

The shape of the threshold curve given by the scaled thickness of the concrete slab $T_W = 3.0\,\mathrm{cm\,g^{-1/3}}$ qualitatively agrees well with the threshold curve given by UFC-3-340-02 [Dalton et al., 2014]. In the range presented, the scaled thickness of $T_W = 3.0\,\mathrm{cm\,g^{-1/3}}$ determined from a residual maximum velocity of $v_x = 0\,\mathrm{m\,s^{-1}}$ predicts, on average, a 15 % lower required concrete slab thickness than that predicted by [Dalton et al., 2014].

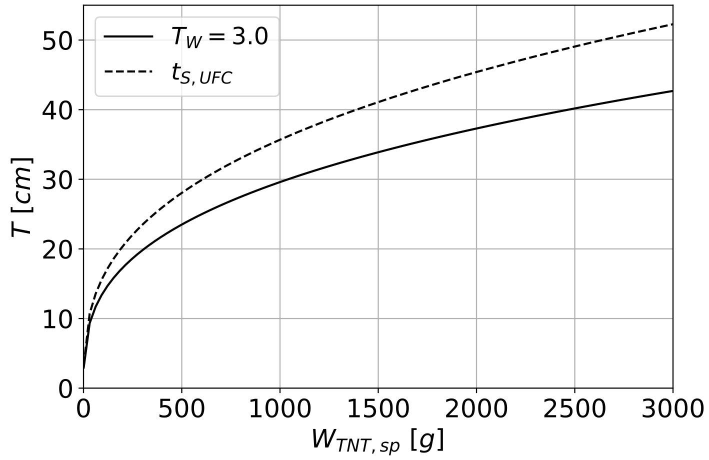

Figure G.1.: Threshold thickness of concrete slab for occurrence of spalling over TNT and spherical equivalent explosive weight $W_{TNT,sp}$

Again, it is important to note, that the threshold curves given in UFC-3-340-02 [Dalton et al., 2014] were calibrated with cylindrical charges oriented side-on to the surface of the concrete slabs, not end-on as in the present tests. To compensate for this, the TNT and spherical equivalent charges were used as input parameters for equation (G.1) along with the parameters discussed for the occurrence of a breach in section 4.5.2.

The tests performed are all below the presented threshold curves and spalling was observed in all cases. Therefore, these tests cannot be used to validate the threshold curves.

G.2. Equivalence factor for hemispherical charge

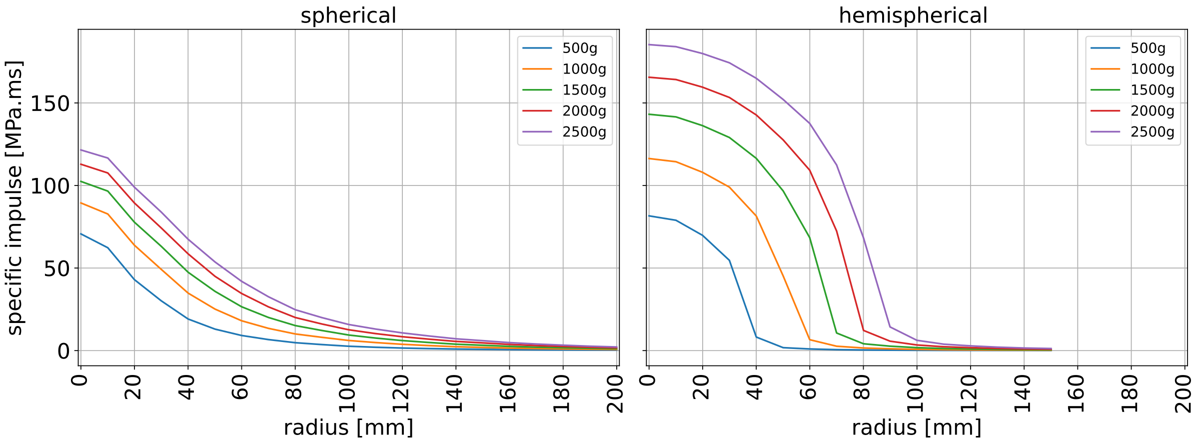

Figure G.2.: specific impulse from spherical (left) and hemispherical (right) explosive charges with different masses

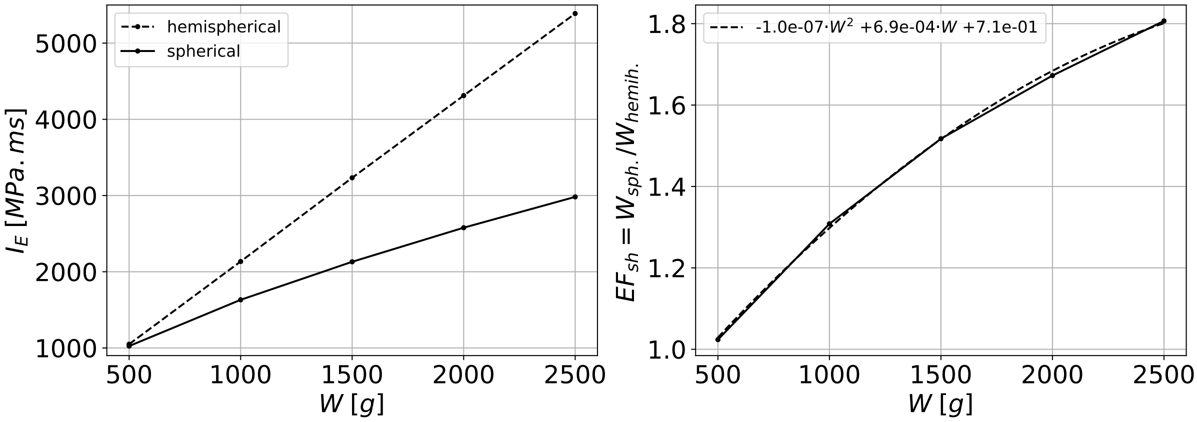

Figure G.3.: Energy equivalent impulse I_E in dependence on explosive mass (left) and resulting equivalence factor (right)

G.3. Tensile stress-strain relation with and without regularization

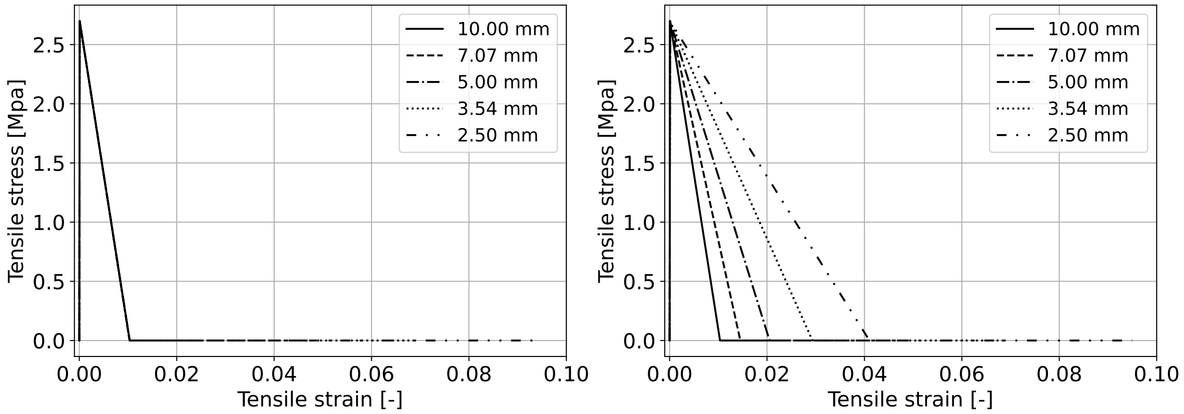

Figure G.4.: RHT: Tensile stress-strain relation with (right) and without (left) regularization

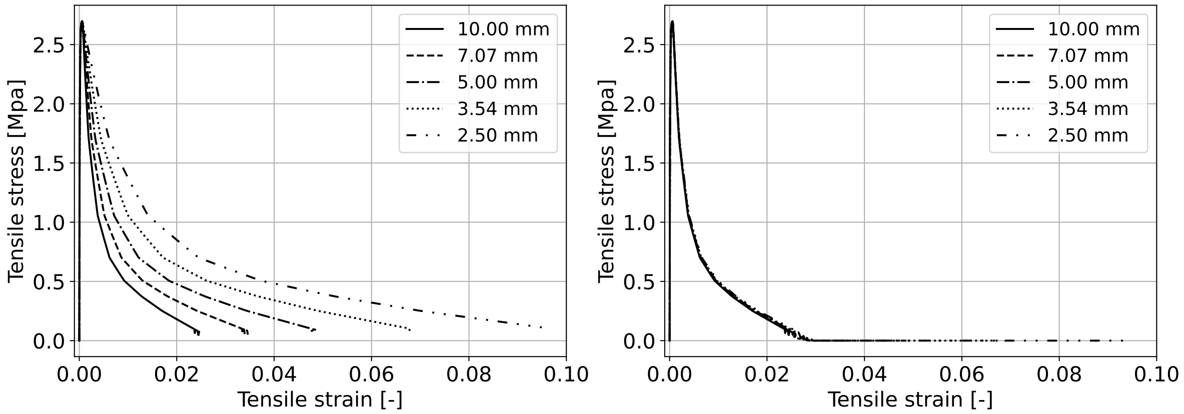

Figure G.5.: KCC: Tensile stress-strain relation with (right) and without (left) regularization

Bibliography

[Bakaert, 2023] Bakaert (2023). Bekaert dramix-4d-65/35 bg. `https://www.bekaert.com/content/dam/corporate/dop/Datasheet_Dramix%204D%206535BG_de-DE_20230210_6535BG_Dramix%204D.pdf`. Accessed: 2023-11-21.

[Barr et al., 2023] Barr, A. D., Rigby, S. E., Clarke, S. D., Farrimond, D., and Tyas, A. (2023). Temporally and spatially resolved reflected overpressure measurements in the extreme near field. *Sensors*, 23(2).

[Bažant and Oh, 1983] Bažant, Z. P. and Oh, B. H. (1983). Crack band theory for fracture of concrete. *Matériaux et Constructions*, 16(3).

[Beppu et al., 2010] Beppu, M., Ohno, T., Ohkubo, K., Li, B., and Satoh, K. (2010). Contact explosion resistance of concrete plates externally strengthened with frp laminates. *International Journal of Protective Structures Vol.1 No.2*.

[Bewick, 2017] Bewick, B. (2017). Fragmentation of solid materials using shock tubes. part 1: First test series in a small-diameter shock tube. Technical report, Defense Threat Reduction Agency (USA).

[Bouguet, 1999] Bouguet, J.-Y. (1999). Pyramidal Implementation of the Affine Lucas Kanade Feature Tracker Description of the algorithm. *Intel Corporation Microprocessor Research Lab.*

[Butcher and Karnes, 1969] Butcher, B. M. and Karnes, C. H. (1969). Dynamic compaction of porous iron. *Journal of Applied Physics*, 40(7).

[Cadoni and Forni, 2015] Cadoni, E. and Forni, D. (2015). Strain rate effects on reinforcing steels in tension. *EPJ Web of Conferences*, 94.

[Carroll and Holt, 1972] Carroll, M. M. and Holt, A. C. (1972). Static and dynamic pore–collapse relations for ductile porous materials. *Journal of Applied Physics*, 43(4).

[Castedo et al., 2020] Castedo, R., Reifarth, C., Santos, A. P., Losada, J. J., López, L. M., Chiquito, M., and Mancilla, J. M. (2020). Application of grid convergence index to shock wave validated with LS-DYNA and ProsAir. *Ingeniería e Investigación*, 39(3).

[Chen, 2020] Chen, H. (2020). On setting up a 2d structured ale model. `https://ftp.lstc.com/anonymous/outgoing/hao/sale/tutorials/Structured%20ALE%20Tutorial%204.pdf`. Accessed: 2023-08-01.

[Chen and Han, 1988] Chen, W. F. and Han, D. J. (1988). *Plasticity for Structural Engineers*. Springer New York.

[Chhabildas et al., 1999] Chhabildas, L., Kipp, M., Reinhart, W., and Wilson, L. (1999). Spall strength measurements of concrete for varying aggregate sizes. Technical report, Sandia National Laboratories.

[Comite Euro-International du Beton, 1993] Comite Euro-International du Beton (1993). *CEB/FIP Model Code 1990*. Thomas Telford.

[Cowan and Hornig, 1950] Cowan, G. R. and Hornig, D. F. (1950). The experimental determination of the thickness of a shock front in a gas. *The Journal of Chemical Physics*, 18(8).

[Crawford et al., 2012] Crawford, J., Wu, Y., Choi, H., Magallanes, J., and Lan, S. (2012). Use and validation of the release iii k&c concrete material model in ls-dyna. Technical report, Karagozian & Case.

[Dalton et al., 2014] Dalton, J. C., Gott, J. E., Parker, P. A., McAndrew, M., and Bowling, C. (2014). Unified facilities criteria (ufc): Structures to resist the effects of accidental explosions. Technical Report UFC 3-340-02, Department of Defense.

[Dobratz, 1981] Dobratz, B. M. (1981). Llnl explosives handbook: properties of chemical explosives and explosives and explosive simulants. *Lawrence Livermore National Laboratory*.

[Dua and Braimah, 2020] Dua, A. and Braimah, A. (2020). Assessment of reinforced concrete slab response to contact explosion effects. *Journal of Performance of Constructed Facilities*, 34(4).

[Duric, 2018] Duric, Z. (2018). *Sättigungsverhalten und Schädigung von Zementstein bei*

Frostbeanspruchung. PhD thesis, Universität Karlsruhe (TH).

[Esteban and Gebbeken, 2017] Esteban, B. and Gebbeken, N. (2017). A detailed comparison of two material models for concrete in the dynamic loading regime, RHT and HPG. *International Journal of Protective Structures*, 8(2).

[fib, 2013] fib, I. F. f. S. C. (2013). *fib Model Code for Concrete Structures 2010.* Wiley-VCH Verlag GmbH & Co. KGaA.

[Forbes, 2012] Forbes, J. (2012). *Shock Wave Compression of Condensed Matter.* Springer.

[Fried and P., 1994] Fried, L. and P., S. (1994). Cheetah: A next generation thermochemical code. *Lawrence Livermore National Laboratory.*

[Gabet et al., 2008] Gabet, T., Malécot, Y., and Daudeville, L. (2008). Triaxial behaviour of concrete under high stresses: Influence of the loading path on compaction and limit states. *Cement and Concrete Research*, 38(3).

[Gebbeken et al., 2006] Gebbeken, N., Greulich, S., and Pietzsch, A. (2006). Hugoniot properties for concrete determined by full-scale detonation experiments and flyer-plate-impact tests. *International Journal of Impact Engineering*, 32(12).

[Gebbeken and Hartmann, 2010] Gebbeken, N. and Hartmann, T. (2010). A new methodology for the assessment of the eos data of concrete. *International Journal of Protective Structures*, 1(3).

[Gebbeken et al., 2013] Gebbeken, N., Hübner, M., Larcher, M., Michaloudis, G., and Pietzsch, A. (2013). Beton und stahlbetonkonstruktionen unter explosion und impakt. *Beton- und Stahlbetonbau*, 108(8).

[Gebbeken et al., 2012] Gebbeken, N., Keuser, M., Linse, T., and Wensauer, R. (2012). Betonstrukturen unter explosion und impakt. In *Beton-Kalender 2012.* Ernst und Sohn.

[Gebbeken and Krauthammer, 2013] Gebbeken, N. and Krauthammer, T. (2013). Understanding the dynamic response of concrete to loading: practical examples. In *Understanding the Tensile Properties of Concrete.* Elsevier, Amsterdam.

[Gensichen, 2006] Gensichen, V. (2006). Zur einheitenanalyse und geometrischen deutung mathematischer und physikalischer gleichungen. Technical report, FH Münster, FB Bauingenieurwesen.

[Grady, 1995] Grady, D. (1995). Impact compression properties of concrete. Technical report, Sandia National Laboratories.

[Grady, 1996] Grady, D. (1996). Shock equation of state properties of concrete. Technical report, Sandia National Laboratories.

[Greulich, 2004] Greulich, S. (2004). *Zur numerischen Simulation von Stahlbeton- und Faserbetonstrukturen unter Detonationsbeanspruchung.* Dissertation, Universität der Bundeswehr München, Fakultät für Bauingenieurwesen und Umweltwissenschaften.

[Grisaro et al., 2021] Grisaro, H. Y., Turygan, S., and Sielicki, P. W. (2021). Concrete slab damage and hazard from close-in detonation of weaponized commercial unmanned aerial vehicles. *Journal of Structural Engineering*, 147(11).

[Grüneisen, 1912] Grüneisen, E. (1912). Theorie des festen zustandes einatomiger elemente. *Annalen der Physik*, 344(12).

[Grunwald, 2023] Grunwald, C. (2023). Fragmentation of concrete under dynamic loading - a numerical multiscale approach.

[Grunwald et al., 2017] Grunwald, C., Schaufelberger, B., Stolz, A., Riedel, W., and Borrvall, T. (2017). A general concrete model in hydrocodes: Verification and validation of the riedel–hiermaier–thoma model in ls-dyna. *International Journal of Protective Structures*, 8(1).

[Hall et al., 1999] Hall, C., Chhabildas, L., and Reinhart, W. (1999). Shock hugoniot and release in concrete with different aggregate sizes from 3 to 23 gpa. *International Journal of Impact Engineering*, 23(1, Part 1).

[Hanchak et al., 1992] Hanchak, S., Forrestal, M., Young, E., and Ehrgott, J. (1992). Perforation of concrete slabs with 48 MPa (7 ksi) and 140 MPa (20 ksi) unconfined compressive strengths. *International Journal of Impact Engineering*, 12(1).

[Hartley and Zisserman, 2004] Hartley, R. and Zisserman, A. (2004). *Multiple View Geometry in Computer Vision.* Cambridge University Press.

[Hartmann, 2009] Hartmann, T. (2009). *Zur mesomechanischen Modellierung von*

Beton und ihrer Anwendung zur makromechanischen Modellbildung. Dissertation, Universität der Bundeswehr München, Fakultät für Bauingenieurwesen und Umweltwissenschaften.

[Hartmann et al., 2010] Hartmann, T., Pietzsch, A., and Gebbeken, N. (2010). A hydrocode material model for concrete. *International Journal of Protective Structures*, 1(4).

[Häussler-Combe, 2022] Häussler-Combe, U. (2022). *Computational Structural Concrete.* Wiley.

[Herrmann, 2002] Herrmann, N. (2002). *Experimentelle Erfassung des Betonverhaltens unter Schockwellen.* Dissertation, TU Karlsruhe, Bauingenieur-, Geo- und Umweltwissenschaften.

[Herrmann, 1969] Herrmann, W. (1969). Constitutive equation for the dynamic compaction of ductile porous materials. *Journal of Applied Physics*, 40(6).

[Hiermaier, 2008] Hiermaier, S. (2008). *Structures Under Crash and Impact.* Springer US.

[Holmquist et al., 1993] Holmquist, T., Johnson, G., and Cook, W. (1993). A computational constitutive model for concrete subjected to large strains, high strain rates and high pressures. Technical report, Warhead mechanisms, terminal ballsitics.

[Hong et al., 2017] Hong, J., Fang, Q., Chen, L., and Kong, X. (2017). Numerical predictions of concrete slabs under contact explosion by modified k&c material model. *Construction and Building Materials*, 155.

[Hordijk, 1991] Hordijk, D. (1991). *Local approach to fatigue of concrete.* Dissertation, TU Delft, Faculty for Civil Engineering and Geosciences.

[IEP, 2023] IEP (2023). Global terrorism index 2023: Measuring the impact of terrorism. Technical report, Institute for Economics & Peace.

[Janser, 1982] Janser, P. (1982). Lethality of unprotected persons due to debris and fragments. Technical report, Basler (Ernst) And Partners Zurich (Switzerland).

[Jeremic and Bajic, 2006] Jeremic, R. and Bajic, Z. (2006). An approach to determining the tnt equivalent of high explosives. *Scientific-Technical Review Vol.LVI, No.1.*

[Johnson and Cook, 1983] Johnson, G. R. and Cook, W. H. (1983). A constitutive model and data for metals subjected to large strains, high strain rates and high temperature. Technical report, Defense Systems Division and Air Force Armament Laboratory.

[Kaehler and Bradski, 2017] Kaehler, A. and Bradski, G. R. (2017). *Learning OpenCV 3: Computer vision in C++ with the OpenCV library.* O'Reilly Media, first edition, second release edition.

[Karlos and Larcher, 2020] Karlos, V. and Larcher, M. (2020). *Guideline, building perimeter protection: design recommendations for enhanced security against terrorist attacks guideline.* European Commission, Joint Research Centre.

[Karlos and Larcher, 2023] Karlos, V. and Larcher, M. (2023). *Protection against unmanned aircraft systems: handbook on UAS risk assessment and principles for physical hardening of buildings and sites.* European Commission, Joint Research Centre.

[Khoe and Weerheijm, 2012] Khoe, Y. S. and Weerheijm, J. (2012). Limitations of smeared crack models for dynamic analysis of concrete. *12th International LS-DYNA Users Conference.*

[Kingery and Bulmash, 1984] Kingery, C. N. and Bulmash, G. (1984). Airblast parameters from tnt spherical air bursts and hemispherical surface bursts. Technical report, ARBRL-TR-02555.

[Knock et al., 2014] Knock, C., Davies, N., and Reeves, T. (2014). Predicting blast waves from the axial direction of a cylindrical charge. *Propellants, Explosives, Pyrotechnics*, 40(2).

[Kong et al., 2018] Kong, X., Fang, Q., Chen, L., and Wu, H. (2018). A new material model for concrete subjected to intense dynamic loadings. *International Journal of Impact Engineering*, 120.

[Kong et al., 2017] Kong, X., Fang, Q., Li, Q., Wu, H., and Crawford, J. E. (2017). Modified k&c model for cratering and scabbing of concrete slabs under projectile impact. *International Journal of Impact Engineering*, 108.

[Kucewicz et al., 2022] Kucewicz, M., Baranowski, P., Gieleta, R., and Małachowski, J. (2022). Investigation of dolomite' rock brittle fracture using fully calibrated karagozian case concrete model. *International Journal of Mechanical Sciences*, 221.

[Landmann, 2001] Landmann (2001). Dokumentation der parameteruntersuchungen des schädigungsverhaltens von stahlbetonplatten unter kontaktdetonationen. Technical report, WTD52.

[Langran-Wheeler et al., 2021] Langran-Wheeler, C., Rigby, S. E., Clarke, S. D., Tyas, A., Stephens, C., and Walker, R. (2021). Near-field spatial and temporal blast pressure distributions from non-spherical charges: Horizontally-aligned cylinders. *International Journal of Protective Structures*, 12(4).

[Lee et al., 1968] Lee, E. L., Hornig, H. C., and Kury, J. W. (1968). Adiabatic expansion of high explosive detonation products. Technical report, Office of Scientific and Technical Information (OSTI).

[Lewis et al., 1978] Lewis, J., Coon, P., Clare, V., and Sturdivan, L. (1978). An empirical/mathematical model to estimate the probability of skin penetration by various projectiles. Technical Report ARCSL-TR-78004, US Army Armament Research and Development Command, Chemical System Laboratory.

[Li et al., 2015] Li, J., Wu, C., and Hao, H. (2015). Investigation of ultra-high performance concrete slab and normal strength concrete slab under contact explosion. *Engineering Structures*, 102.

[Li et al., 2016] Li, J., Wu, C., Hao, H., Wang, Z., and Su, Y. (2016). Experimental investigation of ultra-high performance concrete slabs under contact explosions. *International Journal of Impact Engineering*, 93.

[Li et al., 2009] Li, Q., Lu, Y., and Meng, H. (2009). Further investigation on the dynamic compressive strength enhancement of concrete-like materials based on split hopkinson pressure bar tests. part ii: Numerical simulations. *International Journal of Impact Engineering*, 36(12).

[Lönnqvist, 1993] Lönnqvist, L. (1993). The effects of high explosives in contact with reinforced concrete slabs. Technical report, National Defence Research Establishment (Sweden).

[Lsdyna, 2019] Lsdyna (2019). Ls-dyna® theory manual.

[Lsdyna, 2021] Lsdyna (2021). Ls-dyna keyword user's manual.

[Lu and Li, 2011] Lu, Y. and Li, Q. (2011). About the dynamic uniaxial tensile strength of concrete-like materials. *International Journal of Impact Engineering*, 38(4).

[Lucas and Kanade, 1981] Lucas, B. and Kanade, T. (1981). An Iterative Image Registration Technique with an Application to Stereo Vision. *Proc. Imaging Underst. Work.*

[Luccioni et al., 2018] Luccioni, B., Isla, F., Codina, R., Ambrosini, D., Zerbino, R., Giaccio, G., and Torrijos, M. (2018). Experimental and numerical analysis of blast response of high strength fiber reinforced concrete slabs. *Engineering Structures*, 175.

[Madenci and Oterkus, 2014] Madenci, E. and Oterkus, E. (2014). *Peridynamic Theory and Its Applications.* Springer New York.

[Malvar and Crawford, 1998] Malvar, L. J. and Crawford, J. E. (1998). Dynamic increase factors for concrete. *Twenty-Eighth DDESB Seminar.*

[McVay, 1988] McVay, M. K. (1988). Spall Damage of Concrete Structures (Final Report). Technical report, US Army Engineer Waterways Experiment Station.

[Meyers, 1994] Meyers, M. A. (1994). *Dynamic Behavior of Materials.* Wiley.

[Michaloudis, 2019] Michaloudis, G. (2019). *Numerical Modeling of Embedded Interfaces based on Frictional Contact Formulations with a Covariant Description.* PhD thesis, Universität der Bundeswehr München.

[Morishita et al., 2000] Morishita, M., Tanaka, H., Ito, M., and Yamaguchi, H. (2000). Damage of reinforced concrete slabs subjected to contact detonations and effects of cover soil as a shock absorber (in japanese). *Journal of Structural Engineering (JSCE).*

[Mosig et al., 2021] Mosig, O., Zohrabyan, V., Curbach, M., Braml, T., Keuser, M., and Gebbeken, N. (2021). Spallationsversuche von faserbetonprobekörpern im split-hopkinson-bar. *Beton- und Stahlbetonbau*, 116(6).

[Murray, 2007] Murray, Y. D. (2007). Users manual for ls-dyna concrete material model 159. Technical report, Federal Highway Administration.

[Nahme, 2000] Nahme, H. (2000). Bestimmung der hugoniot-daten von beton mittels planar-impakt-untersuchungen. Technical Report Bericht E38/00, Ernst-Mach-Institut.

[Neel, 2018] Neel, C. (2018). Compaction and spall of UHPC concrete under shock conditions. *Journal of Dynamic Behavior of Materials*, 4(4).

[Oberkampf and Roy, 2010] Oberkampf, W. L. and Roy, C. J. (2010). *Verification and Validation in Scientific Computing.* Cambridge University Press.

[Ožbolt and Riedel, 2013] Ožbolt, J. and Riedel, W. (2013). Modelling the response of concrete structures from strain rate effects to shock induced loading. In Weerheijm, J., editor, *Understanding the Tensile Properties of Concrete*, Woodhead Publishing Series in Civil and Structural Engineering. Woodhead Publishing.

[Remennikov et al., 2018] Remennikov, A. M., Youssef, J., Ngo, T. D., and Mentus, I. (2018). Breach diameter analysis of concrete panels subjected to contact charge detonations. *International Journal of Impact Engineering*, 120.

[Rey-de Pedraza et al., 2018] Rey-de Pedraza, Gálvez, V., F., and Franco, D. C. (2018). Measurement of fracture energy of concrete at high strain rates. *EPJ Web of Conferences*, 183.

[Richardson and Gaunt, 1927] Richardson, L. F. and Gaunt, J. A. (1927). The deferred approach to the limit. *Philosophical Transactions of the Royal Society of London. Series A, Containing Papers of a Mathematical or Physical Character*, 226.

[Rickman et al., 2007] Rickman, D. D., Ehrgott, J. Q., Akers, S. A., Windham, J. E., and Moore, D. W. (2007). Explosive removal of concrete from reinforced walls. *2007 ASME Pressure Vessels and Piping Divison Conference.*

[Riedel, 2000] Riedel, W. (2000). Beton unter dynamischen lasten : meso- und makromechanische modelle und ihre parameter /. *Fraunhofer EMI.*

[Riedel and Forquin, 2013] Riedel, W. and Forquin, P. (2013). Modelling the response of concrete structures to dynamic loading. In Weerheijm, J., editor, *Understanding the Tensile Properties of Concrete*, Woodhead Publishing Series in Civil and Structural Engineering. Woodhead Publishing.

[Riedel et al., 2010] Riedel, W., Mayrhofer, C., Thoma, K., and Stolz, A. (2010). Engineering and numerical tools for explosion protection of reinforced concrete. *International Journal of Protective Structures*, 1(1).

[Rigby et al., 2019] Rigby, S., Akintaro, O., Fuller, B., Tyas, A., Curry, R., Langdon, G., and Pope, D. (2019). Predicting the response of plates subjected to near-field explosions using an energy equivalent impulse. *International Journal of Impact Engineering*, 128.

[Rigby et al., 2021] Rigby, S., Osborne, C., Langdon, G., Cooke, S., and Pope, D. (2021). Spherical equivalence of cylindrical explosives: Effect of charge shape on deflection of blast-loaded plates. *International Journal of Impact Engineering*, 155.

[Ritter, 2013] Ritter, R. (2013). Verformungsverhalten und grenzflächen von ultrahochleistungsbeton unter mehraxialer beanspruchung. *Thesis - TU Dresden.*

[Roache, 1994] Roache, P. J. (1994). Perspective: A method for uniform reporting of grid refinement studies. *Journal of Fluids Engineering; (United States)*, 116:3.

[Roache, 1998] Roache, P. J. (1998). *Verification and validation in computational science and engineering*, volume 895. Hermosa Albuquerque, NM.

[Rohne, 1906] Rohne, H. (1906). *Schießlehre für Infanterie.* Ernst Siegfried Mittler.

[Roos, 1992] Roos, A. J. (1992). Methods for the determination of possible damage to people and objects resulting from releases of hazardous materials (greenbook). Technical Report CPR-16E, Instituut voor Milieu- en Energietechnologie TNO Prins Maurits Laboratorium TNO, Den Haag.

[Samani and Attard, 2010] Samani, A. and Attard, M. (2010). *A Stress-Strain Model For Uniaxial Compression And Triaxially Confined Plain Concrete Incorporating Size Effect.* The University of South Wales.

[Schreer, 2005] Schreer, O. (2005). *Stereoanalyse und Bildsynthese: Mit 6 Tabellen.* Springer-Verlag Berlin Heidelberg.

[Schuler, 2004] Schuler, H. (2004). Experimentelle und numerische untersuchungen zur schädigung von stoßbeanspruchtem beton. *Forschungsergebnisse aus der Kurzzeitdynamik.*

[Schuler et al., 2006] Schuler, H., Mayrhofer, C., and Thoma, K. (2006). Spall experiments for the measurement of the tensile strength and fracture energy of concrete at high strain rates. *International Journal of Impact Engineering*, 32(10).

[Schwer et al., 2015] Schwer, L., Teng, H., and Souli, M. (2015). Ls-dyna air blast techniques : Comparisons with experiments for close-in charges. In *12. International*

LS-DYNA Users Conference.

[Schwer, 2008] Schwer, L. E. (2008). Is your mesh refined enough ? estimating discretization error using gci. In *7.LS-DYNA Anwenderforum.*

[Schwer, 2009a] Schwer, L. E. (2009a). Aluminum plate perforation : A comparative case study using lagrange with erosion , multi-material ale , and smooth particle hydrodynamics. In *7. European LS-DYNA Conference.*

[Schwer, 2009b] Schwer, L. E. (2009b). Strain rate induced strength enhancement in concrete: Much ado about nothing? In *7. European LS-DYNA Conference.*

[Sherkar et al., 2016] Sherkar, P., Shin, J., Whittaker, A., and Aref, A. (2016). Influence of charge shape and point of detonation on blast-resistant design. *Journal of Structural Engineering*, 142(2).

[Shi et al., 2020] Shi, Y., Wang, J., and Cui, J. (2020). Experimental studies on fragments of reinforced concrete slabs under close-in explosions. *International Journal of Impact Engineering*, 144.

[Shirbhate and Goel, 2021] Shirbhate, P. A. and Goel, M. D. (2021). A critical review of tnt equivalence factors for various explosives. In Saha, S. K. and Mukherjee, M., editors, *Recent Advances in Computational Mechanics and Simulations.* Springer Singapore.

[Slater et al., 2000] Slater, J., Dudek, J., and Tatum, K. (2000). The nparc alliance verification and validation archive. Technical report, NASA.

[Solomos et al., 2020] Solomos, G., Larcher, M., Valsamos, G., Karlos, V., and Casadei, F. (2020). *A survey of computational models for blast induced human injuries for security and defence applications.* European Commission, Joint Research Centre.

[Szeliski, 2011] Szeliski, R. (2011). *Computer vision: Algorithms and applications.* Texts in computer science. Springer.

[Thienel, 2018] Thienel, K.-C. (2018). *Faserbeton.* Universität der Bundeswehr, Institut für Werkstoffe des Bauwesens.

[Tu et al., 2019] Tu, H., Fung, T. C., Tan, K. H., and Riedel, W. (2019). An analytical model to predict the compressive damage of concrete plates under contact detonation.

Int. J. Impact Eng., 134.

[Tu et al., 2022] Tu, H., Fung, T. C., Tan, K. H., and Riedel, W. (2022). An analytical model to predict spalling and breaching of concrete plates under contact detonation. *International Journal of Impact Engineering*, 160.

[Tu and Lu, 2009] Tu, Z. and Lu, Y. (2009). Evaluation of typical concrete material models used in hydrocodes for high dynamic response simulations. *International Journal of Impact Engineering*, 36(1).

[van Amelsfort and Weerheijm, 1988] van Amelsfort, R. and Weerheijm, J. (1988). The failure mode of concrete slabs due to contact charges. Technical report, Prins Maurits Laboratory (Netherlands).

[van Mier, 1984] van Mier, J. (1984). Strain-softening of concrete under multiaxial loading conditions.

[Wang et al., 2013] Wang, W., Zhang, D., Lu, F., Wang, S.-c., and Tang, F. (2013). Experimental study and numerical simulation of the damage mode of a square reinforced concrete slab under close-in explosion. *Engineering Failure Analysis*, 27.

[Wang et al., 2021] Wang, Y., Kong, Xiangzhenand Fang, Q., Chen, L., and Fan, J. (2021). Modelling damage mechanisms of concrete under high confinement pressure. *International Journal of Impact Engineering*, 150.

[Wang et al., 2022] Wang, Z., Wen, H., Li, X., and Hu, J. (2022). On the equation of state for concrete-like materials. *Journal of Building Engineering*, 61.

[Weerheijm et al., 1988] Weerheijm, J., Krauthaus, W., and Opschoor, G. (1988). The failure mode of layered concrete constructions due to contact charges. Technical report, Prins Maurits Laboratory (Netherlands).

[Weerheijm and Vegt, 2010] Weerheijm, J. and Vegt, I. (2010). Measurement of fracture energy of concrete at high strain rates. *Fracture Mechanics of Concrete and Concrete Structures-Recent Advances in Fracture Mechanics of Concrete.*

[Willam, K.J. and Warnke, E.P., 1974] Willam, K.J. and Warnke, E.P. (1974). Constitutive model for the triaxial behaviour of concrete. Technical report, IABSE.

[Wu et al., 2010] Wu, C., Fattori, G., Whittaker, A., and Oehlers, D. (2010). Investigation of air-blast effects from spherical-and cylindrical-shaped charges. *International Journal of Protective Structures*, 1.

[Wu et al., 2016] Wu, C. T., Hu, W., and Koishi, M. (2016). A smoothed particle galerkin formulation for extreme material flow analysis in bulk forming applications. *International Journal of Computational Methods*, 13(03).

[Wu et al., 2020] Wu, J., Zhou, Y., Zhang, R., Liu, C., and Zhang, Z. (2020). Numerical simulation of reinforced concrete slab subjected to blast loading and the structural damage assessment. *Engineering Failure Analysis*, 118.

[Xiao et al., 2020a] Xiao, W., Andrae, M., and Gebbeken, N. (2020a). Effect of charge shape and initiation configuration of explosive cylinders detonating in free air on blast-resistant design. *Journal of Structural Engineering*, 146(8).

[Xiao et al., 2020b] Xiao, W., Andrae, M., and Gebbeken, N. (2020b). Influence of charge shape and point of detonation of high explosive cylinders detonated on ground surface on blast-resistant design. *International Journal of Mechanical Sciences*, 181.

[Xu and Wen, 2013] Xu, H. and Wen, H. (2013). Semi-empirical equations for the dynamic strength enhancement of concrete-like materials. *International Journal of Impact Engineering*, 60.

[Xu and Lu, 2006] Xu, K. and Lu, Y. (2006). Numerical simulation study of spallation in reinforced concrete plates subjected to blast loading. *Computers and Structures*, 84(5).

[Yamaguchi et al., 2011] Yamaguchi, M., Murakami, K., Takeda, K., and Mitsui, Y. (2011). Blast resistance of polyethylene fiber reinforced concrete to contact detonation. *Journal of Advanced Concrete TEchnologie Vol.9 No.2.*

[Yin et al., 2023] Yin, X., Li, Q., Chen, B., and Xu, S. (2023). An improved calibration of karagozian & case concrete/cementitious model for strain-hardening fibre-reinforced cementitious composites under explosion and penetration loadings. *Cement and Concrete Composites*, 137.

[Zhao et al., 2019] Zhao, C., Lu, X., Wang, Q., Gautam, A., Wang, J., and Mo, Y. (2019). Experimental and numerical investigation of steel-concrete (sc) slabs under contact blast loading. *Engineering Structures*, 196.

[Zhou et al., 2020] Zhou, R., Chen, H.-M., and Lu, Y. (2020). Mesoscale modelling of concrete under high strain rate tension with a rate-dependent cohesive interface approach. *International Journal of Impact Engineering*, 139.

[Zhou and Hao, 2009] Zhou, X. and Hao, H. (2009). Mesoscale modelling and analysis of damage and fragmentation of concrete slab under contact detonation. *International Journal of Impact Engineering*, 36(12). Seventh International Conference on Shock and Impact Loads on Structures.